Synthesis and Characterisation of Barium Titanate Nanoparticles for Second Harmonic Generation Applications

Omar Matar

Submitted in accordance with the requirements for the degree of

Doctor of Philosophy

The University of Leeds

Institute for Materials Research

School of Chemical and Process Engineering

February, 2017

The candidate confirms that the work submitted is his own, except where work which has formed part of jointly-authored publications has been included. The contribution of the candidate and the other authors to this work has been explicitly indicated below. The candidate confirms that appropriate credit has been given within the thesis where reference has been made to the work of others. The jointly authored publications are referenced [1] & [2] and the contributed work is summarised below:

1. O. Matar, O.M. Posada, N.S. Hondow, C. Wälti, M. Saunders, C.A. Murray, *et al.*, Barium Titanate Nanoparticles for Biomarker Applications, J. Phys. Conf. Ser. 644 (2015) 012037. (Chapter 4 and Chapter 5 in this thesis).
2. O. Matar, N. Hondow, O. Posada, M. Routledge, D. Hernandez-Maldonado, C. Wälti, *et al.*, Analytical electron microscopy of barium titanate and barium-strontium titanate nanoparticles for second-harmonic biomarkers, in: Eur. Microsc. Congr. 2016 Proc., Wiley-VCH Verlag GmbH & Co. KGaA, 2016. (Chapter 5 in this thesis).

Figure 1 in [1] was collected at Diamond Light Source (Synchrotron Facility) by Dr C. Murray, shown in Figure 74, Figure 77 and Figure 83; Chapter 4. Figure 1 in [2] shows the HAADF-STEM data acquired at SuperSTEM by Dr David Hernandez-Maldonado in Section 5.2, Chapter 5.Figure 4 in [1] and Figure 3 in [2] cell culture images were prepared in the presence of Dr Olga Posada and the critical point drying, resin embedding and serial sectioning were performed by Mr Martin Fuller as stated throughout.

Experimental work presented here, was carried out by the candidate (unless stated) under the supervision of Dr A. P. Brown, Dr S. J. Milne and Prof R. M. D. Brydson who provided contributions to this thesis in terms of advice and corrections whilst preparing this manuscript.

Experimental data collected by another user (with the author present) included the collection of electron energy loss spectroscopy data by Dr Michael Ward and Dr David Hernandez-Maldonado and the Cryo-TEM session operated by Dr Nicole Hondow. This copy has been supplied on the understanding that it is copyright material and that no quotation from the thesis may be published without proper acknowledgement.

Acknowledgements

I would first like to extend my gratitude to my supervisors Andy Brown, Steve Milne and Rik Brydson for providing their kind and generous support through this PhD research. I would like to say a special thank you to my primary supervisor Andy who has been great mentor, not only for getting me into good physical shape by welcoming me on the lunchtime jogs, but constantly teaching and providing life advice when it was needed. But I truly couldn't have finished this without your help.

Nicole and Mike, both quite honestly the most wonderful human beings; both of you always provided me with support whenever I needed it, and (from appearance) neither of you took it on as a burden. The support and mentoring I received from both of you is something I will remember always. Mike, Helen and Andy, thank you for my 26th Birthday, I will never forget it. Furthermore, LEMAS staff have always been incredibly welcoming and helpful and I will always be thankful for your support. I would like to thank Christoph Wälti for welcoming me at the beginning; you were always there to provide support/fix the microscope, so thank you. Olga (team NOO), thank you for all your help/time you spent in the lab. They were truly some of my favourite days.

I would like to thank officemates (past and present), it was a pleasure to know you all. Thank you to my friends; Dom and Katy you were both incredible support and wonderful people. My family for supporting me also, you never failed to provide motivation and love whenever it felt like it was getting too much. Finally, Kathryn, you have been such a kind, loving, wise and beautiful soul, I will never forget how much you helped me through it all.

On a personal note I do feel lucky to complete this project, however some days it took its toll on me mentally. Making me feel anxious, afraid and sometimes angry at myself. This whole experience made me feel like an imposter, I thought I worked hard by turning up, putting in effort and never stop thinking about the next task. However, it led to a false sense of security and ambition that I will hopefully learn from and it made me realise that stopping to think about the bigger picture is more valuable than people let on.

Abstract

This thesis presents findings of hydrothermally synthesised barium titanate nanoparticles for biomarker applications. Hydrothermal barium titanate (H-BT) and barium strontium titanate (H-BST) nanoparticles were successfully synthesised and were characterised for their second harmonic generation applications. X-Ray powder diffraction (laboratory and synchrotron) highlighted that H-BT and H-BST had a mixed tetragonal and cubic phase fraction present by Rietveld peak fitting analysis. Regardless of the phase fractions present, all nanoparticles emitted SHG (including a commercial cubic $BaTiO_3$ sample that appeared cubic by XRD). The smaller sized H-BST nanoparticles (45 nm) required an increase in incident laser power compared to the H-BT sample (~140 nm).

The phase of the nanoparticles and origin of SHG was investigated by electron diffraction, electron energy loss spectroscopy and high resolution HAADF-STEM imaging. *In-situ* electron diffraction of barium titanate showed that the tetragonal diffraction pattern transformed to a cubic pattern when heated above the Curie point. The phase transition was also investigated by EELS measurements of the Ti-L_3 edge t_{2g}-e_g peak separation at room temperature and 400 ^oC showing the reduction in t_{2g}-e_g peak separation when the sample transforms from a tetragonal to cubic phase. The surface of the nanoparticles also showed an atomically rough layer with incomplete unit cells, and the 'bulk' of the nanoparticles showed random Ti-atom distortions by HAADF-STEM Ti-atom displacement analysis. This suggests the origin of SHG is likely to be both a cause of surface roughness and local asymmetric distortions in the nanoparticle bulk.

The hydrothermally prepared and PLL-coated nanoparticles were measured to assess the cell viability and DNA damage of cells after a 24-hour exposure. The

nanoparticles were measured by dynamic light scattering to understand the behaviour of uncoated and PLL-coated nanoparticles suspended in different media. The uncoated nanoparticles showed little reduction in cell viability and genotoxicity, whereas the PLL coated nanoparticles showed a reduction in cell viability and a failed comet assay at concentrations ≥10 μg/mL. The nanoparticles were confirmed to be taken up into the cells by electron microscopy of critically point dried and resin embedded cell sections. Cryo-TEM of the H-BT-PLL nanoparticles suspended at 100 μg/mL in complete cell culture media showed that some nanoparticles were coated with a calcium phosphate coating and others not. This resulted in, either cells having a direct exposure to PLL and positively charged nanoparticles, or all the calcium was removed from the media that is required for cell signalling pathways which could lead to a reduction in cell viability.

Table of Contents

List of Tables

List of Figures

List of Publications

Conference Proceedings

1. O. Matar, O.M. Posada, N.S. Hondow, C. Wälti, M. Saunders, C.A. Murray, *et al.,* Barium Titanate Nanoparticles for Biomarker Applications, J. Phys. Conf. Ser. 644 (2015) 012037. (Chapter 4 and Chapter 5 in this thesis).
2. O. Matar, N. Hondow, O. Posada, M. Routledge, D. Hernandez-Maldonado, C. Wälti, *et al.*, Analytical electron microscopy of barium titanate and barium-strontium titanate nanoparticles for second-harmonic biomarkers, in: Eur. Microsc. Congr. 2016 Proc., Wiley-VCH Verlag GmbH & Co. KGaA, 2016. (Chapter 5 in this thesis).

Conference Presentations

International Symposium of Applied Ferroelectrics (ISAF) **2014**. Title: Synthesis of tetragonal barium titanate for use as a biomarker – *Conference presentation*. (Chapter 4 in this thesis).

Microscience and Microscopy Congress (MMC) **2015**. Title: Microscopy of barium titanate nanoparticles for biomarker applications – *Conference presentation*. (Chapter 5 in this thesis).

European Microscopy Congress (EMC) **2016**. Title: Analytical electron microscopy of barium titanate nanoparticles for Second harmonic biomarkers – *Poster presentation.* (Chapter 6 in this thesis).

Chapter 1 – Introduction

1.1 Biomarkers

A biomarker is defined as a material that marks or maps a biological process or function. The most significant breakthrough in biomarkers was the discovery and use of the green fluorescent protein (GFP) from the Jellyfish *Aequorea Victoria* [3,4]. Use of GFP is a well-established technique to mark gene expression and protein targeting in intact cells and organisms [5] and uses the phenomenon of fluorescence under ultraviolet radiation. A major drawback to use of GFP however, arises due to photobleaching. This is the photochemical degradation of the dye where, upon excitation, the fluorophore may undergo an electronic state transition, causing the formation of free radicals. Which can react with the surrounding environment disabling the proteins ability to fluoresce ([6,7] and Figure 1). In addition, fluorescent molecules must be genetically encoded to be used as a biomarker, which can be labour intensive and has caused problems with energy transfer between proteins [8].

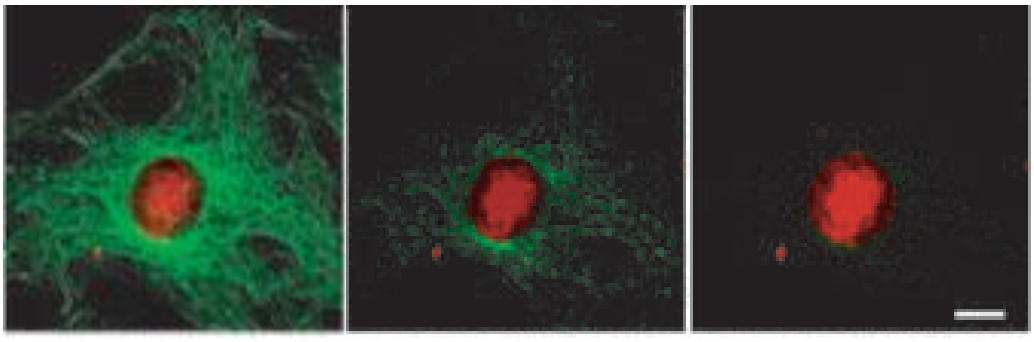

Figure 1. Photobleaching of a AlexaFluor 488 fluorescently tagged 3T3 cell under continuous illumination for the specified times. Highlighting the photochemical degradation of the dye; taken from [9]**.**

A practical solution to GFP bleaching came with the use of semiconductor quantum dots (QDs) as fluorescent biomarkers. QDs are semiconductor nanocrystals which have a higher efficiency of fluorescent emission in comparison to fluorescent proteins. However QDs are known to have problems with intermittency or “blinking” (stochastic on/off fluorescence) when using them as biomarkers which can be problematic when using them for long lifetime tracking ([10] and Figure 2). In addition, semiconductor QDs have a potential lack of biocompatibility due to their composition; e.g. Cadmium Selenide & Cadmium Telluride because cadmium is known to induce cytotoxic responses. This is generally overcome by coating the dots in an inert, inorganic shell such as zinc sulphide [11,12].

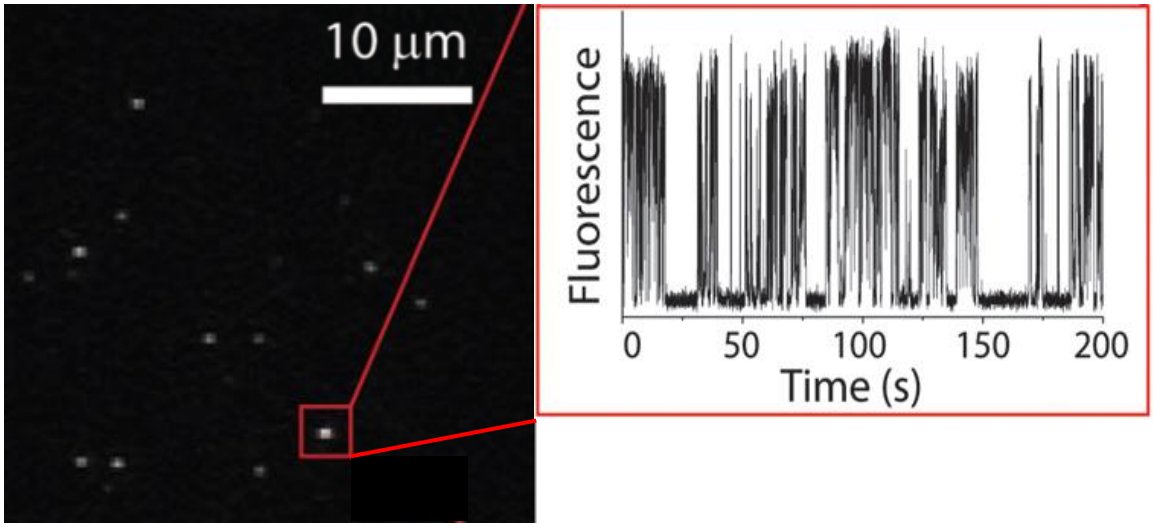

Figure 2. Single frame from a CdSe-CdS (core-shell) video, showing the quantum dot fluorescence over a specified time, with the inset showing the stochastic on/off signal generated; taken from [13]**.**

Developments in fluorescence microscopy have allowed the user to image cells beyond the diffraction limit of light by a number of techniques collectively known as super-resolution microscopy. These techniques are specifically known as

stimulated emission depletion microscopy (STED), photoactivated localisation microscopy (PALM), stochastic optical reconstruction microscopy (STORM) and structured illumination microscopy (SIM) [14,15]. However, the use of harmonic nanoparticles aims to develop inorganic biomarkers that overcome the shortcomings of fluorescent molecules and QDs. This can be achieved by using the phenomena of second harmonic generation (SHG) to make second harmonic nanoprobes. The advantage of second harmonic generation is its stability over continuous illumination periods, making SHG markers suitable for long lifetime tracking. These harmonic nanoparticles do not suffer from photobleaching (as for fluorescent markers, Figure 1) or blinking (as for semiconductor QDs, Figure 2) due to the virtual energy state transition that is induced prior to emission; discussed in Section 1.2 (Figure 3). It is important to note however, that second harmonic light is only generated if the crystal structure is non-centrosymmetric. In the case of perovskite material such as barium titanate, this requires transformation to a tetragonal crystal structure (Section 1.3).

1.2 Second harmonic generation (SHG)

Light can be described as a sinusoidal electromagnetic wave that propagates at an angular frequency ω ($2\pi f$). When this radiation interacts with a centrosymmetric material it induces a linear dipole moment (polarisation) in response to the propagation of the electric field through the material. However, in crystals that are non-centrosymmetric (no inversion symmetry) there can be a non-linear response to the incident radiation, particularly at high incident intensity [16]. Tetragonal $BaTiO_3$ can produce a non-linear optical response

when illuminated by an intense photon source. This second harmonic generation (SHG) of light, also known as frequency doubling is the simultaneous absorption of two near-infrared photons, with re-emission of a single photon of double the incident frequency in the visible region (Figure 3).

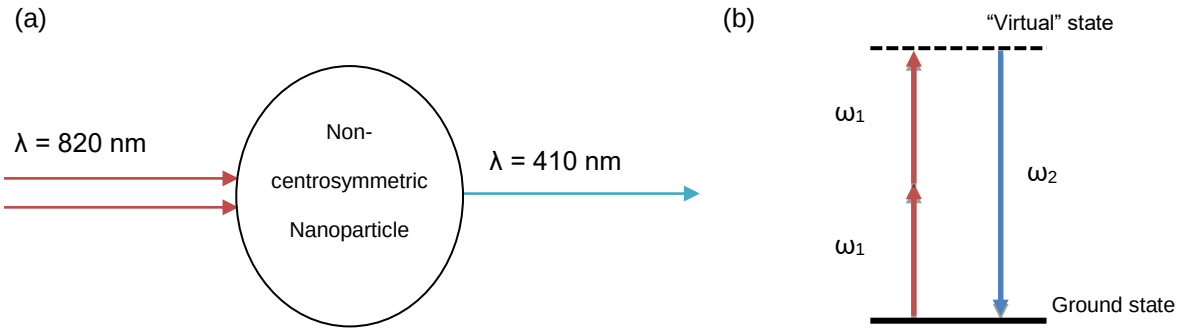

Figure 3. (a) Diagram showing the simultaneous absorption of two near-infrared photons interacting with a non-centrosymmetric nanoparticulate crystal and generating light at double the frequency. (b) Jablonski diagram of SHG; adapted from [17]**.**

This harmonic light generation can provide emission during continuous illumination to circumvent the drawbacks (discussed above) associated with long lifetime imaging and tracking of conventional markers.

1.3 Barium titanate nanoparticles.

Barium titanate adopts a tetragonal crystal structure when below the ferroelectric Curie point (130 ^{o}C for pure $BaTiO_3$), this structure possesses a non-centrosymmetric crystal structure and is one of the most extensively researched perovskite materials to date. It has excellent ferroelectric properties, high dielectric susceptibility and is used in a large variety of applications; the most common being multilayer ceramic capacitors [18]. There

is a demand to make thinner layers in micro-capacitors and therefore smaller particles of $BaTiO_3$ are required. However a problem associated with the size reduction of barium titanate is that the paraelectric cubic phase (centrosymmetric crystal structure) becomes more stable than the tetragonal phase (even below the Curie temperature) – leading to inferior dielectric properties [19].

In order for a material to be ferroelectric there must be a net (electrostatic) dipole moment within the material. In the case of tetragonal barium titanate – a non-centrosymmetric crystal medium – the net dipoles are formed by the titanium atom in the oxygen octahedron being displaced from the centre of the unit cell (see Chapter 2, Section 2.3.1 for a detailed discussion)

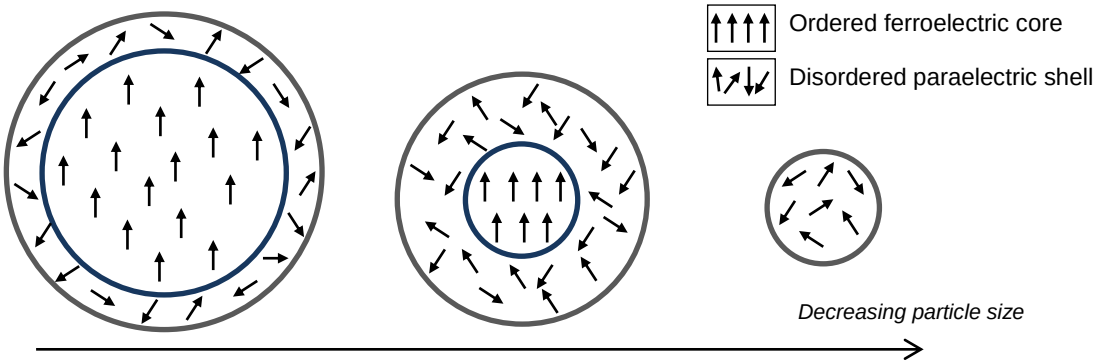

Figure 4. Schematic barium titanate nanoparticle as a function of decreasing particle size; the ferroelectric tetragonal core becomes less dominant in terms of total particle volume, and the paraelectric cubic surface shell ultimately dominates at and below a critical size. As the particle size decreases, naturally the bulk dipole interaction decreases and consequently disorder will eventually dominate the bulk [20]**.**

The addition of strontium into the barium titanate lattice ($Ba_{1-x}Sr_xTiO_3$) lowers the transition (Curie) temperature from the tetragonal to the cubic crystal structure (transition of ferroelectric to paraelectric) and is seen to increase the

dielectric constant of the material (the net titanium dipole, discussed in Section 2.4.1) [21]. It is known that increasing amounts of strontium ions incorporated into the barium titanate lattice shifts the unit cell to smaller lattice parameters as more strontium is incorporated [22]. This implies that if the strontium ions are homogenously incorporated into the barium titanate lattice, they may inhibit particle growth, whilst still retaining a tetragonal phase below the, now lower, Curie point [23,24].

The phenomenon of SHG suggests that non-centrosymmetric $BaTiO_3$ and $Ba_{1-x}Sr_xTiO_3$ nanoparticles can be used as second harmonic nanoprobe biomarkers. This thesis will focus on the unexplored method of the hydrothermal synthesis of barium titanate or barium strontium titanate nanoparticles for use as second harmonic nanoprobes. The thesis will introduce the current research associated with barium titanate and barium strontium titanate biomarkers and will present the characterisation of these nanoparticulate structures. The results include bulk characterisation of the materials such as X-ray diffraction (XRD), dynamic light scattering (DLS) and second harmonic generation (SHG) imaging. In addition, individual nanoparticle characterisation techniques such as transmission electron microscopy (TEM), scanning transmission electron microscopy (STEM) and electron energy loss spectroscopy (EELS) are investigated. Finally, the work will assess cell viability of *in vitro* cells exposed to these particles.

1.4 Aim of this project:

To explore hydrothermally synthesised $BaTiO_3$ nanoparticle systems for biomarker applications.

1.5 Objectives:

- To synthesise barium titanate nanoparticles that produce SHG.
- To incorporate strontium homogenously into the barium titanate lattice to enhance SHG.
- To characterise the $BaTiO_3$ nanoparticle crystal structure by X-Ray diffraction, transmission electron microscopy and electron energy loss spectroscopy.
- To functionalise $BaTiO_3$ nanoparticles for enhanced uptake *in vitro*.
- To measure $BaTiO_3$ nanoparticle dispersions in complete cell culture media in order to understand nanoparticle behaviour before exposure to cells.
- To measure the cell viability on exposure to both uncoated and coated barium titanate nanoparticles.
- To assess the cellular uptake of barium titanate nanoparticles following exposure to cells *in vitro*.

Chapter 2 – Synthesis and Characterisation of barium titanate nanoparticles – Literature review.

2.1 Second harmonic generation (SHG) microscopy

When incident light radiation interacts with a centrosymmetric material it induces a linear dipole moment (polarisation) in response to the propagation of the electric field through the material. However in dielectric crystals that are non-centrosymmetric (meaning that there is no inversion symmetry) such as tetragonal barium titanate there can be a nonlinear response to the incident radiation, particularly at high incident intensity; Figure 5 [16].

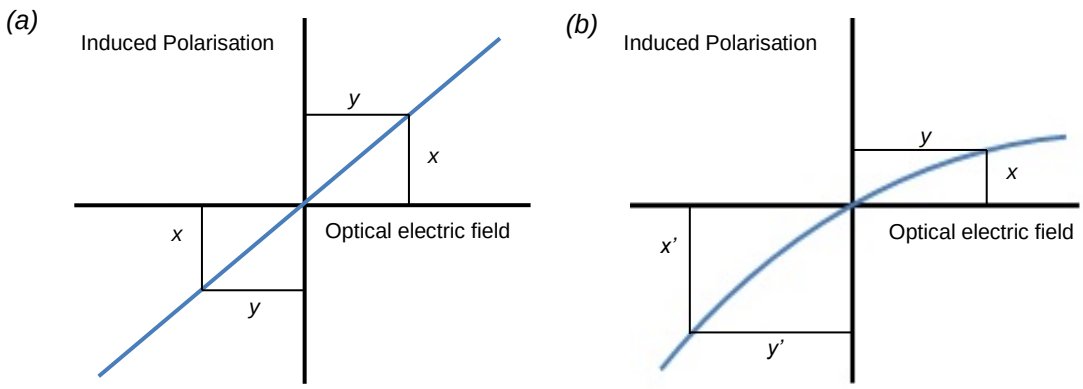

Figure 5. (a) Linear response of induced polarisation to the electric field of light in a centrosymmetric material. (b) Nonlinear response to the incident electromagnetic radiation in a non-centrosymmetric material [16,25]**.**

Though nonlinear optics originates from quantum confinement of electrons in molecules [25], the interpretation of both the quantum mechanical and classical approach can be summarised by the ease of displacement of electrons in a potential harmonic well [25]; Figure 6. An electron is bound to a molecular orbital of a material oscillating at a natural frequency with an equal

displacement '*x*'. The harmonic profile represents the response of the electron by the electric component to the optical field (a sinusoidal varying field) [25,26].

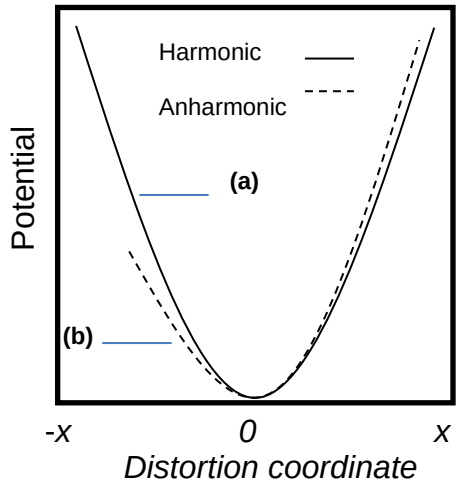

Figure 6. (a) Displacement of an electron in a centrosymmetric material – harmonic profile. (b) A non-centrosymmetric material – anharmonic profile.

A harmonic response in the above figure represents the linear polarisation of a molecule or material where the displacement of the electron is directly proportional to the applied optical field. However if the material is non-centrosymmetric or has a net dipole moment it modifies the incident radiation and the resultant polarisation [25], resulting in an anharmonic displacement of the electron plot shown in the above figure; where the displacement of the electron or molecule is no longer proportional to the incident radiation. This is the origin of nonlinear polarisation and it occurs in a medium that lacks a centre of inversion symmetry such as tetragonal barium titanate.

Second harmonic generation is the production of light at a wavelength half that of the incident photons. It is a nonlinear optical technique where the incident frequency of photons is converted to light of exactly double the frequency but does require an intense (or multiphoton) incident light source; Figure 7.

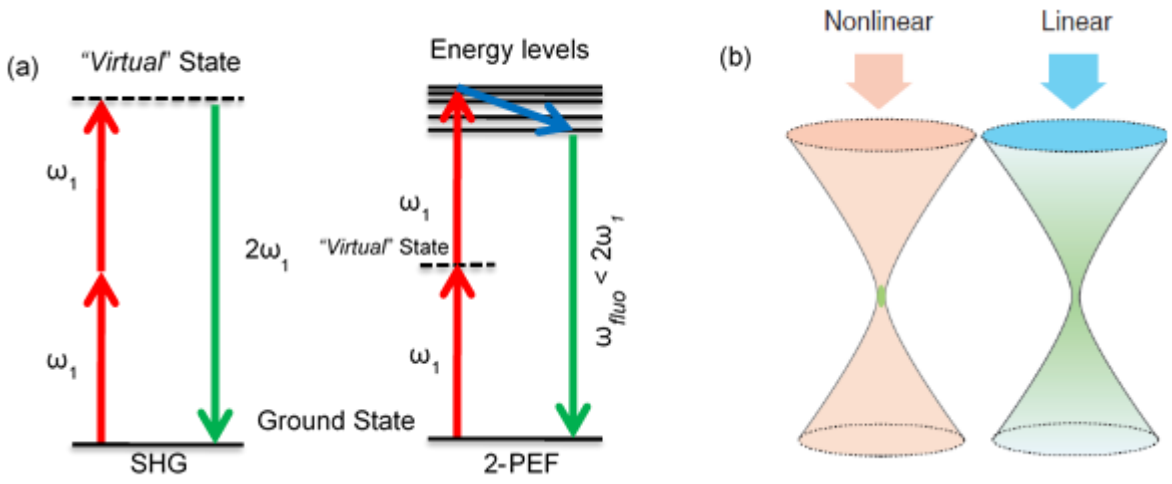

Figure 7. (a) Jablonski diagrams of SHG vs conventional two-photon excited fluorescence (2-PEF). The SHG diagram shows the simultaneous absorption of two photons with the emission of a single photon of double the frequency, compared to 2-PEF where the electrons are excited to higher energy levels and upon relaxation by vibrational losses emits a photon of less than double the incident frequency. (b) Comparison of the illumination mechanisms of SHG (nonlinear) excitement compared to 2-PEF (linear), showing spatial confinement of generated SHG signal at a focal spot generated by the femto-second pulsed near infrared incident beam (orange cone) compared to a cone of fluorescence from conventional fluorescence microscopy (blue cone); taken from [27,28]**.**

Franken *et al.* first demonstrated the phenomenon of second harmonic generation by first deriving the phenomenon mathematically, then showing the macroscopic properties of SHG in a quartz crystal [29]. The mathematical explanation of SHG is discussed in detail in Chapter 3, Section 3.8. However, SHG research has increased over the recent years due to the improvement of laser intensity and the ability to generate good second harmonic intensity.

Second harmonic light is produced by a femtosecond-pulsed laser of near-infrared light. Near-infrared wavelengths are used because of optical windows allowing absorption and scattering from biological tissue (such as: blood, skin, water and fatty tissue), but at longer wavelengths the absorption of light is low and this allows for increased sample penetration depth (ideal for thick tissue samples) [30,31]. The laser is pulsed because it allows a higher flux of photons to be delivered to the sample and the SHG output signal scales quadratically when incident radiation power is increased [32,33]. However, as this technique requires a high intensity laser to generate second harmonic radiation in the first place, it is a less than ideal situation for applications involving radiation sensitive biological tissue. A review of near infrared radiation (NIR) by Karsten König, revealed that peak laser intensities higher than 100 GW/cm^2 are likely to be harmful to intracellular components [34]. Meaning there is a limit to the laser intensity that can be used to image in biological media without inducing damage. Further difficulties are presented by Taatjes *et al.* in that SHG signal is reduced in samples embedded in epoxy resin, fixed with glutaraldehyde and stained with osmium tetroxide (generic electron microscopy sample preparation steps), meaning that correlation microscopy of biological samples requires further research and understanding [35].

One of the first biological SHG experiments was conducted in 1986 [32,33], where membranes in biological samples were visualised by their isotropic endogenous structures (such as collagen, muscle or microtubules) [36]. Campagnola *et al.* exploited the intense endogenous SHG signal that is produced from collagen to characterise collagen stacks in various mouse tissue thicknesses, showing that the SHG of the mouse leg tissue is still present at a

depth of 300 µm [37]. The intense SHG signal was also exploited by Le *et al.* when distinguishing between auto-fluorescent areas and areas that give SHG signal from elastin in swine arteries [38]. Le *et al.* confirmed the SHG signal was generated by collagen and could be collected *in vivo* whereas the auto-fluorescence signal present was from stained elastin components but only imaged *in vitro*. Their results showed an increase in SHG in the diseased arteries because collagen is denser in the diseased tissue; Figure 8.

Endogenous SHG imaging microscopy without the use of nanoparticles has shown signal limitations such as absorption/scattering of the SHG signal in thick samples before reaching the detector and a weakly generated SHG signal in biological tissue [17], leading to the explicit use of nanoparticles as SHG nanoprobes.

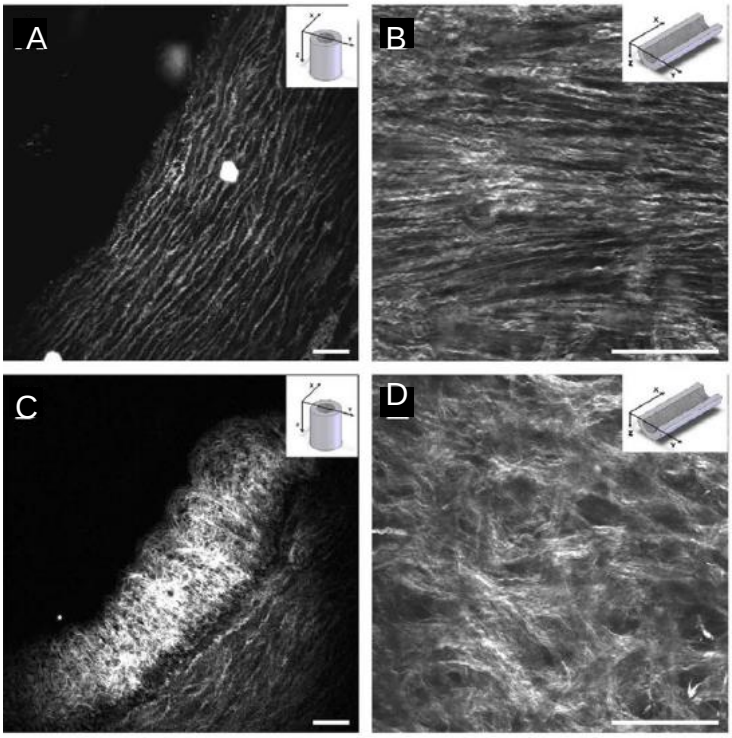

Figure 8. SHG imaging of healthy and atherosclerotic iliac arteries from Ossabaw pigs. (a) Cross-sectional and (b) luminal views of collagen in healthy arteries compared to (c) cross-sectional and (d) luminal views of an atherosclerotic artery. In each case scale bars are at 75 µm; taken from [38]**.**

Kim *et al*. studied the SHG output of sub-100 nm barium titanate nanoparticles down to 22 nm [39]. The research showed the SHG output of $BaTiO_3$ nanoparticles decreased in power when the size of the nanoparticles decreased (from 50 nm to 22 nm). Kim *et al.* characterised the crystal phase of $BaTiO_3$ nanoparticles by XRD, suggesting $BaTiO_3$ is 'pseudo-cubic' i.e. appears cubic by XRD analysis due to the lack of XRD splitting in the (002/200) peak, but has tetragonal features (in that it emits SHG light). The research hypothesized the origin of second harmonic signal in barium titanate particles may *not* have been from a tetragonal phase nanoparticle, but arose from broken inversion symmetry of the surface (surface-roughened) as shown in Figure 9 [39].

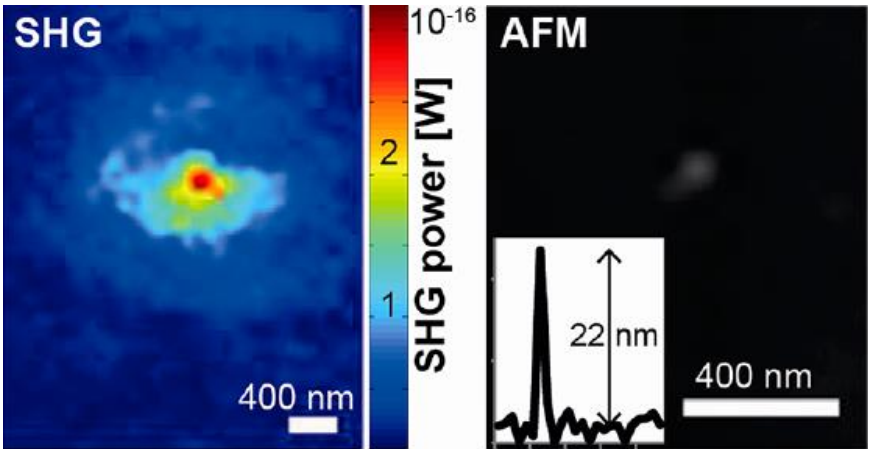

Figure 9. Second harmonic and atomic force microscopy image of a 22 nm sized $BaTiO_3$ nanoparticle on a glass substrate; taken from [39]**.**

Kim *et al.* undertook further work to prove the quadratic dependency of the SHG signal with the incident beam power, providing further evidence that it is SHG of light and not Rayleigh scattering which has produced from 22 nm sized

barium titanate nanoparticles. The authors suggested that the cubic (or non-tetragonal) surface effects dominated at sizes of around 20 nm [39].

Several nanoparticle types investigated for second harmonic applications were investigated by Staedler *et al.* (shown later in Table 2) who presented a survey, detailing the cytotoxic responses to these SHG nanoparticles [40,41]. They investigated the *in vitro* cell uptake of uncoated and PEG-coated bismuth ferrite nanoparticles in A549 cells. Their results showed that the PEG-coated nanoparticles were less toxic than the uncoated nanoparticles, but the uptake into cells was reduced. They stated that in addition to reduced cellular uptake, the uncoated nanoparticle toxicity was due to the electrostatic interaction between the $BiFeO_3$ surface and the cell membrane and reduced cytotoxicity for PEG-coated $BiFeO_3$ was likely due to steric hindrance [41]. Further research by Staedler *et al.* showed the long second harmonic response time of $KNbO_3$ nanoparticles with the ability excited over 5 hours in a fluorescently tagged HTB-182 cell. The SHG emission of these $KNbO_3$ nanoparticles that were stable over a 5-hour period when illuminated by a femtosecond pulsed laser were also shown to be wavelength-tuneable within the near-infrared range (Figure 10) [40].

Figure 10 shows that these nanoparticles can be used for long lifetime imaging, they also have the advantage of simultaneously absorbing two photons and emitting a single photon of double the frequency (Figure 7) implying that they are less likely to photobleach (like fluorescent molecules [9]) and emission blink (like semiconductor quantum dots [13]) shown in Figure 2, Chapter 1. Therefore, these nanoparticles can be used for *in vivo* biological imaging and more importantly have the potential for application *in vivo* intravital microscopy.

Intravital microscopy is the light microscopy-based technique which has become an essential tool in biology. The key advantage to intravital microscopy and second harmonic generation is the use of the near infrared wavelength (longer wavelength) allowing deeper (~120 μm) penetration into the tissue/medium [42].

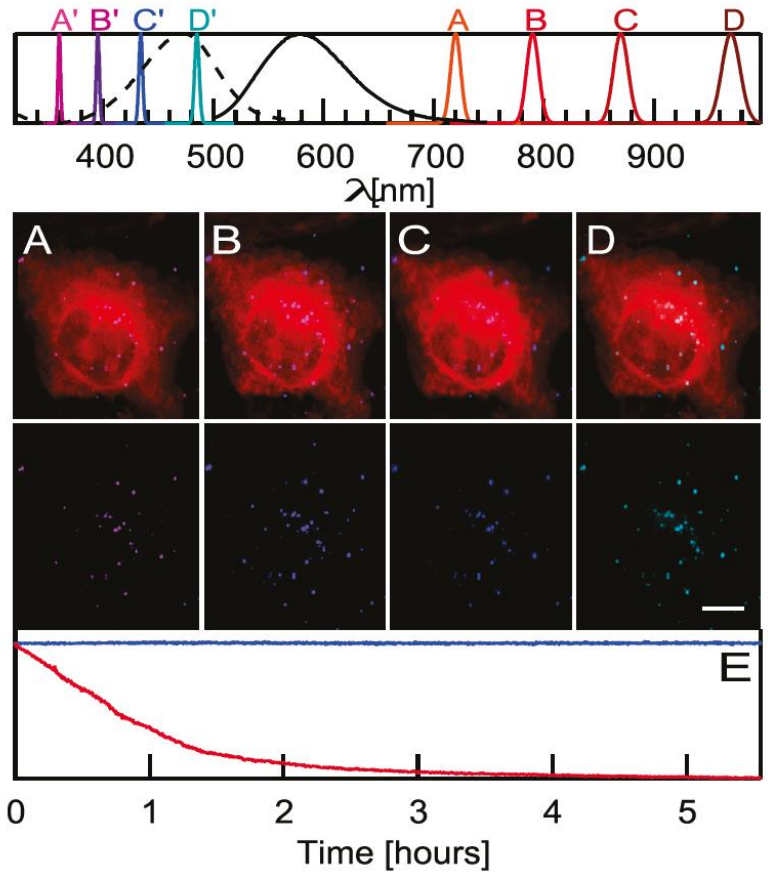

Figure 10. (upper plot) The pulsed laser excitation (A, B, C and D) with the corresponding second harmonic signal (A', B', C' and D'). The absorption (dashed line) and fluorescence (continuous line) spectra of FM1-43 cell membrane dye [40]. (middle plot) The multiphoton images of HTB-182 cells (red) with the second harmonic potassium niobate ($KNbO_3$) shown merged and without the cells underneath (exposed for 24 hours). The scale bar corresponds to 20 μm. (lower plot) The lifetime behaviour of the membrane dye (red) and the second harmonic signal (blue) showing the SHG signal being stable for at least a period of 5 hours compared to ~ 2 hours for the fluorescent dye; taken from [40].

Intravital microscopy in collaboration with SHG biomarkers, requires an incident light beam to excite $BaTiO_3$ or any non-centrosymmetric nanoparticles that are exposed to live mammalian models leading to subcellular resolution, live-tissue imaging [43]. A comprehensive review of intravital microscopy by Condeelis and Segall [44] discusses the use of multiphoton (*in vivo)* intravital microscopy to better understand cancer cells and the movement of invasive tumours. Their research shows cancerous cells migrating along the extracellular matrix using the second harmonic signal arising from the extracellular matrix with fluorescently tagged tumour cells *in vitro*, shown in Figure 11.

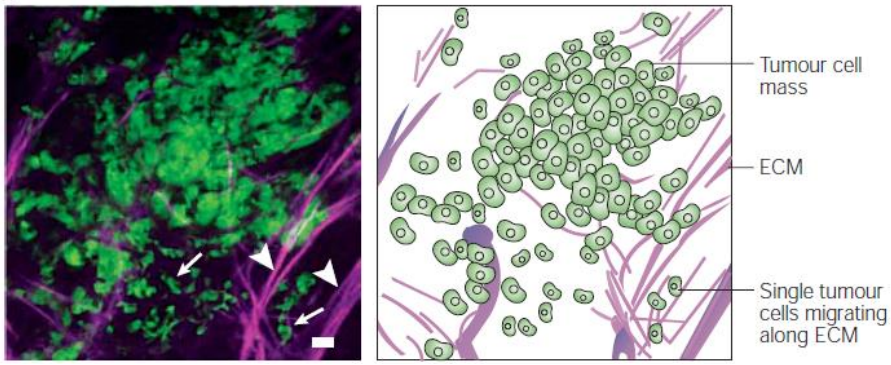

Figure 11. False coloured multiphoton image of tumorous cells *in vitro* (green) moving on extracellular matrix imaged by SHG (purple). The arrows indicate the points of cell-matrix interactions; taken from [44,45]**.**

The first example of *intravital microscopy* using barium titanate nanoparticles as second harmonic nanoprobes was conducted by Pantazis *et al*. who conducted *in vivo* studies of $BaTiO_3$ harmonic nanoprobes injected into zebrafish embryos. The results showed that barium titanate nanoparticles exhibited no toxic effects and appeared physiologically inert during embryonic growth [46]. *In vivo* imaging enabled continuous tracking of specific cells during

tissue growth, and also highlighted the advantage of second-harmonic $BaTiO_3$ nanoparticles which showed a strong signal over 20 minutes of illumination, whilst the Dextran-Alexa 546 fluorescent marker underwent bleaching over the same amount of time (Figure 12) [46]. Further work by Pantazis *et al*. investigated the specific targeting of the zebrafish embryos by labelling $BaTiO_3$ nanoparticles with cyanine (Cy5)-coupled reduced antibodies in order to compare the signal generated by the fluorescence and SHG directly; this revealed a superior signal to noise ratio from the SHG signal [46].

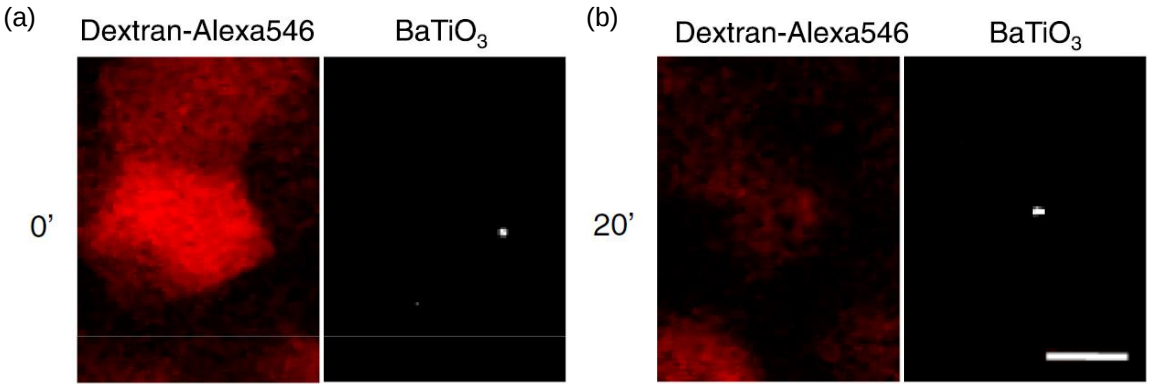

Figure 12. Zebrafish embryos co-injected with the $BaTiO_3$ nanoparticles and 10,000 MW Dextran-Alexa546 molecule and imaged at the 'dome stage' (~4 hours old) of zebrafish embryos [46]**. (a) *In vivo* imaging of the zebrafish embryo with the fluorescent marker in red and the $BaTiO_3$ nanoparticles in white at time = 0 minutes. (b) I*n vivo* imaging after 20 minutes of illumination showing the fluorescent signal from the organic dye decaying in comparison to the stable second harmonic light signal of $BaTiO_3$ nanoparticles. The scale bar corresponds to 20 µm; taken from** [46] **supporting information.**

The research conducted by Pantazis *et al*. (Figure 12) subsequently led to intravital microscopy imaging by Čulić-Viskota *et al*. [47] where uncoated barium titanate nanoparticles and PEG-functionalised nanoparticles were exposed to living zebrafish embryos (Figure 42).

Intravital SHG microscopy of barium titanate nanoparticles was also shown by Grange *et al.* [42]. This proof of concept was first shown *in vitro* by imaging $BaTiO_3$ nanoparticles through different thicknesses of mouse tail tissue using SHG microscopy. The simple experiment involved dropcasting $BaTiO_3$ nanoparticles (~100-300 nm in size) dispersed in methanol onto a glass substrate and a controlled thickness of mouse tail (20 to 200 µm) thick was added on top by conventional histology preparation routes [42]; Figure 13.

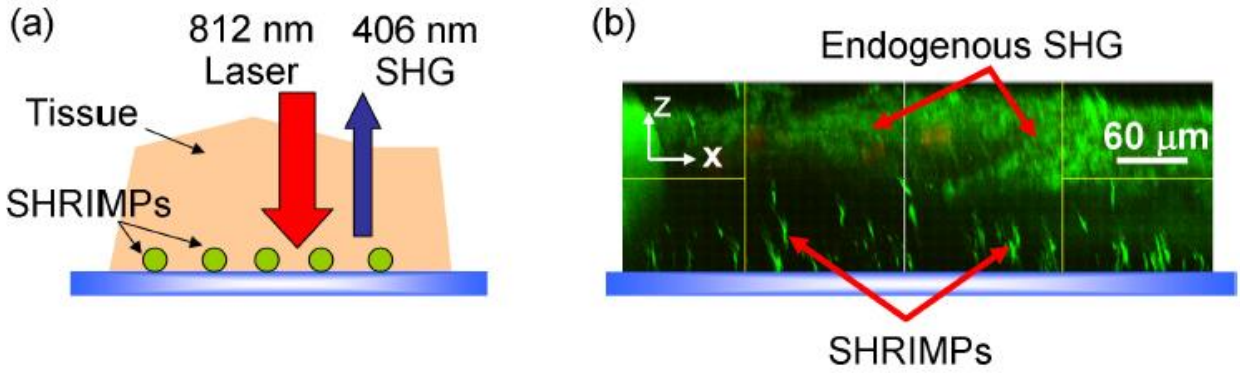

Figure 13. (a) Sample preparation for *in vitro* SHG imaging in mouse tail tissue. SHRIMPS are an acronym for second harmonic radiation imaging probes. (b) SHG imaging of 300 nm $BaTiO_3$ nanoparticles embedded 120 µm below the surface of *in vitro* mouse tail tissue; taken from [42]**.**

With successful *in vitro* SHG imaging of $BaTiO_3$ nanoparticles in mouse tail tissue, *in vivo* SHG imaging was also performed with injected $BaTiO_3$ nanoparticles dispersed in distilled water just under the mouse tail skin (and not in the blood vessels) [42]. The mouse was placed under the microscope after being anesthetized with the tail being immersed in water; shown in Figure 14. The SHG images were collected by determining the position of the particles on the x-y axis, using a marker to position nanoparticle locations on the tail and then imaged on the x-z axis (through the mouse tail). The nanoparticles were

as deep as 100 µm within the mouse tail, with the endogenous SHG of the collagen also being evident. The researchers noted that the elongated signal of the $BaTiO_3$ nanoparticles collected was partly due to the scattering of turbid media and some microscope aberrations [42].

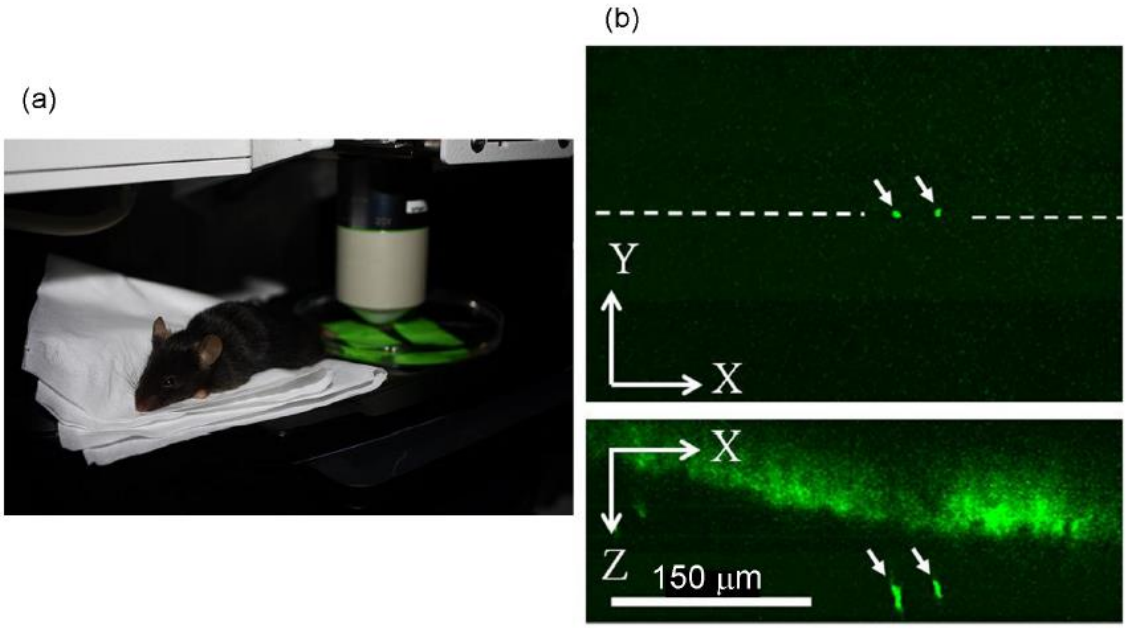

Figure 14. (a) *In vivo* set-up for intravital SHG imaging of $BaTiO_3$ nanoparticles in mouse tail tissue. (b) SHG imaging on the x-y axis where the nanoparticles were first located and then imaged in the x-z axis through the mouse tail showing the endogenous SHG of the collagen in the mouse tail and the nanoparticles embedded within the mouse tail tissue and labelled with the arrows ~100 µm deep; taken from [42]**.**

The *in vivo* studies carried out by Grange *et al*. with second harmonic $BaTiO_3$ nanoparticles in mouse tail tissue (Figure 14) showed that these nanoparticles can be used for intravital microscopy [42], however developments are still required in this field.

2.2 Nanoparticle interactions in cellular environments

The biophysical interaction of inorganic nanoparticles and biological interfaces are a crucial area of biomedical research; where safe use of these nanomaterials is critical for future application in this field. Therapeutic uses of nanoparticles are assessed by *in vitro* cell lines, observing the cytotoxic and genotoxic response to nanoparticle exposure. These nanoparticle exposures are then assessed *in vivo,* to get a better understanding of the nanoparticle exposure, such as: distribution, metabolism and excretion of the nanoparticles [48].

Nanoparticles can physically enter the body through inhalation, ingestion and transcutaneous (skin) pathways. Once in the body and having passed specialised clearance cells (macrophages and other phagocytes), the nanoparticles can enter the cell through a few mechanisms; the main pathway being endocytosis; Figure 15 [49]. Endocytosis is the uptake of extracellular particles across a plasma membrane into a cell. Particles are encapsulated by the cell membrane, transported through the cell in a lipid vesicle and may be broken down in a lysosome. If the particles are unable to be broken down or catalysed then this could lead to cell mutation upon mitosis or cell apoptosis [50].

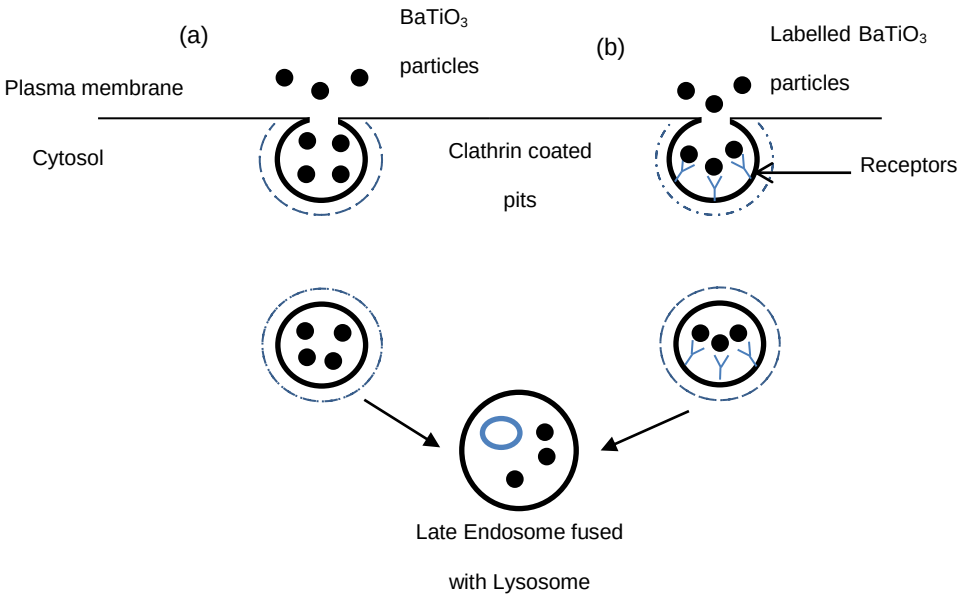

Figure 15. (a) Endocytosis can occur through non-specific labelling and (b) receptor mediated endocytosis. The non-receptor mediated endocytosis is known as pinocytosis and is a continuous process; whereas the receptor mediated endocytosis is a selective uptake of macromolecules; [50]**.**

Outcomes of nanoparticle uptake in biological environments are normally complex *in vivo* as it is difficult to fully characterise the adverse effects that may occur [49,51–54]. A review by Eleonore Fröhlich looked at the role of the nanoparticle surface and surface charge on the cellular uptake and cytotoxicity [51]. It highlights the factors that can cause cytotoxicity such as: generation of reactive oxidative species, the nanoparticles physically damaging the plasma membrane, dissolution of the particles in the suspending medium, or the binding of nanoparticles to membrane proteins/receptors; together with the remainder of the adverse effects shown in Figure 16 [51].

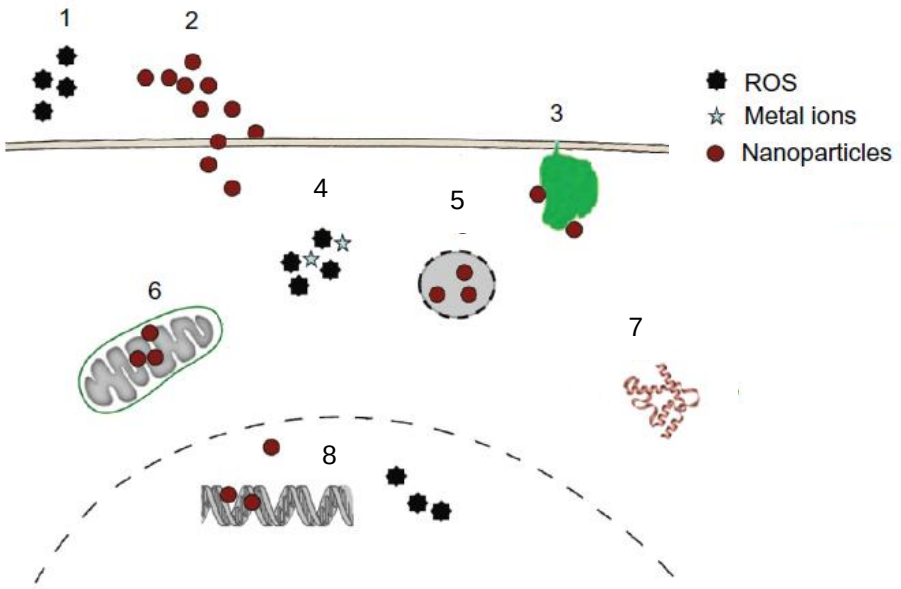

Figure 16. Cytotoxic responses caused when exposing nanoparticles to cells. (1) Reactive oxidative species (ROS) generated extracellularly by nanoparticles, (2) nanoparticles physically damaging the cell membrane or (3) binding to membrane bound proteins/receptors. (4) Intracellular metal ions and reactive oxidative species from lysosomal degradation, (5) lysosomal disruption and (6) interfering with mitochondrial metabolism. (7) Intracellular ROS creates structural alterations of proteins in addition to (8) toxic actions in the nucleus (genotoxic) interfere with transcription (8); taken from [51]**.**

The surface charge of a nanoparticle coating will have an effect on cellular uptake and cytotoxicity as reviewed by Fröhlich (67). This review detailed that positively charged (cationic) nanoparticles have a higher cell uptake in non-phagocytic cells (cells that do not professionally engulf particles) leading to greater cytotoxicity, whereas negatively charged (anionic) nanoparticles have increased cellular uptake in phagocytic cells, thereby exhibiting higher cytotoxicity (67).

A review by Nel *et al.* discussed the nanoparticle characteristics that are likely to affect *in vivo* biocompatibility, and a review of the nanoparticle interactions

when dispersed in biological systems; Figure 17 [49]. Nel *et al*. discussed the key areas that affect nanoparticle *in vivo* biocompatibility; such as: (i) the surface of the nanoparticle; (ii) the reaction medium surrounding the particle interface – when it interacts with components in the surrounding system – and (iii) the nanoparticle-biological interface; shown in Figure 17 [49].

The surface of the nanoparticle is important because it is this that is in contact with the surrounding suspending media. This interaction implies that the surface charge (affecting the zeta potential), the size and morphology (affecting the surface energy) and surface crystallinity and defects (affecting the functional groups) can all alter the nanoparticle interactions with the surrounding medium [49,55,56].

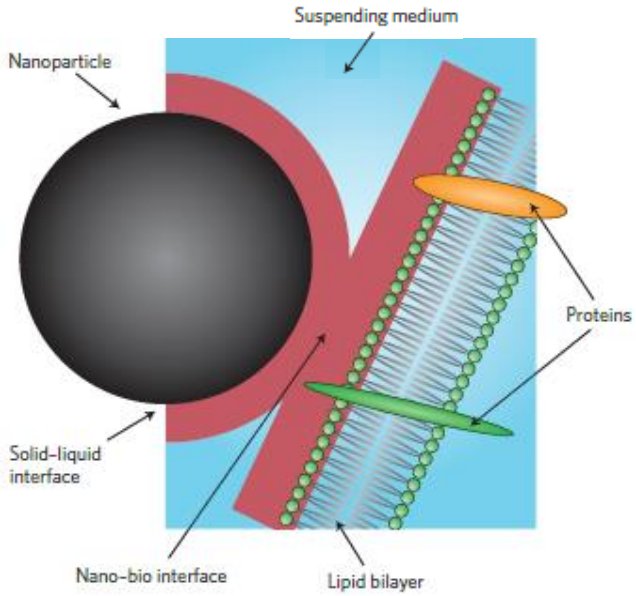

Figure 17. The nanoparticle/biological interface can be affected by any of the labelled components or a combination of them, highlighting the complexity of nanomaterials interacting in biological systems; taken from [49] **and** [55]**.**

The solid-liquid interface between the nanoparticle and suspending media is important as it is the components of the suspending medium that form the

double layer around the nanoparticle (discussed in Chapter 3), which in turn affects the stability and reactivity of the nanoparticle [49,55]. The stability of nanoparticles can be changed by functionalisation of the surface (discussed in Section 2.6) and determines how these nanoparticles interact with the cells, i.e. the amount of nanoparticles taken up by cells and resultant effect on the cell; Figure 18 [57]. It is important to note that the solid/liquid interface is dynamic and changes depending on the surface properties of the nanoparticle.

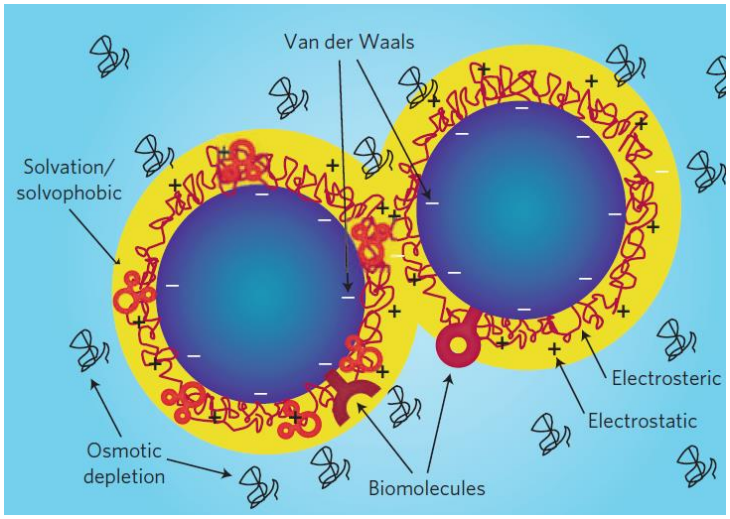

Figure 18. The interaction of two nearby nanoparticles suspended in biological media, highlighting the double layer formation (discussed in Chapter 3) with the attractive Van der Waals, electrostatic repulsive forces and other dynamic surface interactions; taken from [49]**.**

When the suspended nanoparticles come into contact with the cells, the nanoparticles will either bind specifically (if functionalised for a specific membrane target molecule) or non-specifically. The non-specific binding of nanoparticles to the cellular membrane is a result of the nanoparticle properties such as: surface roughness, surface charge and hydrophobicity. It is generally

accepted that positively charged surfaces are likely to be taken up by cells due to electrostatic attraction (discussed by Fröhlich [51]). However, the surface roughness (a result of the local atomic disorder of the surface), has been modelled by Hoek *et al.* who showed that it promoted nanoparticle adhesion to the cell membrane and this would likely result in increased uptake by the cells [49,58].

The hydrophobicity of the nanoparticle is a result of the double layer formed around the nanoparticle (Figure 18) and affects the stability of the nanoparticle. If the nanoparticles have a low hydrophobicity, then they will be colloidally stable in aqueous media and tend to be reasonably dispersed. Compared to nanoparticles with a high hydrophobicity, which will not be stable as they want to minimise the contact with water and the nanoparticles will likely agglomerate [49]. The hydrophobicity of the nanoparticles are also important because of the interaction with the cell membrane lipid bilayers [59]. Verma *et al.* have shown that gold nanoparticles with amphipathic ligands (hydrophilic and hydrophobic compounds) adsorbed to the nanoparticle surface; entered a mouse dendritic cell without causing any damage to the cell membrane [60].

A three-dimensional phase diagram highlighting the factors that can affect biocompatibility of nanoparticles in cells is shown in Figure 19.

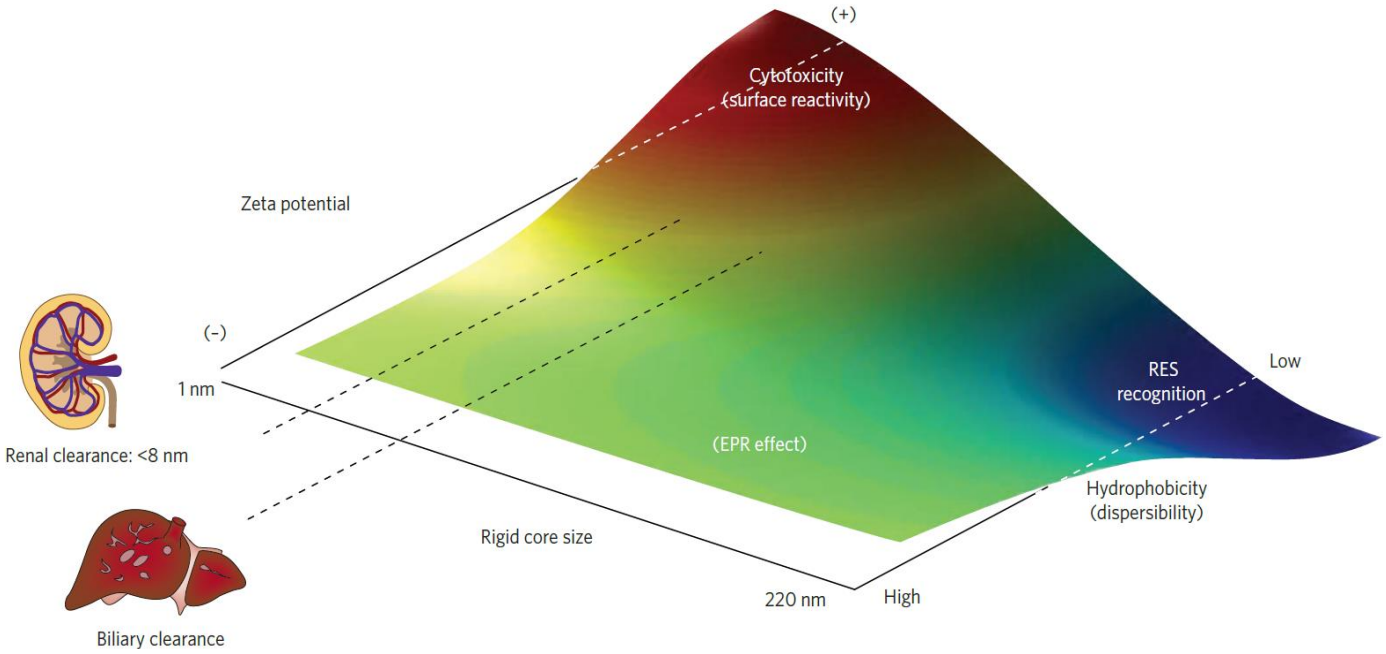

Figure 19. A three dimensional phase diagram showing the biocompatibility trends of 130 nanoparticles screened *in vivo* for therapeutic use [61]**. The dashed lines across the rigid core size (of the nanoparticle) shows the approximate limits of renal and biliary clearance. Particles which can be safely removed by the reticuloendothelial system (RES – component of the immune system) shown in the blue area. The enhanced permeation and retention of particles is shown in the green area (EPR) which are ideal characteristics for therapeutic nanoparticles; taken from** [49]**, courtesy of** [61]**.**

To date, there is no current research involving the functionalisation and characterisation of barium strontium titanate nanoparticles for SHG biomarkers. The literature described here provides a generic overview of nanoparticle interactions with cells to aid the results presented in Chapter 6.

2.3 Structure of $BaTiO_3$ nanoparticles.

A perovskite is a common class of crystalline structures for ferroelectric materials. It has a generic composition of ABO_3 ideally showing a body centred cubic structure (Figure 20) highlighting 8 (A) cations (in the corners) a single (B) cation in the unit cell centre, with oxygen (or other anions) atoms present in the centre of each of the faces (ABO_3). The unit cell structure in Figure 20 has the potential to be ferroelectric if, when the unit cell is repeated – there is a spontaneous net electrostatic dipole moment within the material that can be reversed upon the application of an electric field [22,62]. In the case of $BaTiO_3$ and $Ba_{1-x}Sr_xTiO_3$, the net dipoles are formed by the titanium atom being displaced in the oxygen octahedron, typically transforming to a tetragonal crystal structure; Figure 20 [62].

(a)

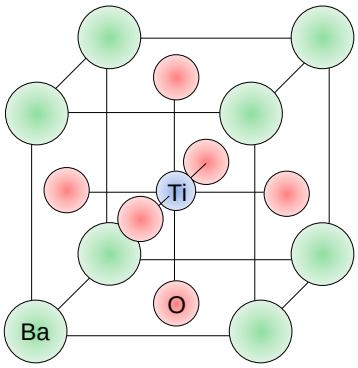

(b)

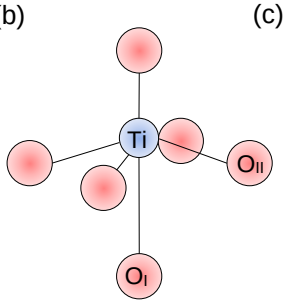

(c)

Bond	Cubic (Å)	Tetragonal (Å)
Ba-Ba	4.0	
Ba-O	2.8	
$Ti-O_I$	1.95	1.8
$Ti-O_{II}$		2.1

Figure 20. (a) The unit cell of an ABO_3 perovskite structure in the case of barium titanate ($BaTiO_3$) with the atoms labelled. (b) In the case of tetragonal barium titanate titanium atom is displaced in the oxygen octahedron, giving rise to a net polarisation and a transformation in crystalline structure, typically to tetragonal symmetry. (c) List of bond lengths for cubic and tetragonal $BaTiO_3$ symmetry.

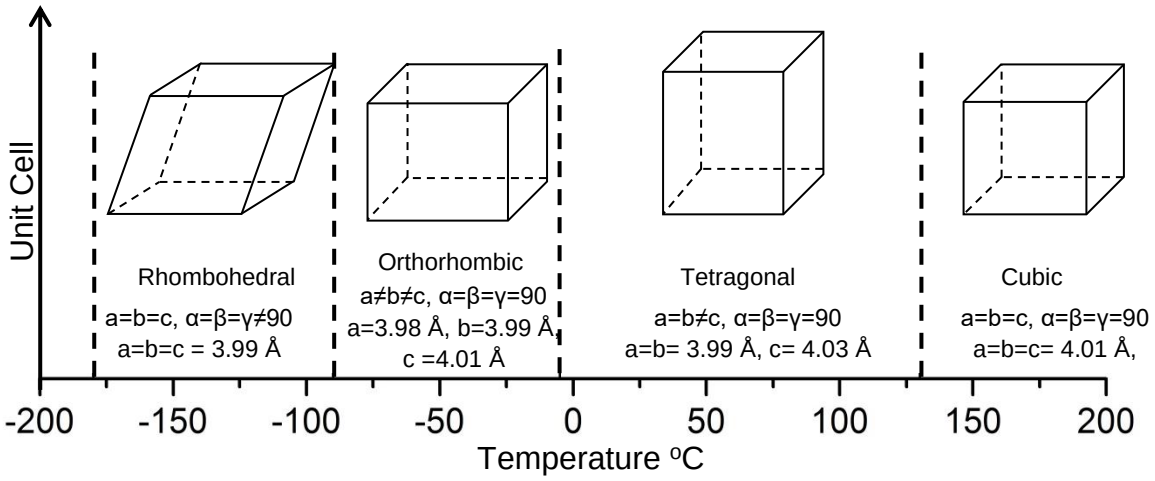

Figure 21. The phase transitions of barium titanate when cooled through the Curie temperature (130 ºC). The unit cell structure and parameters are shown; adapted from [63–65]**.**

The net dipole moment forms when the material cools through the Curie point. The Curie point for $BaTiO_3$ is 130 ºC and ~50 ºC for $Ba_{0.8}Sr_{0.2}TiO_3$ [64,66,67], above this transition Curie temperature the perovskite unit cell is cubic and below it is typically tetragonal (although it can be orthorhombic or rhombohedral at lower temperatures) as shown in Figure 21. It is generally accepted that cubic unit cells are paraelectric (i.e. no net spontaneous polarisation) whereas tetragonal unit cells are known to be ferroelectric, this may not always be the case for nanoparticulate perovskite systems and so care will be taken to clarify the unit cell configurations [68].

The determination of the Curie point for $BaTiO_3$ systems was initially conducted on parallel plate capacitors where the Curie point for course $BaTiO_3$ (>1 μm) was reported to be 120 ºC [22,69]. Upon further studies the transition temperature between ferroelectric and paraelectric was determined to be 130 ºC [22,62,70,71]. Further research suggested that the phase transition was

highly dependent on microstructure [71] and as the particle size decreased (≤100 nm), a depolarisation effect due to size dominated, and $BaTiO_3$ nanoparticles became paraelectric. The evidence supporting the 'critical size' of this phase transition is summarised in Section 2.3.1.

2.3.1 Tetragonal and cubic phase transition based on size

The size dependence of the cubic/tetragonal phase transition of $BaTiO_3$ has long been debated. Overall, there is a broad agreement that the tetragonal phase becomes less stable as the particle size is reduced below 100 nm.

Early research suggested that the phase transition occurs when particle sizes reach the sub-micrometre scale, e.g. 0.12 μm and 0.35 μm [72,73]. As characterisation techniques improved it has become a common view that the critical particle size values are below 100 nm [39] and over the past decade there has been a large discrepancy in determining the absolute critical particle size; values of ~25 nm, ~50 nm and ~70 nm have been reported [74–76].

The discrepancy in values for the size dependant phase transition has led to the adoption of a (broadly) accepted size-dependent mechanism. Involving a tetragonal particle core and a cubic shell, producing a ferroelectric/paraelectric core/shell particle [20]. The core/shell mechanism is widely accepted in most perovskite structures because the paraelectric phase (cubic shell) has no net dipole moment, whereas the ferroelectric phase does (i.e. a tetragonal core with a net Ti-atom dipole). This net dipole moment (sometimes referred to as a "correlation length") is a measure of the range over which the unit cell dipoles interact with each other [20]. As the particle size decreases, naturally the bulk dipole interaction decreases – meaning that the correlation length will

decrease. Consequently, the disordered paraelectric surface will eventually dominate the ferroelectric bulk.

A modification to the generally accepted size dependant tetragonal-cubic phase transition was the suggestion of a gradient lattice strain layer proposed by Hoshina *et al*. [77] which is commonly represented in lattice parameter diagrams. This model is shown experimentally by Rietveld fitting of synchrotron X-Ray diffraction data with extracted unit cell lattice parameters [77]. This model suggests that all nanoparticles have a tetragonal core, a gradient lattice strain layer (GLSL) and a cubic surface which will eventually dominate the bulk when the particle size decreases to sufficiently small values and the surface area/volume ratio is high.

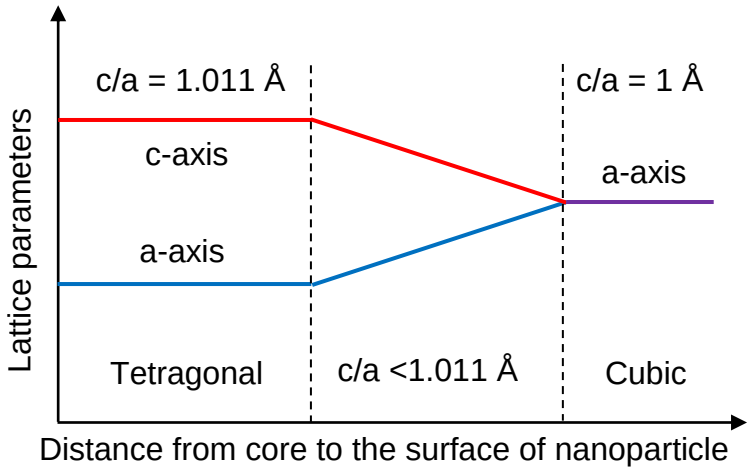

Figure 22. The c/a ratio of the tetragonal/cubic phase transition. The area of the graph with c/a <1.011 Å is the speculated gradient lattice strain layer [77]**.**

A study on the critical particle size phase transition between cubic-tetragonal $BaTiO_3$ was conducted by Smith *et al*. [74] using characterisation techniques that determine global and local nanoparticle structures. The study analysed data obtained using X-Ray synchrotron radiation measurements, temperature

dependant Raman spectroscopy and pair distribution function (PDF) analysis. The research proposed that there is a well-defined phase transition between the ferroelectric phase and the paraelectric phase in bulk $BaTiO_3$ at the Curie point of 130 ^oC. The research also suggested that as the particle size decreased, the volume of the unit cell increased and caused the titanium displacement to increase due to more space being available. They advocate that because smaller nanoparticles have larger Ti atom displacements they are not more ferroelectric, but are more paraelectric because of the increase in unit cells volumes which, reduces the coherence from one unit cell to another, (so no net polarisation) which is a similar principle when bulk $BaTiO_3$ is heated above the Curie point (130 ^oC) [74].

The phase transition mechanisms proposed, either the gradient size dependant strain layer [77] or of the local order in small nanoparticles [74] were suggested using bulk phase analysis techniques (aside from local order analysis by PDF). However, phase analysis of $BaTiO_3$ nanoparticles can also be done using electron microscopy, which can provide information from individual particles.

The ferroelectric order of individual $BaTiO_3$ nanoparticles has been investigated using high resolution electron microscopy and PDF analysis by Polking *et al.* [78]. Their research showed that the ferroelectricity of nanoparticles is likely to be dependent on shape, in addition to nanoparticle size. Specifically, nanoparticles that appear cubic are more ferroelectric, compared to spherically shaped nanoparticles which exhibited a steady decline in ferroelectric dipole coherence by PDF analysis. A comparison of cubic and spherical nanoparticle ferroelectric distortions showed that the coherence length of cubic nanoparticles is ~ 20 Å compared to 10 Å for spherical nanoparticles. The

atomic resolution phase reconstruction and titanium displacement map for a spherical $BaTiO_3$ nanoparticle is shown in Figure 23.

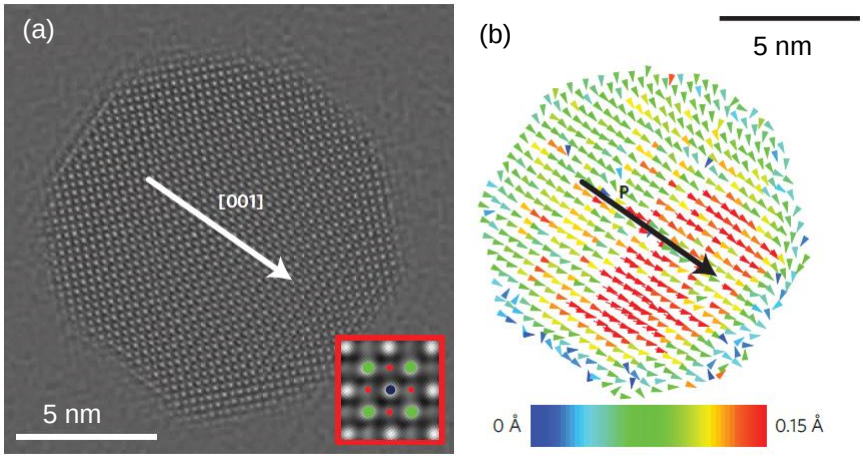

Figure 23. (a) Atomic resolution reconstructed phase image and titanium displacement maps of a spherical barium titanate nanoparticle. The arrow shows the general displacement along the [001]. (b) The colour scale shows the magnitude of the Ti atom displacement; taken from [78]**.**

The research shown by Polking *et al.* suggested that the Ti displacements are 0.15 Å at maximum, but can also show random displacements at the surface of the nanoparticles (Figure 23). This would suggest that although there are Ti-atom displacements present in the unit cell, the nanoparticle is not ferroelectric due to the absence of any net displacement. Further TEM investigation of barium titanate and barium strontium titanate nanoparticles by electron energy loss spectroscopy is discussed in Section 2.5.

2.4 Synthesis of $BaTiO_3$ and $Ba_{1-x}Sr_xTiO_3$ nanoparticles

The mixed oxide route is a common technique for synthesising piezoelectric multilayer ceramic materials. This procedure involves sintering equimolar mixtures of precursor however, the morphology of the resultant product is highly dependent upon the morphology of the precursors [79]. The disadvantage of this synthesis method includes the vast amount of energy needed. Firstly, high temperatures are used, this then leads to the formation of course micrometre sized powders which leads to intensive milling to de-aggregate the synthesised powder. However high intensity ball-milling with precursor material is capable of producing $BaTiO_3$ particles ~ 12 nm in size [80]. This process takes several days, has a large particle size distribution and has issues with impurities such as $BaCO_3$ [79,80].

A common 'wet-based' synthesis procedure is the hydrothermal method and this is used to directly produce sub-micrometre barium titanate from mixed slurries of aqueous ions. Providing a consistent and reliable method when altering process variables such as reaction dwell time and temperature. A key advantage to the hydrothermal method is the relatively low temperature needed for synthesis (70-200 ^oC) in comparison to the mixed oxide route [81,82]. Most hydrothermal preparation methods utilise hydroxide precursors under highly alkaline conditions and high Ba:Ti molar ratios [83]. After reaction, the slurry is initially washed with a dilute acid to remove any adsorbed $BaCO_3$ impurities and then with distilled water thereafter. Once the washing process has been repeated a number of times, the slurry is then dried at a suitable temperature

(60 – 80 ^{o}C) overnight [83]. Eckert *et al.* [84] suggested the formation of barium titanate nanoparticles via the hydrothermal method involved two common dissolution-precipitation formation mechanisms. These are homogenous nucleation of $BaTiO_3$ in solution and heterogeneous nucleation on TiO_2 precursor particles which then transform to $BaTiO_3$. Both mechanisms have been debated; however, both are still considered plausible, Figure 24.

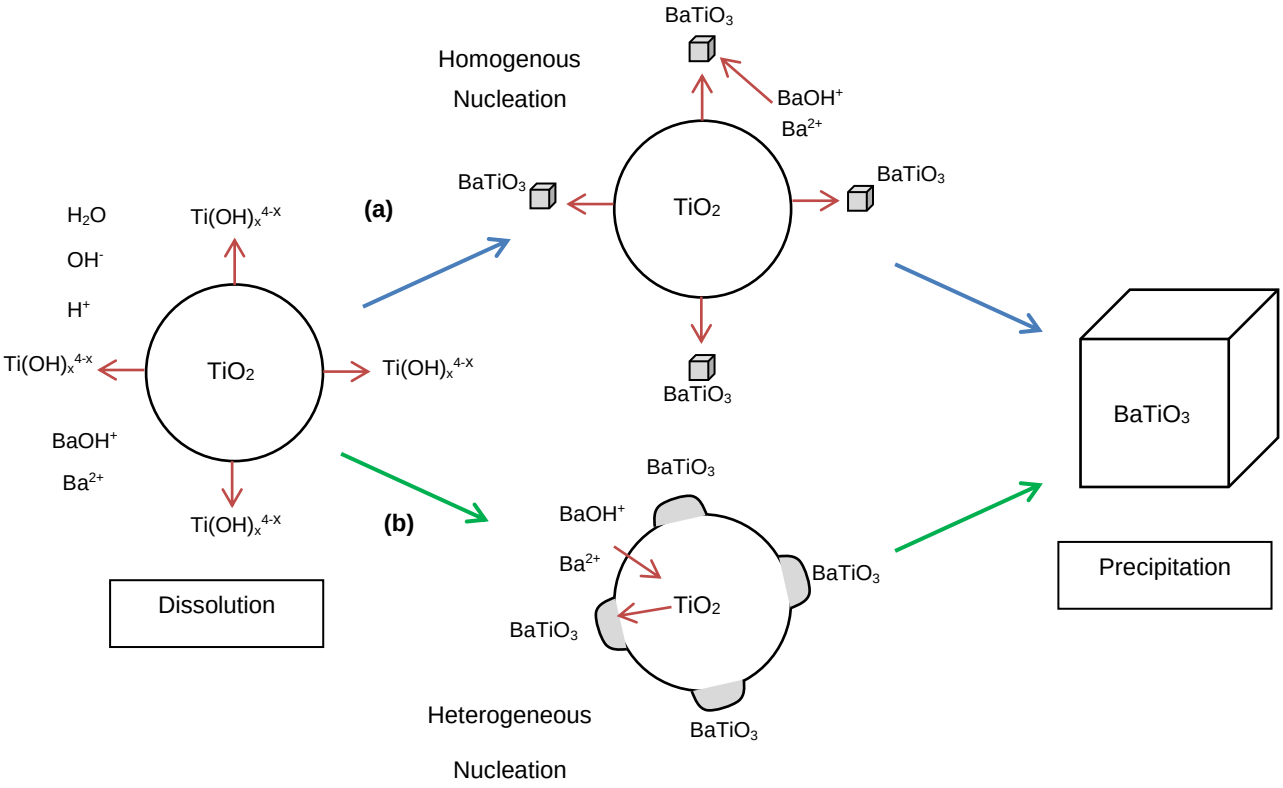

Figure 24. The dissolution-precipitation mechanism containing (a) homogenous (blue arrows) and (b) heterogeneous nucleation (green arrows) of $BaTiO_3$ with the red arrows showing the movement of barium and titanium ions to form $BaTiO_3$ [84]**.**

Eckert *et al.* suggested that the rate determining step for the homogeneous nucleation step was Ti-O bond breaking in titanium dioxide (TiO_2), which can

inhibit the reaction from propagating. TiO_2 is insoluble at high pH solutions however a high pH is favoured for barium titanate precipitation because Ba^{2+} ions leach at low pH, as discussed by Adair *et al.* [85]. Conversely, the rate determining step for heterogeneous nucleation was the diffusion of Ba^{2+} ions through the $BaTiO_3$ layer that eventually forms on the TiO_2 core [84].

Hydrothermally assisted synthesis can be tailored to control the size of the nanoparticles by dissolving metal fatty salts through a co-precipitation method [86]. A typical synthesis procedure involves dissolving a barium precursor ($Ba(NO_3)_2$) in water then adding this to an alkaline (NaOH) solution. A titanium precursor ($Ti(Bu)_4$) is added in excess to provide control over nucleation and dissolved in an alcohol/fatty acid (BuOH/oleic acid) solution [87]. This reagent mixture was placed into a hydrothermal autoclave for 18 hours at 135 ^oC and produced an average nanoparticle size of 22 nm; Figure 25 [86,87].

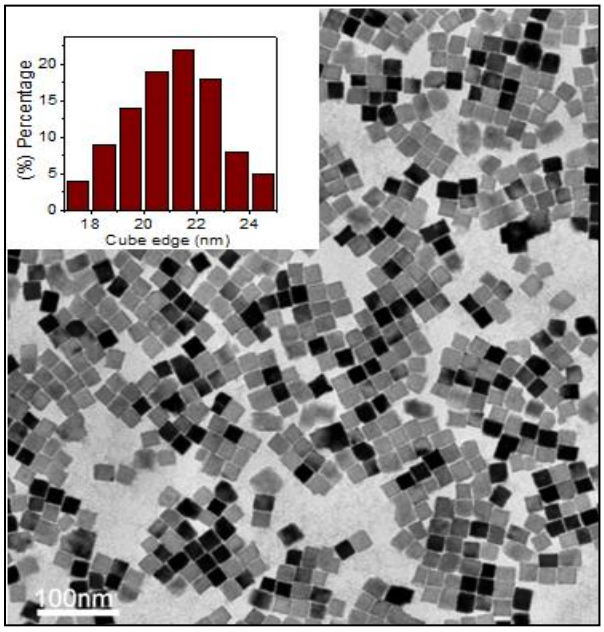

Figure 25. Low magnification bright field TEM image of $BaTiO_3$ nanoparticles synthesised by liquid-solid solution hydrothermally assisted synthesis, inset a histogram of nanoparticle sizes of 100 nanoparticles; taken from [87]**.**

Solvothermal techniques are subtly different to hydrothermal synthesis. This preparation method utilises solvents as the reaction medium (as opposed to water in hydrothermal). The advantage of solvothermal synthesis compared to hydrothermal is quoted to be the production of smaller $BaTiO_3$ particle sizes for similar reaction times [74]. Kwon *et al.* demonstrated this by substituting ethanol in place of de-ionised water as the solvent medium, so as to inhibit particle growth. The findings showed that the particle size could be tuned with appropriate ratios of ethanol and deionised water [88].

This thesis presents results from hydrothermal synthesis based on the procedure described by Eckert *et al*. [84] and the characterisation of the crystallographic phase produced is be discussed in the following chapters.

2.4.1 Barium strontium titanate

When a dielectric material such as tetragonal barium titanate is placed in a parallel plate capacitor, the polar dipoles (of $BaTiO_3$) will shift in the opposite direction to the applied/external electric field and lower the electric field overall. The change in the overall electric field is known as the dielectric constant (or relative permittivity) relative to a vacuum in the parallel plates. When tetragonal $BaTiO_3$ is heated through the Curie temperature, the material becomes cubic (centrosymmetric) a larger electric field is required to polarise the material and the accounts for a peak in relative permittivity measurements (Figure 26) at Curie temperatures [89]. Manipulation of the Curie point in barium titanate is done via the addition of strontium ions into the barium titanate lattice. The addition of strontium ions linearly reduces the Curie point but results in a higher peak dielectric constant (the opposing internal electric field from polarised

molecules) Implying that the polarization of the medium is larger compared to pure $BaTiO_3$ (Figure 26) [22,89]. For a 20 atomic% strontium incorporation, the Curie point is (~50 ^oC) with a higher dielectric constant (and net Ti-atom polarisation). Incorporating strontium into the barium titanate lattice is the reduction of unit cell parameters (and consequently unit cell volume), the $Ba_{0.8}Sr_{0.2}TiO_3$ unit cell contracts by 0.03 Å (cubic $BaTiO_3$ lattice parameter a = 4.015 Å, to a = 3.985 Å for $Ba_{0.8}Sr_{0.2}TiO_3$) [67,90].

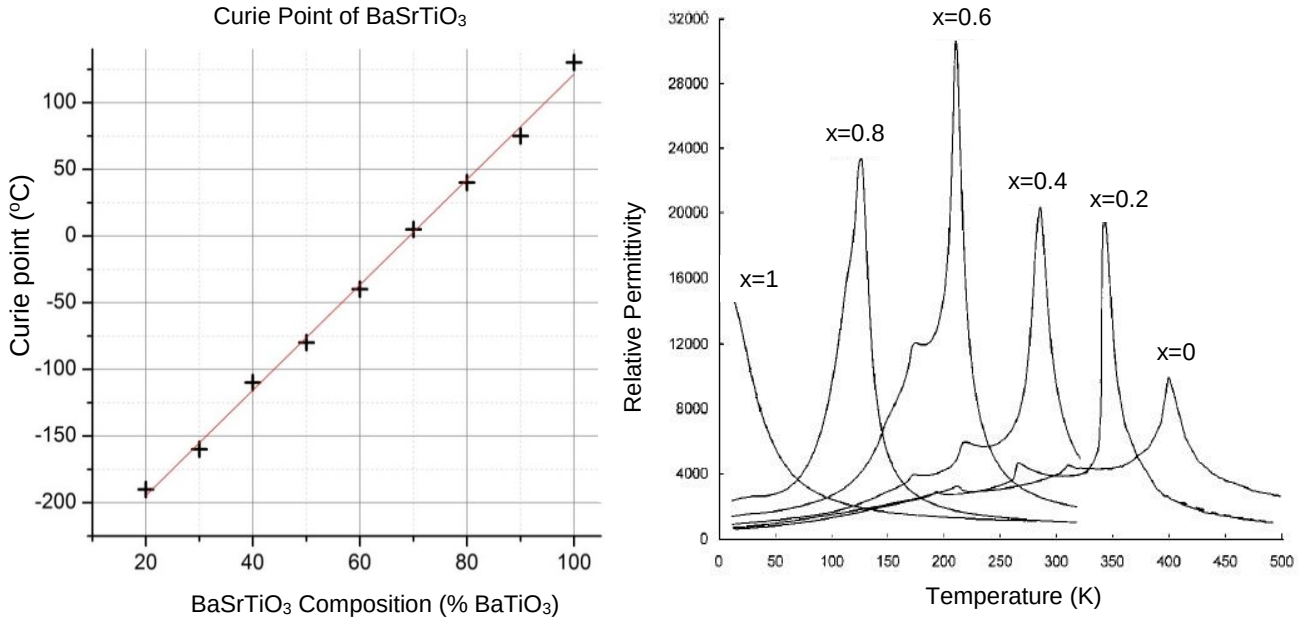

Figure 26. (a) Reduction of the Curie point as a function of strontium ion addition to $BaTiO_3$, highlighting the Curie point for the desired $BaSrTiO_3$ composition to be ~ 40°C ($Ba_{0.8}Sr_{0.2}TiO_3$). (b) The relative permittivity vs. temperature with varying strontium addition ($Ba_{1-x}Sr_xTiO_3$); adapted from [66,67]**.**

Barium-strontium titanate nanoparticles can be also synthesised using the hydrothermal method. However it should be noted that barium and strontium reagents will have different chemical properties including ion mobility and solubility [91]. This can lead to multi-phased systems consisting of barium-rich

and strontium-rich titanate complexes [21,91,92]. Roeder *et al.* conducted a study of the synthesis of single phase and bi-phasic barium-strontium titanate nanoparticles, producing a phase-selection map to summarise the best way to get the desired mol % of strontium into the barium titanate lattice; Figure 27 [92].

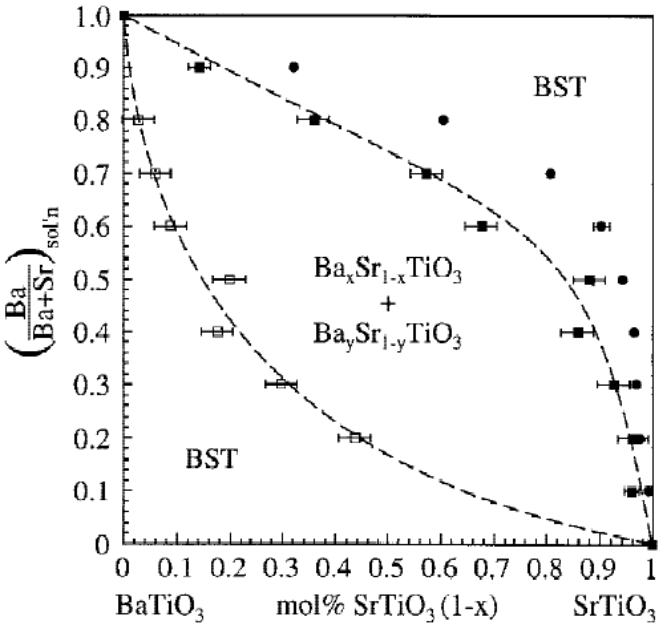

Figure 27. Barium strontium titanate (BST) phase-selection map, highlighting the solution compositions required for stable BST (●) and biphasic BST (□ – barium rich, ■ – strontium rich) compositions; taken from [92]**. The x-axis shows the mol % strontium incorporation, and the y-axis (Ba/(Ba+Sr)) is a ratio of the initial concentration of barium ions to the total Ba+Sr ions in solution (i.e. Ba/(Ba+Sr) = 0.3 will produce a $Ba_{0.7}Sr_{0.3}TiO_3$ incorporation or $Ba_{0.07}Sr_{0.93}TiO_3$.**

It is noted that barium strontium titanate nanoparticles have not been used previously as second harmonic biomarkers, so work presented here would be the first example of using barium-strontium titanate nanoparticles (BST) as second harmonic nanoprobes. In order to determine the crystal phase required for second harmonic biomarkers, characterisation of barium titanate and barium

strontium titanate nanoparticles is required. To fully understand the nanoparticle systems, a range of characterisation techniques are needed, and the techniques used throughout this project are: X-Ray diffraction, electron microscopy and electron energy loss spectroscopy which are reviewed in the following section.

2.5 Characterisation of barium titanate and barium strontium titanate nanoparticles.

Prominent research highlighting the crystal phase determination of varying synthesis and characterisation routes for barium titanate and barium strontium titanate are summarised in Table 1.

2.5.1 X-Ray diffraction

X-Ray powder diffraction (XRD) uses crystallographic scattering to determine the crystal structure from a 'bulk' amount of sample. This leads to difficulties in determining the crystal phase, because nanoparticles have fewer atomic planes (compared to a bulk sample) with the same d-spacing, the diffraction pattern will produce broad peak as there are fewer planes for incident X-Rays to interfere constructively with (known as line broadening). This can lead to difficulties in elucidating the XRD (002/200) peak splitting of the tetragonal phased barium titanate samples (discussed in Chapter 3). Although, Kim *et al.* has shown $BaTiO_3$ to produce SHG even when the XRD pattern appears cubic (due to the diffraction pattern line broadening [39]). Even though XRD can provide the *net* crystal phase of a sample, XRD line broadening makes analysis difficult below 100 nm particle sizes, and in order to locally characterise the crystal phase, electron microscopy and electron energy loss spectroscopy are also extensively used.

Reference	Synthesis	Characterisation	Results
Uchino *et al.* [72]	**Hydrothermal and co-precipitation**	**XRD for crystal phase analysis at room temperature and above the Curie point (200 ^{o}C). Transmission electron microscopy images were used for average particle size distribution**	**XRD shows the tetragonal c/a unit cell parameters changes to cubic unit cell parameters when the nanoparticle size is below 120 nm. TEM images were used to show the difference in particle size/morphology from different synthesis routes.**
Frey *et al.* [73]	**Sol-gel synthesis and post synthesis heat treatment**	**XRD for crystal phase analysis and scanning electron microscopy for determining the particle/grain sizes.**	**$BaTiO_3$ nanoparticles appear cubic by XRD below a particle size of 350 nm. SEM images of the sol-gel, heat treated synthesis shows a variation of particle morphology and grain sizes.**
Hoshina *et al.* [77]	**Two-step sintering method and aerosol deposition method**	**Synchrotron XRD analysis of varying nanoparticle sizes.**	**High resolution synchrotron XRD of varying sizes of $BaTiO_3$ shows a 'gradient lattice strain layer' where the unit cell parameters show a tetragonal core, GLSL and a cubic surface layer.**
Smith *et al.* [74]	**Solvothermal.**	**Synchrotron XRD phase characterisation and pair distribution function (PDF) analysis.**	**Claim that particles as small as 26 nm remain tetragonal until near the phase transition temperature, however PDF analysis suggests that Ba-Ti distortions and titanium off-centring is greater in smaller nanoparticles but these have a smaller c/a ratio due to the lack of small correlation-length.**

Polking *et al.* [78]	**Solvothermal.**	**High resolution TEM, electron holography and PDF analysis**	**Ti-atom mapping shows mono-domain displacements of ~ 0.15 A in magnitude near the bulk of the nanoparticle and local structural distortions are also present. Off axis holography shows dipole switching behaviour when a small bias is applied, implying $BaTiO_3$ nanoparticles are ferroelectric. PDF analysis suggests the surface has a lack of dipole coherence but atoms and displacements are very disordered.**
Eckert *et al.* [84]	**Hydrothermal synthesis**	**XRD crystal phase analysis and TEM with energy dispersive X-Ray (EDX) spectroscopy**	**XRD and Rietveld analysis of the patterns showed the unit cell parameters of the hydrothermal samples produced a tetragonal unit cell splitting. TEM and EDX showed that barium titanate nanoparticles were produced and the morphology of the nanoparticles was smooth.**
Roeder *et al.* [92]	**Hydrothermal synthesis of barium strontium titanate (BST) nanoparticles.**	**XRD crystal phase analysis and TEM imaging of particle sizes**	**XRD analysis of varying BST strontium incorporations, showed biphasic strontium-rich and also barium-rich BST depending on the reagent molar quantities. TEM analysis showed that barium-rich BST particles were much larger in size compared to strontium-rich BST.**

Bugnet *et al.* [68]	**Chemically purchased and mechanically milled**	**Electron energy loss spectroscopy of barium titanate of O-*K* and Ti-$L_{2,3}$ edge at room temperature and 200 ^{o}C.**	**The EELS O-*K* edge at room temperature and 200 ^{o}C shows little difference between the edge onsets. The Ti-L_3 e_g peak at 200 ^{o}C (above the Curie point) shows a shift of 0.05 eV. Highlighting a change in structural distortion.**
Moon *et al.* [93]	**Mixed oxide synthesis**	**Electron energy loss spectroscopy of barium titanate at room temperature and 150 ^{o}C.**	**Investigated the splitting of the Ti-$L_{2,3}$ t_{2g}-e_g peak splitting, suggesting the nanoparticle had a tetragonal surface shell (~ 5 nm) and a cubic core due to the acquired reference spectra collected at room temperature and 150 ^{o}C (above the Curie point).**
Rossell *et al.* [94]	**Hydrothermal synthesis**	**Electron energy loss spectroscopy of barium strontium titanate ($Ba_{0.03}Sr_{0.97}TiO_3$)**	**This study investigated the effect barium dopants have on strontium titanate nanoparticles, suggesting that the barium dopants cluster and cause polar barium-rich nanoregions in the nanoparticle.**

Table 1. Overview of the $BaTiO_3$ and $Ba_xSr_{1-x}TiO_3$ nanoparticle synthesis techniques, characterisation of the nanoparticles and the summary of the results. This is an overview of the literature review to show that the synthesis and characterisation of the perovskite nanomaterials have been investigated by many research groups by similar techniques, yet some of their conclusions are contradictory e.g. [77] **&** [93]**.**

2.5.2 Electron energy loss spectroscopy (EELS)

Electron energy loss spectroscopy (EELS) is a rigorous technique carried out in a TEM that measures inelastic scattering (loss of kinetic energy) when incident electrons interact with the specimen. EELS is capable of providing structural and chemical information about a material with spatial resolution down to the atomic level [95]. A brief background to the technique is given here, however a more detailed explanation of the acquiring technique and analysis of the spectra is discussed in Chapter 3 and Chapter 5.

Figure 28 shows the inelastic scattering of an incident electron exciting an electron bound to the *K* orbital to a range of empty states. The energy required to excite the atomic electron to the range of empty states is the electron energy loss. The electron energy loss can be typically be a range from few electron volts ~2 – 50 eV (known as low loss) up to hundreds of electron volts (high loss typically valued from > 50 eV) [95]. The EEL spectrum is calibrated from the zero loss peak that arises from weak energy loss electrons but primarily consists of elastic, forward scattering electrons (i.e. little to no electron beam interacting with the specimen) [96].

Core-loss edges in electron energy loss spectroscopy are the collection of the inelastically scattered incident electrons that have interacted with the specimen. Electrons that are bound to the atom will be excited to a range of unoccupied density of states, and the transmitted inelastically scattered electrons will reflect this transition to the range of density of states (Figure 28).

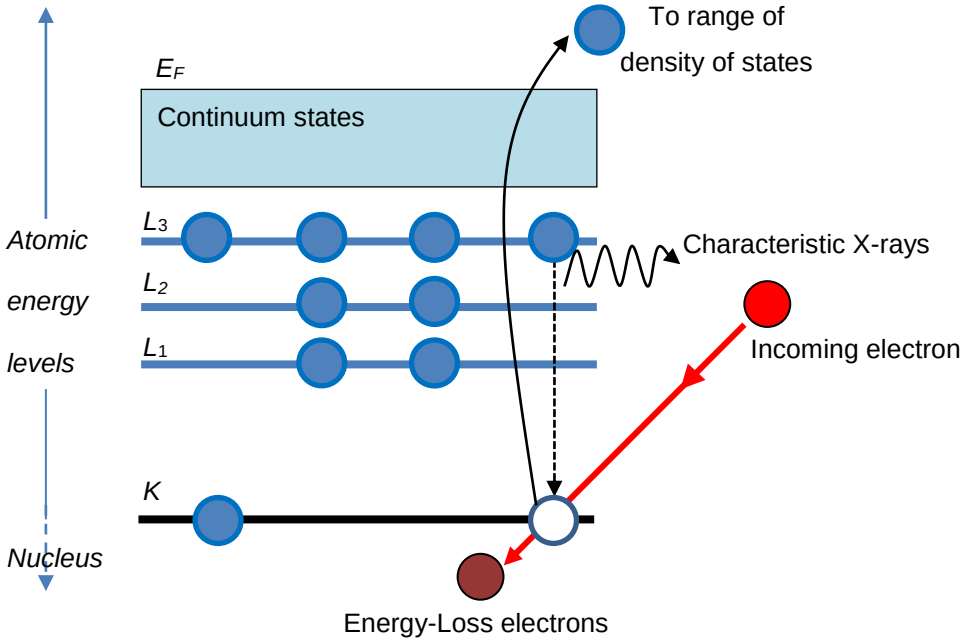

Figure 28. The ionisation process, highlighting the energy loss mechanism from an inner shell electron (K) and ejected to a range of empty sates when the incident beam interacts with the electron and continues; adapted from [96]**.**

Electron energy loss spectroscopy is used here to investigate the phase of barium titanate nanoparticles by investigating the sample at room temperature and above the Curie point, to see if the phase change is evident in the core-edge electron energy loss spectra (i.e. the ~0.1 Å shift in Titanium atom). EELS can provide information about the electronic structure or chemical bonding of the material by interpretation of the EELS core edges (edges are characteristic to the atom and subshells). Any change in density of states will be reflected in the high loss edges or energy loss near edge structures (ELNES) [97]. EEL spectroscopy requires a thin sample (~100 nm) because if the sample is too thick, then the incident beam electrons undergoing energy loss, will endure plural or multiple scattering events. This will result in a loss of spectral information due to a large decaying background [95,98]. The technique is

sufficient to resolve vibrational and electronic modes of energy loss with a typical energy resolution ranging between 0.5–0.1 eV, if using a monochromatic electron source [95,98]. Figure 29 shows the background subtracted EELS data acquired experimentally from a reasonably thin (~150 nm) $BaTiO_3$ sample, highlighting the zero-loss region (ZLP) and the Ti-$L_{3,2}$ edge spectral features.

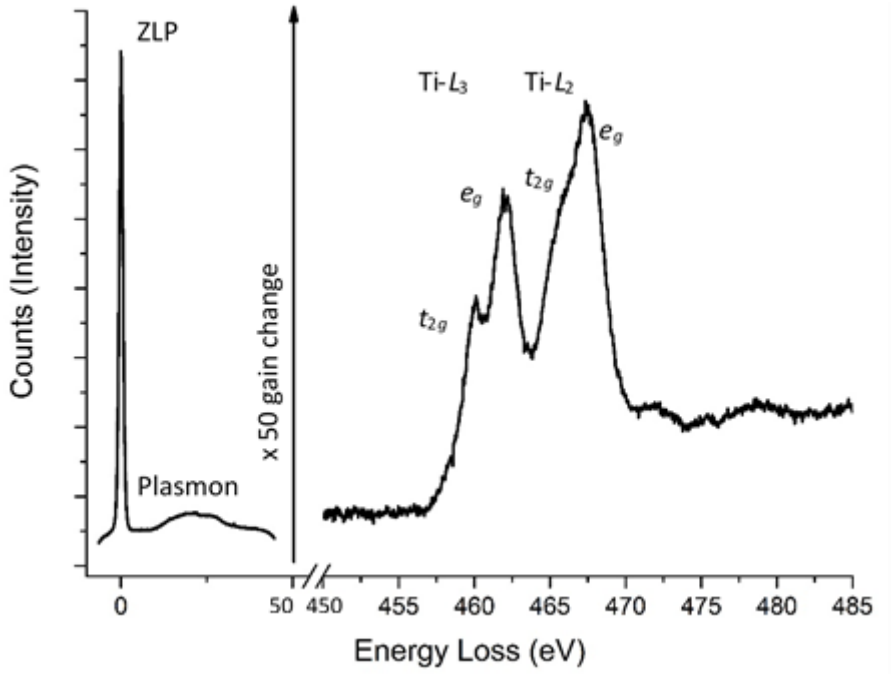

Figure 29. Experimental EEL spectrum showing the zero loss peak and plasmon in the low loss region (x-axis break from 0-50, 450-485 eV). The high loss region (450–485 eV) shows the Ti-$L_{2,3}$ edge t_{2g} & e_g peaks. The background is subtracted to measure the t_{2g}-e_g peak splitting.

The Ti-*L* and O-*K* EELS edges have been extensively characterised by Leapman *et al.* [98] who investigated anatase (TiO_2 has a tetragonal unit cell). This review compared X-Ray absorption spectra with experimental and modelled EELS data with good agreement between data. The molecular orbital diagram for TiO_6^{8-} is shown in Figure 30 highlighting the bonding of titanium

and oxygen in the $BaTiO_3$ unit cell. The Ti-L_3 and Ti-L_2 edges arise due to electrons from the *L*-shell undergoing spin-orbit splitting into $2p_{3/2}$ and $2p_{1/2}$ levels which are then excited to empty *d*-states [98]. The molecular orbital energy level diagram shows that these empty Ti-3*d* states are hybridised with the O-2*p* states. This implies that any change in the chemical or molecular bonding when $BaTiO_3$ changes from tetragonal to cubic phase should also, in principle, change the Ti-$L_{2,3}$ and O-*K* edges because the Ti-3*d*-O-2*p* interactions change as the Ti-O octahedra changes orientation.

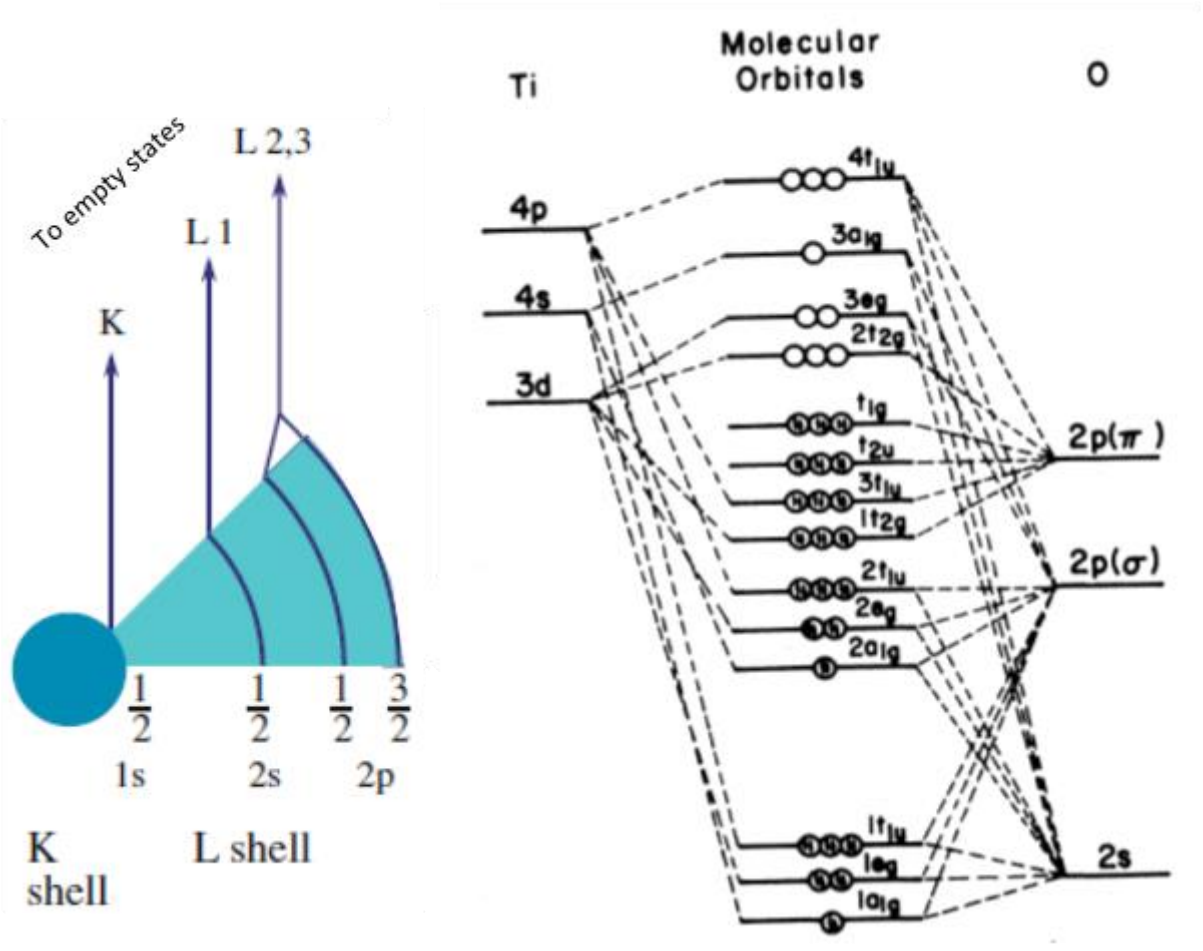

Figure 30. (a) The EELS nomenclature showing the energy shell where the electron originates from; taken from [96] **(b) Molecular orbital energy level diagram of TiO_6^{8-} representing the environment around titanium in TiO_2; taken from** [98]**.**

Bugnet *et al*. have published work on the EEL spectra of barium titanate, investigating not only at the phase transformation from tetragonal to cubic, but also looking to model the O-K edge EEL spectra to gain a better understanding of the distortion and changes in the local electronic structure [68,97]. They modelled the oxygen *K*-edge of $BaTiO_3$ using Density Functional Theory (**WIEN2K** code) and achieved good agreement between the experimentally and modelled spectra [97].

More recent work by Bugnet *et al*. during the writing of this thesis highlighted a difference in the Ti-$L_{2,3}$ edge at room temperature relative to that above the Curie point (the difference is expected given that the crystal phase transition alters the arrangement of atoms in the unit cell). Bugnet *et al*. showed the Ti-L_3 edge e_g energy loss values reduced by ~0.05 eV at room temperature (black) and above the Curie point (red); Figure 31 [68].

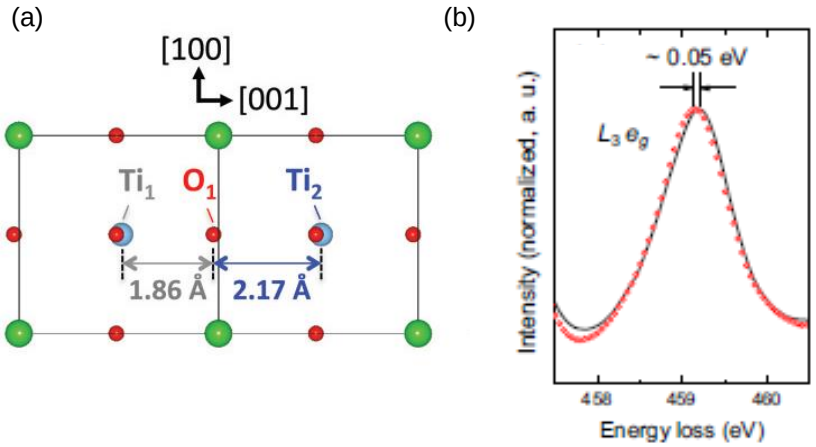

Figure 31. (a) Model of the $BaTiO_3$ unit cells used to calculate the O-*K* edge of barium titanate and highlighting the tetragonal distortion along the [001] direction. The distances shown, are from the oxygen to the nearest (Ti_1) and furthest (Ti_2) titanium atom; taken from [97]**. (b) Highlights the difference between the room temperature (i.e. tetragonal-solid black line) and above the Curie point (i.e. cubic-red open circles) Ti-L_3 e_g peaks acquired at room temperature and 200 ºC respectively; taken from** [68]**.**

Moon *et al.* also suggested there was a change in the Ti-L_3 edge t_{2g}-e_g peak splitting when $BaTiO_3$ was heated above the Curie point [93]. This work also suggested a change in phase measured by EELS data on going from the surface of the nanoparticle to the core of the nanoparticle. This contributes to the theory of a core-shell mixed phase nanoparticle suggested by XRD techniques [74,99–101]. However, the work carried out by Moon *et al*. contradicts the XRD analysis and suggested that the $BaTiO_3$ nanoparticles possess a tetragonal shell and cubic core [93,102,103]. The tetragonal phase was identified at room temperature and the cubic phase was collected by *in-situ* heating of the sample to 150 ^oC. The results showed that the EELS data collected from the surface of the nanoparticles had a larger Ti-L_3 edge t_{2g}-e_g peak separation of 2.36 eV as compared to the cubic phase value of at 1.96 eV; Figure 32 [93].

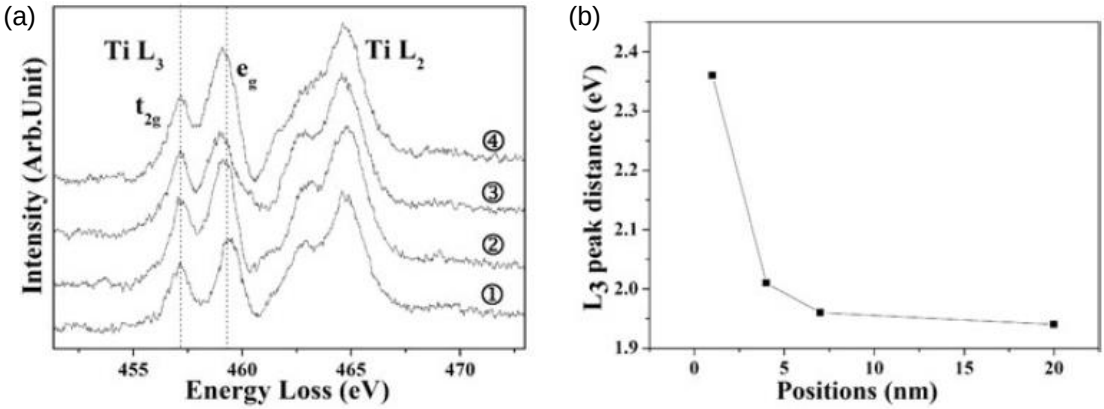

Figure 32. (a) Experimental EEL spectra of 50 nm $BaTiO_3$ nanoparticles showing spectra extracted from (1) 1 nm, (2) 4nm, (3) 7 nm and (4) 20 nm away from the surface of the nanoparticle. (b) Plot of the Ti-L_3 edge t_{2g}-e_g peak splitting showing the decrease the further away from the surface of the nanoparticle; taken from [93]**.**

The work carried out by Bugnet *et al.* and Moon *et al.* suggest a common result: that *in-situ* EELS heating experiments of $BaTiO_3$ above the Curie point

suggests that the cubic phase has a reduced Ti-L_3 edge t_{2g}-e_g peak splitting (a reduction of ~0.3 eV) [68,93]. EELS of $BaTiO_3$ is investigated in Chapter 5 to determine the structure and phase of the nanoparticles at room temperature and when heated above the Curie point.

For barium strontium titanate, little EELS analysis has been conducted to investigate the phase of the nanoparticles, however work carried out by Rossell *et al.* has shown the effect of barium ion doping in $SrTiO_3$ ($Ba_{0.03}Sr_{0.97}TiO_3$) nanoparticles [94]. This work employed EELS as a chemical analysis tool to spatially resolve the Ba dopants in $SrTiO_3$, showing that the barium ions clustered within the nanoparticles.

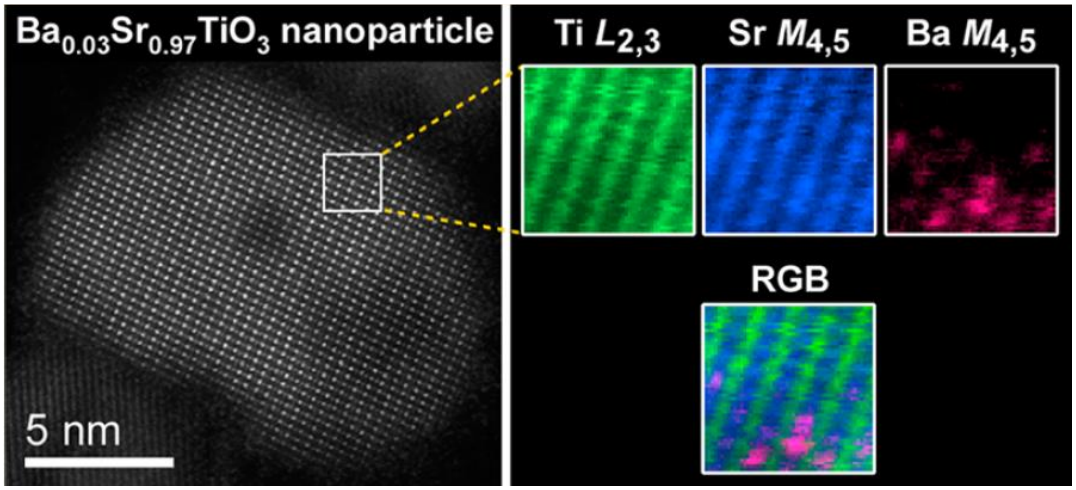

Figure 33. (a) Atomic resolution HAADF-STEM image of barium strontium titanate with the area highlighted to show where the extracted EELS-mapping data were collected from. (b) The colour coded signal showing the Ti-$L_{2,3}$ edge Sr-$M_{4,5}$ edge and Ba-$M_{4,5}$ edge. When the colour coded edges are reconstructed a colour map shows that the barium atoms are clustering in one area of the nanoparticle; taken from [94]**.**

2.6 Functionalisation of nanoparticles to promote cellular uptake.

The functionalisation of barium titanate nanoparticles is important for altering the nanoparticle surface for nanoparticle stability when suspended in media. Functionalisation can be conducted during the synthesis of the nanoparticles (shown by the co-precipitation route [87] in Section 2.4) or post nanoparticle synthesis. Functionalisation is generally used to improve nanoparticle suspensions which can have an effect on other properties e.g. improving dielectric properties for multilayer ceramics [104]. However, functionalisation of $BaTiO_3$ nanoparticles discussed here, shows improved nanoparticle suspensions and specific labelling for improved biomarker targeting. To date, there is no literature about the coating of barium strontium titanate nanoparticles and this will not be discussed here.

Dynamic light scattering (DLS) of nanoparticles and zeta potential measurements are standard techniques to assess nanoparticle stability in suspensions. DLS measures of scattered light intensity and is used to determine nanoparticle behaviour when suspended in media, zeta potential measurements indicate the surface charge of the nanoparticles which can be determined when nanoparticle suspensions are placed under an applied electric field. Both techniques are discussed further in Chapter 3.

The fundamentals of using these techniques are based on DVLO theory which assumes that particle stability is dependent on the interaction of surface charge with the surrounding components of the solvent and the impact this has on the attractive and repulsive forces of nanoparticles in a solvent [105]. The primary

forces for attraction and repulsion are the van der Waals attraction, electrostatic repulsion and polymeric (steric) repulsion. A surface charge originates from nanoparticles being brought into contact with a solvent. In the case of aqueous media containing polar ions such as water, the surface charge of the nanoparticles influences the type and distribution of nearby ions [106]. The charged surface in contact with the suspending media forms an electrical double layer by distributing neutralising co-ions from the solution onto or near its surface, Figure 34.

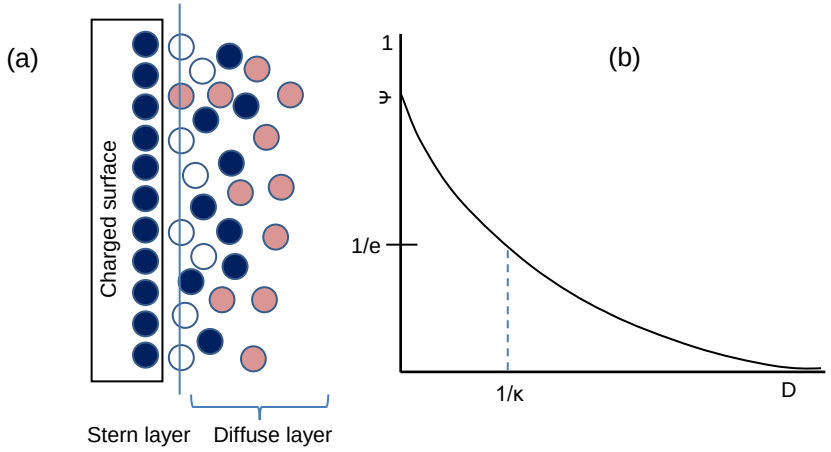

Figure 34. (a) The diffuse electrical double layer of a charged surface (according to the Helmholtz model) due to thermal motion, the Stern layer is not always 1:1 (here a compact layer where opposite ions – pink – adhere to the surface – navy). (b) Graphical representation of the electrical potential of the diffuse double layer where this varies with electrolyte concentration of the diffuse double layer. The 1/κ term is the Debye length which is the double layer thickness at 1/e of the surface potential at 25 ºC in water. *ψ* is the surface potential and *D* is the distance away from the surface [105]**.**

The attractive van der Waals forces are based on intermolecular dipoles aligning and by virtue, these dipoles attract. The attraction of these dipoles are inversely proportional to separation distance. The Born repulsive force is

strongly repulsive, it occurs at minimal separation as it is due to the like charges repelling i.e. the overlapping electron clouds of negatively charged particles. These attractive and repulsive interactions contribute to the DVLO theory and calculations have been made between two charged spheres as to the optimum separation [106]. The attractive and repulsive forces are shown in Equation 1 and Equation 2 respectively, and the total energy interaction is graphically represented in Figure 35.

$$\Delta G_{rep} = \frac{B}{a} e^{-aD}$$

Equation 1. The theoretical approximation of the Born repulsion where *a* and *B* are constants of the intermolecular potential at a distance *D* [105]**.**

$$\Delta G_{att} = -\frac{x.A_H}{12D}$$

Equation 2. The attractive forces summarised by the size of the particle *x*, a constant of the material A_H which is inversely proportional to distance *D* [106]**.**

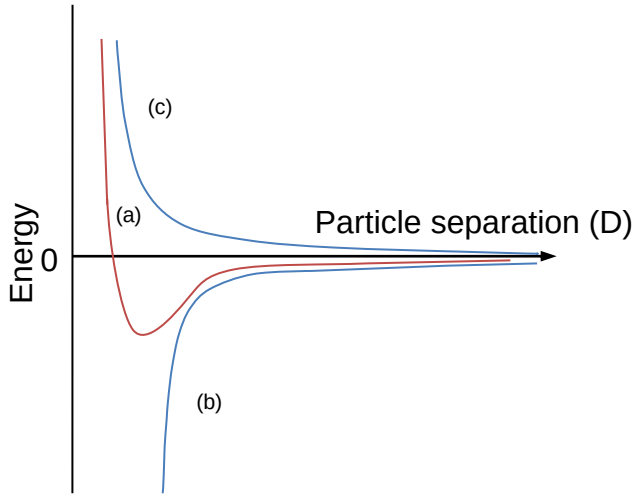

Figure 35. (a) The resultant energy interaction (red) based on (b) the attractive Van der Waals forces (negative) and (c) Born repulsion (positive) as a function of particle separation [105]**.**

The stability of nanoparticles in solution is a combination of these attractive and repulsive forces. Stabilising nanoparticles in solution, i.e. preparing a non-flocculating sample in which the nanoparticles remain dispersed, utilises the electrostatic repulsion from charged nanoparticle surfaces. The magnitude of this charge influences the particle stability.

Nanoparticles can be coated with a polymer to improve dispersion, this is known as steric stabilisation (Figure 36). The polymer conformation that adheres to the nanoparticle surface is affected by the quality of the solvent and the concentration of polymer present. Sterically stabilised nanoparticles repel each other by the overlapping polymer layers when they come close in proximity, however the steric repulsive force can also experience attractive forces [105,106].

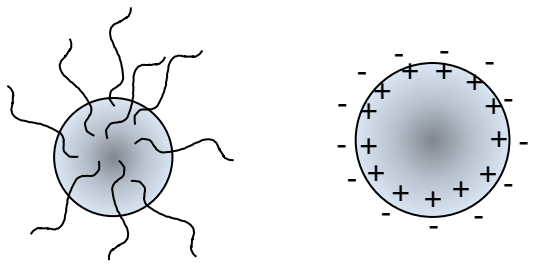

Figure 36. Mechanisms of particle stability. Steric stabilisation can physically improve the stability of nanoparticle suspensions if enough polymer adsorbs to the surface. Electrostatic charge stabilisation uses like charges at surfaces to repel nanoparticles in suspensions [105]**.**

Surface functionalisation is used to alter the surface of the nanoparticle using polymer adsorption or specific labelling with molecules. Specific labelling allows the nanoparticle surface to be coated with a molecule to target an area for the given application [106].

Blanco-Lopez *et al.* investigated the behaviour of uncoated $BaTiO_3$ nanoparticle suspensions in water at varying pH. Characterising the zeta potential of barium titanate nanoparticles across a pH range of 2 to 10 (Figure 37) to better understand the surface charge on the nanoparticles [107]. The researchers also investigated the dissolution of barium titanate nanoparticle surfaces across a similar pH scale; characterising the suspensions by atomic absorption spectroscopy [108,109] shown in Figure 37.

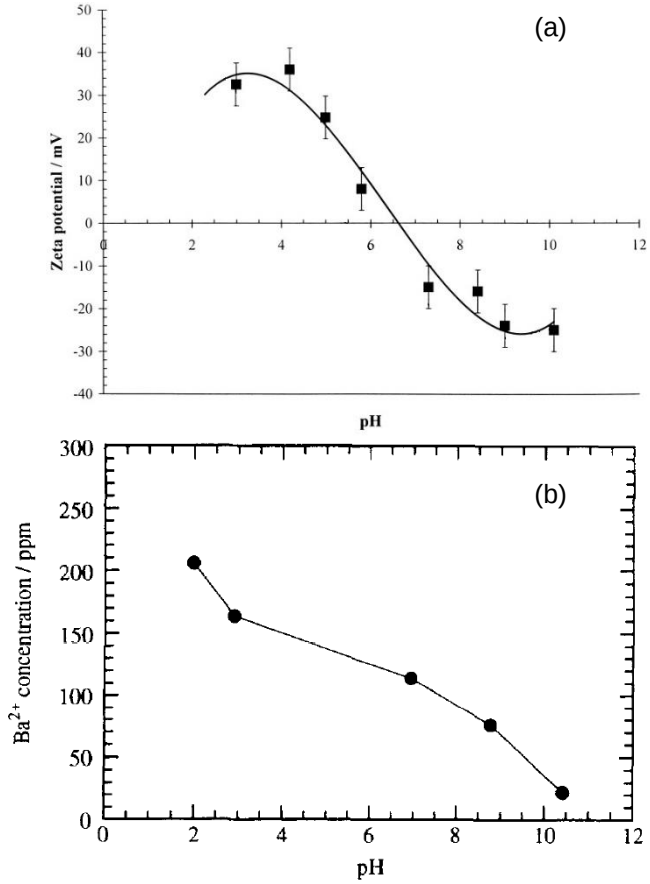

Figure 37. (a) The zeta potential of barium titanate nanoparticles suspensions as a function of pH. (b) Barium ions released from a 0.5 % volume suspension of $BaTiO_3$ over 48 hours at similar pH values in (a); taken from [107,109]**.**

Figure 37 shows that $BaTiO_3$ nanoparticles suspended in aqueous media are stable at acidic pH (pH 3/4) and alkaline pH (pH 10). The isoelectric point (the

pH where the nanoparticle has no net surface charge) is at ~pH 6.5 [107]. Figure 37 shows that $BaTiO_3$ nanoparticles are colloidally stable at acid pH, however the atomic absorption results shows barium ions leach from the nanoparticles at acidic pH (pH= 3 or 4) [107,109]. This will affect the dispersion of $BaTiO_3$ nanoparticles (especially as there are acidic components during nanoparticle cell uptake [110]). The work carried out by Blanco-Lopez *et al*. showed the surface characteristics of uncoated barium titanate, however most nanoparticle systems introduced to biological systems are functionalised and this is discussed below.

Kim *et al.* investigated the coating of barium titanate nanoparticles with a high-dielectric strength polymer in order to help improve the chemical processing of these materials into thin films [104]. Their research showed the nanoparticle stability was improved by sterically coating with *n*-octylphosphonic acid and their proposed phosphate ligand binding mechanisms to the $BaTiO_3$ surface is shown in Figure 38 [111]. Kim *et al*. chemically modified the surface of $BaTiO_3$ with phosphonic acid and poly-ethylene glycol (PEG) organic ligands which decreased the aggregation of the nanoparticles by three-fold (compared to uncoated nanoparticles). The phosphonic acid binder was used with another organic ligand (pentafluorobenzyl) to disperse the nanoparticles in different suspending media in order to improve the casting of these suspensions into thin films [104].

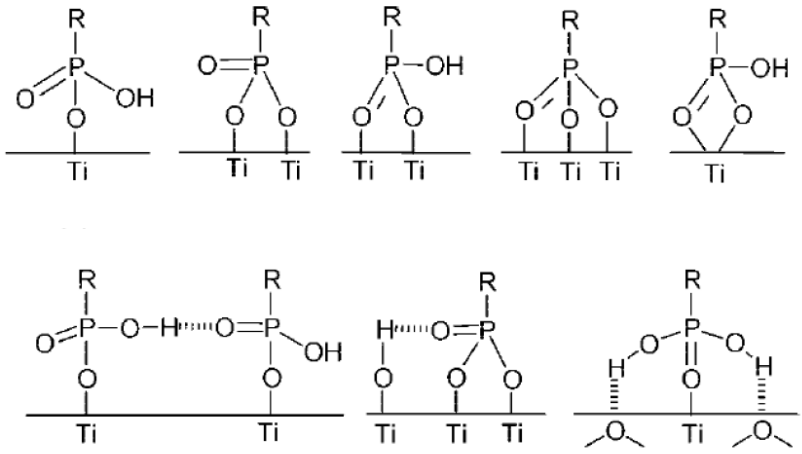

Figure 38. Proposed binding mechanisms of phosphonic acid to the Ti-O surface of $BaTiO_3$; taken from [111]**.**

Other research groups have suggested that barium titanate suspensions could be improved by functionalisation with polymers such as: polyethylneamine (PEI) [112], 3-aminomethylphosphonic acid (AMPA) [113], 3-aminopropyltriethoxysilane (APTES) [114], polyethylene glycol (PEG) [40,115] and poly-L-lysine (PLL) [116].

Dempsey *et al.* showed that barium titanate nanoparticles coated in PEI had improved cellular uptake. The PEI-coated $BaTiO_3$ (PEI-BT) nanoparticles had a low toxicity as compared to uncoated barium titanate in terms of a cell viability MTT assay; Figure 39 [112]. The improved cellular uptake was proposed to be as a result of the net positive surface charge of the PEI-BT nanoparticles.

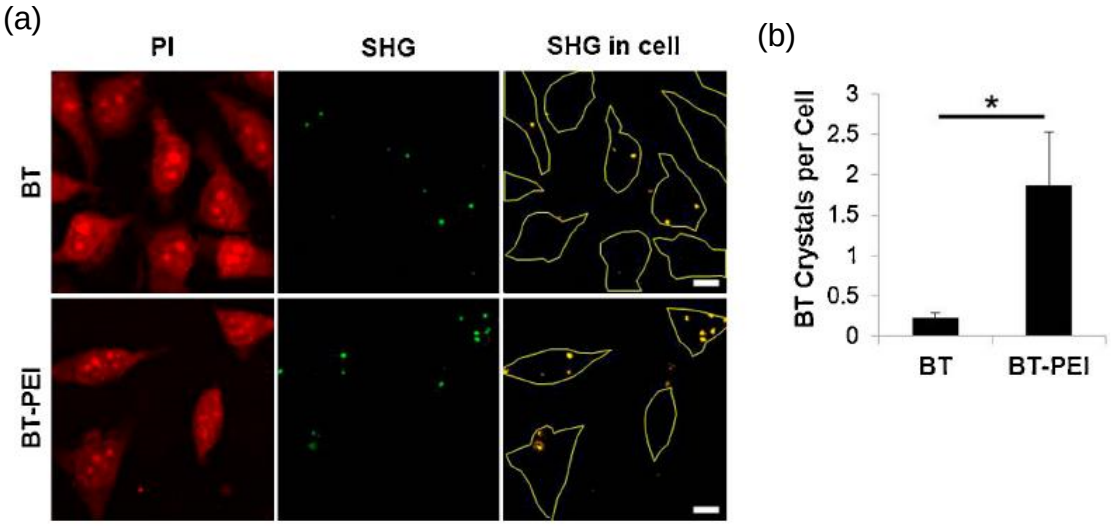

Figure 39. Multiphoton image series, comparing barium titanate (BT) and PEI coated barium titanate (BT-PEI) at a weight ratio of polymer to nanoparticle of 1:40; scale bar is 10 µm. (a) BT and BT-PEI nanoparticles were added to HeLa cells and imaged (multiphoton) to gain the cell boundary outline, the SHG signal from the nanoparticles were collected and the cellular outline overlaid on the SHG image. (b) The comparison of cellular uptake was averaged across 4 different areas and an average number of internalised nanoparticles per cell determined ($p < 0.01$); taken from [112]**.**

Hsieh *et al.* has demonstrated coating $BaTiO_3$ with 3-aminomethylphosphonic acid (AMPA) by sonicating the reagents for a period of 24 hours. The polymer was suggested to bind to the $BaTiO_3$ nanoparticle surface by the PO_4 binding mechanisms shown in Figure 38 [113]. This resulted in electrostatically stabilised $BaTiO_3$ nanoparticles due to the amine groups repelling each other; shown by dynamic light scattering results in Figure 40. The amine group on the surface can be used for further conjugation to proteins for specific labelling [113].

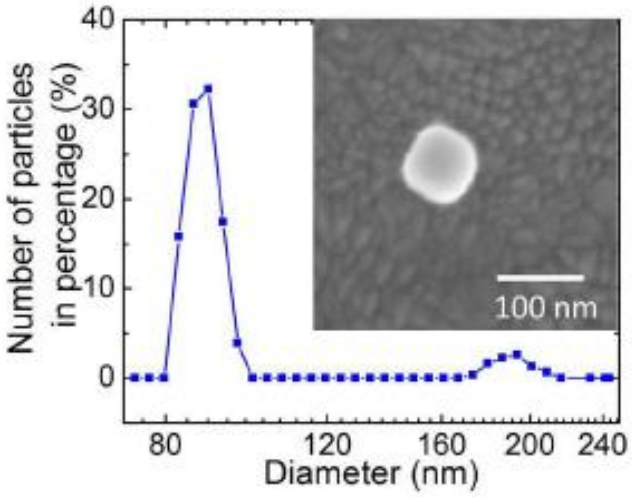

Figure 40. Dynamic light scattering of a BT-AMPA nanoparticle dispersion with an SEM of the nanoparticle shown inset, indicating a similar primary particle size shown by DLS and SEM; taken from [113]**.**

Specific labelling of the barium titanate nanoparticle surface was carried out by Hsieh *et al.* using 3-aminopropyltriethoxysilane (APTES) [114]. This research showed $BaTiO_3$ nanoparticles functionalised to a reduced antibody, that specifically binds to the primary antibody, highlighting the specificity of the nanoparticles in an antibody microarray in Figure 41. The research showed that functionalisation with APTES provided a stable dispersion (not shown) but more importantly, $BaTiO_3$ nanoparticles could be labelled to bind to specific antibodies [114]. The work showed that this type of labelling is highly specific (<5 % non-specific labelling) and the bio-conjugated nanoparticles can also produce SHG; Figure 41. The disadvantage of this highly-specific labelling was the lengthy synthesis procedure required.

Further chemically modified barium titanate surfaces were investigated by Čulić-Viskota *et al*. who produced a protocol for chemically binding PEG for *in-vivo* SHG imaging of zebrafish [47,115].

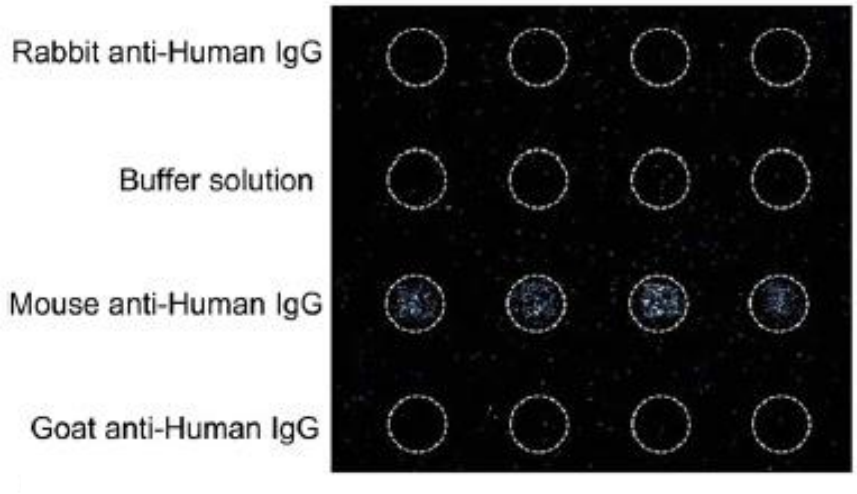

Figure 41. Specific binding to the BT-APTES-antibody on a microarray of primary-antibodies. The dashed circles show the target areas of primary antibodies using two other antibodies for a negative control and buffer solution for a positive control. The printing spot is 90 μm in diameter and 200 μm in between printing areas; taken from [114]**.**

The research published by Čulić-Viskota *et al*. developed a functionalisation protocol for barium titanate nanoparticles used as SHG nanoprobes. First of all the nanoparticles were acid treated with hydrogen peroxide (H_2O_2) to saturate the $BaTiO_3$ nanoparticle surface with -OH groups [47]. This provided a surface for N-aminoethyl-2,2,4-trimethyl-1-aza-2-silicyclopentane (ATSP) molecules to react with the OH groups to leave a new amine rich surface; Figure 42 [115]. The end NH_2 group can then be used for further conjugation with biological molecules. However, this preparation process takes over three days and requires specialist chemistry apparatus [47,115]. The chemically modified BT-ATSP nanoparticles were then further functionalised with the addition of poly-ethylene glycol (PEG), and the composite BT-ATSP-PEG nanoparticles then used for *in vitro* SHG imaging in a zebrafish, as also shown in Figure 42; [47,115].

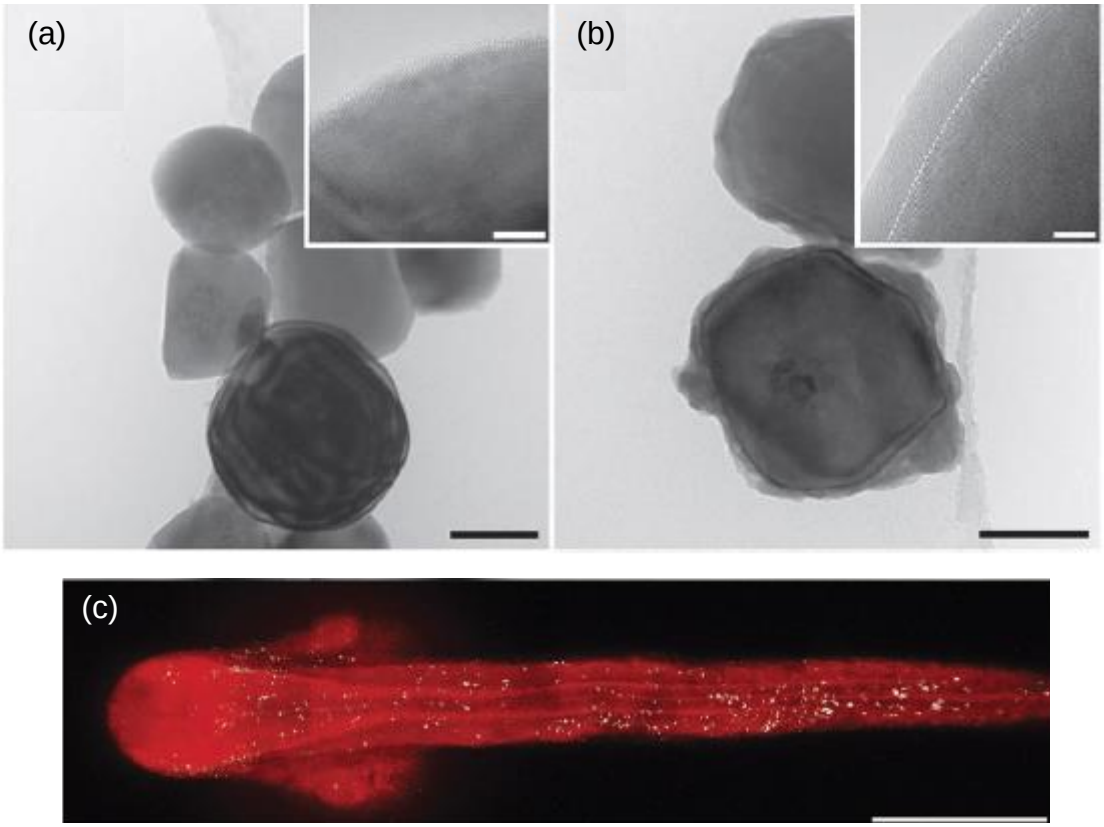

Figure 42. (a) Bright Field TEM image of commercially purchased, uncoated barium titanate nanoparticles with a high magnification image of the surface (inset). (b) Treated nanoparticles with ATSP, resulting in a ~5 nm surface layer shown by the high magnification image of the surface (inset). The scale bars in the main image are 100 nm with a 5 nm scale bar for the insets. (c) Multiphoton and SHG combined image of a stained zebrafish embryo with the BT-PEG SHG nanoprobes shown in white after 24 hour exposure, scale bar 300 µm; taken from [47,115]**.**

Staedler *et al.* produced a review of the harmonic nanoparticles that investigated the SHG output and biocompatibility of nanoparticles. The nanoparticles in the study had PEG adsorbed to the surface to improve the nanoparticle stability [40]. This coating was produced by agitation using an ultrasonicator for a 24-hour period at an acidic pH.

The research by Staedler *et al.* showed that barium titanate was the least cytotoxic compared to potassium titanyl phosphate (KTP), lithium niobate ($LiNbO_3$), zinc oxide (ZnO), potassium niobate ($KNbO_3$) and bismuth ferrite ($BiFeO_3$) in four different cell lines after exposure at 5, 24 and 72 hours, at a concentration of 50 µg/mL $BaTiO_3$ (Table 2) [40]. Hsieh *et al.* produced *in vitro* cytotoxic studies of barium titanate nanoparticles in HeLa cells, highlighting no change in cell viability after a 24 hour exposure (not shown) [117].

Cell Type	**A549**	**HTB-182**	**HTB-178**	**BEAS-2B**
Nanoparticle exposure	**% of surviving cells**			
5 hours	91 ± 5	87 ± 9	87 ± 13	93 ± 1
24 hours	84 ± 4	85 ± 1	91 ± 2	92 ± 4
72 hours	81 ± 8	88 ± 2	74 ± 9	78 ± 9

Table 2. Cytotoxic effect of PEG coated $BaTiO_3$ nanoparticles after exposure for 5, 24 and 72 hours. The cell lines A549, HTB-182 and HTB-178 are human lung cancer cells; BEAS-2B is non-tumorous lung-derived cells. The results shown are the mean ± standard deviation of triplicates of two different experiments; taken from [40]**.**

The research conducted by Staedler *et al.* highlighted a less timely option of coating BT nanoparticles with PEG by ultra-sonicating for 24 hours. I attempted the use of this functionalisation route on hydrothermally prepared $BaTiO_3$ nanoparticles as part of this work; however, the results were not found to be successful.

The polymer chosen for functionalising $BaTiO_3$ nanoparticles in this study was the non-covalent wrapping of poly-L-lysine. Ciofani *et al.* first published the successful preparation and characterisation of BT-PLL nanoparticles [116]. The research suggested that BT-PLL nanoparticles showed improved cellular uptake into H9C2 rat-cardiomyocytes. However, due to the increased uptake of BT-PLL nanoparticles, the MTT assay showed a reduction in cell viability for BT-PLL and PLL at a concentration of around 10–20 µg/mL; Figure 43 [116].

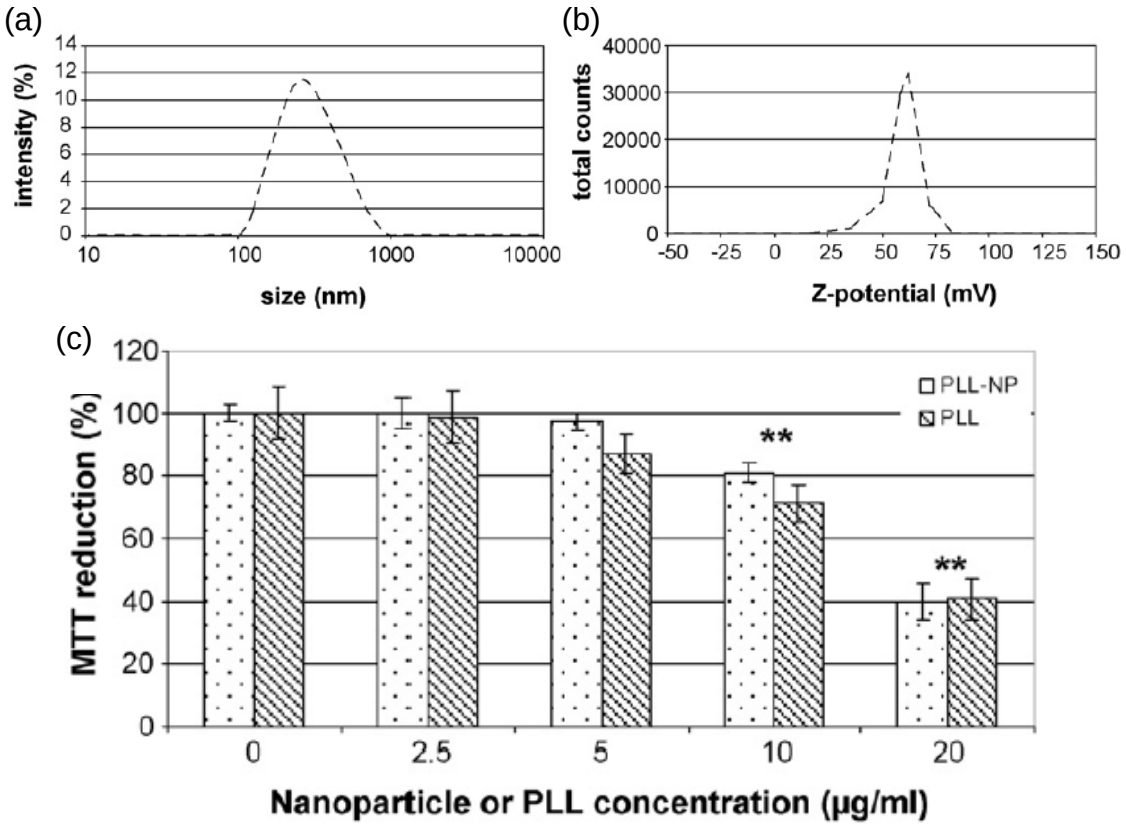

Figure 43. (a) Plot of the dynamic light scattering of BT-PLL nanoparticles in cell culture media, (b) the zeta-potential of BT-PLL nanoparticles showing a net positive surface charge in diluted cell culture medium. (c) MTT assay showing the reduction of cell viability when the BT-PLL (spotted) and PLL (striped) concentrations are increased; taken from [116]**.**

This non-covalently wrapped, electrostatically stabilised poly-L-lysine coating around the $BaTiO_3$ nanoparticles is used to functionalise the hydrothermally prepared $BaTiO_3$ nanoparticles as discussed in Chapter 3. Functionalisation of nanoparticles is important as it is shown to have influence on the cell viability (Figure 43).

2.7 Literature review summary.

This literature review has summarised the scientific background and current research of barium titanate systems for their application as second harmonic biomarkers. This thesis addresses how barium titanate nanoparticles emit SHG and how they can be used as biomarkers, investigating:

- Why fine particles emit SHG when their experimental results suggest the crystal phase of the nanoparticles are cubic (Kim *et al*.) [39];
- If the addition of strontium ions into the barium titanate lattice enhances the output of SHG due to the proposed increase in dielectric constant (i.e. net polarisation) at room temperature (Figure 26) [22,89];
- How the nanoparticles are dispersed in complete cell culture media before they are delivered to cells and what is their suspension behaviour across a range of concentrations;
- Why specific functionalisation of barium titanate systems (with a positive charge) have an effect on cell viability (Ciofani *et al*. [116]).

These are fundamental aspects of using nanoparticles as biomarkers, and elucidation of the above points will help improve the design of these systems for future application.

Chapter 3 Materials and Methods

3.1 Synthesis of $BaTiO_3$ and $Ba_{1-x}Sr_xTiO_3$ nanoparticles

Hydrothermal synthesis is a widely used technique for producing barium titanate and barium strontium titanate nanoparticles. It can result in a high yield of product with a direct route to sub-micron sized powders that are relatively mono-disperse. This procedure allows reagents to be subjected to relatively high temperatures and pressures that are generally achieved in a stainless steel autoclave as shown in Figure 44.

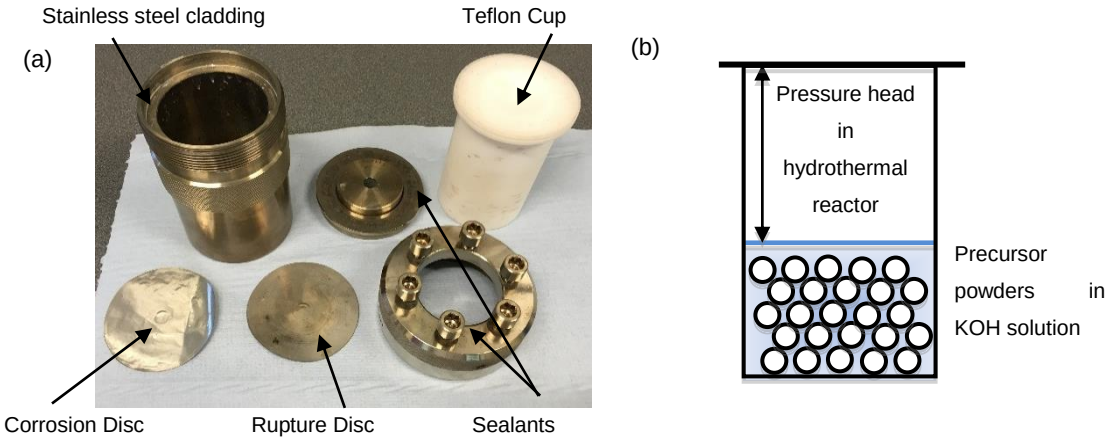

Figure 44. (a) Labelled photograph of the hydrothermal autoclave and Teflon cup equipment used here. (b) Schematic cross-section of the Teflon cup that is placed in the stainless steel cladding.

The potassium hydroxide solution was made by dissolving 6.63 g of KOH (≥90 %, Sigma Aldrich, Dorset, UK) in 40 mL of deionised water to make a 3 M solution inside a 125 mL sized Teflon cup. This was agitated by a magnetic stirrer whilst the other reagents were weighed. The reagents were 19.75 g (1.6 M) of barium hydroxide octahydrate, (≥98 %, Sigma Aldrich, Dorset, UK) and 5.00 g (1.6 M), of titanium (IV) oxide nanopowder, quoted particle size of 21 nm

(≥99.5 %, Sigma Aldrich, Dorset, UK). The reagents were weighed and placed inside the Teflon cup and the slurry was stirred by a magnetically driven bar for approximately 10 minutes or until visibly mixed well. The pH was measured to be ~13 and the Teflon cup was inserted into the stainless steel cladding, (Parr instruments) sealed and placed into a furnace (Pyro Therm, Leicestershire, UK) for 72 hours at 150 ^{o}C with a heating and cooling rate of 5 ^{o}C per minute.

Barium strontium titanate ($Ba_{0.8}Sr_{0.2}TiO_3$) was synthesised in two ways. Both synthesis routes used a 3M solution of KOH, 6.63 g (≥ 90 %, Sigma Aldrich, Dorset, UK) dissolved in 40 mL of deionised water transferred to the Teflon cup. Synthesis route 1 reagents were: 10.10 g (0.8 M) of $Ba(OH)_2.8H_2O$, 3.20 g (1 M) of titanium (IV) oxide nanopowder (≥99.5 %, Sigma Aldrich, Dorset, UK) and 0.97 g (0.2 M) of strontium hydroxide $Sr(OH)_2$ (≥94 %, Sigma Aldrich, Dorset, UK). This was sealed in the Teflon cup as described below.

Synthesis route 2 used an excess amount of barium hydroxide octahydrate 23.31 g (1.8 M) (≥98 %, Sigma Aldrich, Dorset, UK) 1.13 g (0.4 M) of titanium (IV) oxide nanopowders (≥99.5 %, Sigma Aldrich, Dorset, UK), with the addition of 0.56 g (0.1 M) of strontium hydroxide (≥94 %, Sigma Aldrich, Dorset, UK). Both slurries were stirred by magnetic bar for approximately 10 minutes or until well mixed and the pH was measured to be ~13. The Teflon cup was inserted in the stainless steel cladding, sealed and placed at 150 ^{o}C for 48 hours at a heating and cooling rate of 5 ^{o}C per minute.

Once the reaction was complete, the supernatant was decanted and the sediment washed with acetic acid (≥99 % Sigma Aldrich, Dorset, UK) while still in the Teflon cup. The acetic acid/nanoparticle slurry was transferred to polypropylene centrifuge tubes and ultrasonicated for 15 minutes (EMAG

EMMI-30HC 3L, Germany), the sonicated slurry was then centrifuged at 6000 rpm for 5 minutes (Centurion 2000 series, Sussex, UK) and the supernatant was discarded. The washing process was repeated 4-5 times with deionised water. The washed nanoparticle slurry was then placed in a glass petri dish and left to dry overnight at ~100 ^{o}C.

Commercial barium titanate samples were purchased from Sigma Aldrich (Dorset, UK): a cubic phase (≤ 100 nm particle size, ≥ 99 % trace metals basis) and also a tetragonal phase (< 3 μm, 99 % trace metal basis) that was ground using an agate pestle and mortar (Agar Scientific, Essex, UK) to produce a 50 – 450 nm range of nanoparticle sizes; Figure 45. In addition, a cubic barium strontium titanate sample ($Ba_{0.6}Sr_{0.4}TiO_3$) was purchased from PI-KEM of 50 nm (99.5 %, Shropshire, UK).

A table of sample origin and nomenclature is presented in Table 3.

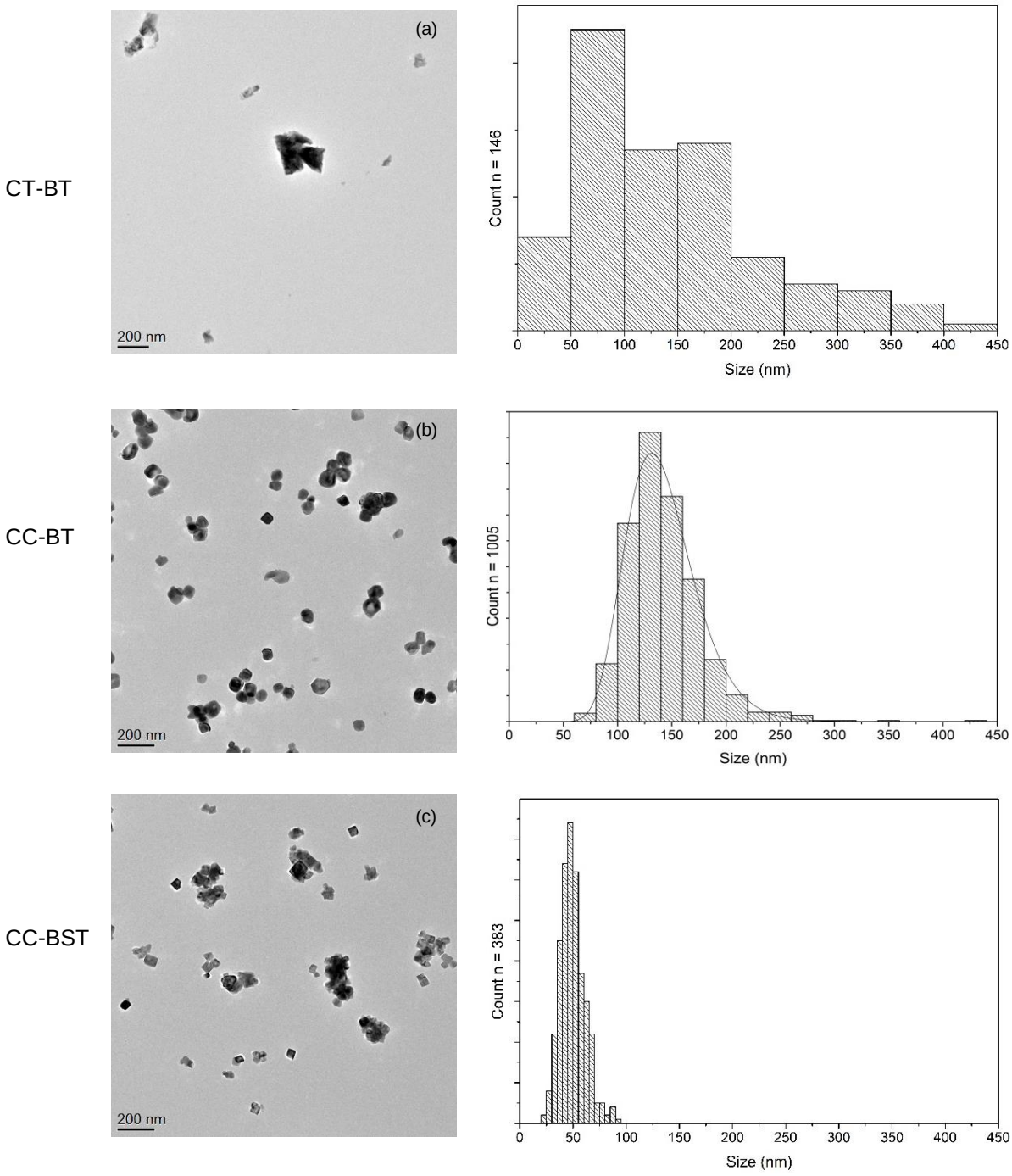

Figure 45. Representative bright field TEM images and the respective particle size distributions of the (a) crushed tetragonal barium titanate (CT-BT), (b) cubic barium titanate (CC-BT) and (c) cubic barium strontium titanate (CC-BST) commercial samples determined by TEM.

3.2 Coating barium titanate and barium strontium titanate nanoparticles with poly-L-lysine (PLL).

Poly-L-lysine is a naturally occurring amino acid that is a common addition to cell culture media because it promotes adherence of cells to a substrate [118]. This is due to a positive poly-L-lysine molecular charge attracting the negatively charged patches of a cell membrane.

When added to the nanoparticles, the polymer poly-L-lysine (PLL) ionises in solution and adsorbs to the $BaTiO_3$ surface. Improving the colloidal stability and cellular uptake by steric stabilisation and electrostatic charge of the nanoparticles [116]. Steric stabilisation is the physical and distinct separation of particles by the physically adsorbed PLL molecules around the nanoparticles. The electrostatic property of the coating should also produce a stable colloid because of like charges repelling, but opposite charges (between the coated nanoparticles and cells) attracting, so as to promote cellular uptake (discussed further in section 3.6).

A nanoparticle/poly-L-lysine suspension was made by dissolving 100 mg of poly-L-lysine hydrobromide, mol wt. 70,000 – 150,000 kDa (Sigma Aldrich, Dorset, UK) into 100 mL of deionised water. This produces a 100 mL poly-L-lysine solution to which 1000 µg of $BaTiO_3$ or $Ba_{1-x}Sr_xTiO_3$ nanoparticles were added. The nanoparticle/PLL suspension was then ultrasonicated for 24 hours (EMAG EMMI-30HC 3L, Germany) and subsequently dried in a container on an indirect heat source for 24 hours.

To prepare coated nanoparticles for cellular exposure in culture media, 50 mg of poly-L-lysine hydrobromide, mol wt. 70,000 – 150,000 (Sigma Aldrich,

Dorset, UK) was dissolved into 0.5 mL Dulbecco's phosphate buffered saline (PBS) solution (Sigma Aldrich, Dorset, UK) to give a concentrated PLL/PBS 100 mg/mL solution. $BaTiO_3$ or $Ba_{1-x}Sr_xTiO_3$ nanoparticles were then added (50 mg) to produce a concentrated suspension that was further diluted by 50 mL of Dulbecco's modified eagle medium (DMEM) for cell culture to produce a 1000 µg/mL BT-PLL-DMEM solution and this was used to treat the cells.

A full list of the samples used in the project are summarised in Table 3 below.

Full sample name	**Acronym**
Poly-L-lysine	PLL
Hydrothermal barium titanate	H-BT
Hydrothermal barium titanate with 1mg/mL PLL coating	H-BT-PLL
Hydrothermal barium strontium titanate – (Route 1)	H-BST-01
Hydrothermal barium excess barium strontium titanate – (Route 2)	H-BST
Hydrothermal barium strontium titanate with 1mg/mL PLL coating	H-BST-PLL
Commercial cubic barium titanate	CC-BT
Commercial tetragonal barium titanate	CT-BT
Commercial cubic barium strontium titanate	CC-BST

Table 3. A list of samples either prepared hydrothermally or available commercially, with the corresponding nomenclature that will be used herein.

3.3 Characterisation of $BaTiO_3$ and $Ba_{1-x}Sr_xTiO_3$ nanoparticles.

3.3.1 X-Ray powder diffraction (XRD)

This characterisation technique determines or identifies the crystal structure of a sample and it utilises the 'reflections' of X-Rays by crystallographic atomic planes. At critical (Bragg) incident angles, X-Rays interfere constructively after scattering from planes (each with a specific interatomic spacing) within an irradiated sample. Figure 46 shows a schematic for the derivation of Bragg's equation for constructive interference i.e. for a phase difference of λ ($n\lambda = 2d\sin\theta$), which is the physical origin of how X-Rays can diffract and be used to determine a crystal structure.

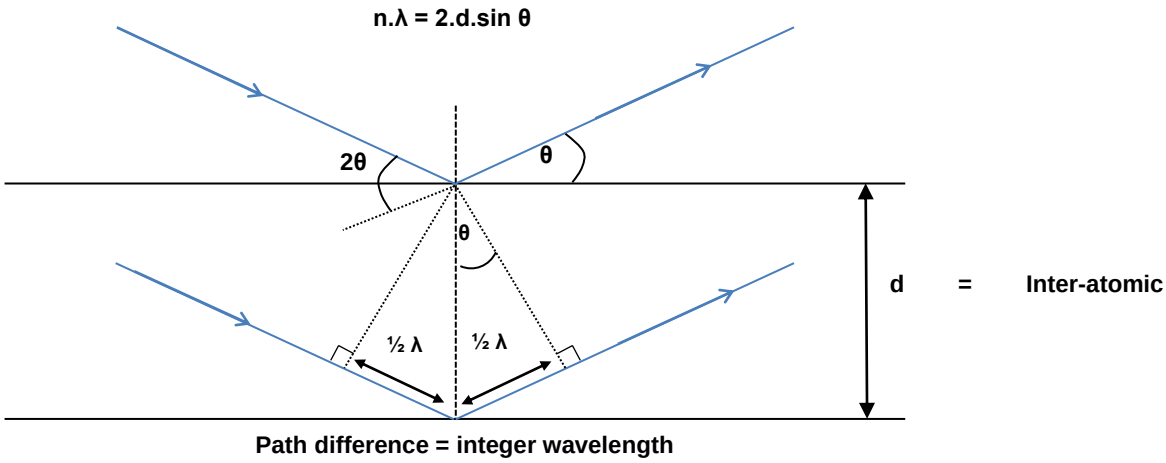

Figure 46. Graphical representation of the Bragg equation $n\lambda = 2d\sin\theta$. Two incident X-Rays are in phase by a full wavelength at an incident angle of θ for an interatomic spacing d and so the scattered rays interfere constructively to give a 'reflection' peak in the XRD pattern [65]**.**

Here, this technique can determine the crystal phase content and estimate the relative amounts of each phase present in the barium titanate and barium strontium titanate nanoparticle samples. The phase fraction determination is conducted post data collection by Rietveld refinement – in this case a linear combination of cubic and tetragonal reference patterns was fitted to the experimental data.

A distinguishing feature of the tetragonal barium titanate X-Ray diffraction (XRD) pattern is the splitting of the (002/200) peak at ≈ 45 $^{o}2\theta$ (for Cu *K*α X-Rays, λ = 1.540 Å). In cubic barium titanate only a single peak is generated. Figure 47 shows an example diffraction pattern of cubic and tetragonal perovskite and the tetragonal offset of the unit cell that gives splitting of the (002/200) peak.

The lab-based X-Ray diffractometer used here was a Bruker D8 powder diffractometer with a Vantec detector using a Cu-Kα source (1.540 Å). A step size of 0.033 $^{o}2\theta$ over a scan range of 20 – 80 $^{o}2\theta$ was used to give a total scan time of 45 minutes. ~0.5 g of sample was prepared by pressing powders and small agglomerates flat in a shallow, circular holder specific for this diffractometer (approximate diameter = 4 cm x depth = 1.5 cm). Rietveld peak fitting was conducted using X'Pert HighScore Plus software with calculated ICDD files: 04-013-5890 and 01-078-4475 for the tetragonal and cubic $BaTiO_3$ fitting models respectively. For $Ba_{0.8}Sr_{0.2}TiO_3$, experimental ICCD files 04-006-6507 and 04-015-2711 were used for the tetragonal and cubic fitting models respectively.

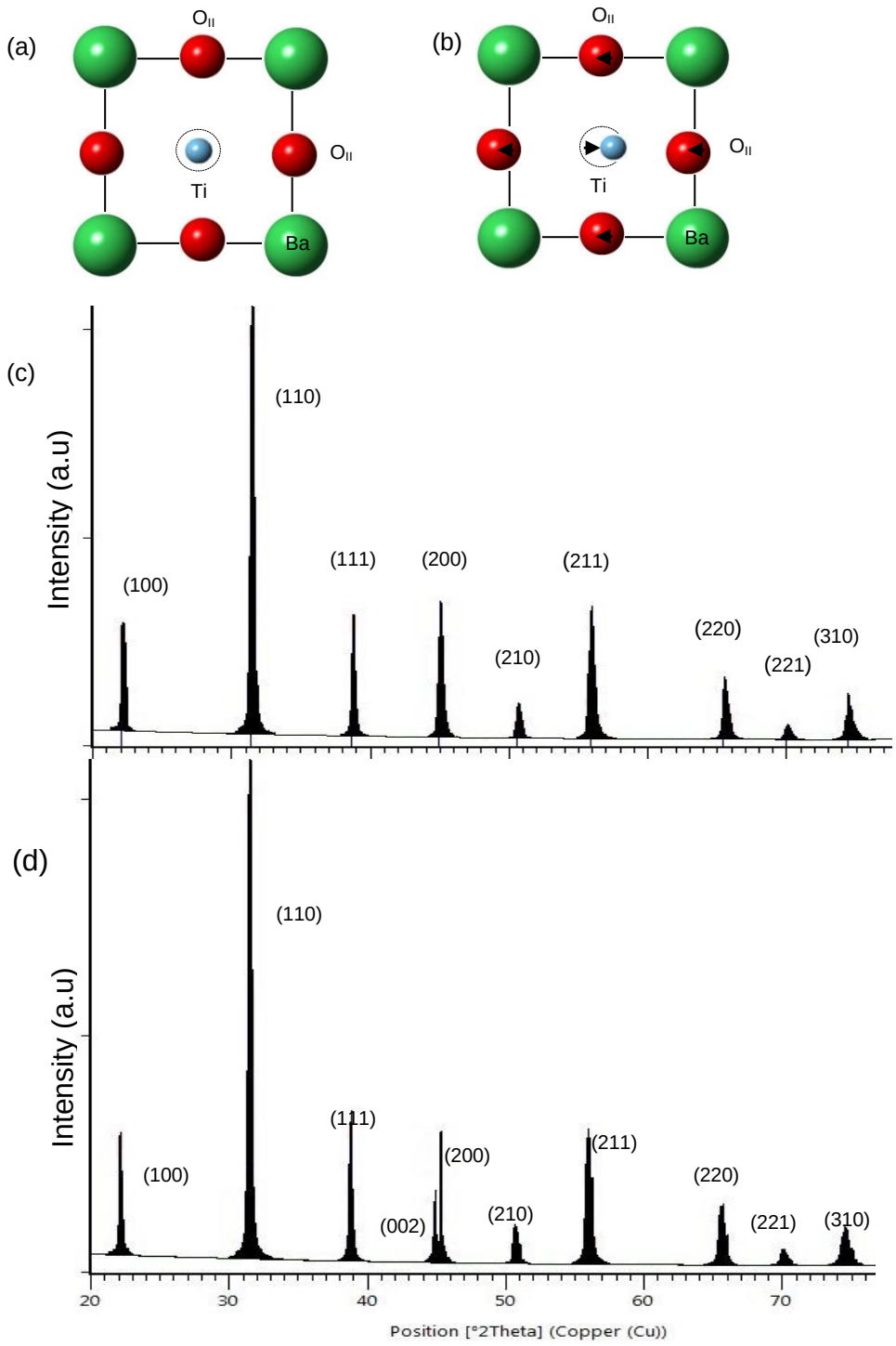

Figure 47. (a) Unit cell [100] view of a cubic barium titanate lattice with the face centred O_I oxygen atoms removed for ease of viewing. (b) The modified unit cell highlights the offset of the titanium and oxygen atoms to produce tetragonal barium titanate. Typical Ti-atom displacement values are ~ 0.1 Å [74]**. (c) The CC-BT powder X-Ray diffraction pattern labelled with the Miller indices. (d) The CT-BT X-Ray diffraction pattern showing the tetragonal splitting of the 002/200 peak labelled with the Miller indices.**

Hot stage XRD was conducted on a Bruker D8 advance diffractometer operated with a Copper Kα source (1.541 Å) at 170 ^{o}C using an Anton Parr TTK450 hot stage holder. The aluminium oxide sample holder (approximate dimensions 1.5 cm x 1 cm x 0.2 cm) was coated in a conductive grease (Anton Parr, Austria). The sample was heated to 170 ^{o}C at a rate of 30 ^{o}C min^{-1} and data were collected using a 0.035 ^{o}2θ step size over a scan range of 20 – 80 ^{o}2θ, giving a total scan time of 45 minutes. Rietveld peak fitting was conducted in X'Pert HighScore Plus with calculated ICDD files: 04-013-5890 and 01-078-4475 for the tetragonal and cubic $BaTiO_3$ fitting models respectively. The varying Rietveld fitting parameters were: unit cell lattice, diffraction pattern background and peak-width parameters.

The average crystallite size was determined using the Scherrer equation which is used for polycrystalline powders is shown in Equation 3. [65]

$$D = \frac{k.\lambda}{\beta \cos\theta}$$

Equation 3. Scherrer equation used to calculate the average crystallite size D. A particle shape constant *k* = 0.9 and the wavelength of the incident radiation (~1.540 Å) over the instrumental broadening at full width half maximum (FWHM) and the angle of the measured FWHM.

The instrumental broadening of the Bruker D8 diffractometer (laboratory-XRD and hot-stage XRD) was calculated using a NIST aluminium standard giving a peak broadening of 1.218 x10^{-3} (arb. units) and 1.17 x10^{-3} (arb. units) respectively. These values were subtracted from the experimental peak FWHM value when determining the average crystallite size (the potential micro-strain of the XRD patterns were not taken into account).

3.3.2 Synchrotron powder diffraction

Synchrotron powder diffraction was conducted at the Diamond light source, Beamline I11 (Oxford, UK). Synchrotron X-Ray powder diffraction is advantageous because of the large flux, highly collimated and shorter wavelength X-Ray source in comparison to a laboratory-XRD. The large flux and collimated beam allow for higher angular resolution of scattering data to be obtained which is critical for analysing (002/200) peak splitting in $BaTiO_3$ patterns. The shorter wavelength used and the beamline's multianalysing crystal devices (Figure 48) reduce the sample fluorescence and improve the data resolution [119,120].

Synchrotron data were gathered using the rapid access facility at the Diamond Light Source (Oxford, UK, Beamline I11). The incident radiation was a Cu-Kα source (0.826 Å) at a step size of 0.001 $^{o}2\theta$ over an angular range of 3-150 $^{o}2\theta$ giving a total scan time of 1 hour. ~0.25 g of sample was loaded into a borosilicate glass capillary tube (0.5 mm diameter, Capillary Tube Supplies Ltd, Cornwall, UK) with a total sample length of 40 – 50 mm. Data were collected automatically using a multi-analysing crystal (MAC) detector array and a capillary spinner under the supervision of Professor Chiu Tang and Dr Claire Murray (Diamond Light Source, Oxford, UK) [119].

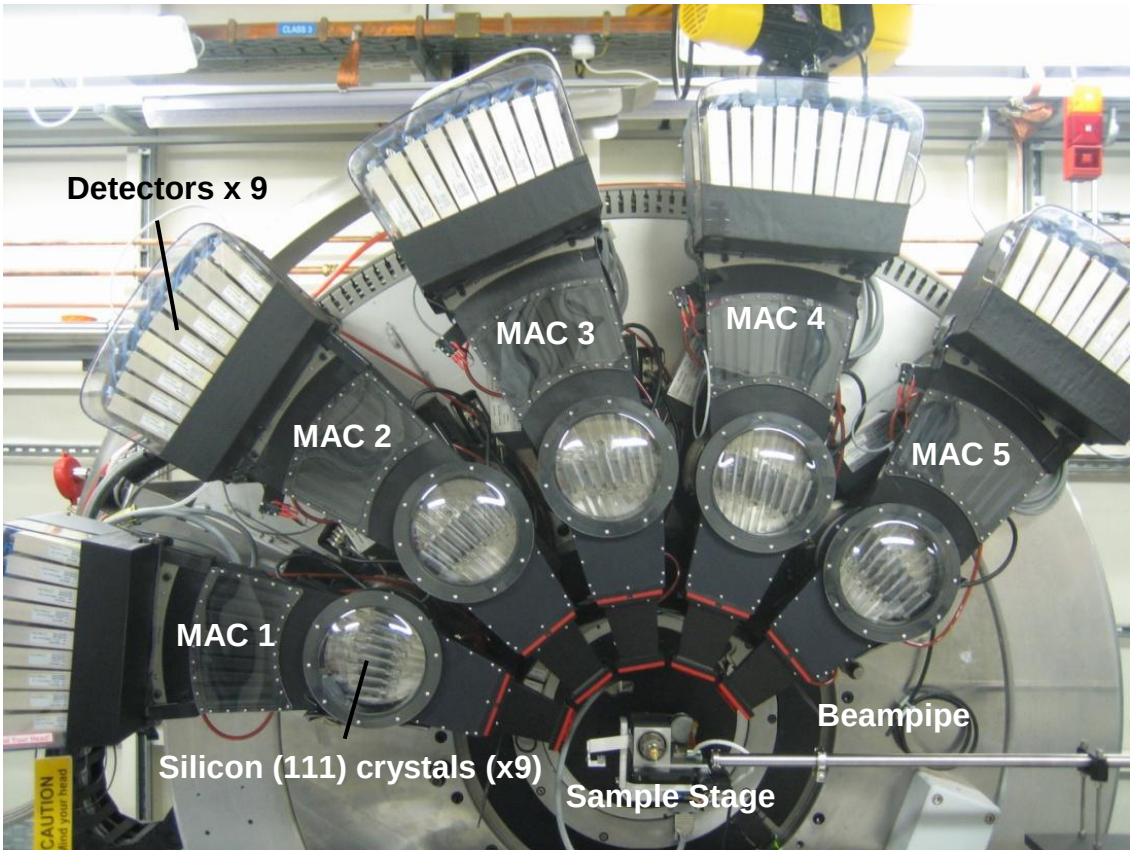

Figure 48. Labelled photograph showing the diffractometer set-up at the Diamond Light Source, beamline I11. The multianalysing crystal (MAC) detectors are mounted on the 2θ circle over a 40 ^{o}2θ rotating stage; taken from [120]**.**

3.4 Electron Microscopy

Imaging and characterisation were used to investigate the particle size and size distributions, confirm the crystal structure, chemical composition and cellular uptake of $BaTiO_3$ nanoparticles through scanning, transmission and scanning transmission electron microscopy (SEM, TEM and STEM). Electron microscopy (EM) overcomes the drawback of using visible-light for microscopy which until recently [121–123] limited the resolving power to reveal fine detail at 200 – 300 nm resolution [124]. The resolving power can be approximated by Abbe diffraction limit (Equation 4) which governs the smallest distance that can be resolved, as depicted by the Airy disk intensity profiles in Figure 49.

$$\text{Abbe resolution} = \frac{\lambda}{2.NA}$$

Equation 4. The wavelength (λ) of radiation for visible light ranges between ≈ 700 nm to ≈ 300 nm, the numerical aperture (NA) [96]**.**

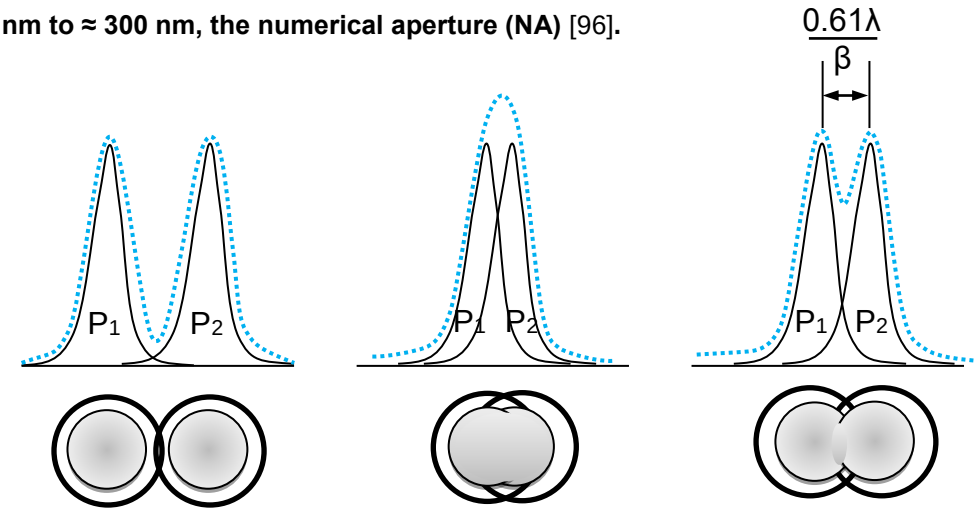

Figure 49. Airy disk intensity profiles of individual, incoherent sources (black) the resultant intensity profile is shown in blue (a) two separated peaks (P_1 & P_2) with discernible points. (b) Two peaks that cannot be resolved, whereas (c) the minimum overlap that is resolvable and is the depiction of the Rayleigh criterion [96]**. The grey disks are the projected zero-order airy disks of the above intensity profiles with the first-order shown as a black ring.**

For an optical microscope with visible-light of wavelength 500 nm and a numerical aperture of 1.3. The resolving power is ≈ 380 nm which is not suitable for analysing nanometre detail or atomic structure of samples, for example the unit cell of barium titanate is approximately 0.3 – 0.4 nm^3.

Electrons have a wave-particle duality that can relate the electron momentum to the wavelength through Planck's constant. This relationship is utilised in EM to control the electron wavelength by changing the accelerating voltage of the microscope. The relativistically corrected relationship of electron wavelength to the accelerating voltage is summarised in Equation 5.

$$\lambda = \frac{h}{[2m_0 eV\left(1 + \frac{eV}{2m_0 c^2}\right)]^{\frac{1}{2}}}$$

Equation 5. *h* is Planck's constant, m_0 is the rest mass of the electron, *e* is the electron charge, V is the accelerating voltage of the microscope and *c* is the speed of light in a vacuum.

The electron source for the TEM used here is a thermally assisted or Schottky field emission gun (FEG), which is an extremely fine tungsten cathode tip with a ZnO coating and the electrons tunnel from the tip by means of a small extraction voltage applied from an anode, a second anode then accelerates the electrons to the desired energy (voltage); as shown in Figure 50. The SEM and dedicated STEM used a cold field emission gun. A cold field emission gun benefits from a narrower beam energy spread as it is not thermally assisted (i.e. lower temperature), but produces a lower overall probe current [96,125]. The anodes that extract and accelerate the electrons from the emission tip (the gun), cause a beam crossover the exact position of which is controlled by magnetic lenses (discussed later) [96].

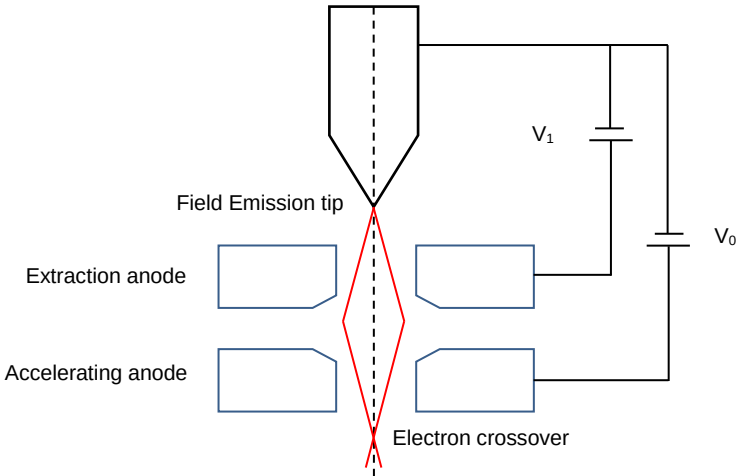

Figure 50. Schematic of field emission gun highlighting a sharp cathode tip with two-sets of anodes. The first anode is the extraction voltage (typically 3-5 kV) from the FEG-tip and the second anode is the accelerating voltage (up to 30 kV for SEM and up to 300 kV for TEM).

The accelerating voltages for TEM, SEM and STEM can be altered to produce different signals from the specimen, e.g. a high accelerating voltage in the SEM produces poor spatial resolution due to a larger interaction volume, but provides good backscattered electron signal. Typical values for accelerating voltage, wavelength and resolution for each of the microscopy techniques are summarised in Table 4.

Electron microscopy	Accelerating voltage (kV)	Wavelength (pm)
SEM	2, 5,10 & 15	27.3, 17.3, 12 .2 & 9.9
TEM	80, 200 & 300	4.1, 2.5, 2.0
Nion dedicated STEM	100	3.7

Table 4. Summary of the electron microscopy techniques and the associated wavelength of typical accelerating voltages of the microscopes. Taken from [96]**.**

The electron beam generated from the electron gun is then focussed onto the sample by a series of electromagnetic lenses. The working resolution is

significantly worse than the wavelength-limited resolution because of aberrations in the main imaging lenses. The electron microscope schematics for both SEM and TEM are shown in Figure 51 [126,127].

Although Equation 4 & Equation 5 show that the shorter the wavelength the more the working resolution is improved, the image is not necessarily improved because the lenses used to ‘collect’ electrons are imperfect. This imperfection in lenses is known as spherical aberration, where the electron beam that passes closer to the optic axis of the lens is focussed less strongly than that at the edge of the lens; Figure 52.

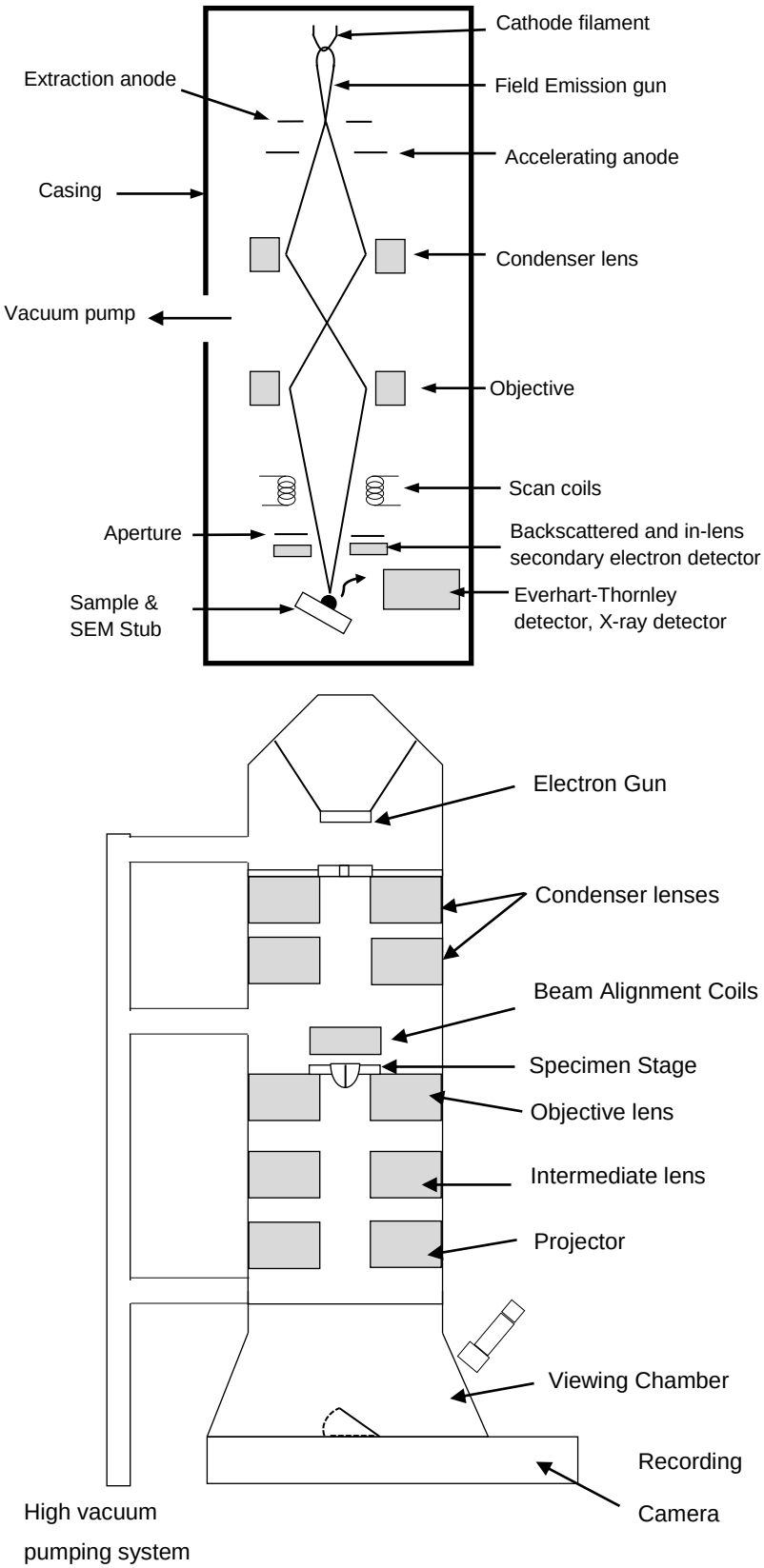

Figure 51. (a) Simple cross-section sketch of SEM highlighting components and (b) cross sectional view of transmission electron microscope, taken from [96,127]**.**

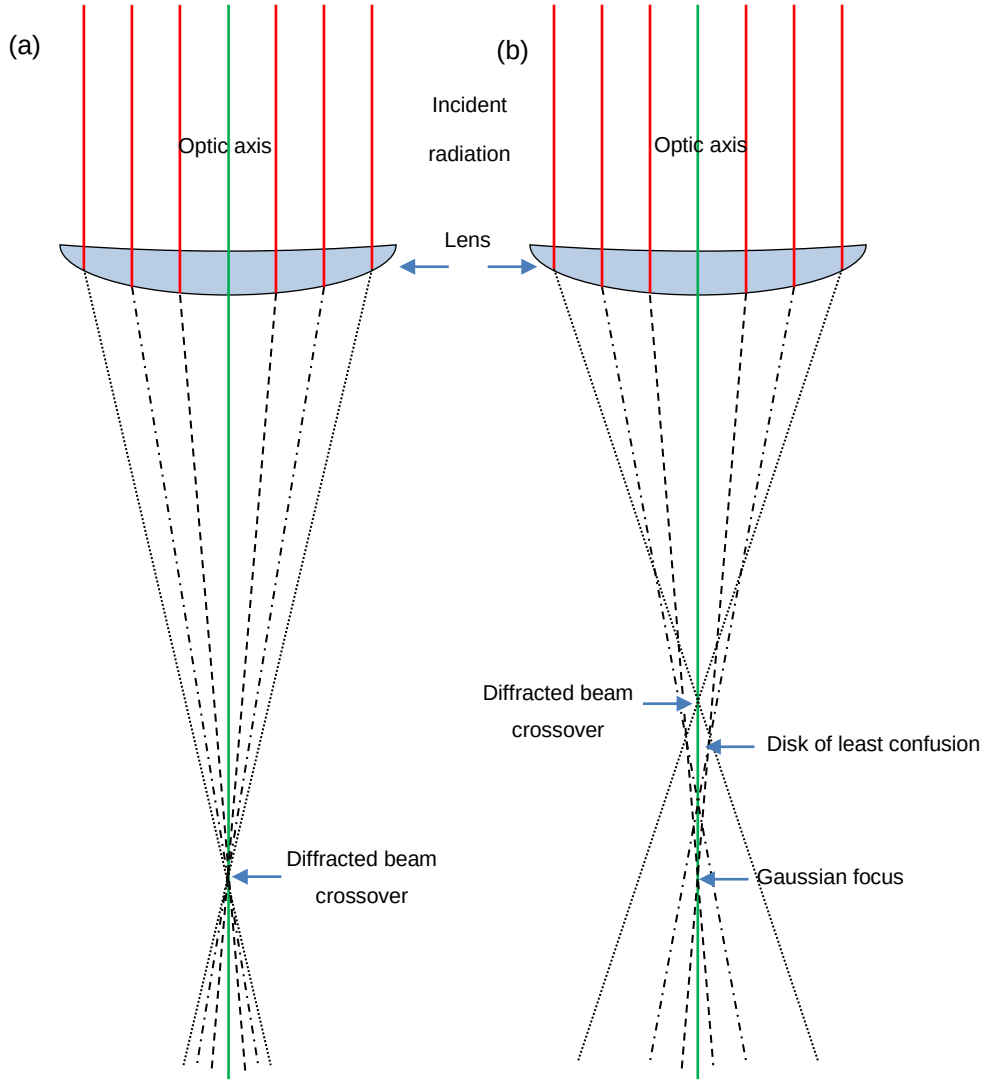

Figure 52. (a) A perfect lens shows illumination focused to a spot. (b) A realistic beam path construction of illumination passing through a lens that has spherical aberration [127]**.**

Lenses also suffer from chromatic aberration where electrons of different energy are brought to a different focus, this then blurs the image of specimens that strongly scatter incident electrons inelastically and change their wavelength (i.e. thick specimens). The incident electrons that have been

scattered and lost energy are focused more strongly in comparison to electrons with no energy loss which focus at the Gaussian image plane; Figure 53.

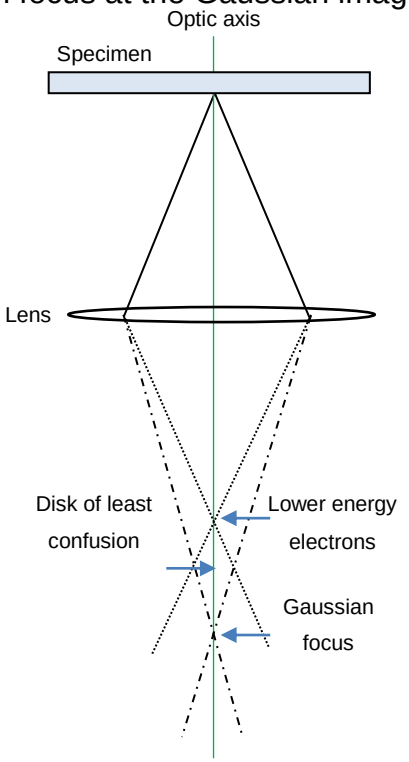

Figure 53. Chromatic aberration results in electrons with varying energy loss being focussed on different planes. The electrons that have no energy loss are more likely to have a longer focal length than electrons that have energy-loss by scattering from the specimen [96]**.**

Chromatic blurring can be reduced by monochromating the electron source. This chromatic-aberration correction is used in the FEI Titan microscope (explained in TEM section 3.4.2). Spherical aberration correction can improve the wavelength limited resolution of a microscope [128] and in this research a Cs-corrected dedicated STEM microscope was used at SuperSTEM (Section 3.4.3).

3.4.1 Scanning electron microscopy (SEM)

The scanning electron microscope uses a focussed, convergent primary electron beam (Figure 51) which interacts with the sample to produce a number of electron and X-Ray (light) signals, and these signals can be used to provide information on the surface structure and composition of the sample. Secondary electrons are generated by the primary electrons and originate from the surface of the specimen allowing for morphology and topography to be imaged [127]. Secondary electrons are low energy and are imaged by in-lens and conventional Everhart-Thornley (EH) detectors. The in-lens detector is on top of the final pole piece in the SEM chamber whereas the EH detector is positively biased and outside the lens [129,130].

Backscattered electrons (BSE) provide atomic number contrast due to incident electrons being elastically scattered ‘back’ by the atomic nucleus towards the detector. The heavier elements will backscatter electrons more readily as they have high atomic number and will appear brighter in the image (assuming the specimen is flat).

Emission of X-Rays and energy dispersive X-Ray analysis (EDX) is used in tandem with the imaging techniques because it is able to determine the elemental composition of the samples (explained in section 3.4.4). The interaction volume of the incident electrons in the SEM shows the volume of the sample from which these signals arise, shown in Figure 54.

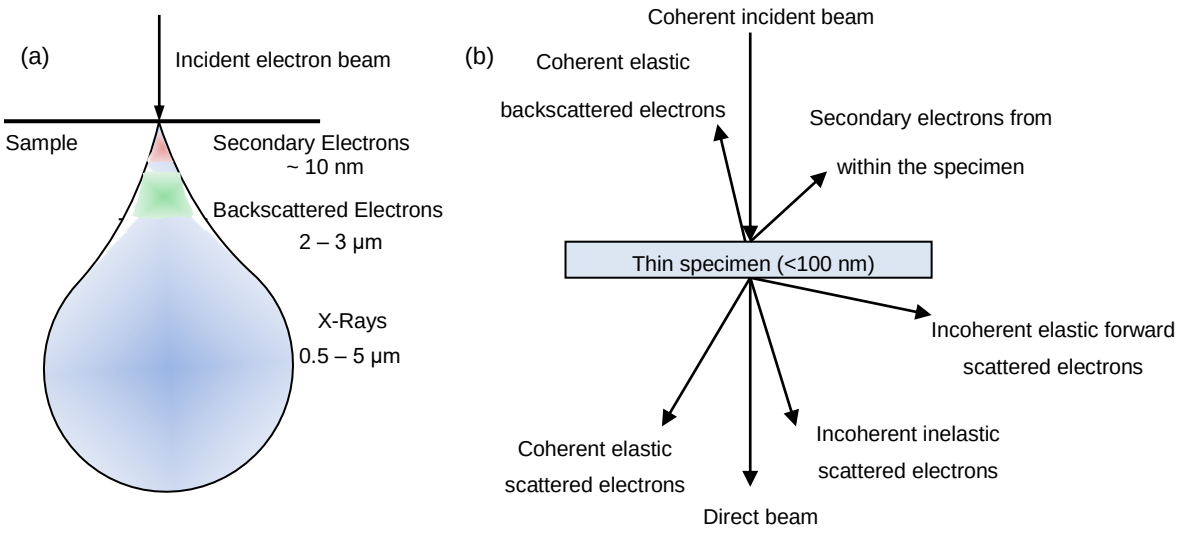

Figure 54. (a) Schematic of the interaction volume from scanning electron microscopy. The separated area's show where the respective SE, BSE and X-Ray signals originate from (the scale of signal values are dependent on atomic number and accelerating voltage). (b) Schematic of electron interaction for a thin sample. Other signals mentioned here and collected in the TEM are discussed in the following section [96,131]**.**

A Hitachi SU8230 scanning electron microscope using a cold field emission gun was operated between 2 – 15 kV depending on the signal desired from the sample i.e. secondary electron surface imaging or EDX spectroscopy was used in this study. The microscope was fitted with an Oxford instruments X-Max 80 mm^2 silicon drift EDX detector that increases the count rate of X-Rays collected giving higher sensitivity as a result of the large collection area in comparison to traditional silicon-lithium detectors [96,132].

3.4.2 Transmission electron microscopy (TEM)

Transmission electron microscopy uses a number of different imaging modes, summarised in Figure 55. Bright field microscopy uses a parallel beam of electrons focused to reveal fine detail in a specimen and the objective aperture collects the direct beam and blocks highly scattered electrons, whereas dark-field (DF) imaging uses one or more of the diffracted spots collected by the displaced objective aperture (or by tilting – not shown) [127].

Bright field microscopy shows areas that scatter as dark on a bright background (analogous to an X-Ray projection), where electron scattering from the sample gives rise to a number of contrast modes. Mass-thickness contrast depends on the amount of inelastic scattering due to the thickness and mass (density or atomic number) variations within the specimen [65]. Diffraction contrast arises due to crystallinity of the sample where electrons are reflected close to (or at) Bragg angles. This leads to dark image contrast from crystalline areas that are diffracting [65]. Phase contrast relies on the phase difference of the direct (undiffracted) beams and the diffracted beam(s) so as to produce an interference pattern which is visible at high magnifications [133].

Electron diffraction is the Bragg scattering of incident electrons from a crystalline specimen and it can be imaged directly in the back focal plane of the objective lens. The electron diffraction pattern is acquired by inserting a selected area aperture on an area of the sample (visible in the image) and then exciting the intermediate (diffraction) lens [133].

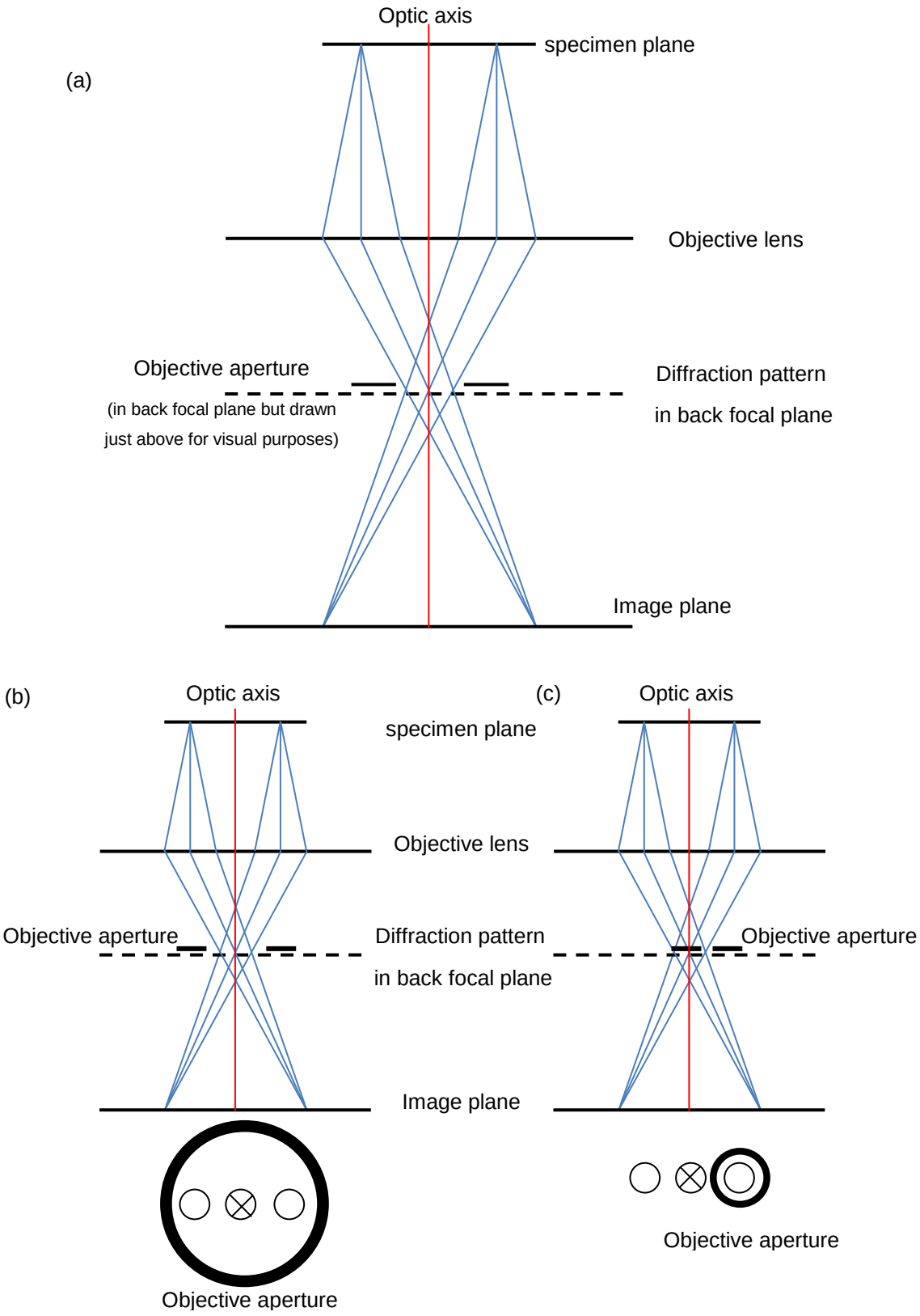

Figure 55. (a) Simplified beam path of image formation. (b) Bright field image formation where the objective aperture collects the direct beams and blocks the diffracted beams (c) Dark field image achieved with an objective aperture centred on a diffracted beam in the back focal plane. [96,127,134].

The transmission electron microscopes used in this study were a FEI Tecnai F20 microscope operated at 200 kV, fitted with a Gatan Orius SC600A CCD camera and an Oxford instruments 80 mm X-max SDD detector and a FEI Titan Themis^3 300 TEM operated with a high brightness X-FEG at 300 kV, a monochromator giving a 0.2 – 0.3 eV energy spread (when in use without monochromator on; ~ 1.3 eV energy spread). The latter microscope is fitted with a windowless Super-X, 4 detector silicon drift detector EDX system and a Gatan GIF quantum ER imaging filter for high speed electron energy loss spectroscopy (EELS).

TEM samples were prepared by drop casting suspensions onto a copper grid coated with a holey carbon support film (Agar scientific, Essex, UK). This is allowed to dry and then placed in the specimen holder and inserted into the microscope vacuum.

In this work the TEM was primarily used to determine the average particle sizes, atomic lattice spacing, crystallography and energy dispersive X-Ray analysis (EDX) was used to confirm the nanoparticles were chemically synthesised successfully.

HAADF-STEM imaging of resin embedded cell sections was undertaken using an FEI Tecnai F20 FEG microscope (probe size of ~2 nm) at Leeds. HAADF-STEM and STEM-EELS of the nanoparticles was also conducted on the FEI Titan Themis^3 (probe size of ~0.4 Å). The HAADF detector (50-170 mrad) was inserted and images were collected.

After HAADF-STEM imaging of the resin embedded cell sections, bright field TEM imaging and EDX spectroscopy of the same nanoparticles were collected.

3.4.3 Scanning transmission electron microscopy (STEM)

Scanning transmission electron microscopy utilises a convergent, scanning beam across a thin sample for bright field and dark field STEM imaging. Throughout this project high angle annular dark field (HAADF) STEM is primarily used as it can directly interpret atomic structure when imaged, particularly from the high Z-contrast of barium titanate and barium strontium titanate nanoparticles.

This technique is also inherently suited for combination with EDX and electron energy loss spectroscopy; (section 3.4.5) the latter gives STEM-EELS spectrum images producing highly spatially resolved linescans and maps across nanoparticles to elucidate the chemistry of the elemental components [96,134]. The electron beam path of STEM image formation is shown in Figure 56.

The STEM probe diameter is limited by the condenser aperture and probe convergence semi-angle (α) at the specimen. As the electrons are scanning across the sample, they are transmitted through the sample and depending on the angular range or scattering, collected by a bank range of detectors, producing: bright field (0 to 6 mrad), annular dark field (35 to 100 mrad) and HAADF images (70 to 210 mrad) [135].

A dedicated Cs-aberration corrected STEM at Daresbury labs, Nion UltraSTEM 100 was used in this project operating at 100 kV (probe size of ~0.8 Å). Cs-aberration correctors are an assembly of octupole/quadrupole Cs-correctors prior to the probe forming objective lens. The microscope is fitted with an UHV Enfina EEL spectrometer; Figure 57.

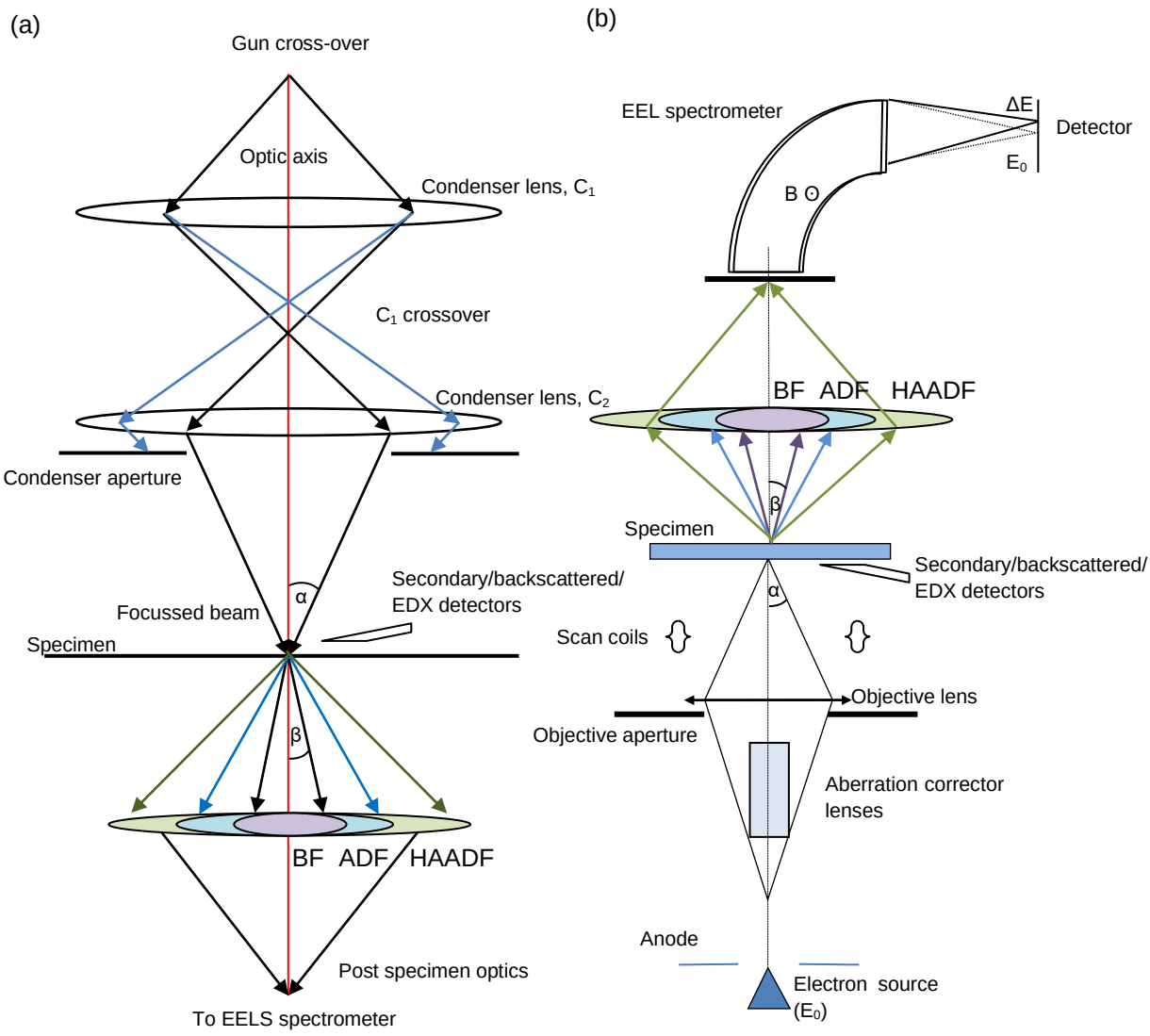

Figure 56. (a) Beam path of a conventional TEM being used for STEM. (b) The beam path of a dedicated STEM (spherical aberration corrected) similar to SuperSTEM; It is inverted in comparison to conventional TEMs which is key for gun stability [96,134]**.**

Examples of HAADF-STEM data collected by these microscopes are shown in Figure 57.

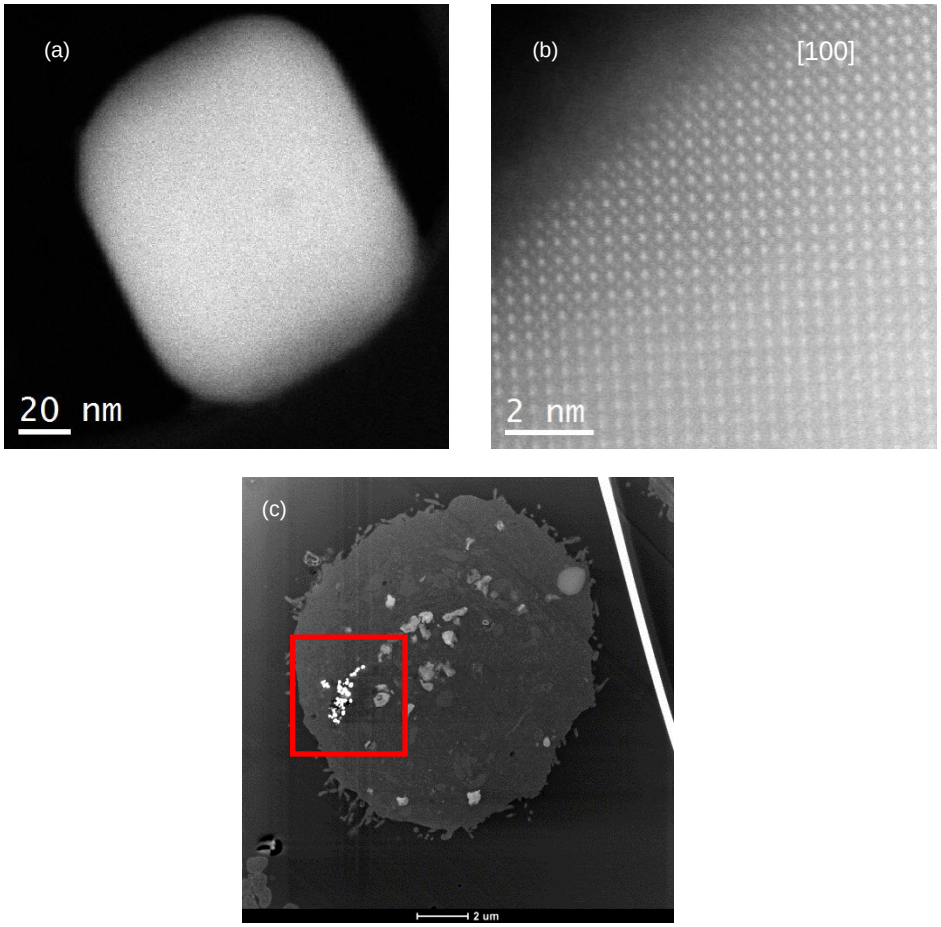

Figure 57. (a) HAADF-STEM image of a $BaTiO_3$ nanoparticle from the aberration corrected SuperSTEM microscope together with, (b) high resolution atomic lattice HAADF-STEM image of $BaTiO_3$ nanoparticle viewed down the [100] direction. (c) HAADF-STEM image of $BaTiO_3$ nanoparticles internalised (red box) in a resin embedded A549 cell section that was taken on FEI Tecnai running in STEM imaging mode.

3.4.4 Energy dispersive X-Ray (EDX) spectroscopy

EDX is capable of semi-quantitative elemental analysis in small (μm) volumes of a specimen; it is critical here for determining the successful hydrothermal synthesis of $BaTiO_3$ and $Ba_{1-x}Sr_xTiO_3$ nanoparticles.

The technique relies on the characteristic X-Ray emission from atoms. If atomically bound electrons (e.g. in the *K* or *L* shell) have been ionized or excited to a higher empty energy level (by say a high energy incident electron), this atom has an electron hole that can be filled by an electron coming down from a higher energy level [96,133]. The characteristic difference in energy between these two states is emitted in the form of an X-Ray photon of particular energy [127]; Figure 58.

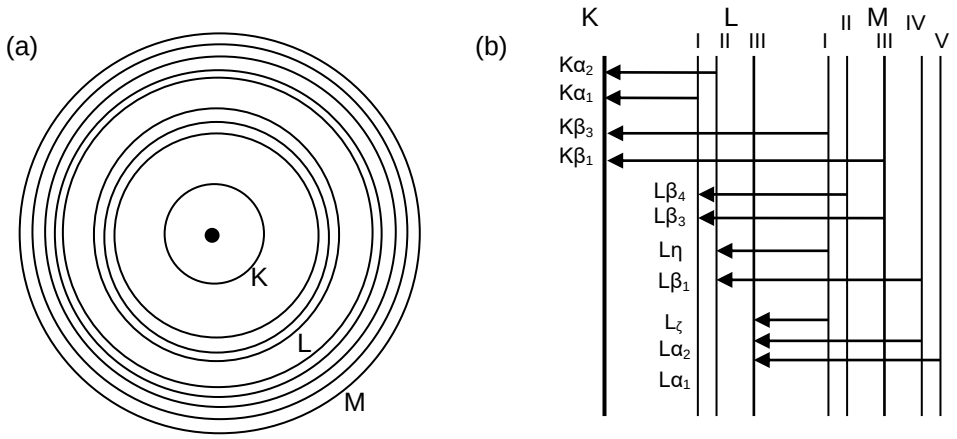

Figure 58. (a) Atom schematic with electron subshells spectroscopically labelled for which electrons from the outer orbitals cascade to lower orbitals in EDX spectroscopy. (b) Schematic of X-Ray production after an incident electron ionises an atom it produces a characteristic X-Ray when the higher energy orbital electrons cascade into the lower energy orbitals [127,131,133,134]**.**

Figure 59 shows example EDX spectra obtained from barium titanate and barium strontium titanate nanoparticles, using the Ba-*L*, Ti-*K, L* and Sr-*K*, *L* X-Ray lines.

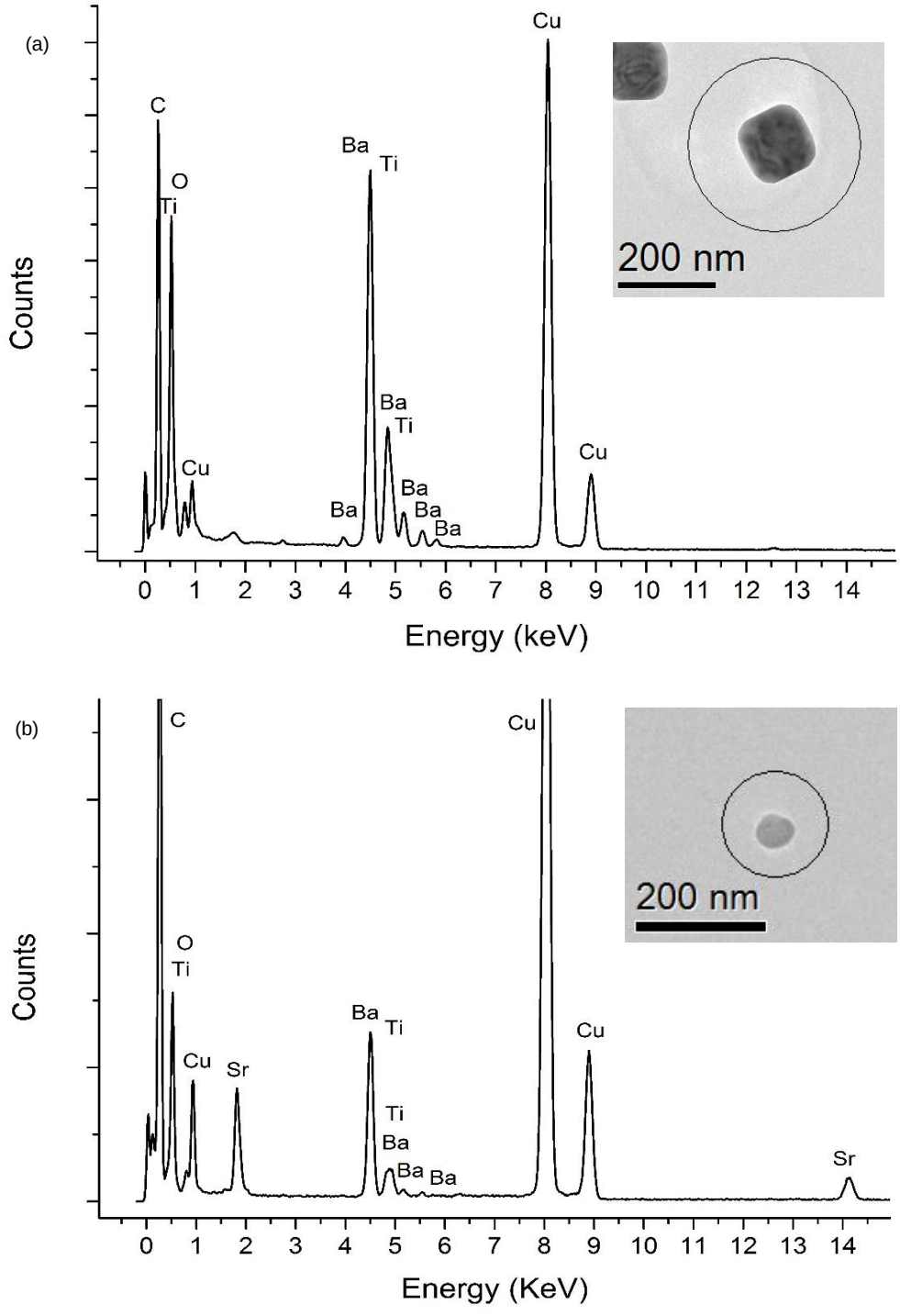

Figure 59. (a) EDX spectrum of barium titanate with a TEM image of the nanoparticle inset. (b) EDX spectrum of barium-strontium titanate with a TEM image of the nanoparticle inset. The grids have a carbon background support film hence the signal and the copper is from the support grid and microscope.

3.4.5 Electron energy loss spectroscopy (EELS)

Electron energy loss spectroscopy (EELS) is a complimentary technique to EDX and is a highly spatially resolved analytical technique that produces an energy loss spectrum of the incident electrons that have lost energy by interacting inelastically with electrons in the specimen [134]. The transmitted electrons are passed through a magnetic field spectrometer which separates the electron beam in terms of energy [133].

STEM-EELS linescans were used to probe the structure and composition across barium titanate and barium strontium titanate nanoparticles. The chemical composition and bonding of atoms is reflected in characteristic peaks known as core-loss edges [134]. Electron energy loss spectroscopy is due to the incident electron beam interacting with the specimen and the atomic electrons being excited to a range of energy states causing energy losses (ΔE) in the transmitted primary beam; Figure 60. The main features of the electron energy loss spectrum are shown in examples of energy loss spectra from $BaTiO_3$; Figure 61.

The elastically scattered electrons (with no energy transfer) are generally transmitted through the specimen to give a single sharp peak known as the zero-loss peak (ZLP) in the EEL spectrum. The ZLP full width half maximum (FWHM) is limited by the energy spread of the electron source and this parameter effectively determines the overall energy resolution of the technique [134]. The low loss region of the energy-loss spectra ranges from 0 to 50 eV, contains the ZLP and the excitation of electrons in the outermost atomic orbitals (valence electrons) and this low loss region is dominated by resonant oscillations of the valence electrons known as plasmons [134];

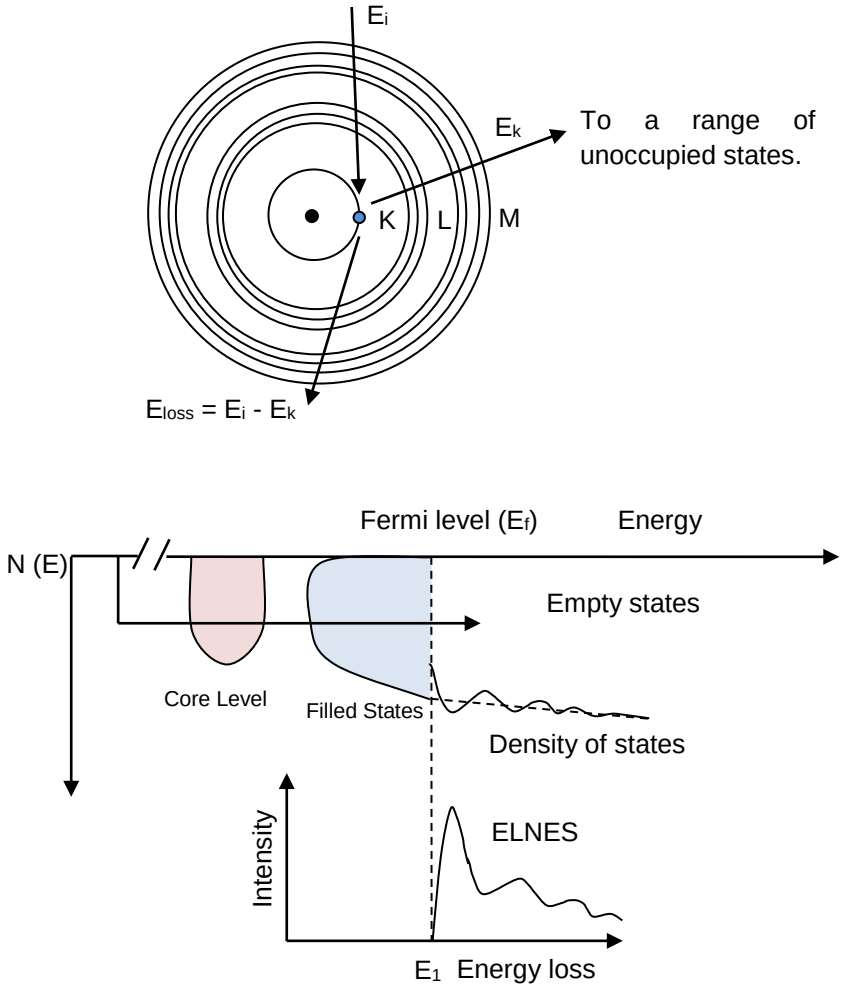

Figure 60. (a) A single atom representation of core electron interaction for EELS. The Incident electron radiation excites an electron from a core energy level to a range of unoccupied states and the transmitted electron is collected with the resultant energy loss. (b) The background subtracted energy loss near edge structures (ELNES) schematic shows how the atomic electrons are excited from a single core state to a range of unoccupied states that reflect the unoccupied density of states (DOS) [96,127,134]**.**

The high loss region of the EEL spectrum ranges from 50 eV to several thousand electron volts and core-loss edges in this region correspond to the excitation of localised core electrons to range of states to just above the Fermi

level. The excitation of electrons from inner-shell energy levels show an ‘edge’ superimposed on a decaying background signal and are known as edges. The core loss edges for Ti-$L_{2,3}$ and O-*K* are dominated by transitions of electrons from 2*p* to 3*d* and 1*s* to 2*p* atomic states respectively; shown in Figure 61.

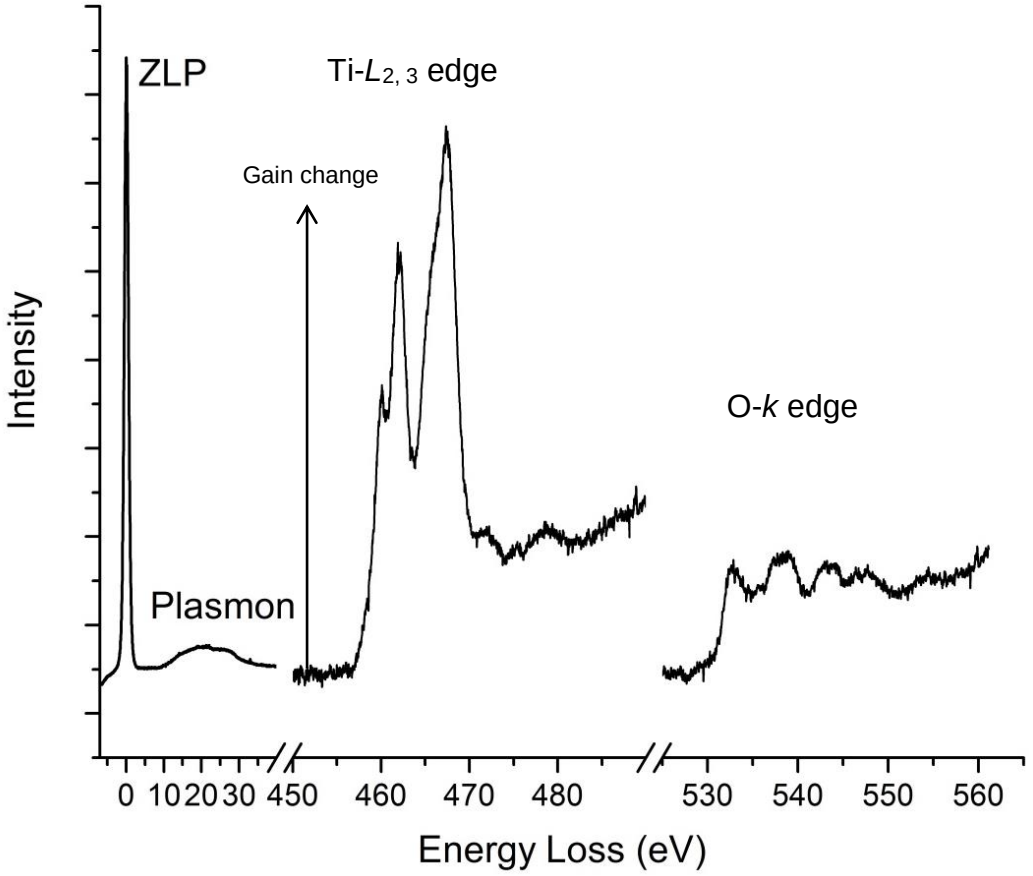

Figure 61. Low-loss and background subtracted high-loss barium titanate experimental data collected from the FEI Titan. The prominent zero loss peak (ZLP) and plasmon peak are shown in the low energy loss spectrum, whereas the core loss requires a gain change to visualise the Ti-$L_{2,3}$ edge and O-*K* edge on a subtracted, decaying background. The x-axis is broken for visual purposes.

In the case of STEM-EELS linescans, a spectrum image is produced at each probe position which generates a data ‘cube’ of information when the probe is

scanning across a $BaTiO_3$ nanoparticle. Two-dimensions of the data cube reflect the spatial information regarding the image and the third axis contains the EEL spectra; Figure 62.

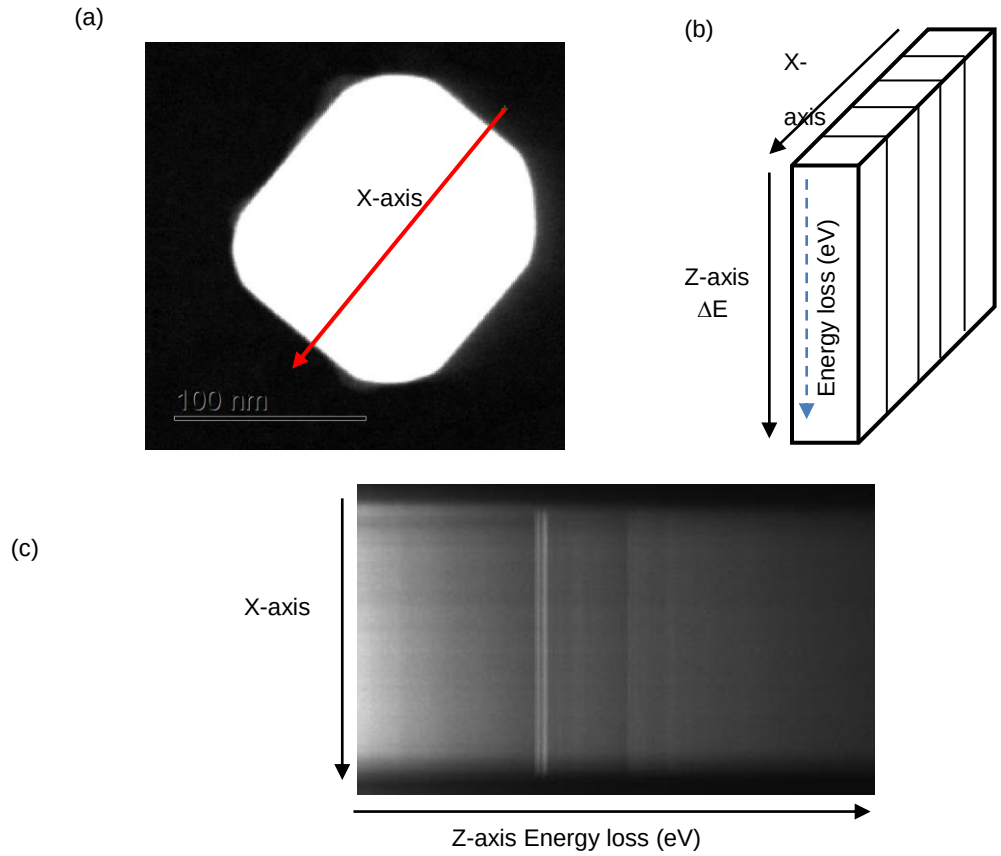

Figure 62. (a) STEM-EELS linescan across a nanoparticle shown by the red arrow acquired by the FEI Titan with the axes shown. The axis dimensions are also shown in (b). Showing a data 'cube' generated during STEM-EELS linescans. The x-axis is the spatial information generated in STEM as the fine probe is scanned across the sample. Each pixel in the x-axis has a spectrum recorded at the spatial points which is recorded on the z-axis (the EEL spectrum). (c) The corresponding spectrum image (ΔE) for the linescan shown in (a) [133,134,136,137]**.**

As the detector has a fixed array of detector channels, there is a set energy loss range of the spectra that can be collected depending on the energy dispersion in the magnetic spectrometers. A larger EELS collection range or dispersion means a lower energy loss resolution is acquired. For certain edges (like the Ti-$L_{2,3}$ edge and the O-*K* edge) a balance is required. For higher resolution data, a lower dispersion is needed i.e. each pixel collects a small energy loss per channel (e.g. 0.025 eV/channel collected using the FEI Titan microscope). However; this will only collect the Ti-$L_{2,3}$ edge *or* the O-*K* edge. Whereas the dedicated microscope at SuperSTEM is able to collect both the Ti-$L_{2,3}$ and O-*K* edges using a lower resolution dispersion of 0.3 eV/channel.

The benefits of STEM-EELS data for nanoparticles is that spatial information of the sample can be related to the spectral information which will potentially allow us to determine the chemical bonding and phase within individual nanoparticles [136]. EDX data can be collected in tandem with EELS; EDX is the transition to a single energy state giving a broad single peak, which is good for heavier elements (Ba, Sr), whilst EELS is a transition to a range of states and giving an edge shape that reflects the density of states and is good for light elements.

In-situ heating and electron energy loss spectroscopy can be performed on barium titanate samples to collect EEL spectra above the Curie point (the transition of tetragonal crystal structure to cubic crystal structure). Monochromated EEL spectra were collected on the commercial sample CT-BT to obtain reference tetragonal and cubic data. The resolution obtained from the zero-loss peak for the CT-BT sample was 0.425 eV.

The *in-situ* heating holder used was a 3 x 7 mm silicon nitride chip (Nano-chip XT) with a ~ 300 μm wide membrane area with a number of 5 x 20 μm^2

transparent carbon film windows approximately 20 nm thick (DensSolutions, Wildfire, Netherlands). This design supports a heating rate of 200 ^{o}C per millisecond up to 800 ^{o}C.

3.4.6 Cryo-scanning transmission electron microscopy (Cryo-TEM) and plunge freezing.

Cryo-TEM is the operation of the microscope with the sample at cryogenic temperatures (~ -180 ^{o}C). The aim of plunge freezing a solution by rapid immersion in liquid ethane is to look at a vitrified sample i.e. no water crystallisation, so the sample is very close to its native hydrated state. If we allow a liquid sample to dry, then drying fronts can move constituents around.

An advantage of plunge-freezing, is the observation of a biological sample close to its natural environment without post treatment of the specimen. Plunge freezing was achieved here by use of an FEI Vitrobot system where a 3.5 µL nanoparticle suspension was put onto a plasma cleaned TEM-grid, the grid was blotted to produce a thin film and plunge frozen into liquid ethane (sample cools at a rate of ~ 10^{6} Ks^{-1}). The sample was then transferred to a cryogenically cooled Gatan single-tilt cryo-transfer holder under liquid nitrogen and either imaged cold using the FEI Titan microscope or vacuum dried for subsequent analysis (dehydration by sublimation i.e. without moving constituent components around).

3.5 Attenuated total reflectance Fourier transform infrared spectroscopy (ATR-FTIR)

FTIR is an optical spectroscopic analysis tool that can determine bonding in molecules and chemical species, including vibrations of light elements [138]. Conventionally the infrared radiation is transmitted through the sample, at certain wavelengths the sample absorbs the incident radiation by excitation of the molecules in the specimen and changes to the dipole moment of the molecules. The resulting variation of transmitted radiation produces an infrared spectrum.

The components of an FTIR include: a radiation source, monochromator, beamsplitter and a detector. The incident beam is split into two optical beam paths before recombining to produce an interferogram which contains all the infrared frequencies simultaneously to allow for rapid measurements. This rapid interferogram measurement is a function of the beamsplitter. It contains a stationary and moving mirror that produces the interference signal with all the frequencies, however as it passes through the sample the signal must be Fourier-transformed (transformed from a time to a frequency domain) in order to get a plot of intensity at each separate frequency [139].

There are three main sampling methods for FTIR, the first being transmission in which the incident beam is transmitted through the sample and collected; this method can be used for most samples and is cost effective [140]. The second is a diffuse reflectance technique where the beam is directed towards scattering samples and reflections at different frequencies are collected. In both

cases the sample is usually mixed into a KBr optically transparent matrix (transparent due to the ionic bonding of KBr).

Finally, the third method (which is used here) is ATR-FTIR that uses a totally internally reflected incident laser beam that passes through a crystal, where evanescent wave 'spills' out of the crystal towards a sample pressed flat on the crystal top. The beam is then collected by a detector, shown in Figure 63. The benefit of using this technique in comparison to the other two methods is sample preparation i.e. because it is a non-transmission technique, the ionic KBr holders are not needed [140].

An example of ATR-FTIR is shown in Figure 63 with an example of a water molecule (for description purposes) to demonstrate the types of vibrations that absorb the light energy at a specific frequency leading to changes in an intensity frequency plot.

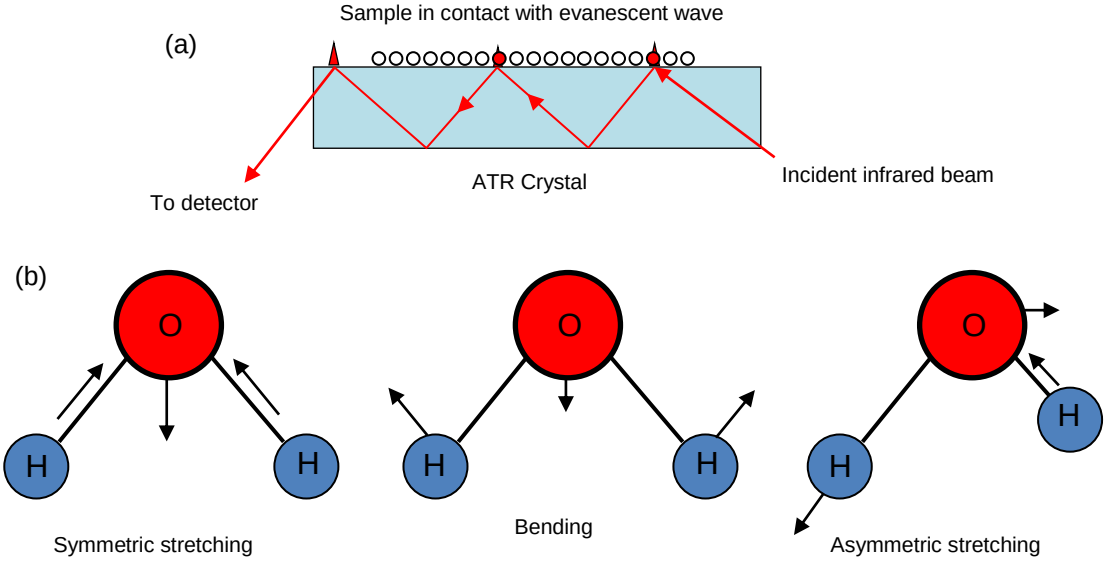

Figure 63. (a) Schematic of ATR-FTIR mechanism where an evanescent infrared wave is in contact with the sample on top of the transmitting crystal. (b) The common vibrational modes of the bonds shown by water molecules: symmetric stretching (~3000 cm^{-1}), bending (~1750 cm^{-1}), and asymmetric stretching (~1200 cm^{-1}). These types of vibrational modes are common to most samples [141,142]**.**

The ATR-FTIR used was a Thermo Scientific Nicolet™ iS™ FTIR Spectrometer to analyse barium titanate, barium strontium titanate, poly-L-lysine and coated $BaTiO_3$/$Ba_{1-x}Sr_xTiO_3$ nanoparticles. The data were manually assigned molecular vibrations using references [143,144]. The polymer poly-L-lysine was used to coat barium titanate and barium strontium titanate nanoparticles to improve colloidal stability by steric separation of the nanoparticles and by altering the surface charge coating the nanoparticle (discussed later in 3.6).

The FTIR spectra show the observable peaks of poly-L-lysine spectra within the 1250 – 3500 cm^{-1} range (below 1250 cm^{-1} is the crystal lattice fingerprint region). The structure of poly-L-lysine is shown below.

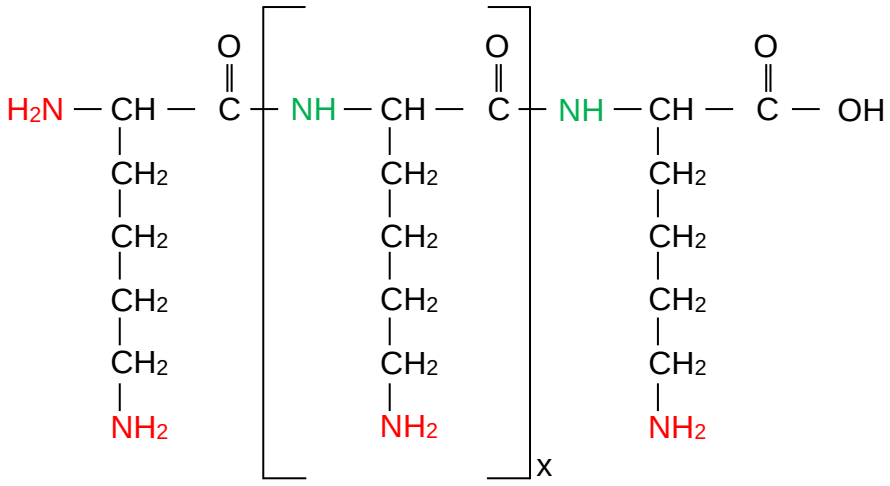

Figure 64. Sketch of polymer poly-L-lysine hydrogen bromide labelled with primary amines and secondary amides.

The amide NH group produce vibrations from the neutral amide within the main chain of the polymer and there is also a vibration from the side chain NH_2 amine group. The two broad peaks at 3280 cm^{-1} and 2865 cm^{-1} are attributed to the peptide (OC-NH-) bond and the CH_2 stretching mode respectively. The next distinguishable peak at 1650 cm^{-1}, is the primary amine NH_2 group

stretching mode and the in plane deformation of the secondary amide group at 1538 cm^{-1}. The primary amine and secondary amide are distinctive PLL peaks as shown in experimental data (Figure 65).

The 'CH_2NH_2' molecule produces a wagging vibration in the range of 1470 – 1430 cm^{-1}. The medium peak at 1390 cm^{-1} is the O-H bending for carboxylic acids. The Amide III peak is the range 1330 – 1220 cm^{-1} along with the weak peaks in the 1295 –1145 cm^{-1} range being the rocking/twisting of NH_2.

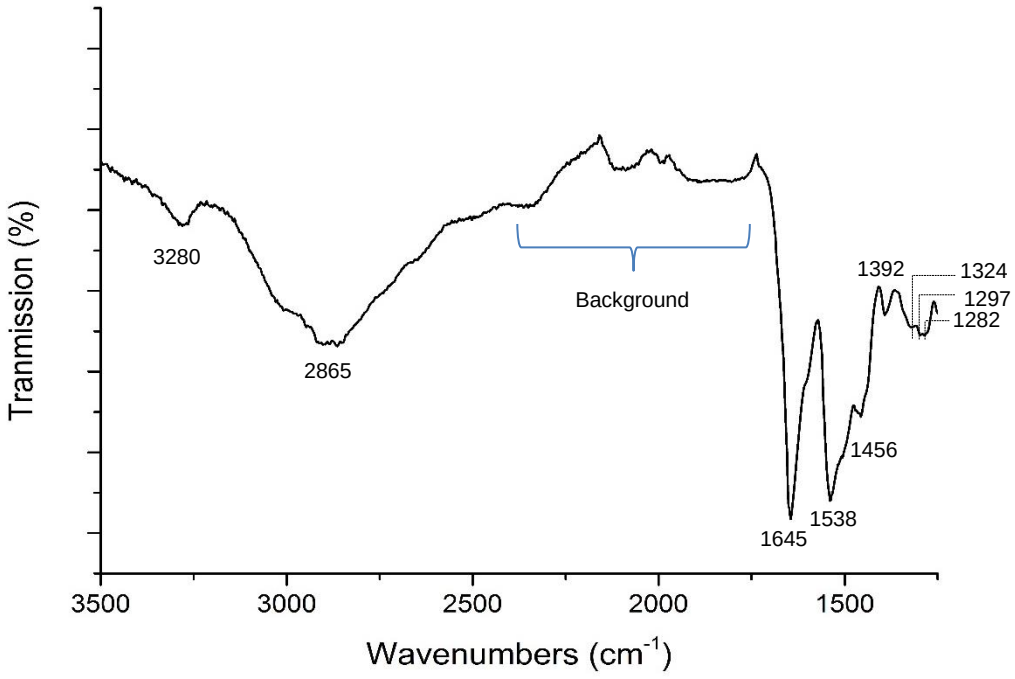

Figure 65. Experimental FTIR spectrum taken in this study of poly-L-lysine with the major peaks labelled and referenced in the text.

An FTIR spectrum of H-BT is shown in Figure 66 with the vibrations labelled on the spectrum.

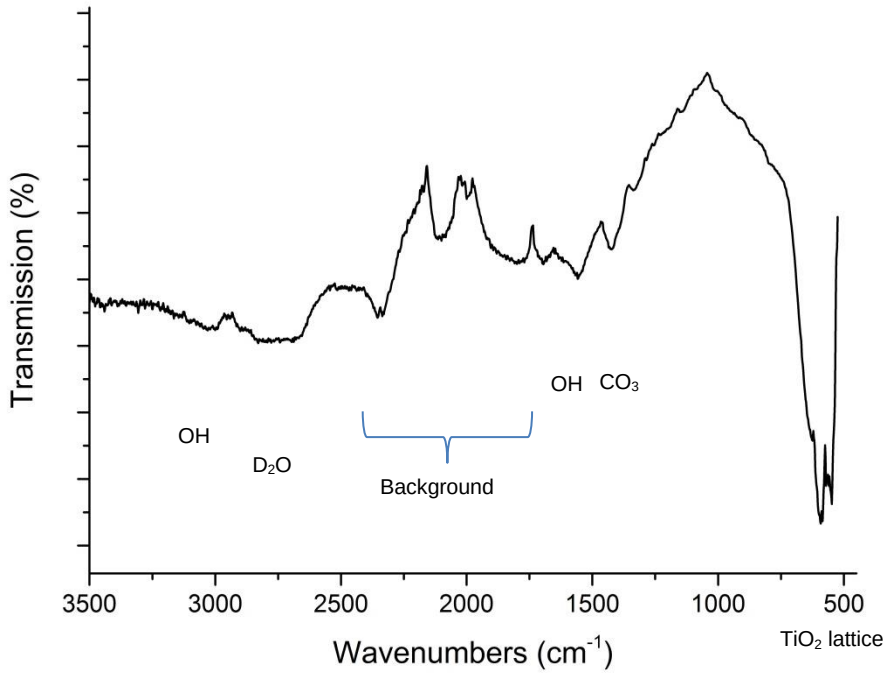

Figure 66. Experimental FTIR spectrum of H-BT with the major peaks labelled and referenced by [99]**. Lattice vibrations of the TiO_2 lattice are shown at ~550 cm^{-1}, barium carbonate species are present due to air exposure at ~1440 cm^{-1}. Adsorbed water is present as hydroxyl ions vibrations (~1600 cm^{-1}, 3200 cm^{-1}) in addition to adsorbed heavy water (D_2O) at ~ 2600 cm^{-1}.**

3.6 Dynamic light scattering (DLS) and zeta potential measurements.

DLS is the measurement of scattered monochromatic light by nanoparticles that are moving due to Brownian motion in a suspending medium. The Stokes-Einstein equation relates the mobility due to Brownian motion of the nanoparticles to the hydrodynamic size of the particles in the sample, defined by the diffusion coefficient of the medium.

$$\gamma = \frac{k_B T}{6\pi\eta a}$$

Equation 6. γ is the diffusion coefficient, k_B is the Boltzmann constant, T is the temperature, η the viscosity of the medium and α the hydrodynamic radius of the suspended particle in an aqueous solution.

DLS assumes that the suspended particles in the solvent are spherical and the technique can measure a large sample volume in comparison to microscopy techniques i.e. 1 mL in DLS vs. 10 μL in TEM.

A drawback to dynamic light scattering is the sensitivity towards larger particle size fractions, meaning that *if* impurities are present or samples are polydisperse this will produce poor results (the Rayleigh approximation shows the intensity of scattered light is proportional to sixth-power of the particle diameter, d^6 [105,145,146]). It provides no other information in terms of the properties of the sample (shape or structural information), but importantly does indicate how the nanoparticle sample is dispersed in a suspending medium.

This analysis technique can provide information based on the intensity of scattered light against the size (intensity distribution), number-weighted distribution against size (number-distribution) and volume-weighted distribution based on the conversion of the intensity profile using Mie theory. This conversion assumes larger spherical particles have a smaller angle of scattering relative to the incident beam in comparison to smaller particles [146]. All these outputs are different when samples are not monodisperse (which is the case here for the $BaTiO_3$ and $Ba_{1-x}Sr_xTiO_3$ nanoparticles). The DLS data were collected and replotted mathematically using the Malvern Zetasizer

software. The stability of PLL-coated $BaTiO_3/Ba_{1-x}Sr_xTiO_3$ and bare $BaTiO_3/Ba_{1-x}Sr_xTiO_3$ nanoparticles were determined using DLS (Figure 67).

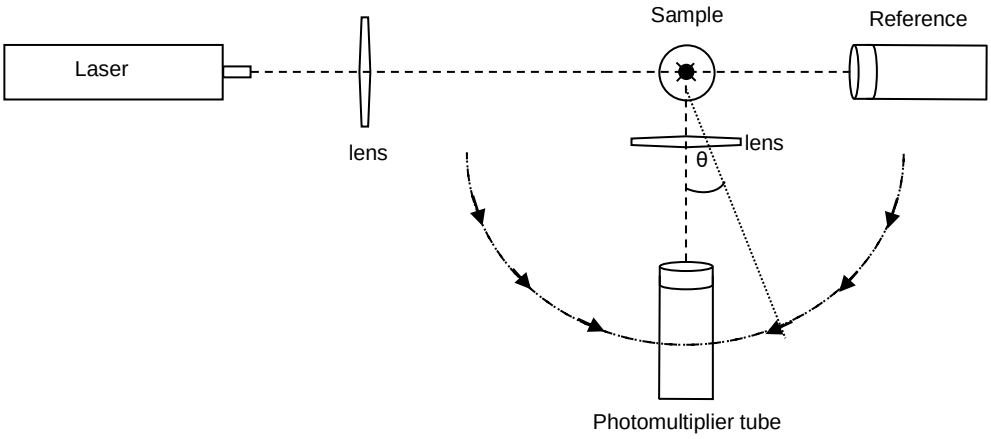

Figure 67. Schematic for dynamic light scattering set-up. The intensity of light scattered by the nanoparticles in the colloidal suspension is measured directly by the photomultiplier tube on a moving arm against the reference laser intensity [106]**.**

The measurements were conducted on a Malvern Zetasizer Nano ZS spectrometer. A total of 60 measurements per sample were collected from 5 repeats of 12 subset measurements for both DLS and zeta potential data collection. The material refractive indices employed were 2.44 for $BaTiO_3$ [147] and 2.27 for $Ba_{1-x}Sr_xTiO_3$ [148] respectively. The dispersant refractive index was measured using a refractometer (1.33 water, 1.35 serum free cell media, 1.35 complete cell media). Nanoparticle suspensions were prepared at 5 different concentrations: 1000, 100, 10, 1 and 0.1 µg/mL. A 1 mL aliquot of the nanoparticle suspensions were pipetted into disposable folded capillary cells (DTS1070, Malvern instruments, Malvern, UK) for DLS and zeta potential measurements in water, and a dip cell (ZEN1002, Malvern instruments,

Malvern, UK) for zeta potential cell culture media measurements. However, the zeta potential of cell culture media suspensions failed to produce quality data because of the complex nature of the medium containing ions, proteins and nanoparticles. An example of mono- and polydisperse nanoparticle systems are shown in Figure 68.

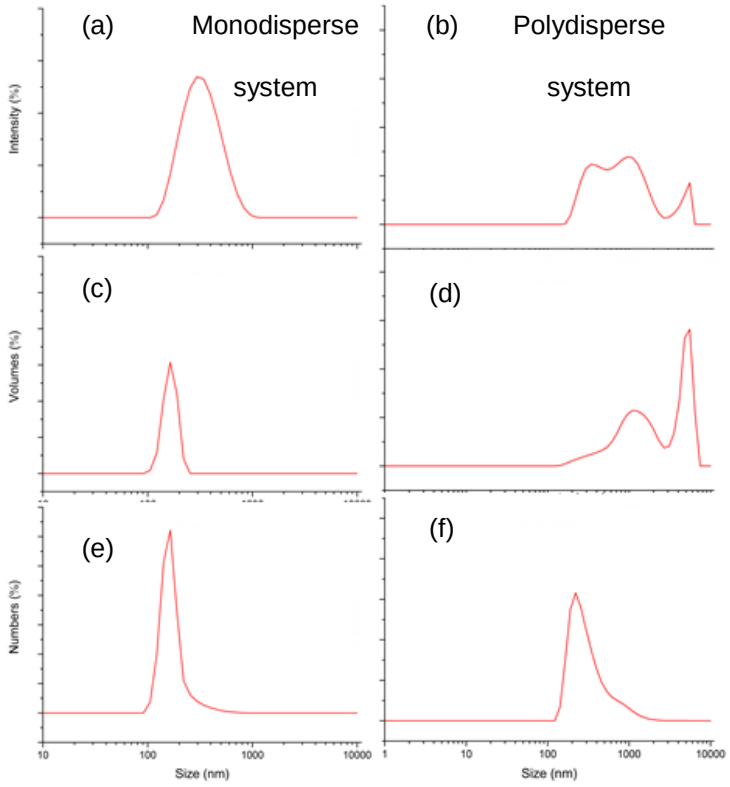

Figure 68. Typical dynamic light scattering data highlighting the difference between a monodisperse system (a), (c) and (e) and a polydisperse system (b), (d) and (e); showing the intensity, volume and number distributions in each case.

3.6.1 Zeta potential measurements

The negatively charged nanoparticle surface in contact with the suspenspending media forms an electrical double layer by distributing

neutralising co-ions from the solution onto or near its surface (Chapter 2). The zeta potential of a nanoparticle suspension is the measurement of the charge on the partially dissociated ions around the nanoparticle that gives rise to a net electrostatic charge based on the DVLO diffuse double layer (Chapter 2, Figure 34).

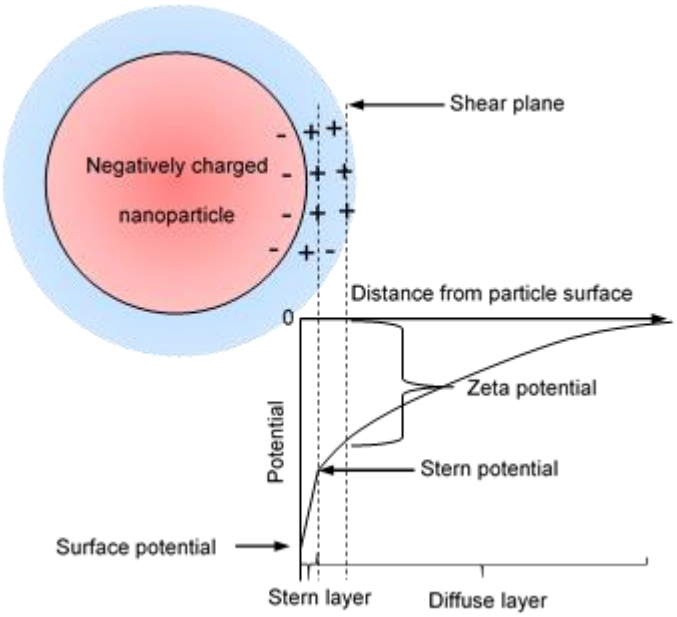

Figure 69. Schematic showing the origin of zeta potential measurements of a negatively charged nanoparticle in a suspending medium. The negatively charged nanoparticle (e.g. $BaTiO_3$ & $Ba_{1-x}Sr_xTiO_3$) has a stern layer where positively charged ions in the suspending medium surround the nanoparticle to lower the surface potential. This is known as the stern potential and this stern layer is surrounded by a shear plane which is where there is a larger concentration of non-bonded positive ions. This creates a potential difference between the particle surface and the shear plane, known as the zeta potential. Then a diffuse layer follows and the potential decays to zero as a function of distance from the particle surface [105,106]**.**

3.7 Biological electron microscopy, cell toxicity and genotoxicity

3.7.1 A549 cell seeding and culture.

Lung epithelial A549 cells derived from a lung adenocarcinoma [149] were used in this work. The biological electron microscopy preparation was conducted with Dr Olga Posada-Estefan from the Leeds Institute of Cardiovascular and Metabolic Medicine and Mr. Martin Fuller from the School of Molecular and Cellular biology.

Cells were cultured in Dulbecco's modified eagle medium (ThermoFisher Scientific, Loughborough, UK) for growth of the A549 cells under a controlled environment of 95 % Air and 5 % CO_2 at 37 ^oC; this allows the epithelial cells to proliferate (multiply) and attach to a growth substrate – in this case, a disposable cell culture flask (Sigma Aldrich, Dorset, UK); until the cells have reached 70 % confluence. The cell culture medium was aspirated and the cells were washed with phosphate buffered saline (PBS) and the enzyme trypsin, to break down extracellular matter and proteins and to prevent cells adhering to the disposable flask (which were placed back in the incubator for 10 minutes). The enzyme trypsin was then inhibited by the addition of complete cell culture media. The mixture of cells, complete media and trypsin were then washed by aspirating the supernatant and re-suspended in either serum free media or complete media (carried out in the disposable flask).

The clean re-suspended cells were counted by placing an aliquot of the cell suspension onto a counting grid and covered with a glass coverslip. An Olympus optical microscope at 10 x magnification was used to approximate the

number of cells in each of the 200 µL wells in a 96-well plate (1 x10^4 cells). The solution of cells and media were then set-up in three different ways. For MTT and Comet assays the cell suspensions were placed back into the 96 well-plate so that the A549 cells could attach to the surface of the wells; for TEM the cell suspensions were centrifuged in Eppendorf tubes so they could then be used for resin embedding; Finally, for SEM imaging a glass coverslip was used at the bottom of the 96 well plate for the cells to adhere to. After the cell suspensions were incubated for 24 hours with the culture media, the media was aspirated and fresh medium (either serum free or complete) added along with exposure to barium titanate nanoparticles or barium-strontium nanoparticles at specific concentrations and incubated for a further 24 hours.

3.7.2 MTT (3-(4, 5-dimethylthiazole-2-yl-2, 5-diphenyl tetrazolium bromide) cell viability assay.

MTT is a colorimetric assay that determines which cells are metabolically active, the viability of cells were assessed by the cells ability to enzymatically convert the yellow MTT dye into insoluble formazan crystals, which can be solubilised using dimethyl sulfoxide (DMSO) into a purple coloured solution [150]. Viable cells produced (in this case) a deep purple colour. Dead cells go a paler lilac colour e.g. if these are overloaded by a high concentration of barium titanate or barium strontium titanate nanoparticles and are unable to enzymatically convert MTT to formazan crystals (which are then solubilised by DMSO). It was important to obtain accurate and reliable results for *in vitro* cytotoxicity assays for initially screening the toxic effect of nanoparticles to

cells, however it should be noted that the accuracy of the cell toxicity can vary depending on a number of factors (user experience, cell line, contamination and nanoparticle interaction with the dye) hence some statistical tests were applied (student t-test and analysis of variance) [150].

3.7.3 The Comet assay

The Comet assay is an electrophoresis study of DNA damage where denatured DNA separates from bulk double stranded DNA to produce a 'comet' with a 'tail' when imaged using epifluorescence microscopy. If the $BaTiO_3$ or $Ba_{1-x}Sr_xTiO_3$ nanoparticles proved to be genotoxic (by DNA strand breaking), then it would result in small fragments of the negatively charged DNA breaking off and these would migrate to the anode during electrophoresis [151].

The treated cells were pelleted and mixed with low melting point agarose gel at 37 ^oC, which was then deposited onto a microscope slide and left on ice for a short period of time to immobilise the cells. The cells were then treated with a lysis buffer containing EDTA, NaOH, detergent and then treated with neutralising buffer for 5 minutes. The slides were washed with deionised water and placed in an electric field. Ethylene dibromide was used to stain the DNA samples and when imaged using an epifluorescence microscope they showed a bright centre of stained DNA that remained unbroken with a plume of denatured DNA following, analogous to a 'comet'. The DNA damage was summarised in terms of % tail DNA and 100 samples were measured with image analysis software.

3.7.4 Preparation of cell uptake experiments for electron microscopy.

Preparing cells for scanning electron microscopy required the cells to be seeded on a cover slip (Thermo Scientific, Lehndorf, Germany) placed in a 24-well plate. When preparing samples for transmission electron microscopy cells were prepared as described in section 3.7.1, but once the cells were pelleted the subsequent steps described here are performed in Eppendorf tubes. Treated A549 cells with barium titanate and barium strontium titanate nanoparticles were washed with pre-warmed PBS and fixed with 2.5 % EM grade glutaraldehyde for 15 minutes at 37 ^{o}C. The fixative was then aspirated and replaced with fresh 2.5 % glutaraldehyde at 4 ^{o}C for 4 hours. The cells were washed with a maintenance buffer solution containing di-sodium hydrogen orthophosphate dihydrate ($Na_2HPO_4.2H_2O$) and sodium dihydrogen orthophosphate monohydrate ($NaH_2PO_4.H_2O$). Now the cells were dead (fixed) they were post fixed/stained with osmium tetroxide (Millonigs 100 mM phosphate buffer, pH 7.3) in 1 % concentration added to the maintenance buffer solution and incubated at room temperature for 2 hours in the dark. This osmium tetroxide solution was aspirated and the samples dehydrated by a series of ethanol washing steps, starting at 10 % ethanol for 10 minutes, 50 % for 15 minutes, 70 % for 15 minutes and 100 % for 10 minutes.

This was replaced with fresh ethanol and taken for the final processing steps for SEM (Critical point drying) and TEM (resin embedding and sectioning) that were both performed by Mr Martin Fuller. Critical point drying (SEM) is where the dehydration of the cells previously immersed in ethanol was replaced by

critically point dried liquid carbon dioxide to maintain the biological integrity (i.e. avoid rupture of membranes). A Polaron E3000 CPD unit was used at 1200 psi.

Resin embedded cell sectioning for TEM preparation used an epoxy resin (AGAR Araldite CY212, Essex, UK), hardener (DDSA, Sigma Aldrich, Dorset, UK) and accelerator (DMP-30, Sigma Aldrich, Dorset, UK) and once cured (at 60 ^{o}C overnight) these were cut into thin sections using an ultra-microtome (Reichert-Jung Ultracut-E) to produce sections from the resin-block face to a desired thickness (nominally 100 nm) and these were floated onto 3 mm copper TEM grids.

3.8 Second harmonic generation microscopy

Second harmonic generation is the production of light at a wavelength half that of the incident photons. It is a nonlinear optical technique where photons of a certain frequency are converted to light of exactly double the frequency (half the wavelength). It relies on the non-centrosymmetry of the scattering medium (or a net polarisation); which is determined by the amplitude of the electric field applied by the optical wave [33]. The non-linear polarisation susceptibility is summarised in Equation 7.

$$P_t = \varepsilon_0[\chi^1 E + \chi^2 E^2 + \chi^3 E^3] \ldots$$

Equation 7. The dipole moment per unit volume *P* is a function of the nonlinear susceptibility constants χ, χ^2, χ^3 for first, second and third order respectively and *E* is the electric field of the optical wave and ε_0 is the permittivity of free space [152]**.**

This equation represents the molecular dipole moment of the medium, where the larger the dipole moment the larger the second harmonic conversion will be. The electric field component of the incident light can be written as a sinusoidal wave; Equation 8 and substituted into Equation 7 to produce Equation 9 and show the nonlinear response to light.

$$P = \varepsilon_0 \chi_1 E_0 \cos(\omega t)$$

Equation 8. E_0 is the amplitude of the wave and ω is the angular frequency. This equation is used to calculate induced polarisation for linear-polarised material.

$$P = \varepsilon_0 (\chi_1 E_0 \cos(\omega t)) + (\chi_2 {E_0}^2 \cos^2(\omega t)) + \cdots$$

Equation 9. The first, second and higher orders susceptibilities all affect the induced polarisation; we can assume third order affects and above are negligible because χ_3 is small.

Using trigonometric identities, $\cos^2 \omega t = ½ (1 + \cos 2(\omega t))$ and by expanding the brackets the equations can be rearranged to give Equation 10 [153,154].

$$P = \varepsilon_0 \chi_1 E_0 \cos(\omega t) + \frac{\varepsilon_0 \chi_2 E_0^2}{2} \cos(2\omega t) + \frac{\varepsilon_0 \chi_2 E_0^2}{2} \ldots$$

Equation 10. The fundamental frequency (red) is the linear polarisation of light, the middle component (blue) is a waveform generated at double the frequency (the second harmonic waveform). The DC offset (green) is a sum of the second harmonic and fundamental amplitudes [16,25]**.**

If Equation 10 were drawn in waveform, the colour co-ordinated components highlighted in the equation are shown with the same colours in Figure 70.

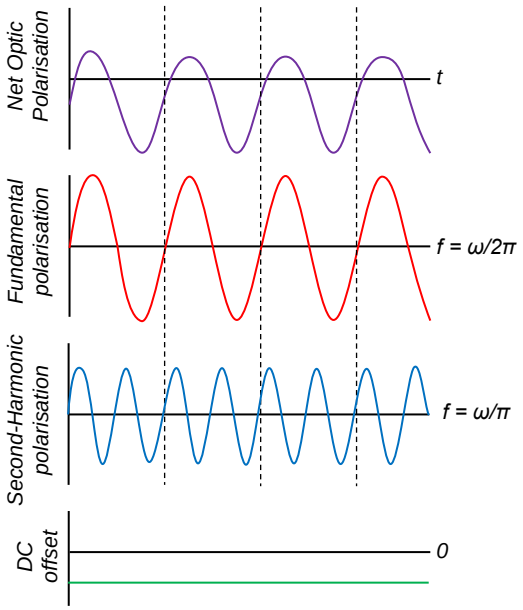

Figure 70. The net optic polarisation (purple). With the fundamental polarisation (red), the second harmonic waveform (blue) and the negative DC offset (green) [16,25]**.**

There are a few assumptions that are made in order for this classical model to apply. The first being that χ_2 is non-zero in a non-centrosymmetric material, and the value rapidly decreases with increasing inversion symmetry. Also in the above equations we are assuming that higher order susceptibilities are negligible. The equations are a classic explanation of second harmonics; further explanation of nonlinear optics can be derived using quantum mechanics. Full theory into nonlinear susceptibilities and electron interactions are explained by Bloembergen [155]. SHG was detected using an Olympus confocal laser scanning two-photon microscope (FluoView FV1200) utilising a Ti: Sapphire laser source at 200 mW pulsed wave power. The laser was pulsed at 80 MHz with a pulse width of 100 fs, giving a peak laser intensity of 100 GW/cm^2 in a beam area of 25 μm^2. A light path diagram of the modified 2-photon confocal microscope used for both optical microscopy and SHG is shown in Figure 71.

The signal was detected in reflected epi-geometry using an 820 nm near infrared source, and a band pass filter centred at 410 nm (± 5 nm). SHG images were collected at a line scanning speed of 20, 40 or 100 µs/pixel and a noise reduction Kalman filter was applied over 20 frames. The two-photon confocal microscope for second harmonic generation in epi-geometry is shown in Figure 71. The SHG samples were prepared by dropcasting 200 µL of the nanoparticle suspensions onto a 22 x 22 mm glass coverslip (Thermo Scientific, No. 1 thickness, New Hampshire, USA). The images were usually taken on 20x or 40x magnification with 0.75 and 0.90 numerical aperture values respectively. An example of commercial barium titanate (CT-BT) SHG is shown in Figure 72.

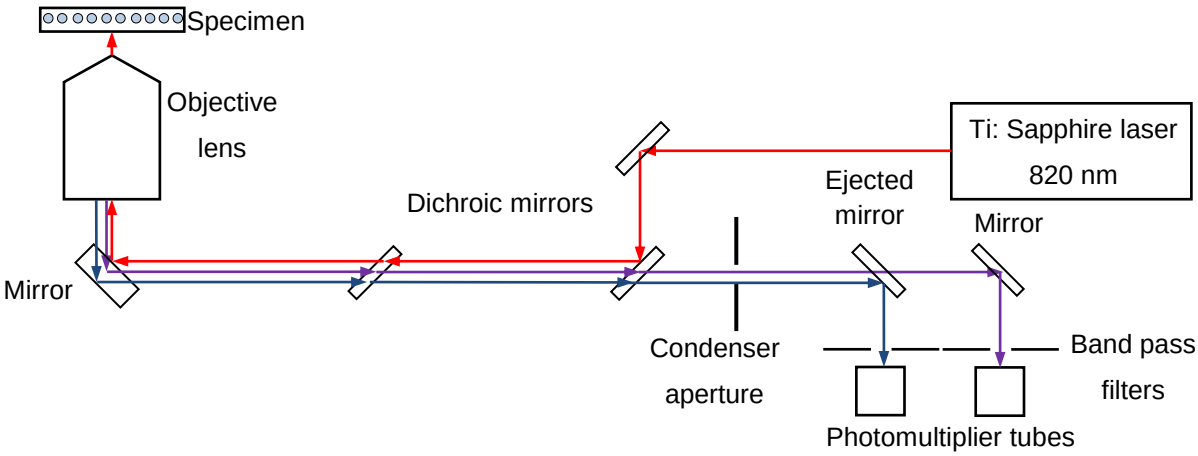

Figure 71. The light path in a modified two-photon confocal microscope for an optical microscope image. The femtosecond pulsed laser enters the objective lens and interacts with the specimen. Incident radiation is shown by the red arrows going through a series of dichroic mirrors filtering out broader wavelengths and the reflected signal (purple for visual purposes) is eventually collected by the photodetector. The light path diagram for second harmonic generation (blue) is produced and includes the fundamental wave (not shown in the diagram). This is collected by a photomultiplier tube with a band pass of 405 – 415 nm for collection of the second harmonic signal.

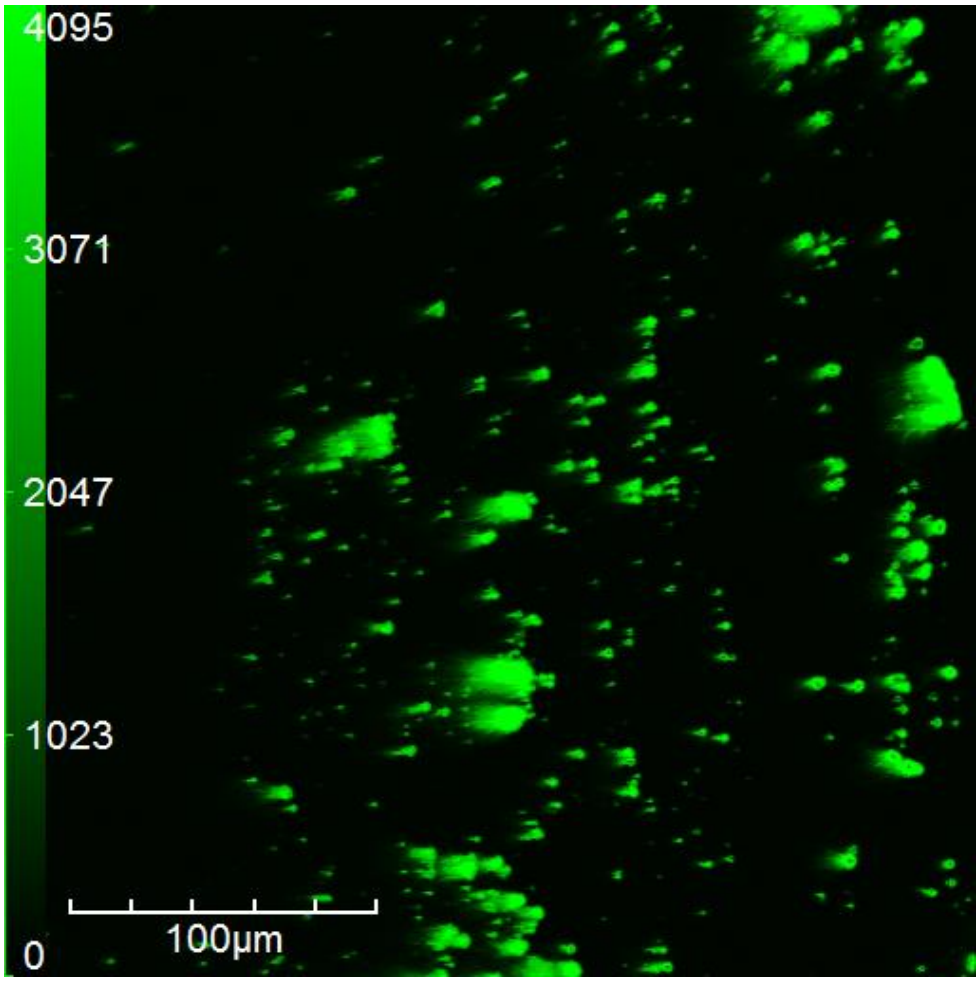

Figure 72. Second harmonic light image collected from the modified two-photon microscope of agglomerated CT-BT nanoparticles. The image was collected at 750 V laser power and the scale shows an arbitrary scale of SHG output.

Characterisation of the commercial and hydrothermally prepared nanoparticles will be discussed in the following chapters.

Chapter 4 – Characterisation of barium titanate and barium strontium titanate nanoparticles.

This chapter will investigate the crystal phase content, particle size distributions and second harmonic optical output of the commercial reference samples and the hydrothermally synthesised nanoparticles. Results for: X-Ray diffraction, synchrotron powder diffraction, second harmonic imaging, secondary electron SEM images and bright field TEM images with EDX are presented.

Characterisation of the commercially purchased samples are shown here to assess the suitability of using them as reference electron energy loss spectroscopy standards in the following chapter. The crystal phase fractions of commercial samples: CC-BT, CT-BT, CC-BST and hydrothermal samples: H-BT, H-BST-01 and H-BST are estimated by X-Ray powder diffraction, (laboratory and synchrotron) and Rietveld peak fitting. Rietveld peak fitting was done with high-energy synchrotron calculated models of cubic (01-078-4475) and tetragonal (04-013-5890) barium titanate and experimental models of cubic (00-034-0411) and tetragonal (00-044-0093) barium strontium titanate contained in ICDD files. The varying fitting parameters were: the unit cell lattice parameters, diffraction pattern background and peak-width parameters.

CC-BT and CT-BT (Sigma Aldrich, Dorset, UK) were commercial standards bought to assess the suitability of using these as calibration standards for Rietveld peak fitting for determining the cubic and tetragonal $BaTiO_3$ phases respectively. CC-BST (PI-KEM, Shropshire, UK) is used as a cubic standard for $Ba_{1-x}Sr_xTiO_3$ samples. Rietveld refinement of the commercial samples shows that the standards are not 100 % phase pure, except for CT-BT.

Bright field TEM images and particle size distributions of the commercial samples are shown in (Figure 45, Chapter 3).

The average particle sizes and composition of the hydrothermally produced barium titanate nanoparticles are measured by TEM with EDX. For barium-strontium titanate (H-BST-01 and H-BST) hydrothermal preparation routes, the incorporation of strontium ions into the barium titanate lattice is characterised by spot-EDX of ~ 100 nanoparticles.

Second harmonic light generated from the hydrothermal samples are qualitatively analysed against the commercial calibration standards. Correlative SHG images of H-BT are compared to SEM images of the same area.

4.1 Characterisation of commercial and hydrothermal samples.

The XRD of commercial samples (laboratory and synchrotron) are presented with the Rietveld peak fitting of their diffraction patterns. These samples (CC-BT, CT-BT and CC-BST) are fitted with the calculated and experimental ICDD phase standards to determine the suitability of Rietveld peak fitting for the hydrothermal samples (H-BT, H-BST-01, H-BST). The presence of a tetragonal crystal phase is important for SHG and determination of such phase fraction will link to the SHG output intensity.

The X-Ray diffraction data set presented herein shows the full diffraction pattern (20 - 80 $^{o}2\theta$), the cubic Rietveld refinement of the (111) and (002/200) peaks and the tetragonal Rietveld refinement of the same peaks with the difference plot displayed underneath. The (111) peak is shown because it

should always be a single peak that displays no splitting and the peak can be used to determine the average crystallite size by application of using the Scherrer equation (Equation 3, Chapter 3). Whereas the (002/200) peak can be used to elucidate the tetragonal phase fraction percentage and the c/a lattice constant ratio, as estimated by Rietveld refinement. The Rietveld fittings in the subsequent figures are shown overlaid on the experimental data. Although the refinement was done with both of the reference patterns at the same time, the reference tetragonal data (purple) and the cubic reference data (blue) patterns are shown separately to show their individual fit to the experimental data.

The discrepancy between the experimental diffraction pattern and the fitted reference patterns is shown as a *difference plot*. The difference plot is the sum of the tetragonal and cubic reference patterns (thin blue line) subtracted from the experimental pattern (black diffraction peaks). The direction and magnitude of the difference plot is a result of the combined reference patterns either over or under-fitting the experimental data (difference plot peaks up or down respectively) and the magnitude is the amount in which the over/under-fittings occur.

The weighted r-profile (W_{rp}) is a software generated value which is an indication of the intensity match of the reference peaks to the experimental data. This value decreases as the experimental and reference profiles (sum of cubic and tetragonal) approach being equal in area. Fittings that have a weighted r-profile value close to 1 are considered an excellent fit whilst fittings with a value of 10 and above are considered a poor fit.

A software generated value known as the ‘goodness of fit’ is also presented. This is a non-empirical software-generated value of how well the user has fit

the reference data to the experimental peaks to the software's best estimate [156,157]. Both the W_{rp} and GoF fitting values are given in the summary tables at the end of each section.

Because the work presented here will be assessing the suitability of Rietveld peak fitting in determining the phase of the sample, the (%) uncertainty for the estimated phase fractions will not be given. However, laboratory and synchrotron XRD W_{rp} fitting values will indicate the accuracy of these values.

The average crystallite sizes are determined by the Scherrer equation (Equation 3, Chapter 3) involving a value for the instrumental broadening of the diffractometer. This is obtained by analysing a corundum (Al_2O_3) sample (not shown), where the FWHM of the (110) peak is measured [158]; but for synchrotron analysis this was not measured and so the average crystallite sizes for the synchrotron data are not provided.

4.1.1 X-Ray diffraction of Commercial standards.

The commercial barium titanate samples (CC-BT, CT-BT) are fitted with the calculated cubic and tetragonal ICDD reference patterns by Rietveld refinement. The crosshairs in the diffraction pattern unfortunately cannot be altered but represent the unmodified ICDD reference pattern and Rietveld refined pattern labelled in the laboratory XRD Rietveld peak fitting of CC-BT in Figure 73.

The Rietveld peak fitting of CC-BT laboratory XRD data shows that there is actually a 53 % tetragonal phase fraction present. This tetragonal phase fraction has a c/a ratio of 1.006 (unit cell parameters: c = 4.027 Å, a = 4.002 Å). This sample was analysed further by synchrotron radiation at the Diamond

Light Source (Beamline I11, rapid access) under the supervision of Professor Chiu Tang and Dr Sarah Day (Diamond Light Source, UK); Figure 74.

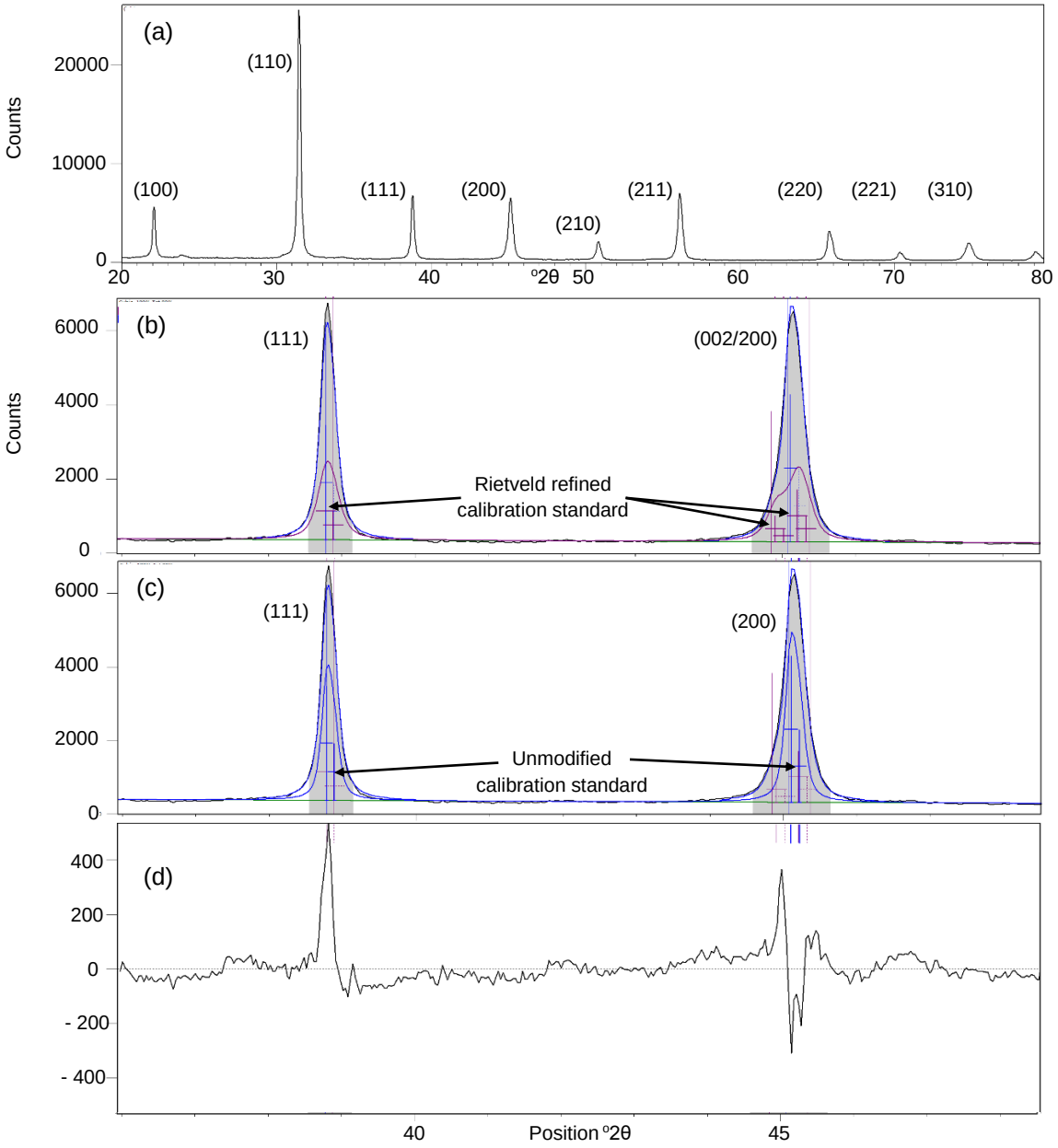

Figure 73. (a) Laboratory-XRD pattern of CC-BT labelled with the Miller indices. (b) Tetragonal Rietveld peak fitting of the (111) and (002/200) peaks, suggests the powder has a 53 % tetragonal phase fraction. (c) Cubic Rietveld peak fitting of the (111) and (200) peaks, suggests the powder has a 53 % cubic phase fraction. The crosshairs in the diffraction pattern for both (b) and (c) show the unmodified and Rietveld refined calibration standards. (d) Difference plot of the reference patterns subtracted from the experimental pattern.

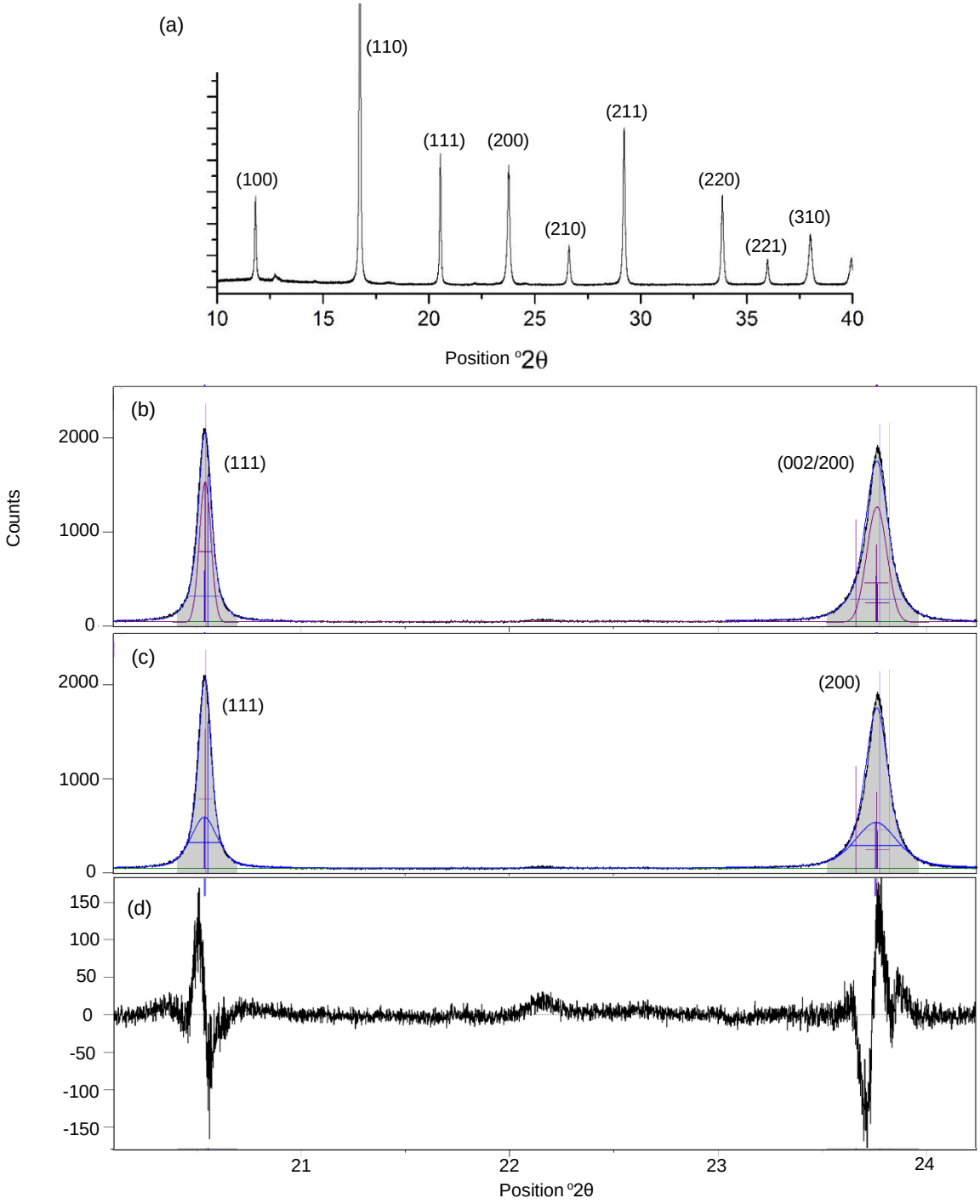

Figure 74. (a) Synchrotron powder diffraction pattern of CC-BT labelled with the Miller indices. (b) Tetragonal Rietveld peak fitting of the (111) and (200) peaks, suggests the powder has a 50 % tetragonal phase fraction. (c) Cubic Rietveld peak fitting of the (111) and (002/200) peaks, suggests the powder has a 50 % cubic phase fraction. (d) Difference plot of the reference patterns subtracted from the experimental pattern.

Both the laboratory-XRD and synchrotron powder diffraction Rietveld peak fitting data of CC-BT sample (Figure 73 & Figure 74) suggest a ~50 % tetragonal phase fraction is present, implying that the sample will produce SHG (imaging of second harmonic light production will be shown in Section 4.2). This sample is expected to be all cubic but found that ~50 % of the sample has a small tetragonal like distortion. Both the experimental data show no obvious tetragonal phase splitting of the (002/200) peak, and the tetragonal phase reference pattern is fit to a single (200) experimental peak. This indicates that the reference tetragonal phase fraction has an almost equal unit cell c/a ratio (the tetragonal unit cell c/a ratio is 1.01 for both laboratory and synchrotron). The estimated tetragonal unit cell parameters for laboratory Rietveld refinement and synchrotron Rietveld refinement are: c = 4.027 Å, a = 4.002 Å, and: c = 4.016 Å, a = 4.013 Å respectively. Showing the estimated laboratory-XRD data to have a greater estimated tetragonal phase fraction present (c/a = 1.006), than the weaker c/a ratio estimated by synchrotron radiation (c/a = 1.0008).

To see if a better fitting is achieved with the two reference ICDD phases (tetragonal and cubic) as opposed to a solo reference phase (cubic), the software is instructed to fit the reference cubic and tetragonal ICDD phase patterns separately to the experimental CC-BT sample with the difference plots shown; Figure 75.

Showing that for accurate Rietveld peak fitting of CC-BT, both the reference cubic and tetragonal ICDD patterns are required.

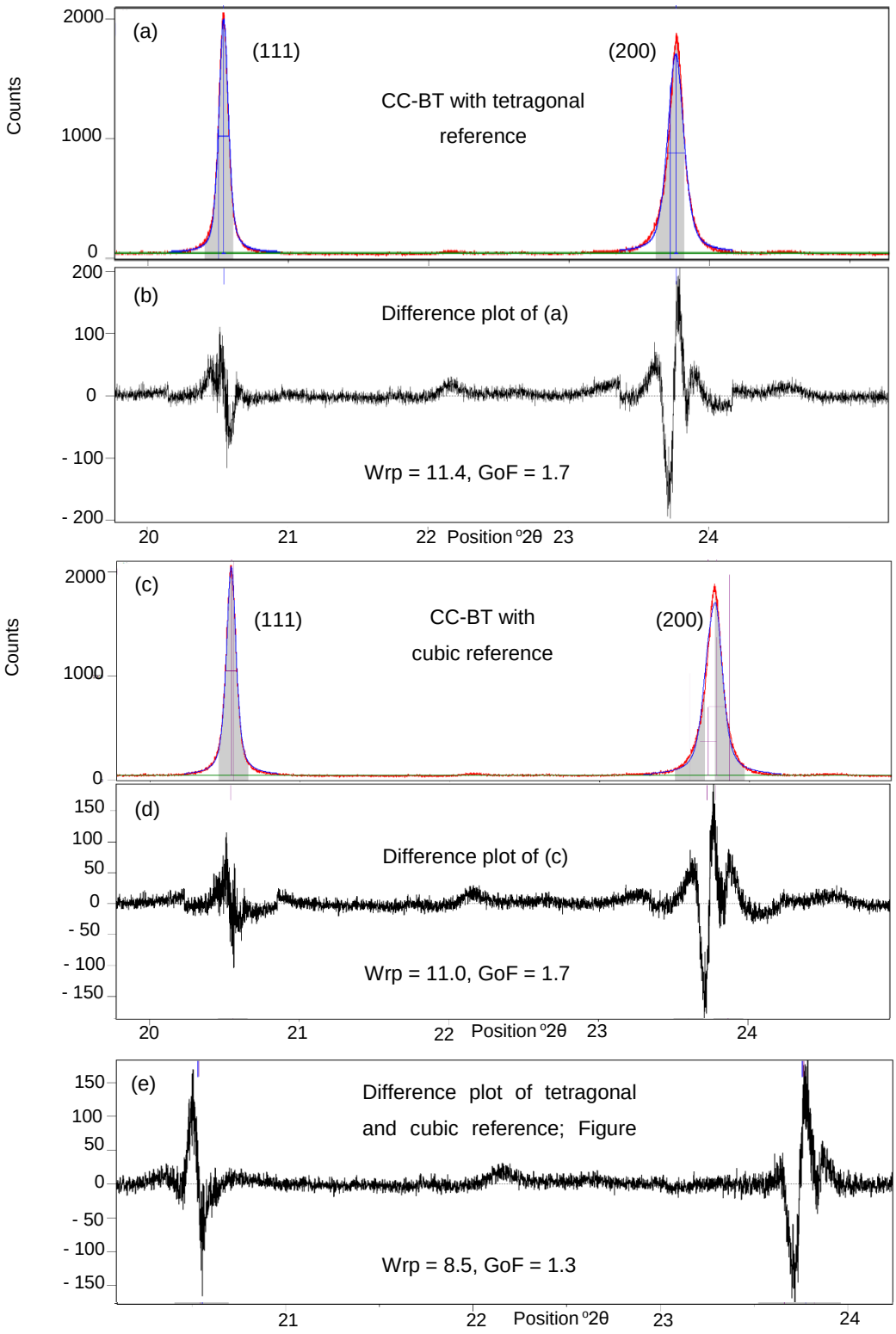

Figure 75. (a) Synchrotron diffraction pattern of CC-BT with the tetragonal reference pattern (purple) Rietveld peak fitted to the experimental data (red). The difference plot is shown in (b). The reference cubic pattern is Rietveld peak fitted with the reference cubic pattern in (c). In addition to the difference plot shown in (d). (e) Difference plot of synchrotron CC-BT with cubic and tetragonal fittings.

Figure 75 shows the variation in the difference plots fitted with the cubic and tetragonal phases. Visually, the single phase fitting difference plots are under-fitting (rather than overfitting) just before the (111) and (200) peaks in the residual plots. Whereas a flatter residual fitting either side of the (111) and (200) residual peak fits is shown in the difference plot when both reference patterns are used. This indicates that the fittings require both the cubic and tetragonal reference patterns; which will be continued throughout.

A commercial tetragonal sample, CT-BT (Sigma Aldrich, Dorset, UK) was analysed to determine the phase fraction by Rietveld peak fitting. Figure 76 shows the laboratory XRD pattern with the pattern labelled with the Miller Indices.

The laboratory-XRD of CT-BT shows only a ~ 75 % tetragonal phase fraction by Rietveld peak fitting. The Rietveld fitting suggests the CT-BT sample is a mixture of two phases (cubic and tetragonal) with a clear and well defined splitting of the (002/200) peaks. The reference tetragonal phase after Rietveld fitting shows a c/a ratio of 1.01 (c = 4.035 Å, a = 3.99 Å). However, the (002/200) peak splitting is not as well defined as two-sharp peaks (as expected for a calculated reference tetragonal diffraction pattern). Therefore, this sample was analysed further by the Diamond Light Source (Beamline I11, rapid access) under the supervision of Professor Chiu Tang and Dr Sarah Day;

Figure 77.

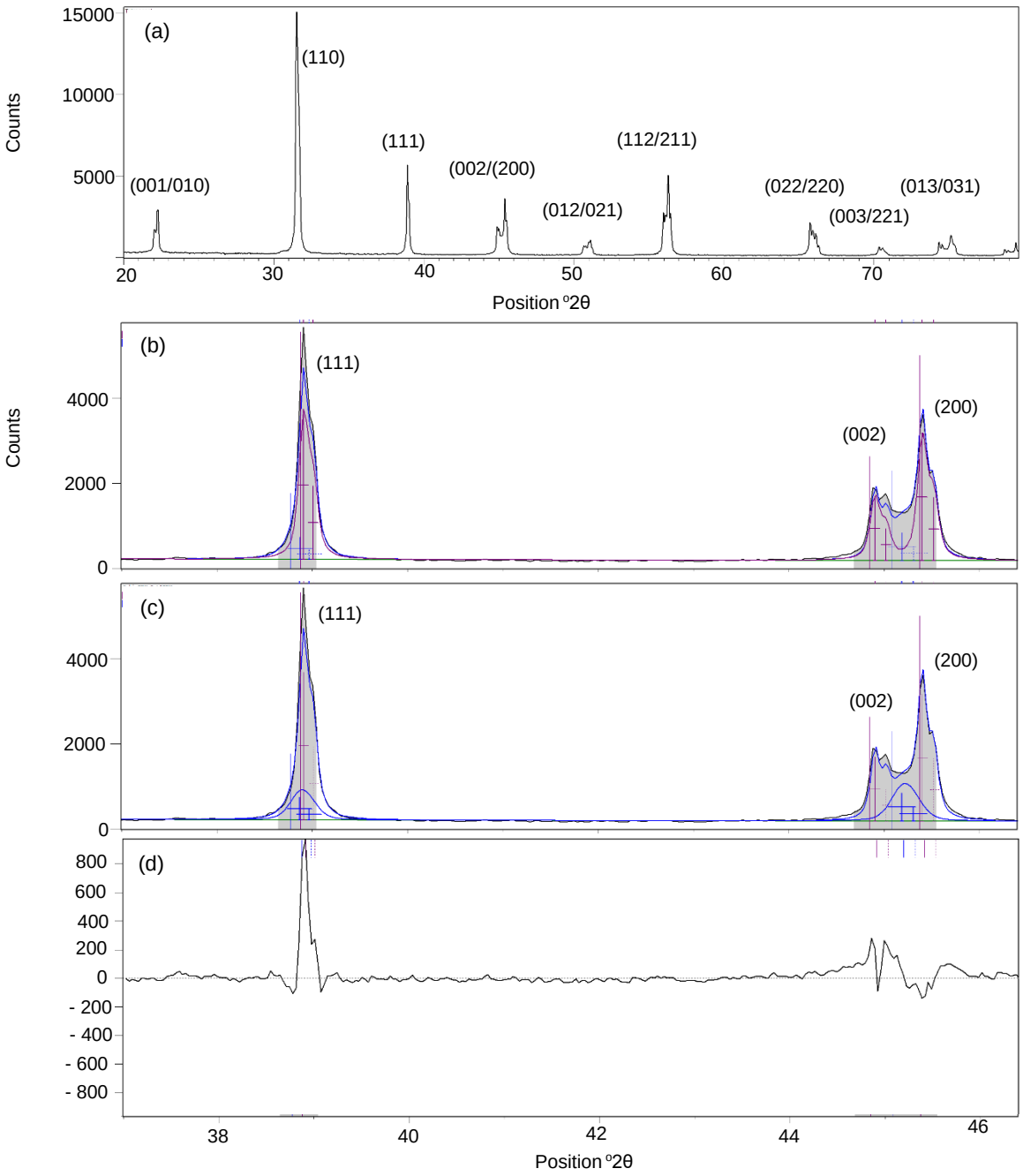

Figure 76. (a) Laboratory X-Ray diffraction pattern of CT-BT labelled with the Miller indices. (b) Tetragonal Rietveld peak fitting of the (111) and (200) peaks, suggests the powder has a 76 % tetragonal phase fraction. (c) Cubic Rietveld peak fitting of the (111) and (002/200) peaks, suggests the powder has a 24 % cubic phase fraction. (d) Difference plot of the reference patterns subtracted from the experimental pattern.

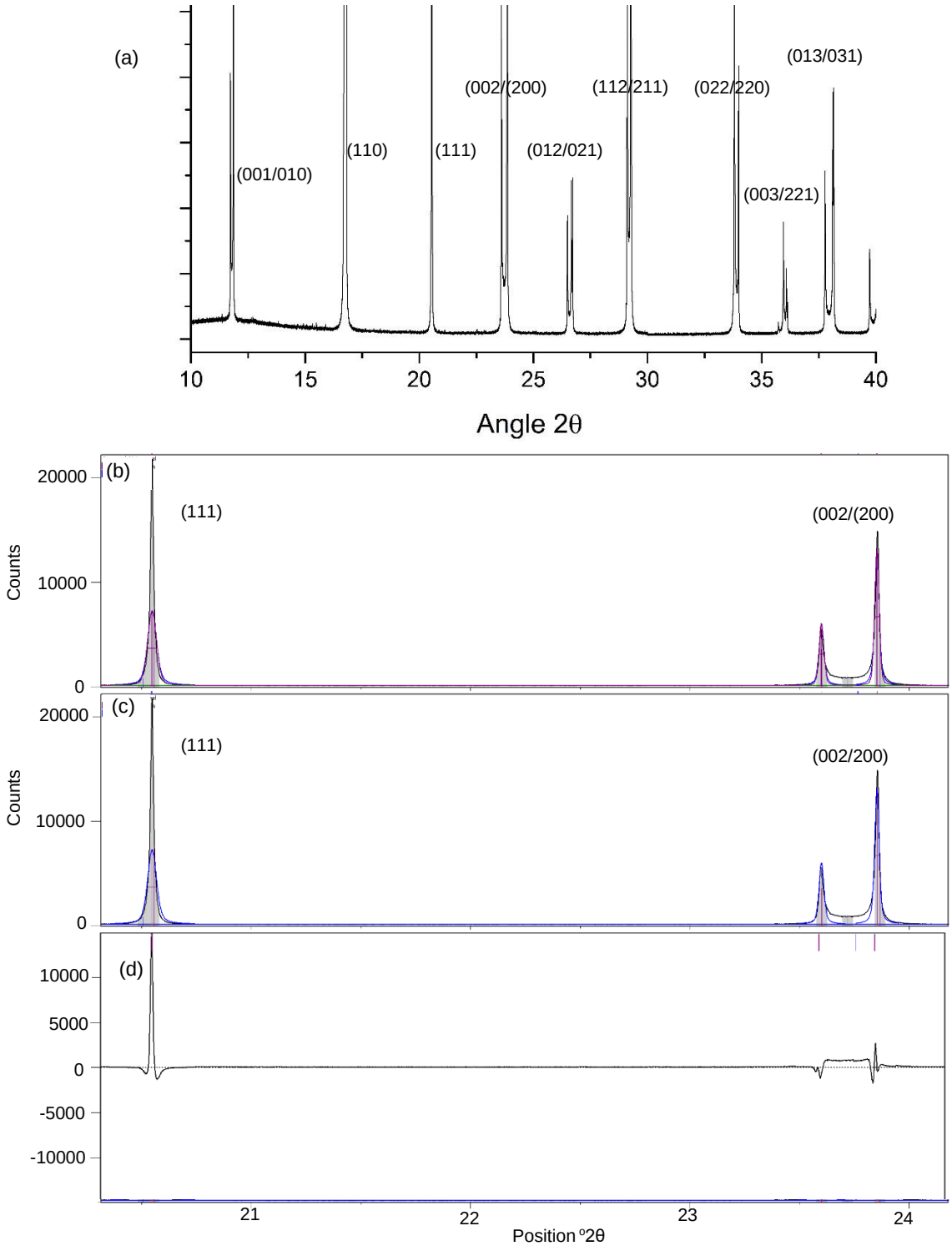

Figure 77. (a) Synchrotron powder diffraction pattern of CT-BT labelled with the Miller indices. (b) Tetragonal Rietveld peak fitting of the (111) and (200) peaks, suggests the powder has a 100 % tetragonal phase fraction. (c) Cubic Rietveld peak fitting of the (111) and (002/200) peaks, suggests the powder has a 0 % cubic phase fraction. (d) Difference plot of the reference patterns subtracted from the experimental pattern.

The synchrotron powder diffraction of CT-BT shows a 100% tetragonal phase fraction is present. The difference plot shows a very sharp (111) peak in which the reference cubic and tetragonal patterns are struggling to fit to the sharp peak (shown in the difference plot), which accounts for a poor residual fitting and a large W_{rp} (= 47.2).

Thus we conclude that the CT-BT samples shows a 100 % tetragonal phase fraction; which is ideal for a reference pattern; giving a c/a ratio of 1.01 (c = 4.04 Å, a = 3.99 Å). Rietveld peak fitting suggests CC-BT has a 50 % tetragonal phase fraction present, which isn't ideal to use as a standard and so the CT-BT sample was heated above the Curie temperature (above the tetragonal to cubic transition) and used as a model cubic sample for subsequent work in Chapter 5.

For an ideal cubic reference, the CT-BT sample was heated to 170 ^{o}C (~ +40 ^{o}C above the Curie point) to ensure that the sample undergoes a tetragonal-to-cubic transition above the temperature shown in Figure 78 [73].

In Figure 78, the Rietveld fitting of CT-BT still suggests there is a tetragonal component despite the sample being at 170 ^{o}C, where it should all be transformed to a cubic-phase barium titanate. However, closer inspection shows the tetragonal component is no longer has a clear (002/200) peak splitting as seen in Figure 76, but is now closer to a single peak indicating an extremely weak tetragonal distortion: c/a = 1.0002 (c = 4.032 Å, a = 4.031 Å) with a Wrp = 15.2. This suggests a single referenced cubic pattern is more plausible to the experimental data based on the magnitude of the residual fit. The single cubic Rietveld peak fitting is shown in Figure 79 and summarised in

Table 5.

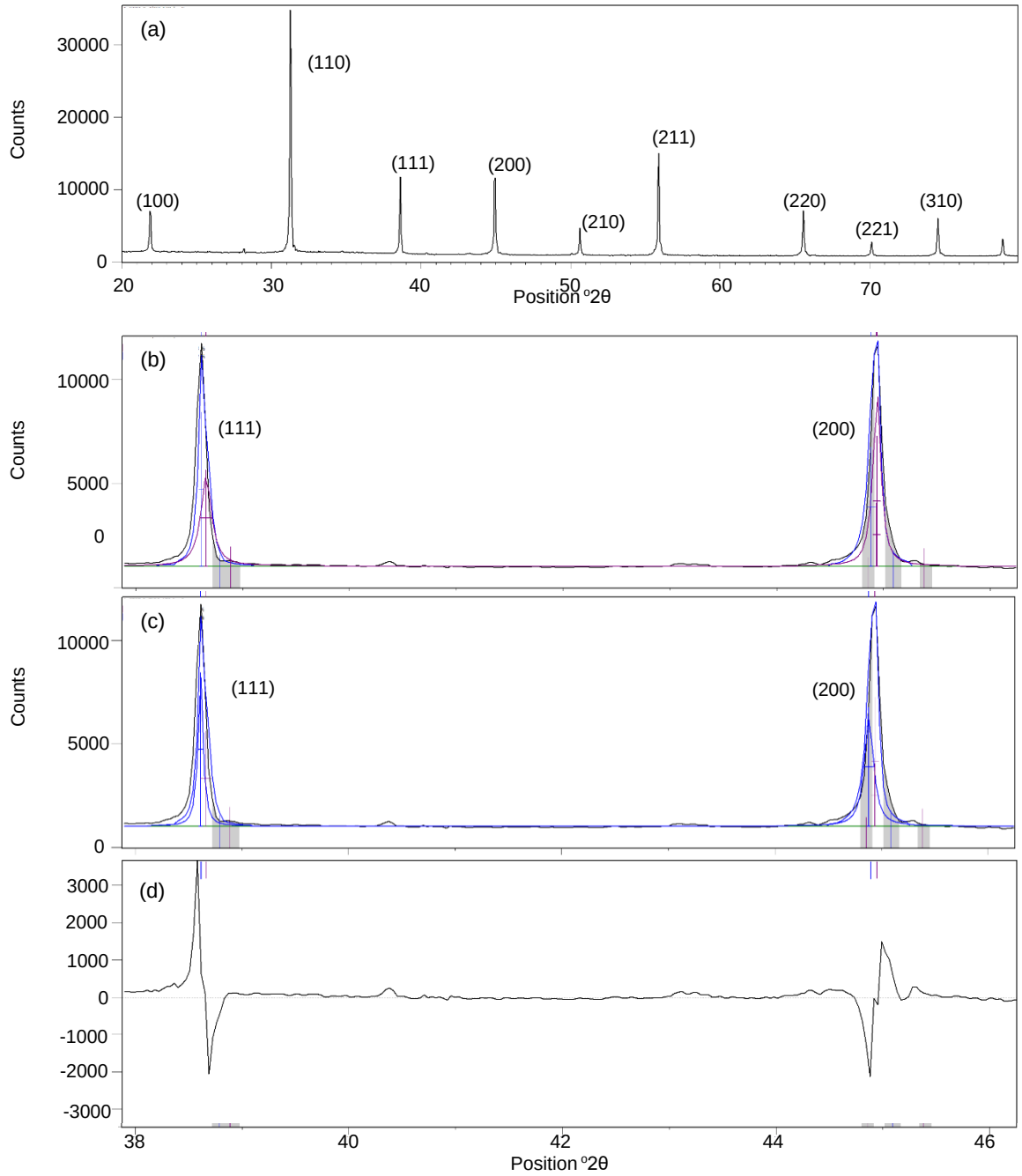

Figure 78. (a) Laboratory X-Ray diffraction pattern of CT-BT collected at 170 ºC labelled with the Miller indices. (b) Tetragonal Rietveld peak fitting of the (111) and (200) peaks, suggests the powder has a 53 % tetragonal phase fraction. (c) Cubic Rietveld peak fitting of the (111) and (002/200) peaks, suggests the powder has a 47 % cubic phase fraction. (d) Difference plot of the reference patterns subtracted from the experimental pattern.

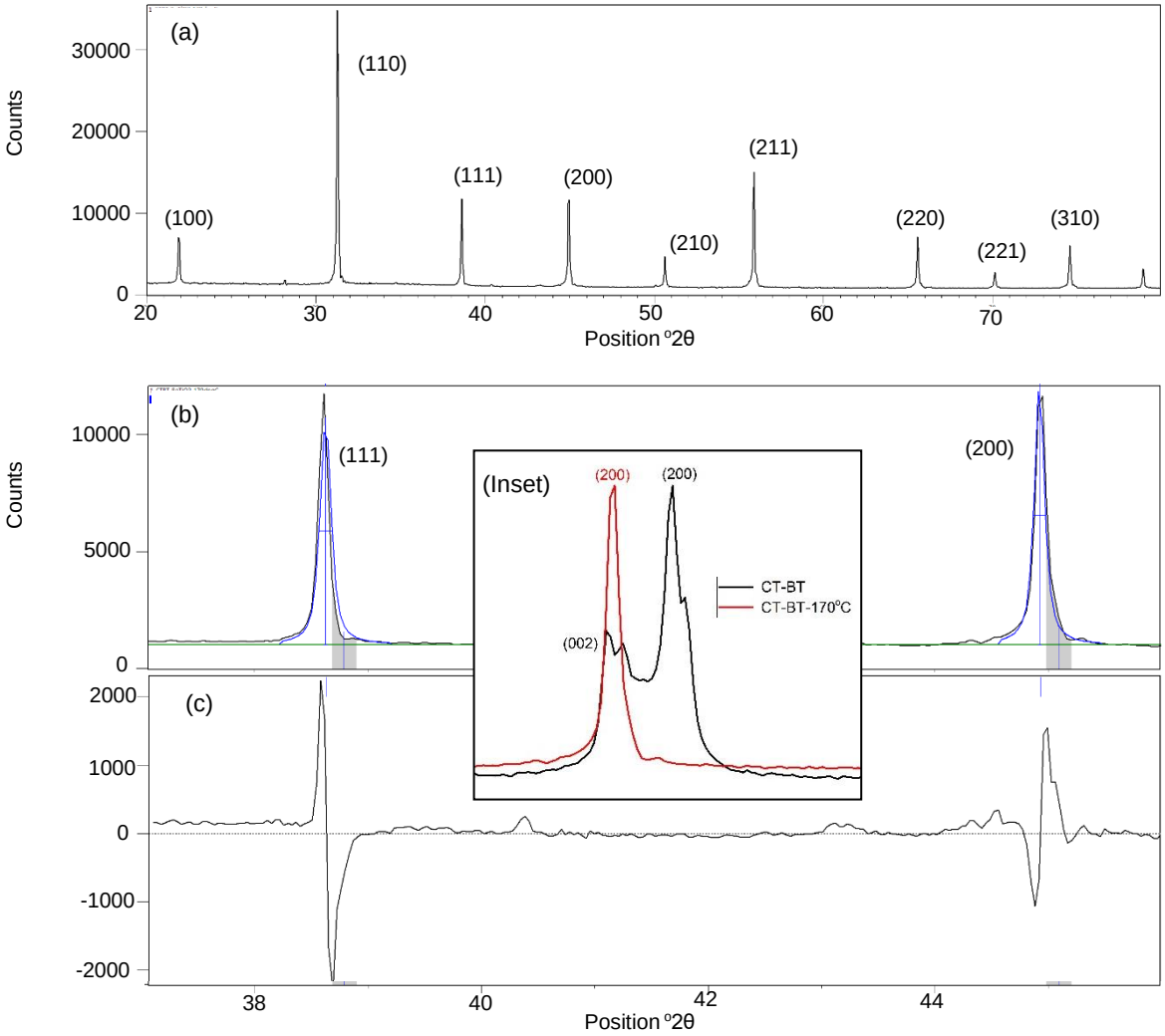

Figure 79. (a) Laboratory X-Ray diffraction pattern of CT-BT collected at 170 ºC labelled with the Miller indices. (b) Cubic Rietveld peak fitting of the (111) and (200) peaks. (c) Difference plot of the reference patterns subtracted from the experimental pattern. (Inset) Comparison of laboratory-XRD CT-BT (black) and CT-BT-170ºC (red) data at normalised (200) peak intensity, showing the change in tetragonal (002/200) peak splitting to a cubic single (200) diffraction peak at ~ 45 º2θ; consistent with the expected transition to a cubic phase.

The best set of fitting parameters for the commercial samples are summarised in Table 5. The results presented are based on a combined reference pattern that includes the individual reference patterns for both tetragonal and cubic phases (shown in Figure 77 & Figure 79 respectively). Reference cubic and

tetragonal samples for EELS analysis, will be taken from the CT-BT sample below (tetragonal) and above (cubic) the Curie temperature. A summary of Rietveld peak fitting data for the laboratory-XRD and synchrotron powder diffraction data for the commercial samples are shown in Table 5.

Sample	Average crystallite size (nm)	Rietveld fitted tetragonal unit cell parameters	c/a ratio	Tetragonal phase fraction (%)	Weighted r-profile (Wrp)	Goodness of fit (GoF)
CC-BT	81.7	c = 4.027 Å a = 4.002 Å	1.006	53	4.3	8.0
	Synchrotron	c = 4.016 Å a = 4.013 Å	1.0008	50	1.3	8.5
CT-BT	174.4	c = 4.04 Å a = 3.99 Å	1.01	76	4.8	9.6
	Synchrotron	c = 4.04 Å a = 3.99 Å	1.01	100	47.2	38.3
CT-BT @ 170 °C	152.6	c = 4.032 Å a = 4.031 Å	1.0002	53	15.2	17.3
		Cubic fitting only (N/A)			12.6	11.6
CC-BST	28.7	c = 4.03 Å a = 3.99 Å	1.01	8	5.3	5.1
	Synchrotron	c = 3.966 Å a = 3.964 Å	1.0005	30	1.2	7.4

Table 5. Summary of the Rietveld peak fitting for laboratory-XRD and the Synchrotron powder diffraction data. The average crystallite size is determined using the Scherrer equation (Equation 3, Chapter 3). The c/a ratio is a tetragonal ratio known as the longer 'c' unit cell parameter over the 'a' parameter. These values were estimated during Rietveld fitting. The estimated tetragonal phase fraction, weighted r-profile (ideally = 1) and goodness of fit (a software generated fit value, ideally <10) by Rietveld peak fitting are shown.

Table 5 shows a tetragonal phase fraction is present in all samples and a cubic phase fraction is present in all except one of the commercial samples (CT-BT,

that is assumed to be fully tetragonal). The use of Rietveld refinement is a robust method of phase identification of the commercial samples, and the best measure of the phase is acquired from the synchrotron powder diffraction data because of the increased resolution. The unit cell parameter values from the refined data are in good agreement the ICDD unit cell parameters (a = 4.01 Å for cubic ICDD file and c= 4.04 Å, a = 3.99 Å for the tetragonal ICDD file), shown in Table 5.

The Rietveld refinement of CT-BT suggested that it is 100 % tetragonal and the model tetragonal refined unit cell parameters for CT-BT were: c = 4.04 Å, a = 3.99 Å (c/a = 1.01). The W_{rp} = 47.2 and GoF = 38.3 suggest a poor fitting of the synchrotron data (Figure 77), which can be attributed to a poor residual fit to the (111) peak intensity. The CC-BT sample shows no suitable cubic phase can be fit to the synchrotron data, therefore would expect this sample to produce SHG.

The Rietveld refinement of CT-BT-170^{o}C with both the cubic and tetragonal reference patterns suggested a ~50 % tetragonal phase fraction (the model tetragonal unit cell parameters being: c = 4.032 Å, a = 4.031 Å with c/a = 1.0002). However, the c/a ratio (1.0002) is a much smaller distortion than in the model tetragonal reference pattern fitted to the commercially purchased cubic (CC-BT) sample (Table 5). A better W_{rp} of CT-BT-170^{o}C is obtained by fitting only the reference cubic model (W_{rp}=12.6) as compared to when both tetragonal and cubic model patterns are used (W_{rp}=15.2). The CT-BT-170^{o}C W_{rp} and GoF fitting parameters suggests the sample is likely to be fully cubic and wouldn't expect this sample to produce SHG. The phase of CT-BT-170^{o}C is investigated further in Chapter 5.

The CC-BT Rietveld refinement suggests a ~ 50 % tetragonal phase fraction present with the model tetragonal unit cell parameters for CC-BT: c = 4.016 Å, a = 4.013 Å giving a c/a = 1.0008. Because the c/a ratio is small, the unit cell is more centrosymmetric (i.e. more of a cubic-like unit cell) and hence the model tetragonal and cubic reference patterns are almost equal. The synchrotron data shows a better W_{rp} (1.3) than the laboratory-XRD data (W_{rp} = 4.3). The sample is not phase pure by either measure (laboratory or synchrotron XRD) therefore this sample would be expected to produce SHG light.

The commercially purchased cubic barium strontium titanate sample (CC-BST) laboratory-XRD pattern is shown in Figure 80. A commercial tetragonal sample was unavailable. Rietveld peak fitting of XRD of the sample indicates a cubic and tetragonal phase fraction are present. This sample was analysed further by the Diamond Light Source (Beamline I11, rapid access) under the supervision of Professor Chiu Tang and Dr Sarah Day; Figure 81.

The laboratory XRD of CC-BST sample shows an 8 % tetragonal phase fraction present; with a c/a ratio of 1.01 (c = 4.03 Å, a = 3.99 Å). The Rietveld peak fitting of this sample may be affected by the small average particle size ~ 50 nm by TEM imaging (~30 nm average crystallite size by laboratory-XRD), causing a broadening of the (002/200) peak (in comparison to the µm sized CT-BT sample).

The Synchrotron powder diffraction of CC-BST also shows the presence of a tetragonal phase; however, the phase fraction is somewhat larger (30 %). The estimated unit cell parameters are: c = 3.96 Å, a = 3.92 Å, giving a c/a = 1.0005. This suggests a weakly distorted tetragonal phase which indicate that the sample is actually fully cubic. The synchrotron fitted data shows an

improved W_{rp} value of 1.2 in comparison to the laboratory-XRD W_{rp} fitting value of 5.3; Figure 80.

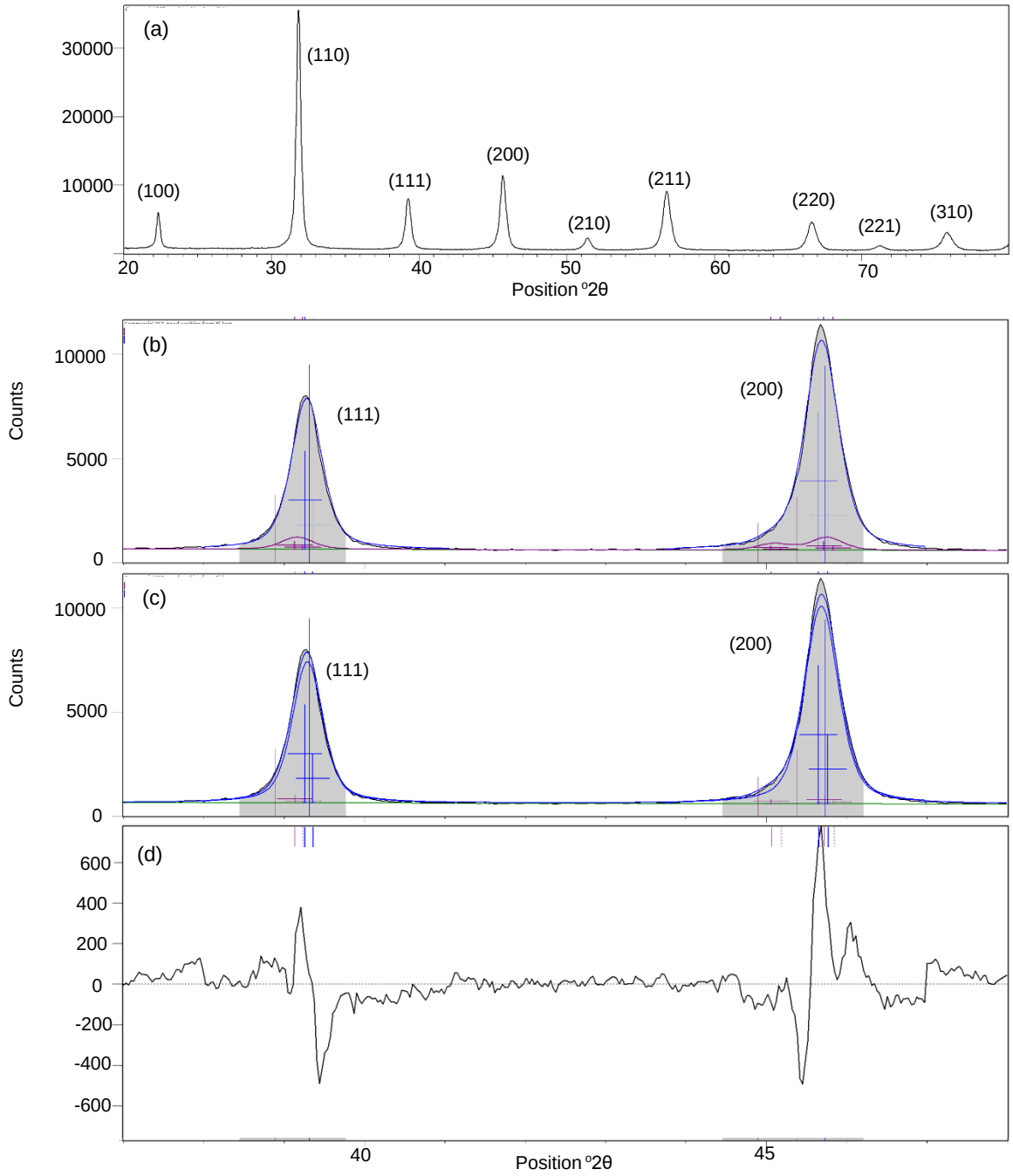

Figure 80. (a) Laboratory X-Ray diffraction pattern of CC-BST labelled with the Miller indices. (b) Tetragonal Rietveld peak fitting of the (111) and (200) peaks, suggests the powder has an 8 % tetragonal phase fraction. (c) Cubic Rietveld peak fitting of the (111) and (002/200) peaks, suggests the powder has a 92 % cubic phase fraction. (d) Difference plot of the reference patterns subtracted from the experimental pattern.

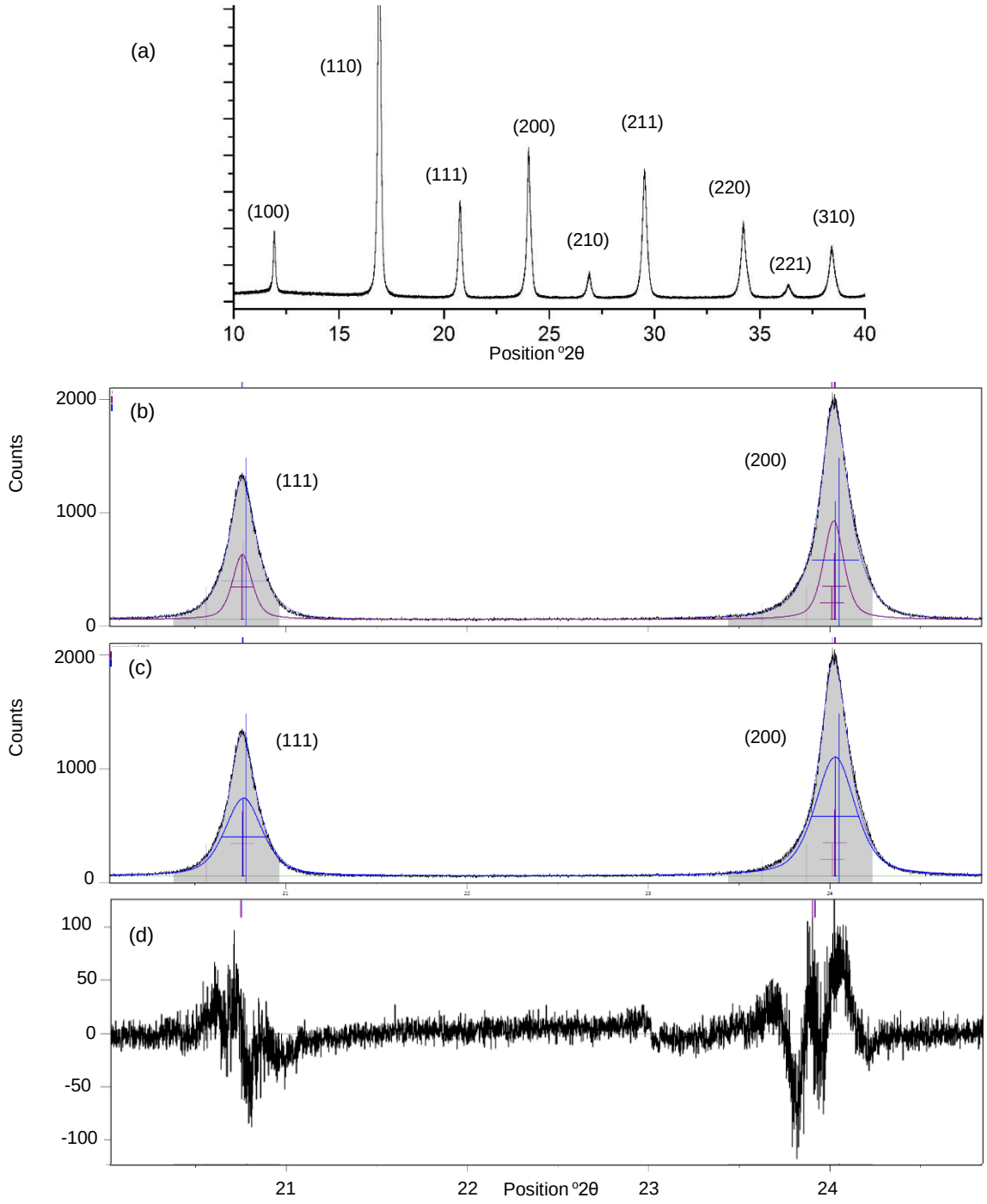

Figure 81. (a) Synchrotron powder diffraction pattern of CC-BST labelled with the miller indices. (b) Tetragonal Rietveld peak fitting of the (111) and (200) peaks, suggests the powder has a 30 % tetragonal phase fraction. (c) Cubic Rietveld peak fitting of the (111) and (002/200) peaks, suggests the powder has a 70 % cubic phase fraction. (d) Difference plot of the reference patterns subtracted from the experimental pattern.

The Rietveld refinement of the commercial samples suggested that there is a tetragonal phase fraction present in all samples; indicating that SHG should be possible from all these samples.

The summary of diffraction and Rietveld refinement data in Table 1 lists an estimated volume fraction of tetragonal phase in addition to its distortion from cubic symmetry by providing the refined unit cell parameters. This allows us to go ahead with some confidence in the analysis of the unknown hydrothermally prepared barium titanate and barium strontium titanate samples.

The XRD (laboratory and synchrotron) of hydrothermally prepared barium titanate (H-BT) is presented in section 4.1.2.

4.1.2 Hydrothermally prepared barium titanate.

The laboratory-XRD pattern of hydrothermal barium titanate nanoparticles is shown in Figure 82. The crystal phase fractions were estimated by Rietveld peak fitting.

The H-BT sample shows a clear splitting of the (002/200) peak suggesting a tetragonal phase fraction is dominant. Rietveld peak fitting of H-BT shows a ~75 % tetragonal phase fraction is present. The difference plot shows a good residual fit and a low W_{rp} (2.4). Indicating a good fit of the (111) and (002/200) peaks H-BT sample; Figure 82.

The H-BT sample was analysed at the Diamond Light source, beamline I11 (Rapid Access, Didcot, UK) under the supervision of Professor Chiu Tang and Dr Sarah Day and the data is shown in Figure 83.

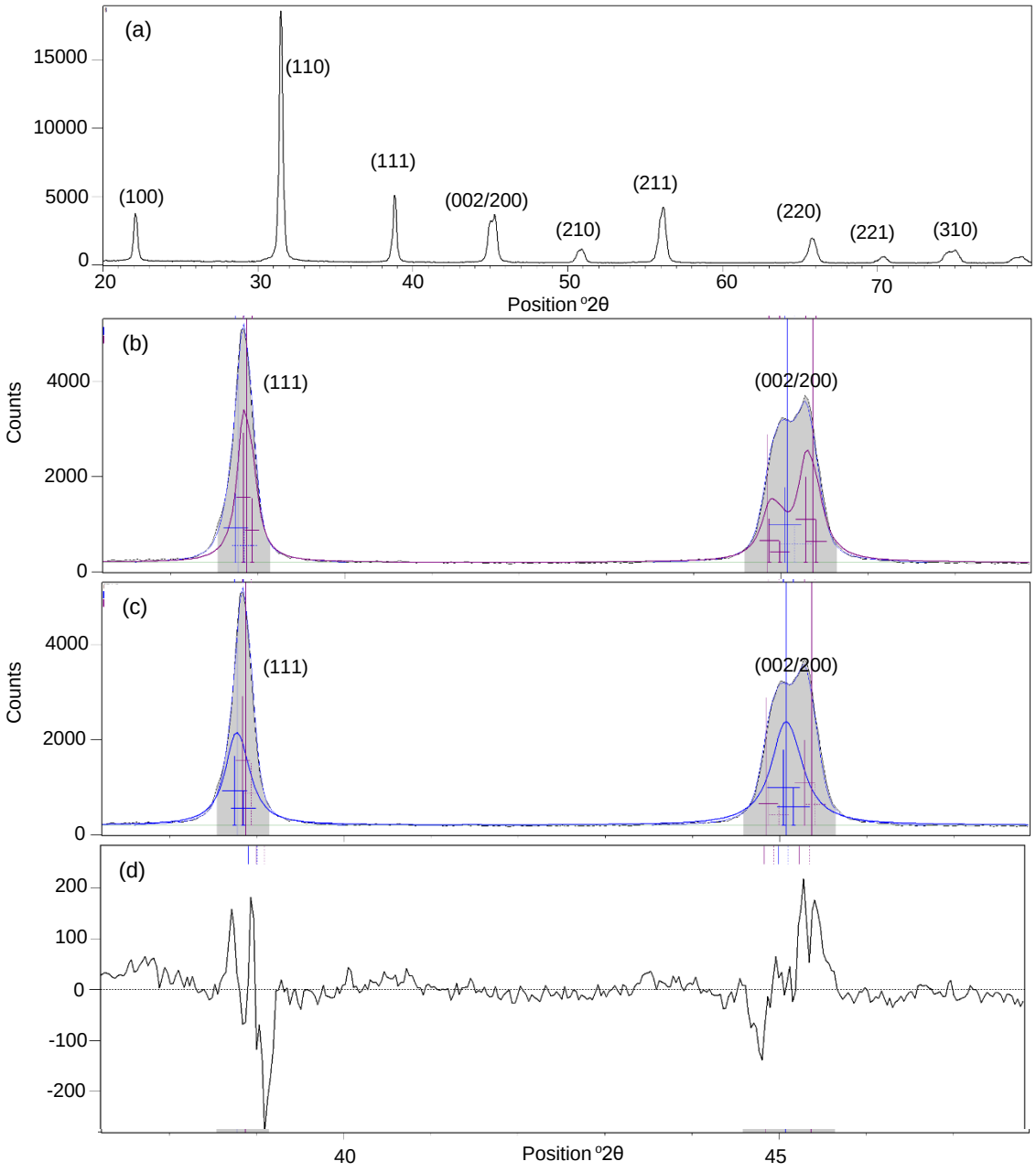

Figure 82. (a) Laboratory X-Ray diffraction pattern of H-BT labelled with the Miller indices. (b) Tetragonal Rietveld peak fitting of the (111) and (002/200), suggests the powder has a 74 % tetragonal phase fraction. (c) Cubic Rietveld peak fitting of the (111) and (002/200) peaks suggests the powder has a 26 % cubic phase fraction. (d) Difference plot of the reference patterns subtracted from the experimental pattern.

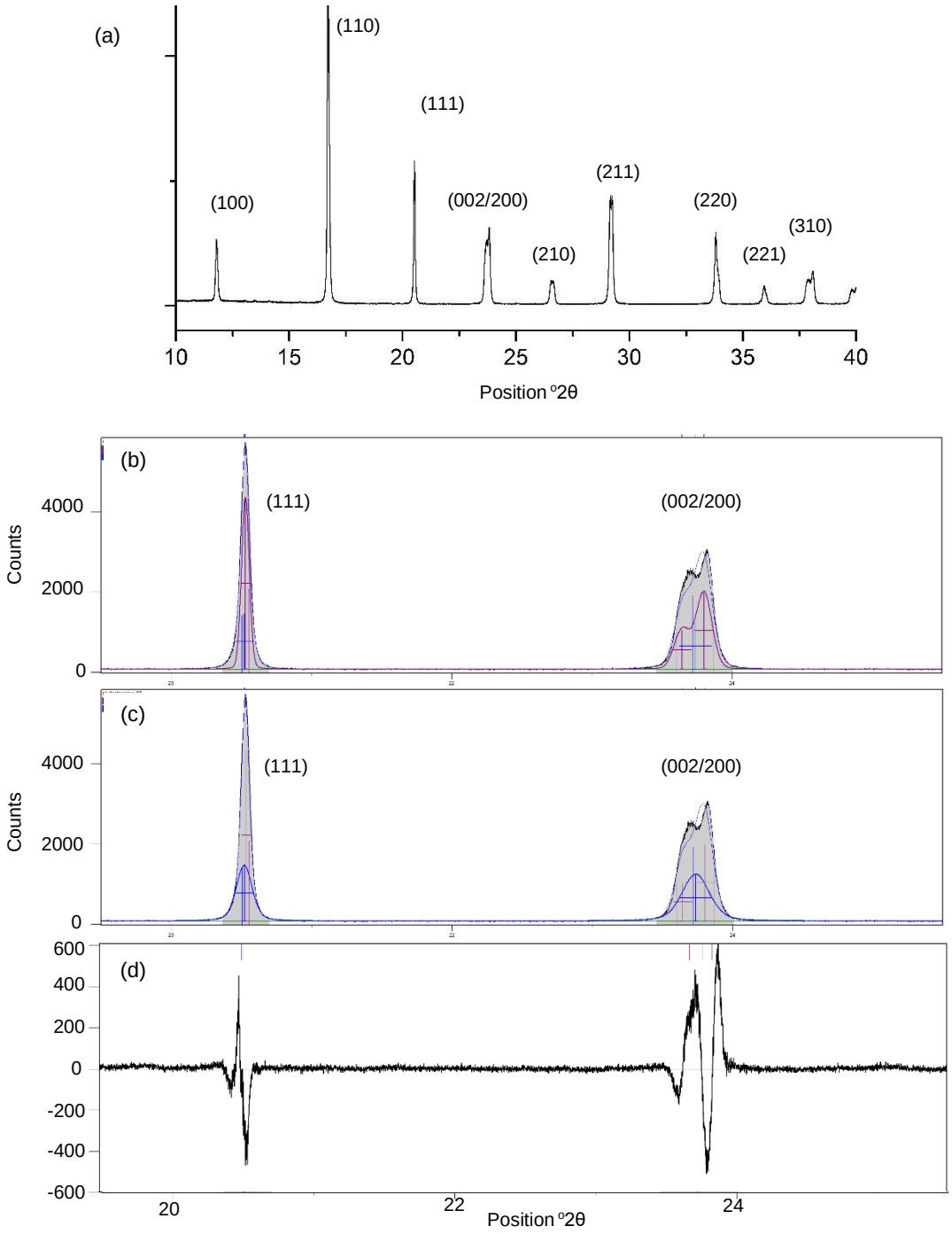

Figure 83. (a) Synchrotron powder diffraction pattern of H-BT labelled with the Miller indices. (b) Tetragonal Rietveld peak fitting of the (111) and (002/200) peaks, suggests the powder has a 59 % tetragonal phase fraction. (c) Cubic Rietveld peak fitting of the (111) and (002/200) peaks, suggests the powder has a 41 % cubic phase fraction. (d) Difference plot of the reference patterns subtracted from the experimental pattern.

The synchrotron powder diffraction of the H-BT sample (Figure 83) shows a more pronounced splitting of the (002/200) peak compared to the laboratory-XRD data. However, the Rietveld fitting estimates a lower tetragonal phase fraction (58 %). The Rietveld peak fitting for laboratory and synchrotron powder diffraction data are shown in Table 6. The synchrotron data shows a substantial reduction in tetragonal phase fraction compared to laboratory-XRD, suggesting that even though the (002/200) splitting is better resolved in the synchrotron data, the tetragonal phase is actually less distorted (suggested by the Rietveld tetragonal model c/a ratio decreasing from 1.008 to 1.006). The W_{rp} values for laboratory and synchrotron XRD decreases from 2.4 to 3.3 respectively.

This suggests the Rietveld fitting is poorer for the synchrotron fitting, which is likely due to the mismatch in fitting across the more pronounced (002/200) peak splitting, resulting in a poorer residual fit (shown in Figure 83).

When the H-BT sample is heated above the Curie point to ensure a tetragonal-to-cubic transition occurs (H-BT-170^{o}C) a single (200) peak becomes prominent (Figure 84), with a disappearance of the (002/200) tetragonal splitting indicating that there is indeed a phase transformation.

However, the (200) peak does show an asymmetric broad base which can be fitted using a tetragonal reference pattern, giving a c/a ratio of 1.007 (c = 4.06 Å, a = 4.03 Å). The data were also fitted with the cubic reference only to see if it improved the W_{rp} and GoF of the H-BT-170^{o}C sample and to indicate which phase combination is the best fit; Figure 85.

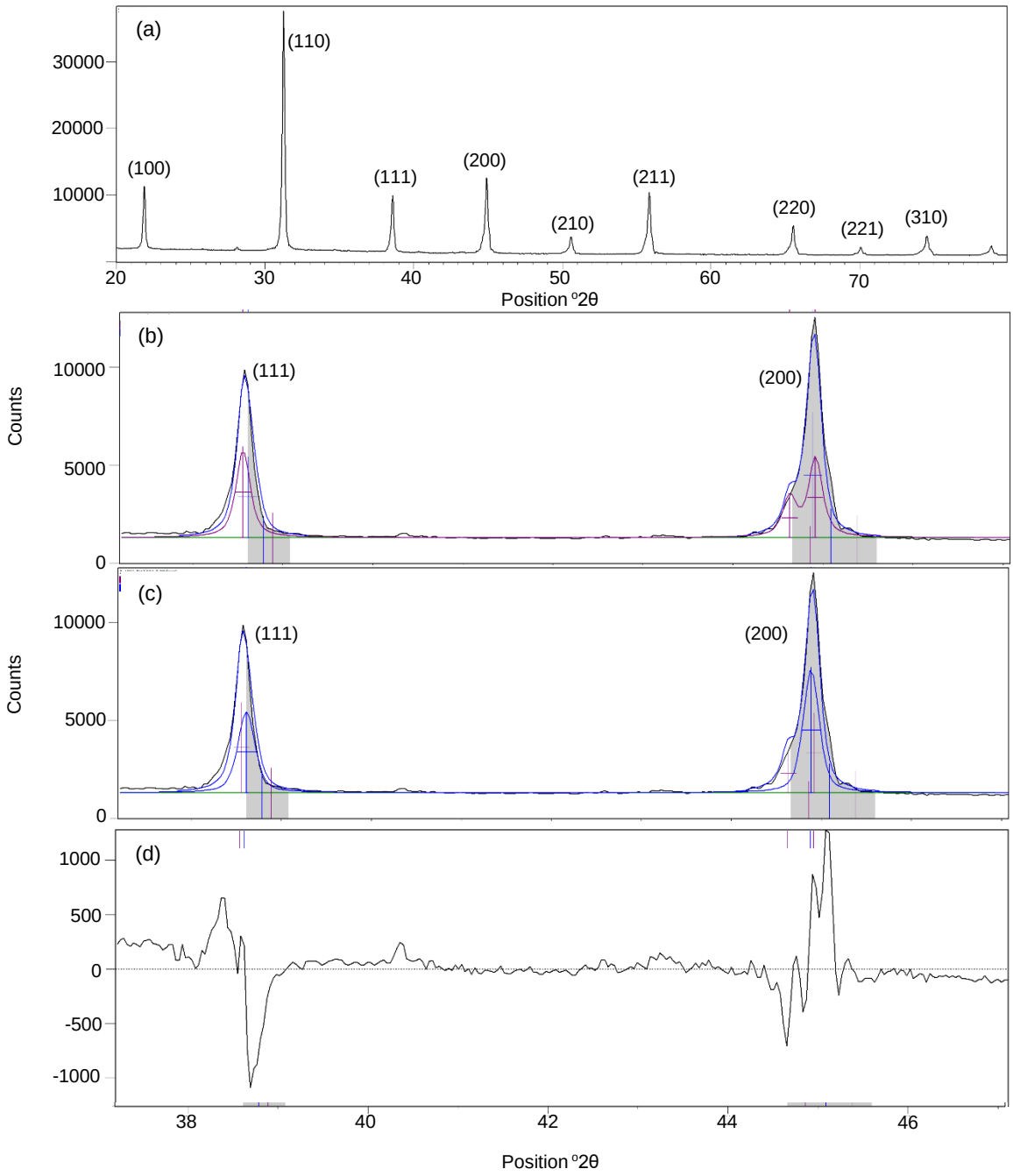

Figure 84. (a) Laboratory X-Ray diffraction pattern of H-BT collected at 170 °C labelled with the Miller indices. (b) Tetragonal Rietveld peak fitting of the (111) and (002/200), suggests the powder has a 54 % tetragonal phase fraction. (c) Cubic Rietveld peak fitting of the (111) and (002/200) peaks suggests the powder has a 46 % cubic phase fraction. (d) Difference plot of the reference patterns subtracted from the experimental pattern.

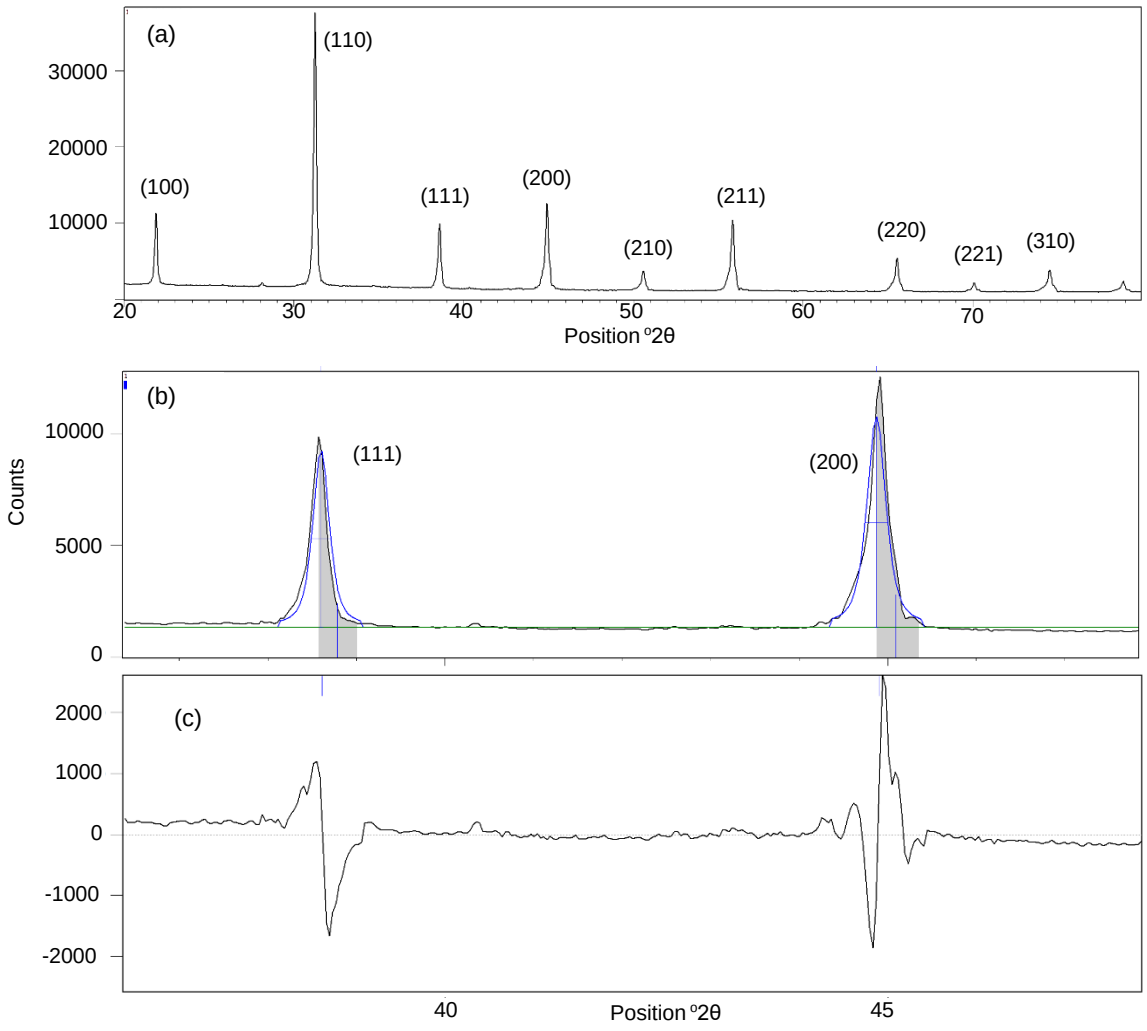

Figure 85. (a) Laboratory X-Ray diffraction pattern of H-BT collected at 170 ºC labelled with the Miller indices. (b) Cubic Rietveld peak fitting of the (111) and (200) peaks. (c) Difference plot of the reference patterns subtracted from the experimental pattern.

The Rietveld fitting parameters for Figure 84 and Figure 85 are summarised in Table 6.

Sample	Average crystallite size (nm)	Rietveld fitting tetragonal unit cell parameters	c/a ratio	Tetragonal phase fraction (%)	Weighted r-profile (W_{rp})	Goodness of fit (GoF)
H-BT	71.8	c = 4.03 Å a = 3.99 Å	1.008	75	2.4	6.3
	Synchrotron	c = 4.03 Å a = 4.005 Å	1.006	58	3.3	10.0
H-BT @ 170 ºC	84.2	c = 4.06 Å a = 4.03 Å	1.007	54	9.0	8.0
		Cubic fitting N/A			15.7	12.9

Table 6. Summary of the Rietveld peak fitting for laboratory-XRD and Synchrotron powder diffraction data for H-BT. The average crystallite size is determined by the Scherrer equation. The c/a ratio tetragonal phase fraction, W_{rp} and goodness of fit are all parameters generated by the Rietveld peak fitting.

The Rietveld analysis of H-BT-170^{o}C above the Curie point suggested a better fit when including the tetragonal reference data (W_{rp} = 9). Furthermore, the Rietveld refinement data suggested the H-BT tetragonal phase decreases when analysing laboratory and synchrotron XRD (from 75 % to 58 %).

The powder diffraction data of the H-BT sample shows a tetragonal crystal phase fraction is consistently present in the majority even after heating above the Curie temperature. However, its exact phase fraction (75–60 %) is difficult to elucidate through Rietveld peak fitting. To confirm H-BT nanoparticles were successfully synthesised, the morphology and crystal structure of the nanoparticles were investigated by SEM and TEM data as shown in Figure 86 & Figure 87 respectively.

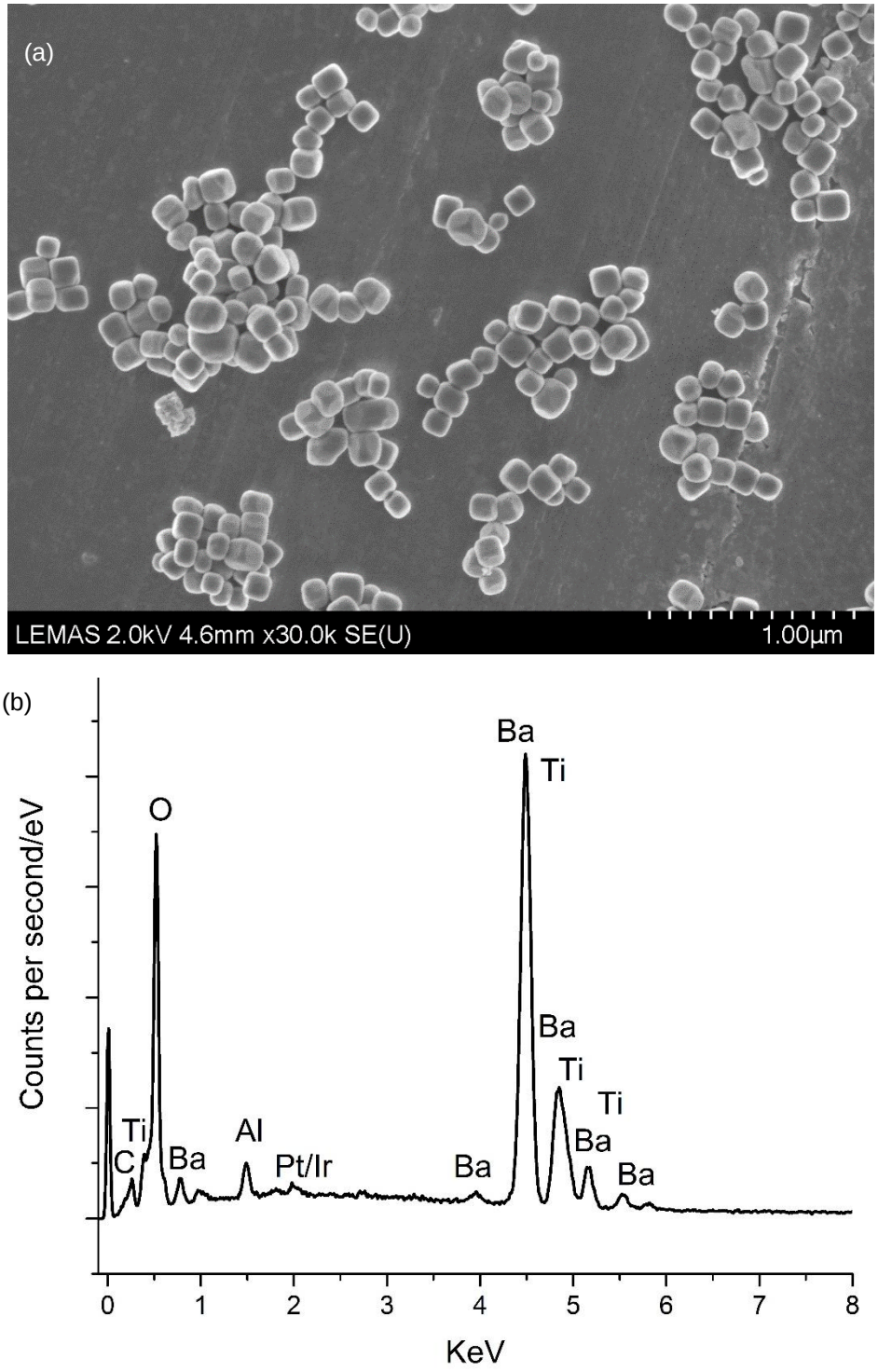

Figure 86. (a) Secondary electron SEM image of agglomerated barium titanate nanoparticles hydrothermally synthesised at 150 ºC for 72 hours. (b) EDX spectrum of nanoparticles. The nanoparticles were dropcast onto a SEM stub and coated in a 5 nm platinum/iridium coating for SEM analysis. The spectrum is labelled with the elements.

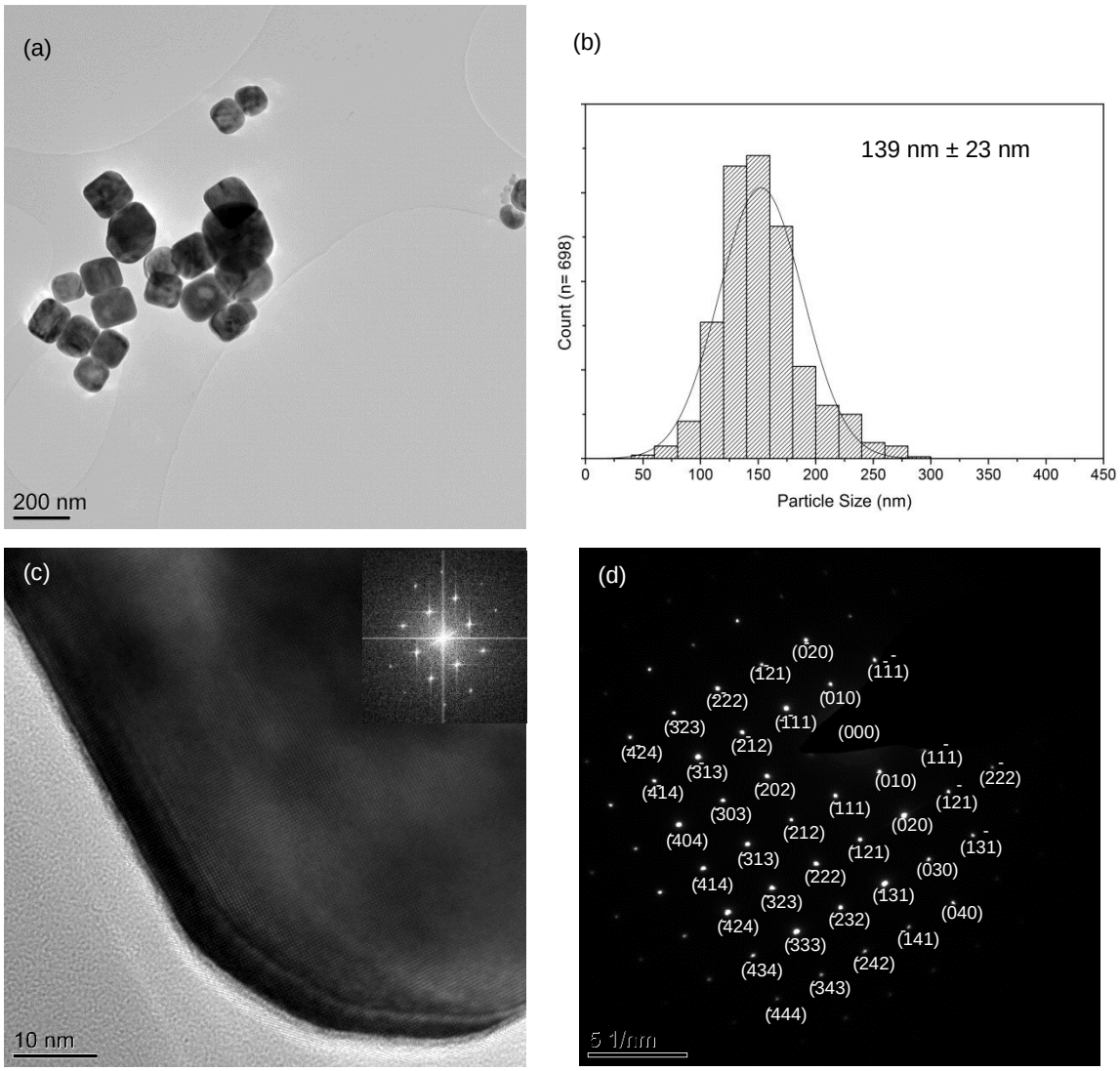

Figure 87. (a) Bright field TEM image of flocculated barium titanate nanoparticles produced by hydrothermal synthesis at 150 ºC on a holey carbon support film. (b) The particle size distribution shows an average particle size of 139 ± 23 nm. (c) High resolution bright field lattice image with FTT shown inset. (d) Labelled electron diffraction pattern from the nanoparticle down the [101] axis.

The SEM image (Figure 86) shows agglomerated barium titanate nanoparticles on a SEM stub with the respective EDX spectrum showing a barium and titanium signal at ≈ 4 keV. The barium titanate nanoparticles show a variation in size (< 1 µm) and a square morphology with truncated facets.

The bright field TEM image (Figure 87) shows flocculated H-BT nanoparticles with a particle size distribution centred around 140 nm. A high resolution image (with an FFT inset) and a labelled electron diffraction pattern with the Miller (hkl) indices is also shown.

The data suggest successful hydrothermal synthesis of barium titanate nanoparticles by laboratory XRD, synchrotron powder diffraction, SEM, TEM, EDX and electron diffraction. There is still a question over the precise phase content and distribution of the nanoparticles (although evidence suggests they are 60–75 % tetragonal) which will be analysed and discussed further by electron energy loss spectroscopy (EELS) in Chapter 5.

4.1.3 Hydrothermally prepared barium strontium titanate.

Barium strontium titanate nanoparticles were synthesised in order to increase the dielectric constant of the nanoparticles for use as biomarkers (Figure 26, Chapter 2) [67].

For hydrothermally prepared BST samples, only the synchrotron data are reported. This is because Rietveld refinement of the Commercial CC-BST sample shows that it produced a better fit for the higher resolution synchrotron data as compared to the laboratory-XRD.

The synchrotron XRD data of the first $Ba_{1-x}Sr_xTiO_3$ synthesis route H-BST-01 is shown in Figure 88. The data show a splitting of the (002/200) peak. However, there is a peak asymmetry at the right side of the (002/200) peaks which could indicate a compositional change for H-BST-01. Which gives rise to an additional (200) peak. This peak asymmetry and extra peak could indicate the presence of a strontium-rich BST phase that results in a peak at higher $^{o}2\theta$

values [92] consisting with a barium-rich BST which is responsible for the major intensity peak.

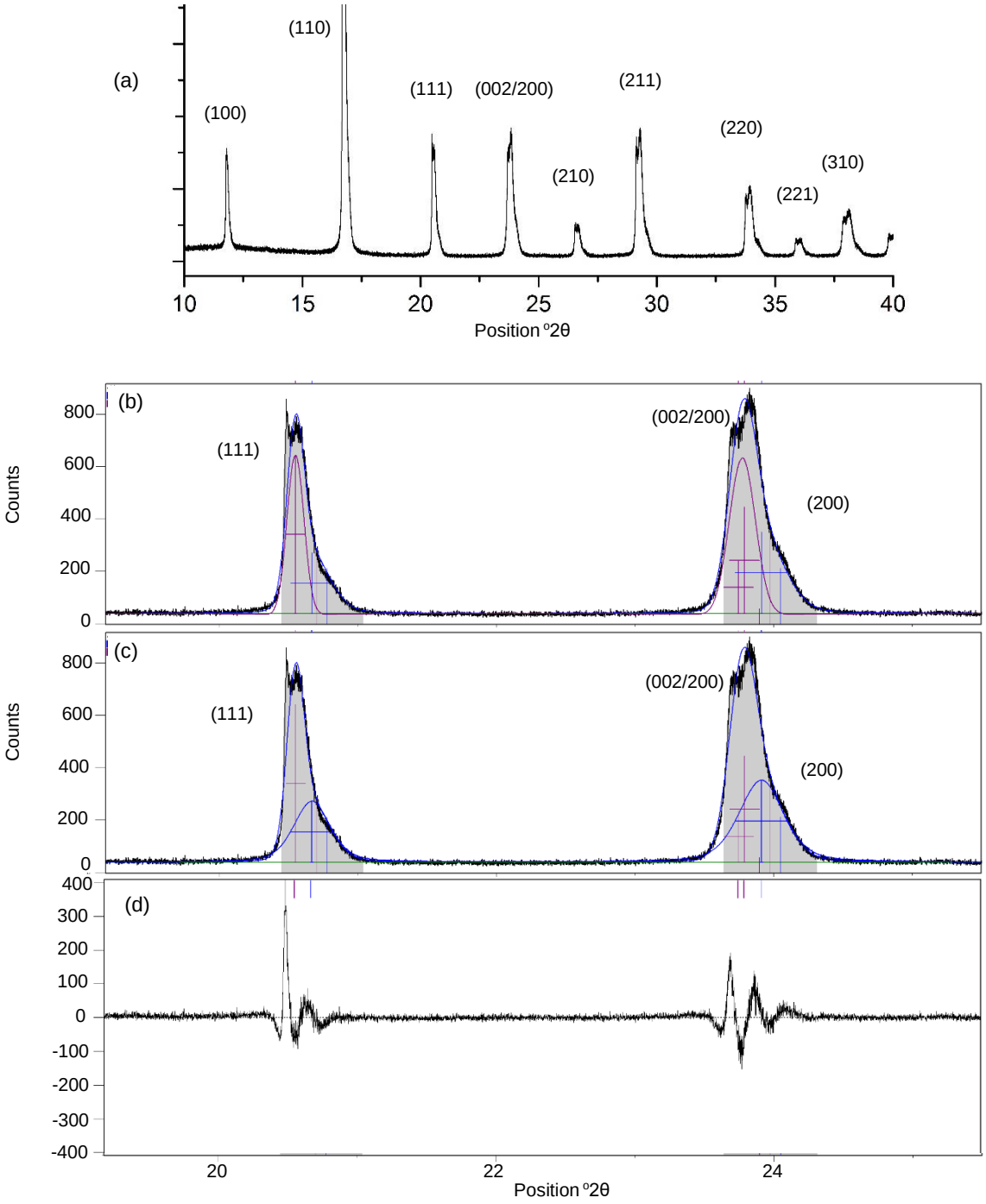

Figure 88. (a) Synchrotron powder diffraction pattern of H-BST-01 labelled with the miller indices. (b) Tetragonal Rietveld peak fitting of the (111) and (200) peaks, suggests the powder has a 53 % tetragonal phase fraction. (c) Cubic Rietveld peak fitting of the (111) and (002/200) peaks, suggests the powder has a 47 % cubic phase fraction. (d) Difference plot of the reference patterns subtracted from the experimental pattern.

Overall the diffraction data implies a barium-rich BST that is the major (002/200) peak (~ 1 µm crystallite size) and a strontium-rich BST (~ 65 nm crystallite sizes – Table 7) that diffracts at higher angles of $^{o}2\theta$, implying a near equal mixture (53 % vs 47 %) of a tetragonal phased (barium-rich) powder and a cubic phased (strontium-rich) powder. The addition of Strontium ions into the barium titanate lattice shifts the pattern to higher 2θ angles (as shown by the (111) peak in Figure 88) because the smaller ionic radius of Sr reduces the lattice constants (cubic lattice parameters for BT = 4.019 Å and for BST = 3.965 Å). It might be expected that the tetragonal Ba-rich phase would exhibit SHG, whilst the cubic Sr-rich phase would not.

The incorporation of Strontium ions into the barium titanate lattice for H-BST-01 was further analysed by TEM with EDX and he results are shown in Figure 89 & Figure 90.

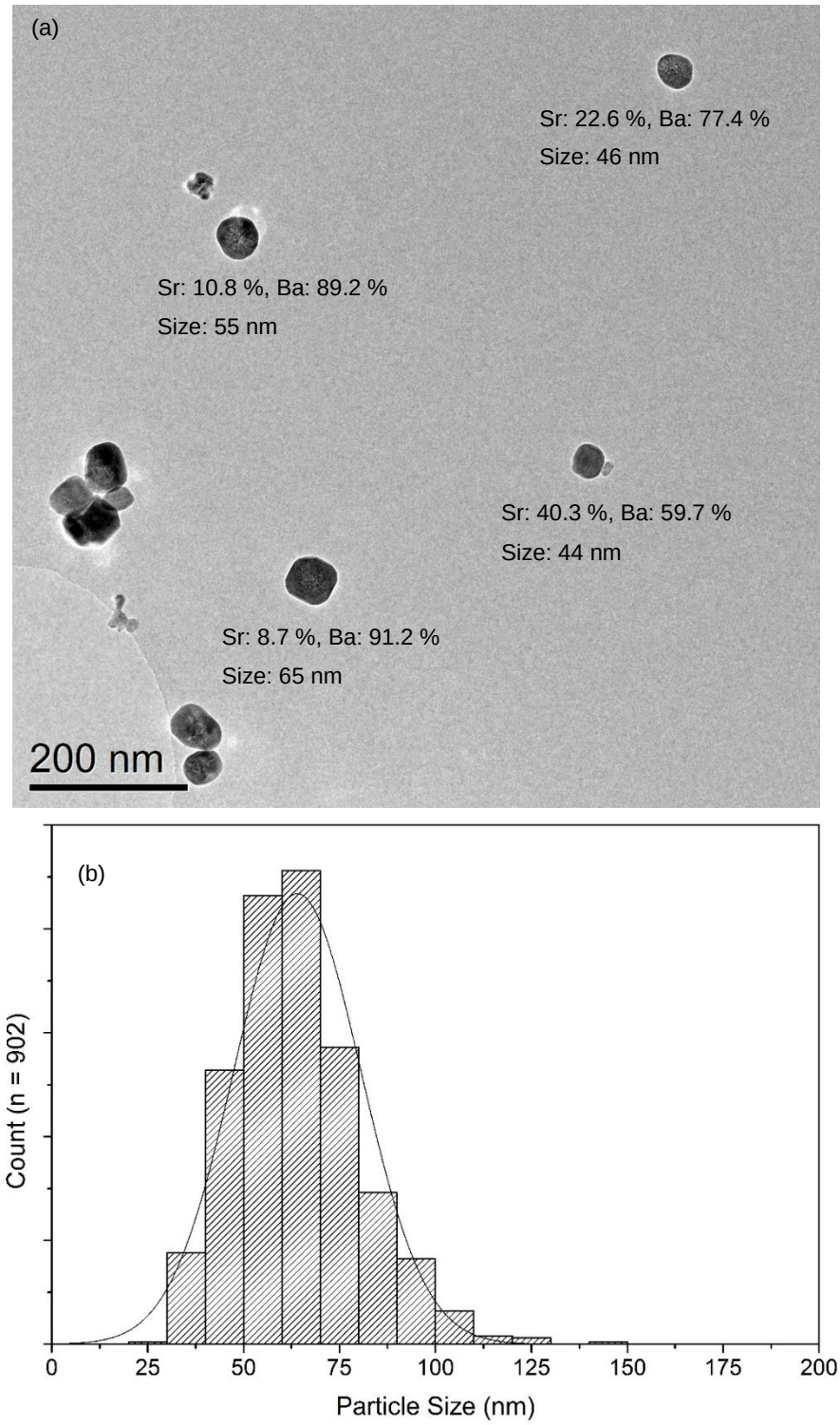

Figure 89. (a) Bright field TEM image of H-BST-01 nanoparticles. The annotations show the size of the nanoparticles and the atomic % of Sr-K series and Ba-L series determined by spot-EDX. The largest difference of strontium incorporation is ≈ 30 atomic %. (b) Particle size distribution of H-BST-01 nanoparticles with a bi-phasic strontium incorporation (Figure 88). The average particle size ~65 nm ± 16 nm.

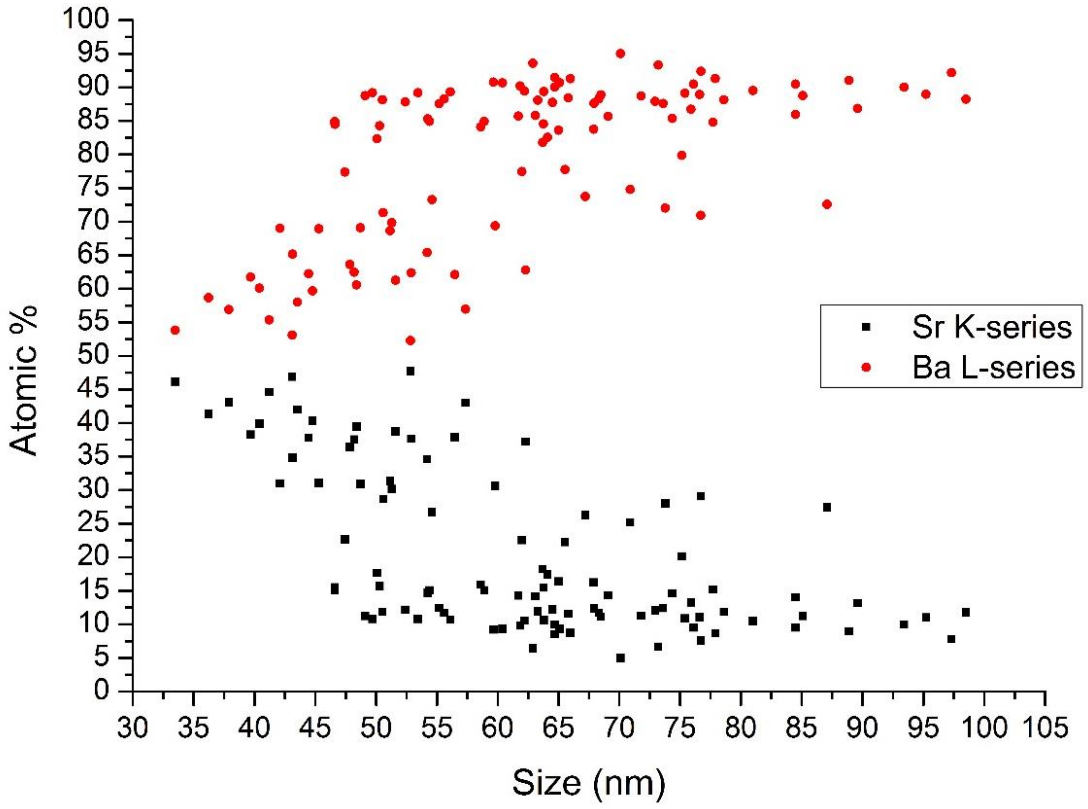

Figure 90. Plot showing TEM-EDX analysis of the composition of 100 H-BST-01 nanoparticles showing a biphasic strontium incorporation. The trend generally shows that smaller nanoparticles (below ~50 nm) have a higher incorporation of strontium. The desired incorporation for hydrothermal BST is $Ba_{0.8}Sr_{0.2}TiO_3$, but the graph shows a bi-modal distribution of composition corresponding to ≈ $Ba_{0.88}Sr_{0.12}TiO_3$ and ≈ $Ba_{0.65}Sr_{0.35}TiO_3$.

TEM-EDX revealed that the H-BST-01 sample showed bi-phasic strontium incorporation (Figure 90). This was accompanied by a peak asymmetry in the (002/200) peak in synchrotron diffraction data (Figure 88). The asymmetric (200) peak at higher $^{o}2\theta$ suggested a cubic strontium-rich BST phase. This strontium-rich BST revealed a broader and lower diffraction intensity XRD peak as compared to the barium-rich BST which exhibited a split (002/200) peak. The strontium rich phase would appear to form smaller crystalline particles,

however varying amounts of strontium incorporation (Figure 90) might also be expected to broaden the (200) diffraction peak from the cubic Sr-rich phase.

TEM-EDX of H-BST-01 confirms the bi-phasic incorporation of strontium into barium titanate forming particles of differing average sizes. This outcome would not be ideal for second harmonic biomarker applications as the smaller, strontium-rich cubic phased BST nanoparticles might not produce SHG.

If this sample was introduced as a biomarker and adverse toxicological effects were experienced, there would be uncertainty as to the source of these effects (i.e. either from tetragonal barium-rich BST or the cubic strontium-rich BST). Furthermore, they would also not be suitable for use as a 'biomarker' if the cubic phased nanoparticles cannot be tracked. Hence this suggests that synthesis of a new hydrothermal barium-strontium titanate sample with more homogenous strontium incorporation is required for second harmonic generation and biomarker applications.

Following this analysis, the hydrothermal synthesis of barium-strontium titanate was modified based on work by Roeder *et al.* [92]. Here, the barium reagent was added in excess so as to reach the desired $Ba_{0.8}Sr_{0.2}TiO_3$ ratio. The resulting synchrotron diffraction pattern of this newly synthesised sample is shown in Figure 91.

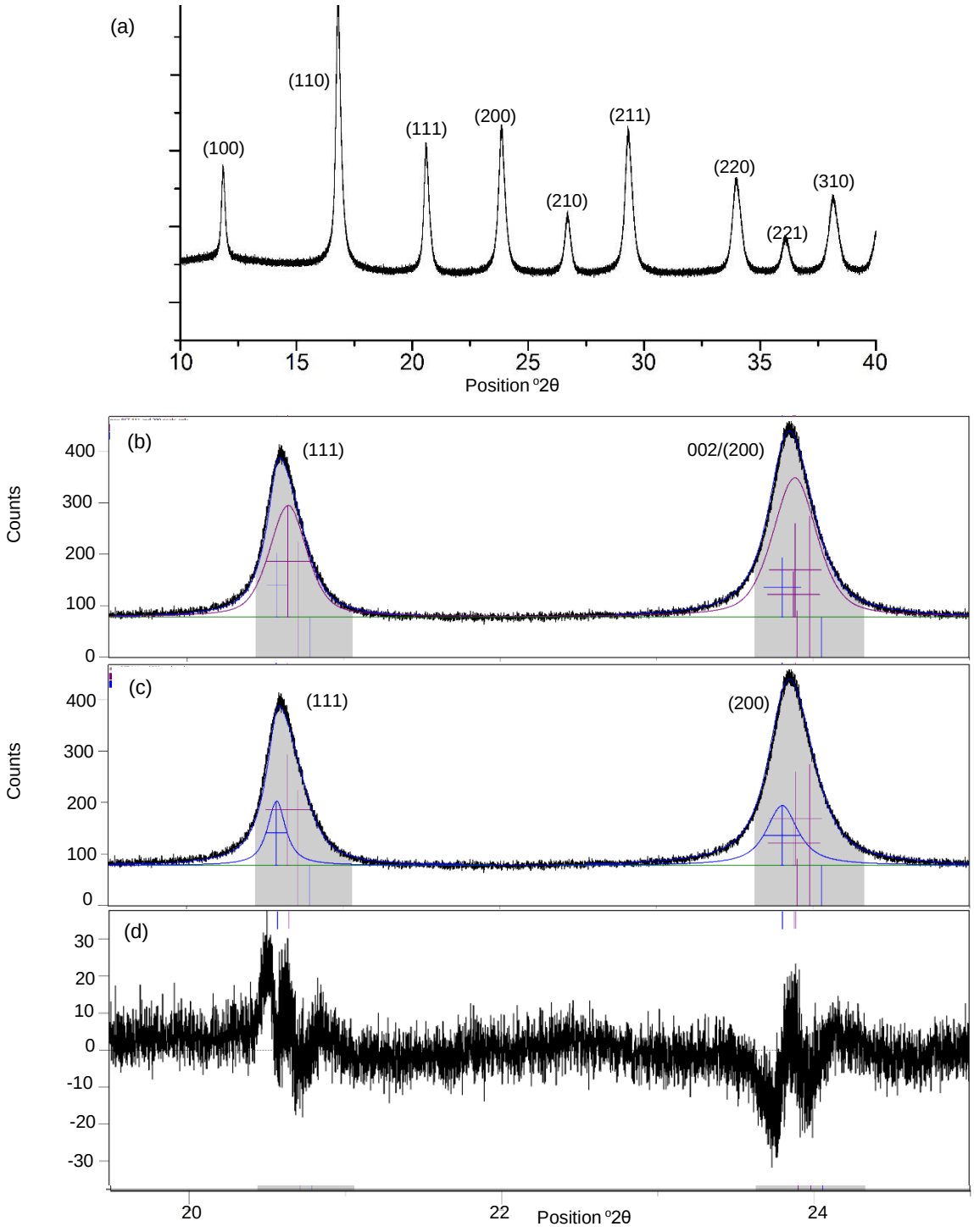

Figure 91. (a) Synchrotron powder diffraction pattern of H-BST that appears cubic, labelled with the Miller indices. (b) Tetragonal Rietveld peak fitting of the (111) and (200) peaks, suggests the powder has a 74 % tetragonal phase fraction. (c) Cubic Rietveld peak fitting of the (111) and (002/200) peaks, suggests the powder has a 26 % cubic phase fraction. (d) Difference plot of the reference patterns subtracted from the experimental pattern.

The synchrotron data of H-BST shows no peak splitting or importantly asymmetry, suggesting a lack of bi-phasic incorporation of Sr. Rietveld peak fitting of the data suggests a ~ 74 % tetragonal phase fraction is present together with a much lower W_{rp} (0.027) than was achieved for the previously synthesised sample (H-BST-01, W_{rp} = 1.9); Table 7. A W_{rp} <1 is considered a perfect fit; meaning that the user fit is better than the software estimate fit of the experimental reference pattern. The H-BST sample also shows a higher, albeit small c/a ratio (1.0004) as compared to the previous H-BST-01 sample (1.0002) i.e. effectively a minor tetragonal distortion.

TEM-EDX analysis of H-BST nanoparticles (Figure 92) showed that the atomic ratio of Barium-*L* series and Strontium-*K* series X-Rays from 100 particles indicated a single-composition BST phase close to the desired composition.

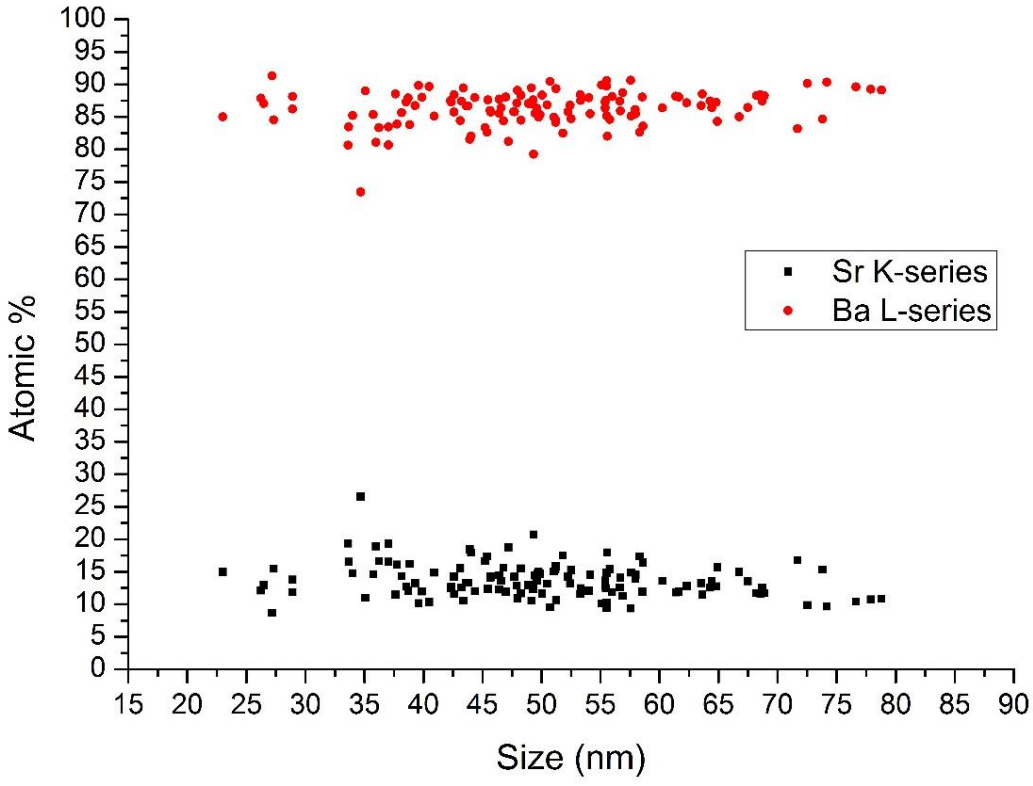

Figure 92. Plot showing TEM-EDX of 100 H-BST nanoparticles suggesting a reasonably single-composition H-BST sample. The average incorporation of strontium is ≈ 15 % and closer to the desired $Ba_{0.8}Sr_{0.2}TiO_3$ stoichiometry.

Furthermore, the H-BST nanoparticles showed a narrower particle size distribution and a smaller average particle size of ≈ 45 ±10 nm (Figure 93). This sample (H-BST) will be the barium strontium titanate sample used for subsequent nanoparticle biomarker analysis (Chapter 6).

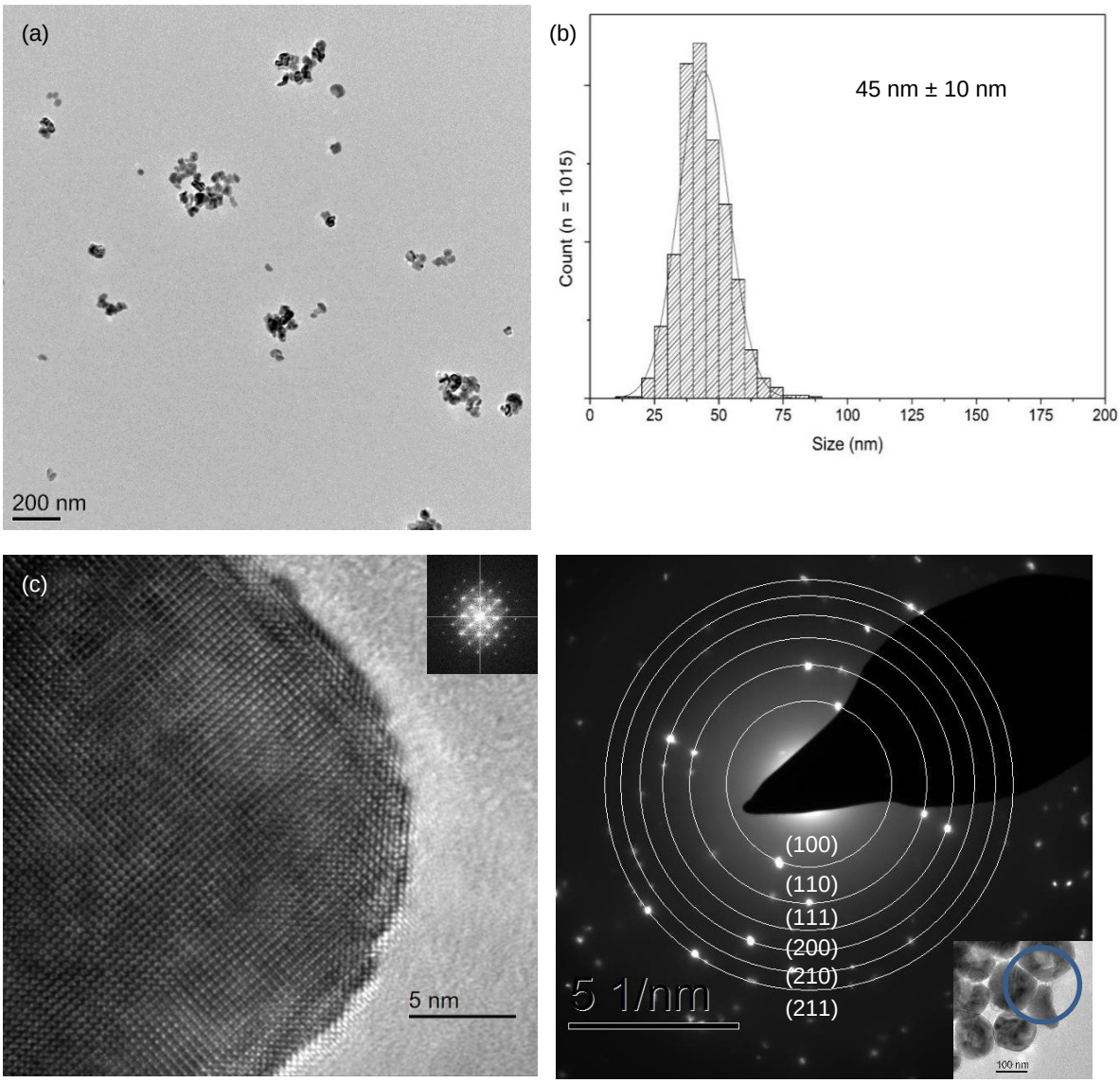

Figure 93. (a) Bright field TEM image of H-BST nanoparticles and (b) Particle size distribution of H-BST nanoparticles with an average particle size ≈ 45 nm. (c) High resolution bright field lattice image down the (111) axis and (d) labelled electron diffraction pattern of the highlighted area in the nanoparticle cluster (inset) from the cubic barium strontium titanate ICDD file 00-034-0411.

Sample	Average crystallite size (nm)	Rietveld fitting tetragonal unit cell parameters	c/a ratio	Tetragonal phase fraction (%)	Weighted r-profile	Goodness of fit
H-BST-01	Synchrotron	c = 3.98 Å a = 3.97 Å	1.0002	47	1.9	13.4
H-BST	Synchrotron	c = 3.988 Å a = 3.986 Å	1.0004	74	0.027	4.65

Table 7. Summary of synchrotron XRD of H-BST-01 and H-BST. The c/a ratio, tetragonal phase fraction, weighted r-profile and goodness of fit are produced by the software.

In summary, the H-BST-01 sample showed a bi-phasic incorporation of strontium which was corrected by altering the starting stoichiometry of the reagents to produce H-BST. The H-BST sample showed ~ 74 % tetragonal phase fraction by synchrotron peak fitting, however the tetragonal distortion was small.

Rietveld peak fitting of H-BST shows a low weighted-r profile and low goodness of fit (similar to that of the laboratory XRD data, not shown). The c/a ratios of H-BST and H-BST-01 are small, giving 1.0004 and 1.0002 (approx. c = 3.988 Å, a = 3.986 Å and c = 3.98 Å, a = 3.97 Å) respectively. However, Rietveld refinement strongly suggests there is a tetragonal phase fraction present in all the samples. Therefore, SHG of light would be expected from all samples and this is discussed in section 4.2.

4.2 Second Harmonic Generation

Rietveld fitting of XRD data for both the commercial and hydrothermally synthesised nanoparticles suggested a mixed phase of cubic and tetragonal components in all bar the CT-BT sample that was 100 % tetragonal. Figure 94 shows the second harmonic light output for all of the CT-BT, CC-BT, H-BT and H-BST nanoparticle samples.

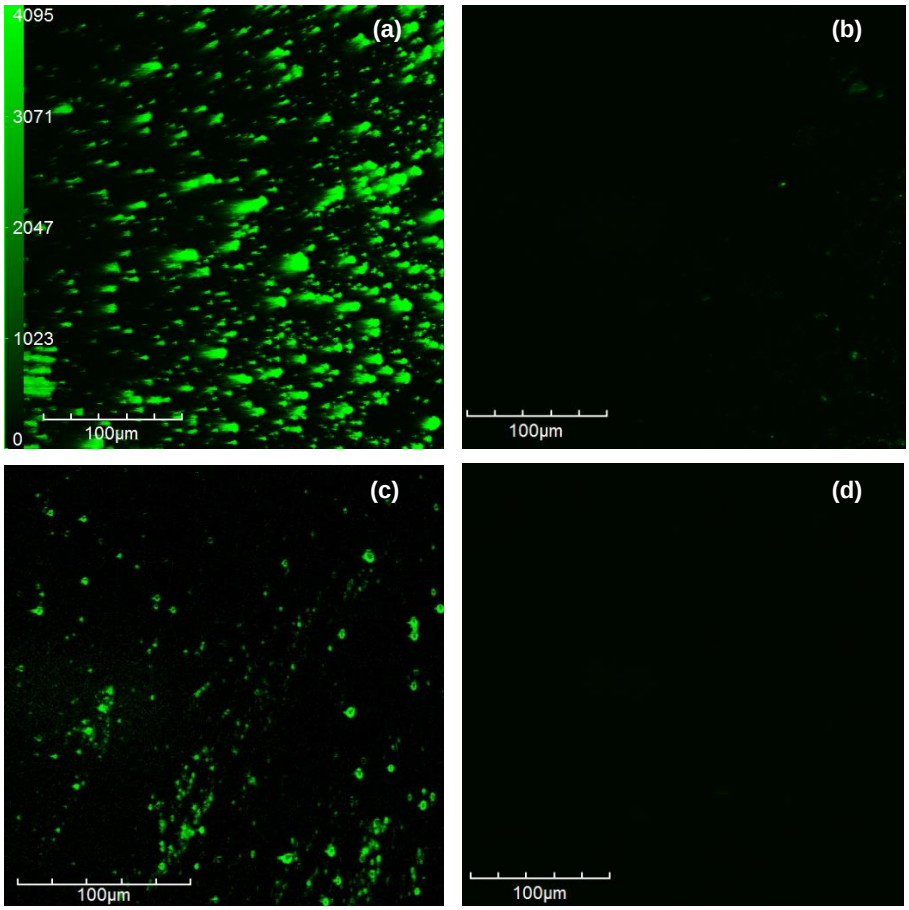

Figure 94. SHG images taken at 40 x magnification, 0.75 numerical aperture at 750 V laser power of (a) CT-BT, (b) CC-BT, (c) H-BT, (d) H-BST. The CT-BT sample was acquired at 750 V laser power to normalise the remaining samples as the maximum intensity that can be collected is 4095 (arb. Units).

The maximum intensity that can be collected using the photomultiplier tube is 4095 (arbitrary units) and all images were normalised to the intensity of the CT-BT sample as the Rietveld peak fitting suggested that this sample was 100 % tetragonal. The CC-BT and H-BST show little to no second harmonic production of light, however when the laser power was increased, SHG output was increased (Figure 95).

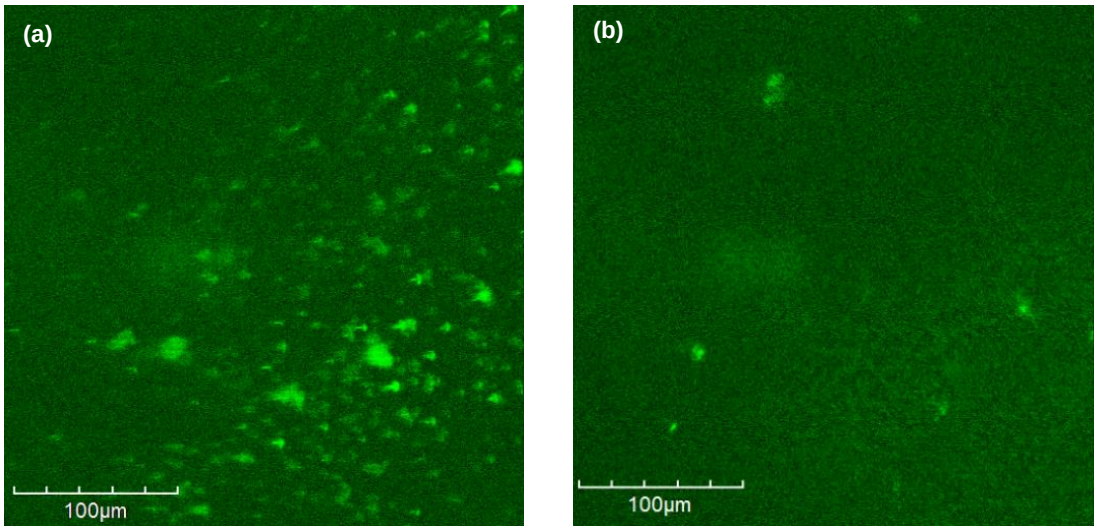

Figure 95. SHG production from (a) CC-BT and (b) H-BST nanoparticles at 1125 V laser power, showing that SHG of light is produced by both these samples.

The SHG images show that all the samples can produce second harmonic light even for the commercial cubic standard and the fine particle H-BST sample. However, SHG production in these samples did require a higher flux of incident photons produced by an increase in laser power).

Rietveld peak fitting of the samples suggested that a tetragonal phase often with a small c/a ratio was present in all samples. However, it was unclear from the XRD analysis as to whether this tetragonal phase was distributed *between*

the nanoparticles (*inter*-particle) or *within* the nanoparticles (*intra*-particle). Correlative SHG and secondary electron SEM images, shown in Figure 96, suggests the tetragonal phase distribution is *intra*-particle as all the particles imaged emit SHG to some extent.

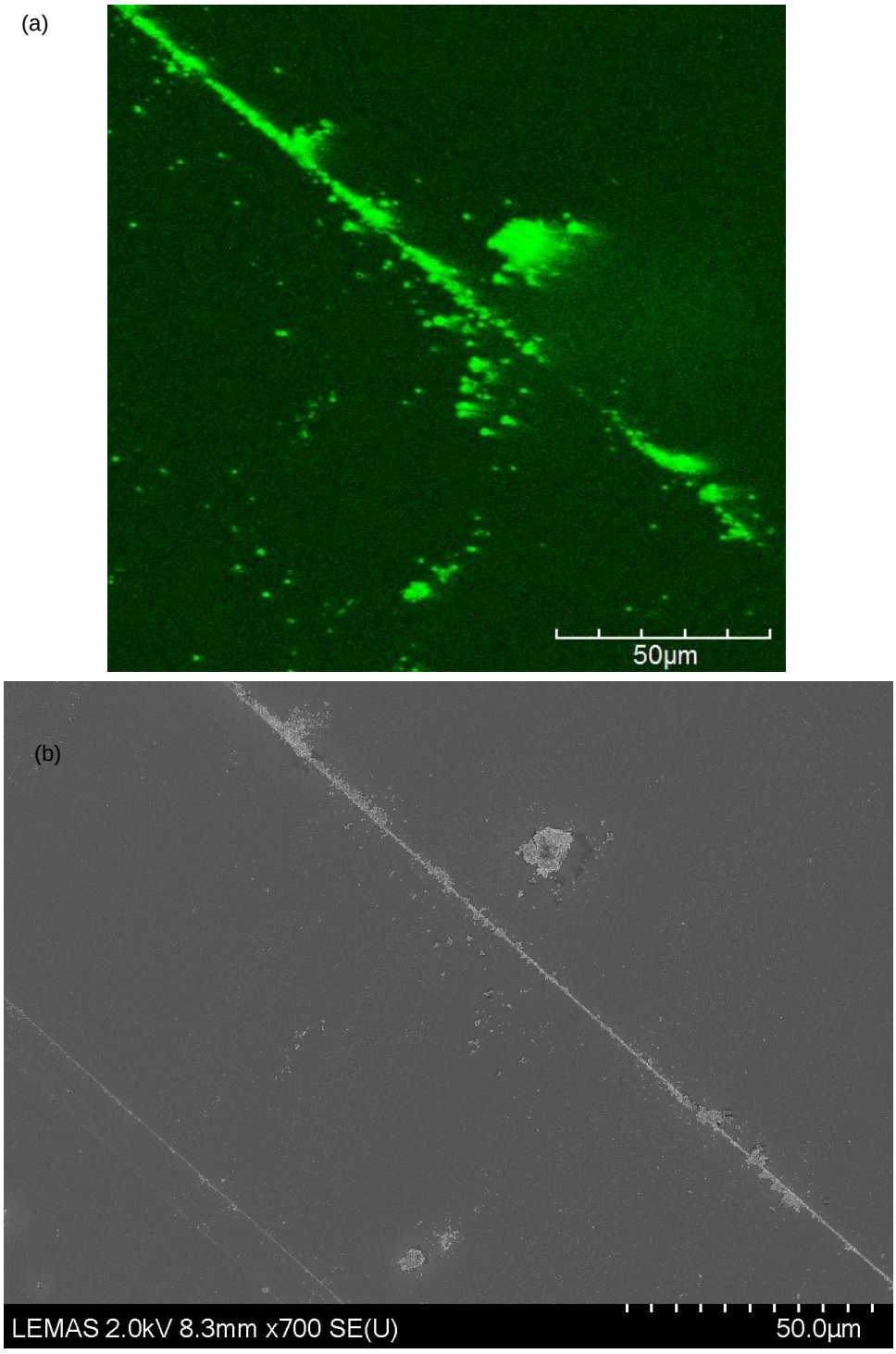

Figure 96. (a) SHG image of agglomerated H-BT nanoparticles on a glass coverslip. (b) Secondary electron SEM image of the same nanoparticles.

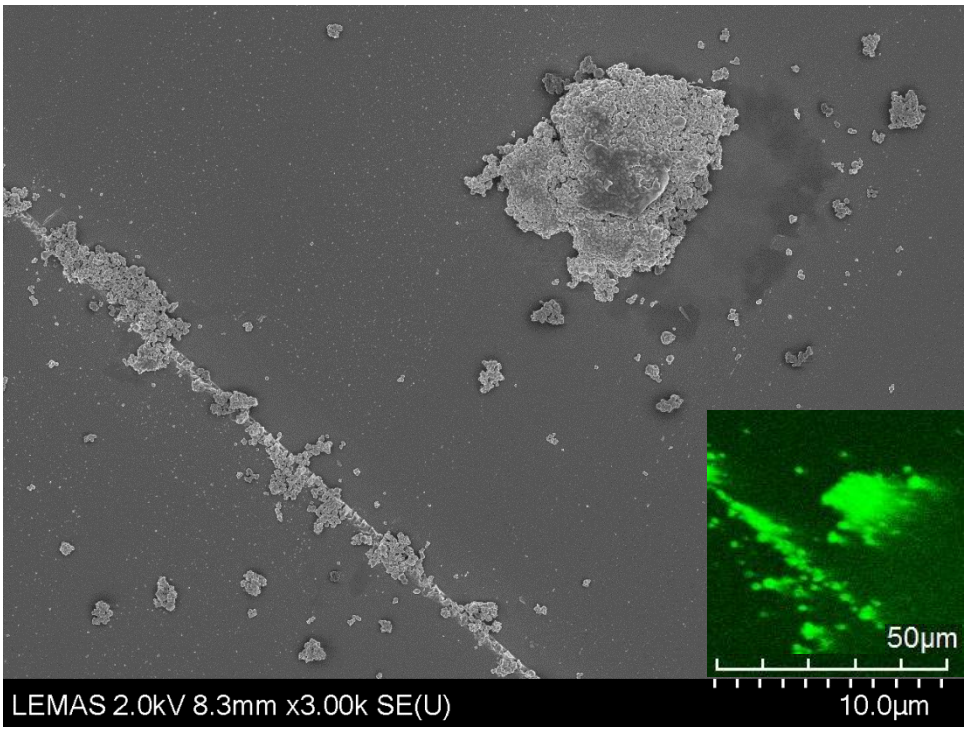

Figure 97. Secondary electron SEM image at a higher magnification of H-BT agglomerated nanoparticles, correlated with the same area in the cropped SHG image.

Figure 96 and Figure 97 show a distinct correlation between second harmonic light and electron microscopy images, qualitatively showing that all the barium titanate nanoparticles present were emitting second harmonic light. This suggests that the tetragonal phase is distributed within each particle (*intra*-particle).

This *intra*-particle phase theory required analysis of the chemical and molecular bonding of individual nanoparticles which has been characterised by electron energy loss spectroscopy (EELS) in the following chapter.

4.3 Chapter Summary

- Rietveld peak fitting of the CT-BT synchrotron powder diffraction data suggests it was 100 % tetragonal phased with a c/a ratio of 1.01.
- CC-BT was a ≈ 50 % tetragonal phase fraction with a c/a ratio of 1.0008.
- H-BT was a ≈ 60 % tetragonal crystal phase fraction with a c/a of 1.006.
- Evidence of a phase transition to a cubic phase was shown when laboratory-XRD was collected at 170 ^{o}C (above the Curie point) for CT-BT and H-BT.
- H-BST-01 showed a bi-phasic level of strontium incorporation as characterised by TEM-EDX analysis.
- H-BST was synthesised to overcome the problem of the bi-phasic strontium incorporation so as to produce a homogenous BST phase.
- H-BST had a ~75 % tetragonal phase fraction but with only a small tetragonal distortion of 1.0002.
- All samples (except CT-BT) showed a mixture of tetragonal and cubic crystal phase fractions; however, all samples produced SHG of light (albeit requiring an increase in laser power for the CC-BT and H-BST samples)
- Correlative SHG and secondary electron SEM images of the H-BT sample showed that all nanoparticles emitted SHG light, suggesting that the nanoparticles have an *intra*-particle phase distribution of cubic and tetragonal phase fractions.

Chapter 5 – Electron energy loss spectroscopy (EELS) of barium titanate and barium strontium titanate nanoparticles.

The XRD (laboratory and synchrotron) data presented in Chapter 4 suggest that all $BaTiO_3$ (excluding CT-BT) and $Ba_{0.8}Sr_{0.2}TiO_3$ nanoparticle samples possessed both a cubic and tetragonal phase fraction (whereas the CT-BT sample is 100 % tetragonal). The second-harmonic generation results indicated that all the nanoparticle samples emit light – including the cubic phase samples which are not expected to emit at all. Correlative SEM and second-harmonic light images of the H-BT sample showed that all nanoparticles emit. This implies there was non-centrosymmetric crystal symmetry present in all particles and a combination of cubic and tetragonal crystal phases existed within each particle (*intra*-particle) as opposed to in separate particles (*inter*-particle).

Electron energy loss spectroscopy results are presented here in order to investigate the chemical bonding of the titanium-oxygen atoms in the $BaTiO_3$ unit cell. Changes in the titanium-oxygen octahedron are expected to alter the characteristic Ti-*L* and O-*K* core-loss edges fine structure (ELNES).

EELS data were collected from nanoparticles both at room temperature (RT) and above the Curie temperature of 130 ^oC (collected here at 400 ^oC), so forcing $BaTiO_3$ to undergo a phase transition from the tetragonal to the cubic phase. EELS data were collected using diffraction-coupled TEM-EELS (EELS from a whole nanoparticle), STEM-EELS linescans (using a convergent beam scanned across a single nanoparticle) and STEM-EELS mapping (convergent beam scanned around a projected area of the nanoparticle).

Diffraction-coupled TEM-EELS of the tetragonal (CT-BT) and transformed (cubic) sample (CT-BT heated to 400 ^{o}C) were used as calibration tetragonal and cubic spectra respectively. The CT-BT and CT-BT-400^{o}C EELS data was used to interpret the crystal phase of the hydrothermally synthesised barium titanate (H-BT) nanoparticles. The processing of the acquired Ti-*L* and O-*K* EELS edges was conducted using Gatan Digital Micrograph software and is summarised in Figure 98.

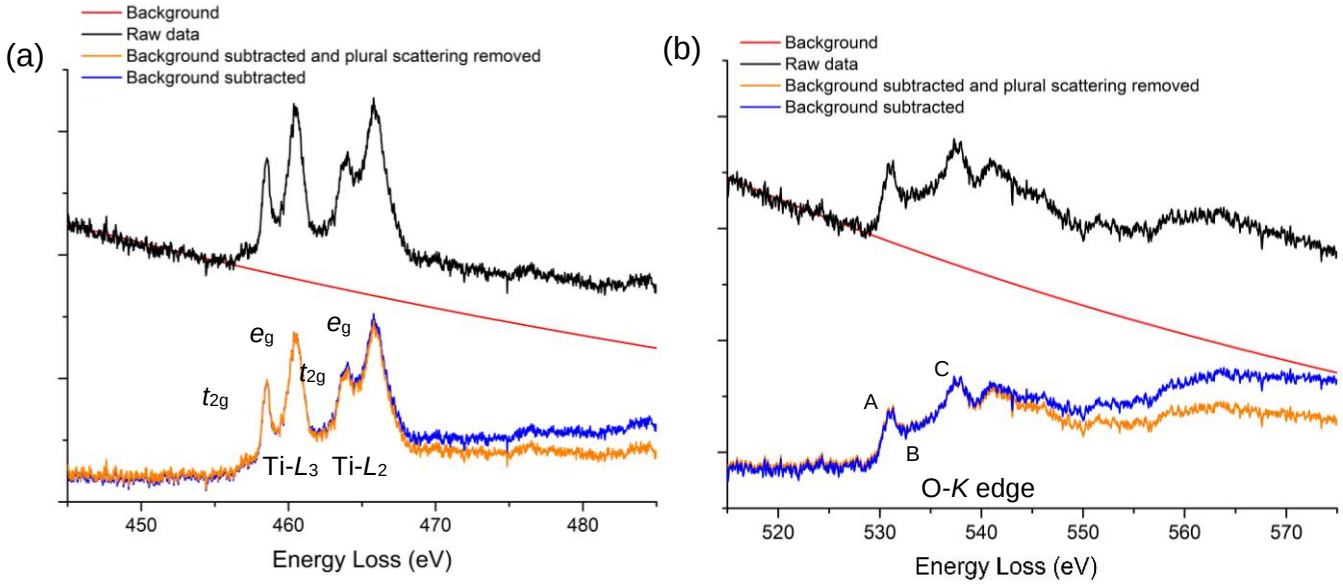

Figure 98. Extracted Ti-$L_{2,3}$ and O-*K* EELS edges from the CT-BT sample at room temperature. (a) The Ti-$L_{2,3}$ edge with the unprocessed EELS edge on a decaying background signal. The raw data is background-subtracted and plural scattering is removed. (b) An O-*K* edge with the unprocessed EELS edge on a decaying background signal. The spectrum is background-subtracted and plural scattering is removed. The near edge features labelled by the letters are referenced in the text.

The titanium-$L_{2,3}$ and oxygen-*K* core-loss edges (Figure 98) are present on a decaying background, which was subtracted by power-law fitting [159]. If the sample is thick (≥100 nm) plural scattering effects can be removed by Fourier

deconvolution using the associated low loss spectra (shown in Figure 29, Chapter 3). Plural scattering effects were relatively negligible on the samples presented here (Figure 98), so they were not applied to the remaining data. The Ti-$L_{2,3}$ experimental data were then fitted with four Gaussian peaks (Figure 104) to determine the peak centre and FWHM of the crystal field features labelled t_{2g} and e_g. The O-*K* edges were only qualitatively analysed with respect to the peak shape (ELNES) features labelled A, B and C in Figure 98 and which are described below.

Each of the characteristic core-loss edges shown in Figure 98 represents energy losses of the incident beam electrons which correspond to excitation of bound electrons from atomic core states or shells (e.g. *K*, *L*, *M*) to a range of unoccupied states above the Fermi level (quantum states 1*s* → 2*p*, 2*p* → 3*d*, correspond to shells *K* and *L* respectively – Figure 30, Chapter 2). Electron energy loss transitions from one quantum state to another follow the dipole selection rule (the change in angular momentum quantum number $\Delta\ell \pm 1$), if the experimental collection angle is sufficiently small (≤ 30 mrad at 200 kV). This rule means that electron transitions from 1*s* → 2*s*, 2*p* → 3*p* or 1*s* → 3*d* quantum states are *not* allowed.

The Ti-$L_{2,3}$ edge (Ti-2*p* → unoccupied states with Ti-3*d* character, Figure 98) shows crystal field splitting of both the Ti-L_3 and Ti-L_2 edges into 4 peaks known as the t_{2g} and e_g antibonding peaks. The separate Ti-L_3 & Ti-L_2 edges occur because the initial Ti-2p state undergoes spin-orbit splitting [98,160].

The O-*K* edge represents a transition from the Oxygen-1*s* orbital to unoccupied states with O-2*p* character [98]. In the $BaTiO_3$ unit cell, the Ti atom is bonded to six surrounding oxygen atoms in an octahedral arrangement (TiO_6^{8-}) and the

Ti-3*d* and O-2*p* orbitals are hybridised resulting in a molecular orbital of mixed character. This results in a O-*K* edge transition from an O-1*s* orbital to an empty hybridised O-2*p*, Ti-3*d* orbital, exhibiting characteristic features similar to the Ti-L_3 edge which correspond to t_{2g} (A) and e_g (B) antibonding orbitals. Feature (C) is related to transitions to states formed from the interaction of O-2*p* states with Ba-5*d* states [1,97,98].

The commercial tetragonal (CT-BT) standard will first be investigated as a tetragonal calibration standard because XRD data indicate it to be phase pure.

5.1 Commercial tetragonal barium titanate (CT-BT)

The X-Ray powder diffraction and Rietveld refinement data suggested that the CT-BT sample was 100 % tetragonal and therefore it was used as a reference tetragonal EEL spectra. To confirm that the commercially purchased sample is phase pure, bright field TEM, electron diffraction and EDX mapping data were collected; Figure 99.

Figure 99 shows a bright field TEM image of CT-BT particles at room temperature and EDX elemental mapping of a CT-BT nanoparticle is shown inset to confirm the sample is barium titanate. The electron diffraction pattern from the large CT-BT particle is also shown.

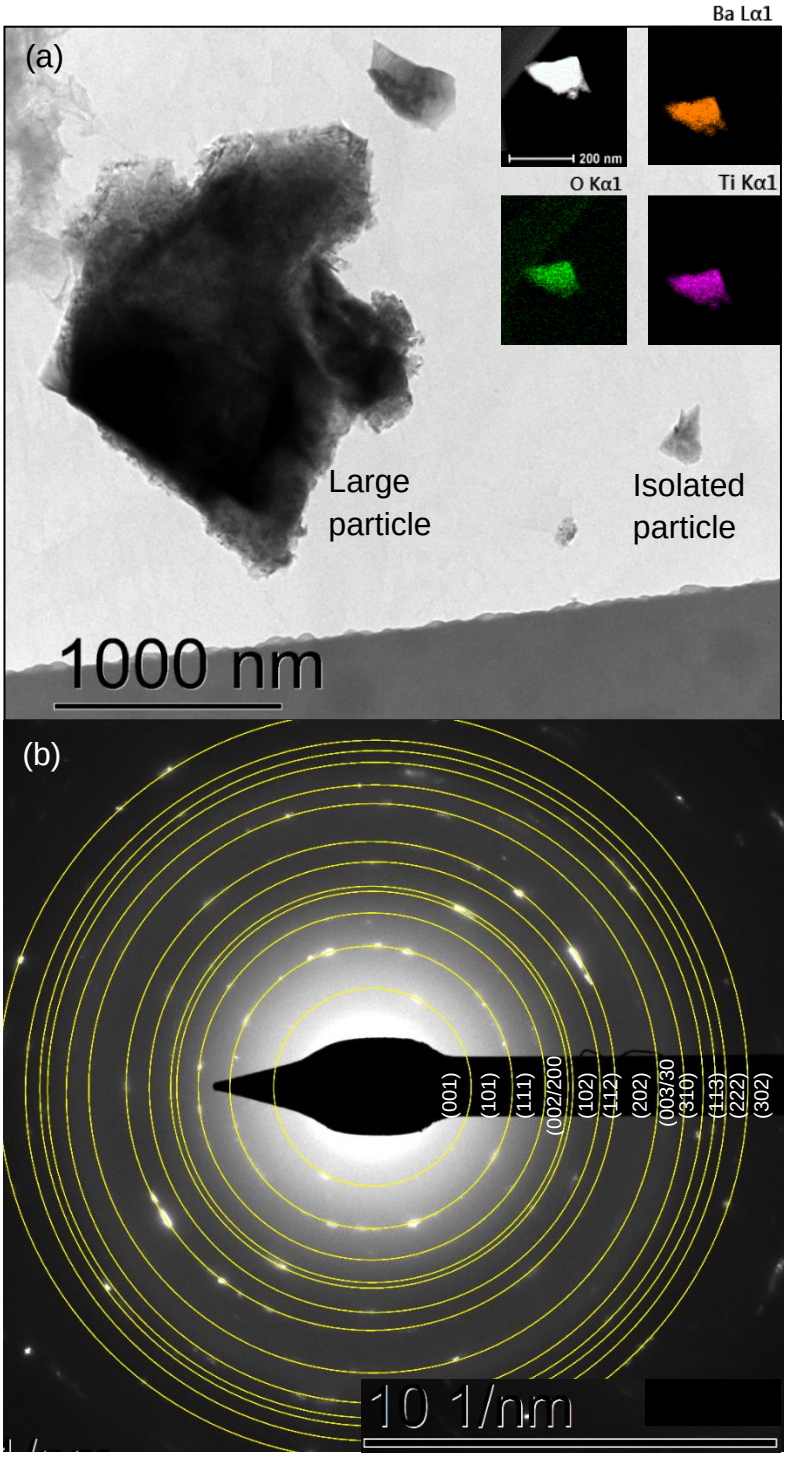

Figure 99. (a) Bright field TEM image of CT-BT particles. The rough appearance of the particle is due to the purchased sample being ground by pestle and mortar, to produce sufficiently thin particle fragments for TEM. (inset) EDX elemental map of a different CT-BT nanoparticle, confirming the presence of elements that compose barium titanate. (b) Electron diffraction pattern collected at room temperature of the large particle shown in (a). The rings shown were referenced against the tetragonal ICDD file: 04-015-2711 (collected below the Curie point); Table 8.

Bright field TEM of an isolated CT-BT nanoparticle (Figure 100) and its electron diffraction pattern was also analysed in Figure 101.

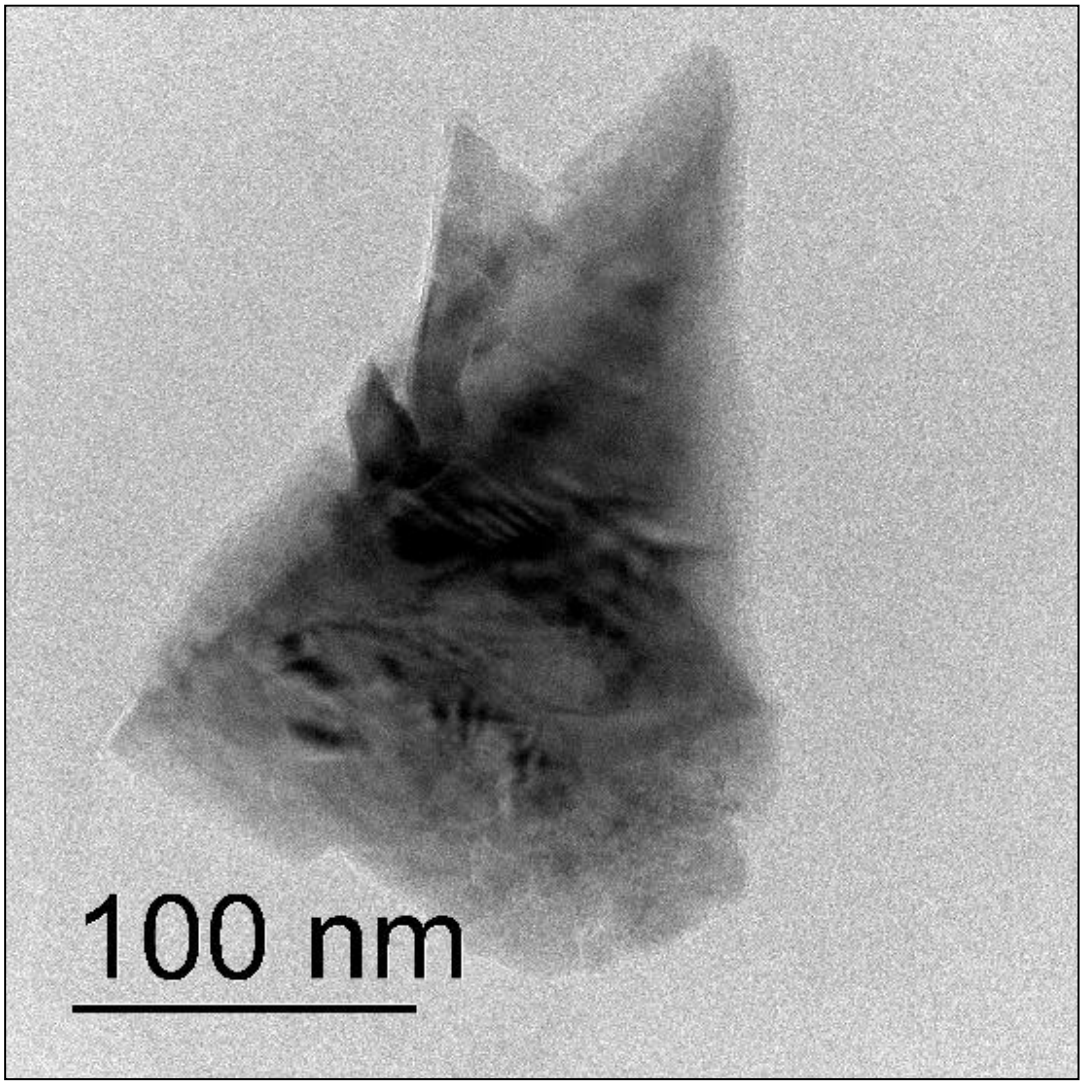

Figure 100. Bright Field TEM image of the isolated CT-BT nanoparticle (in Figure 99) from which electron diffraction and EEL spectra were collected. This image was collected at room temperature (RT).

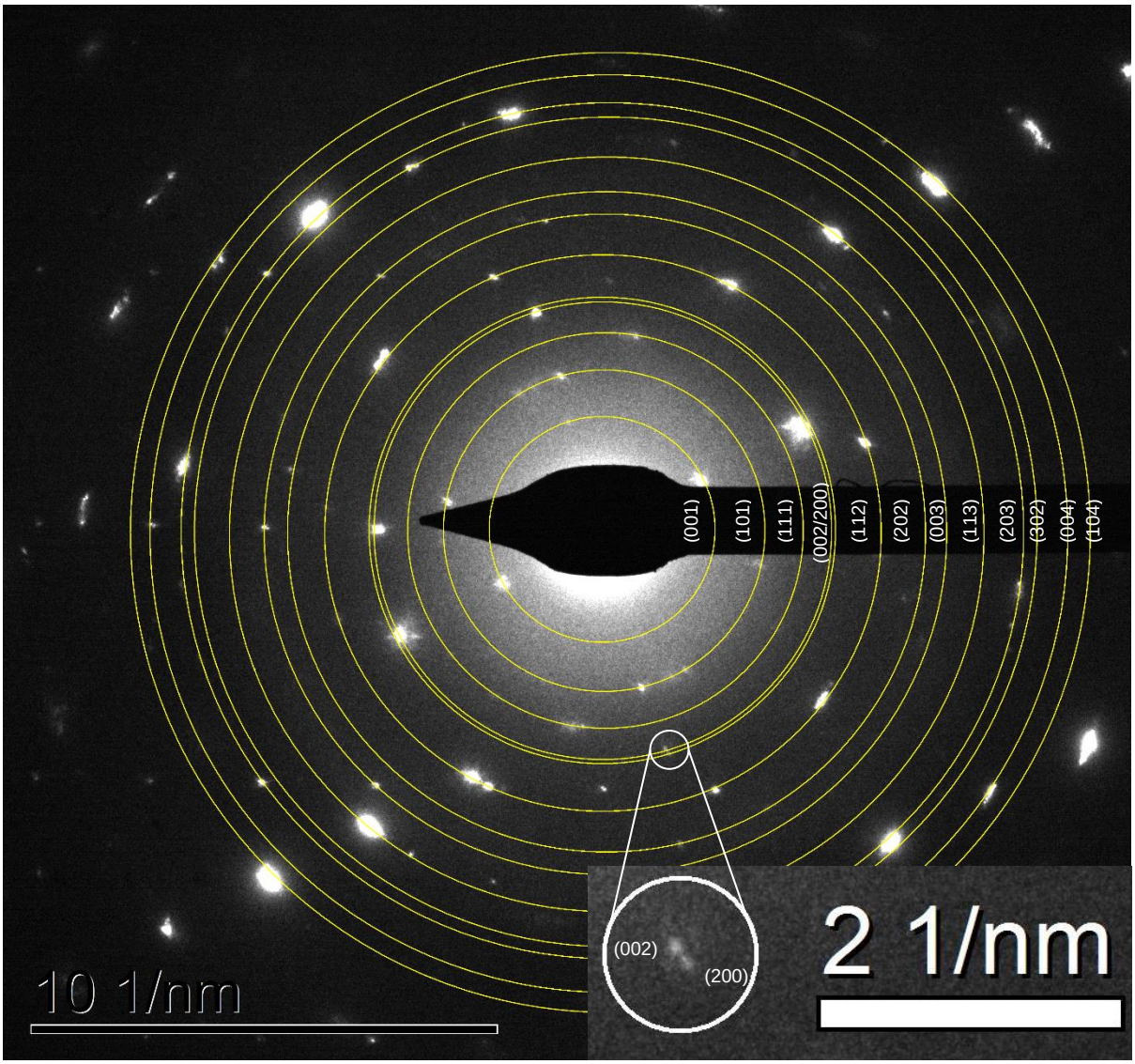

Figure 101. Electron diffraction pattern collected from the polycrystalline isolated nanoparticle collected at room temperature; Figure 100. The rings shown were referenced against the tetragonal ICDD file: 04-015-2711 (Table 10) with the tetragonal (002/200) splitting shown inset.

The electron diffraction data show that the CT-BT sample is tetragonal in agreement with the XRD (laboratory & synchrotron) data summarised in Chapter 4. The CT-BT sample was heated in the microscope (*in-situ*) to 400 ^{o}C (above the Curie point) and was used as a cubic reference standard (Figure 102).

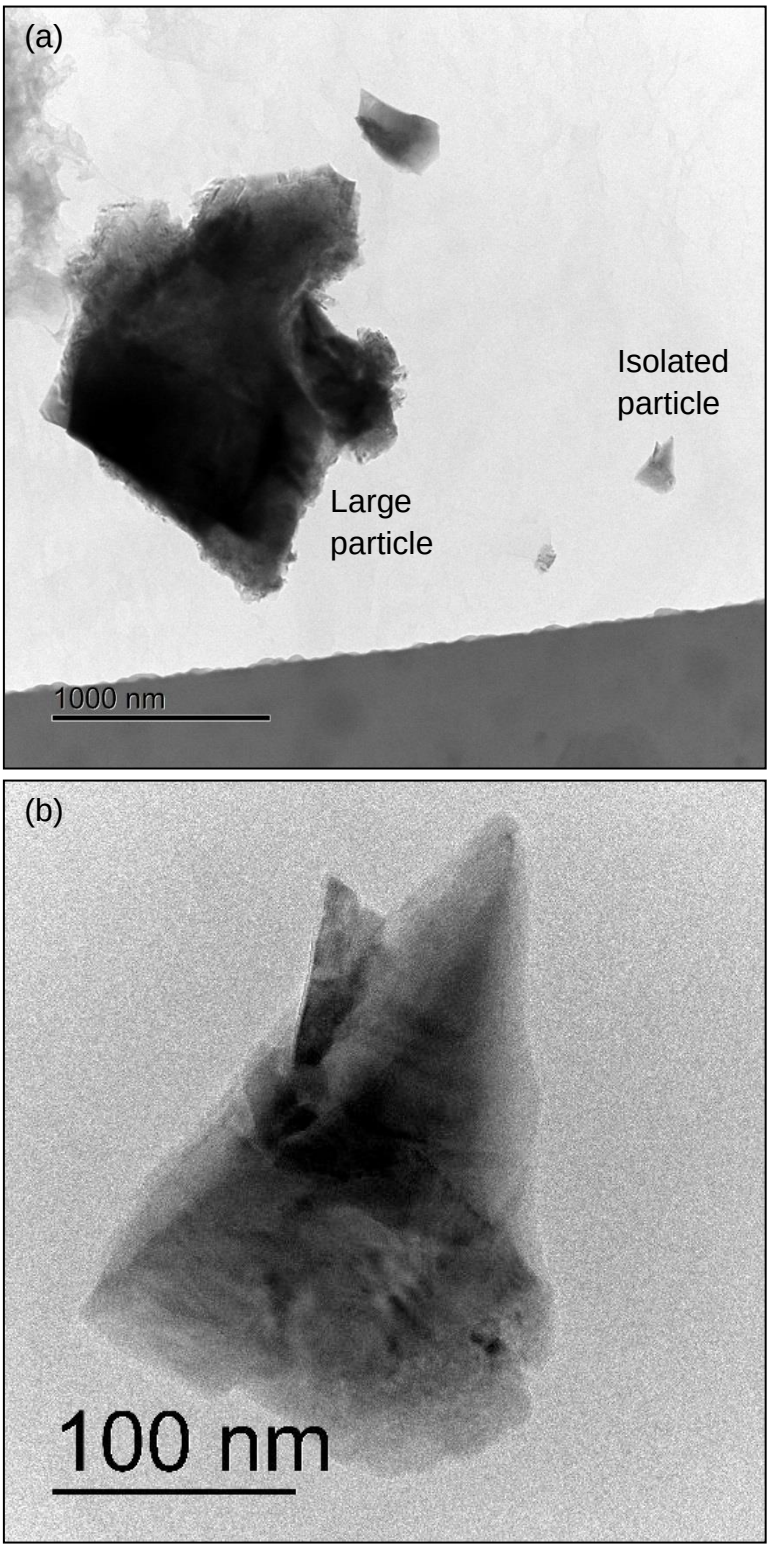

Figure 102. (a) Bright field TEM overview of the same CT-BT nanoparticles at 400 ºC with the copper grid in the foreground. (b) The isolated CT-BT nanoparticle from which EEL spectra were collected at 400 ºC; electron diffraction patterns collected at 400 ºC are shown in Figure 103.

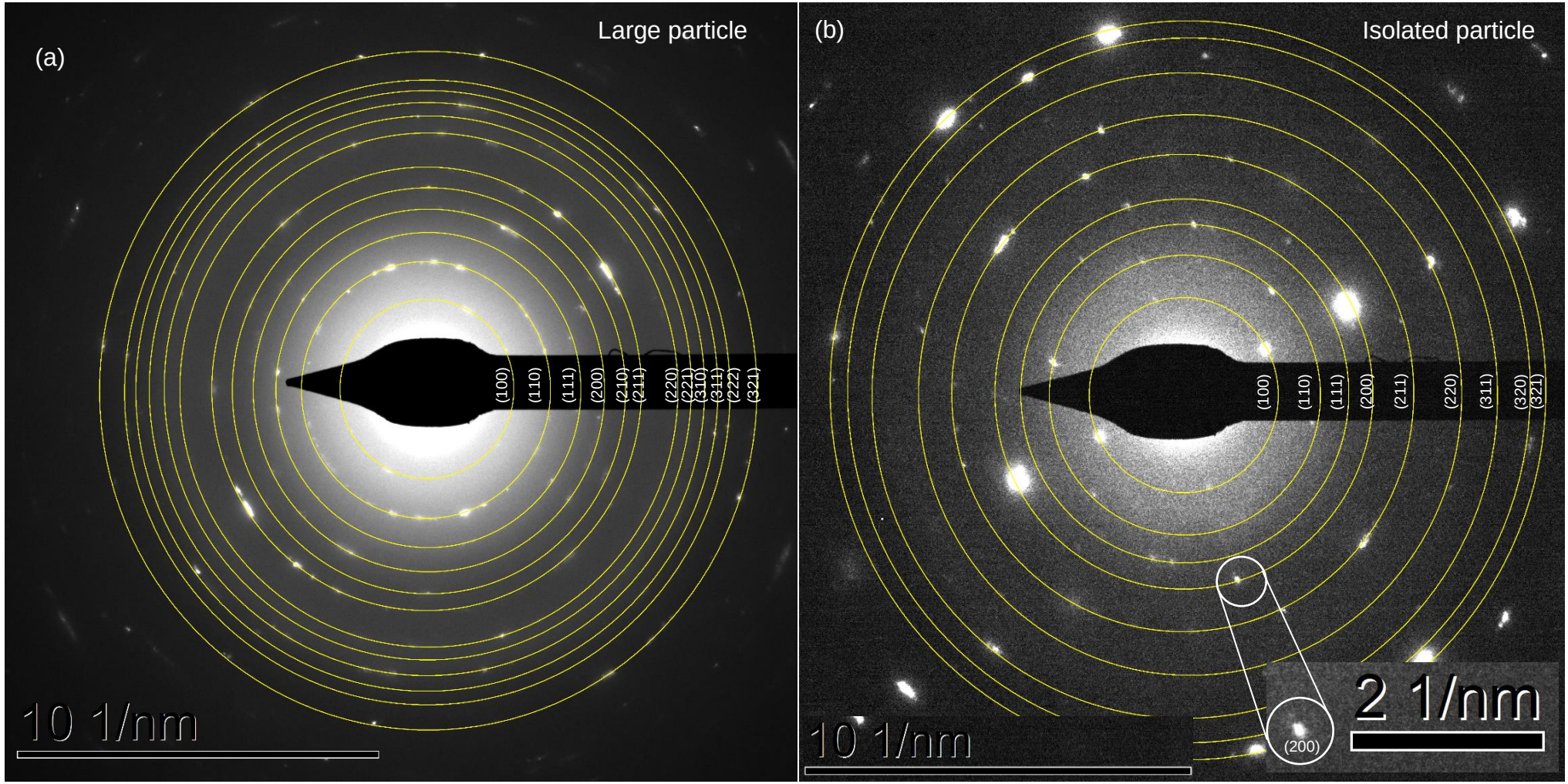

Figure 103. Electron diffraction pattern collected at 400 ºC of (a) the large particle (Table 9), (b) the isolated nanoparticle; Figure 102. The rings were referenced against the cubic ICDD file: 01-078-4475 (Table 11) and the same (200) peak as shown in Figure 101 (inset) highlights that there was no tetragonal splitting.

CT-BT nanoparticle cluster - RT			
Ring number	**Ring radius (1/nm)**	**d-spacing (Å)**	**(hkl)**
1	2.410	4.148	001
2	3.468	2.882	101
3	4.232	2.362	111
4	**4.769**	**2.096**	**002**
5	**4.901**	**2.040**	**200**
6	5.491	1.821	102
7	5.959	1.677	112
8	6.937	1.441	202
9	**7.452**	**1.341**	**003**
10	**7.533**	**1.327**	**300**
11	7.990	1.251	310
12	8.233	1.214	113
13	8.540	1.170	222

Table 8. Electron diffraction data shown in Figure 99 collected from the large CT-BT particle. The d-spacing is referenced against the tetragonal ICDD file and labelled with the (hkl) indices. The tetragonal splitting of the (002)/(200) and (003)/(300) rings are highlighted.

CT-BT nanoparticle cluster – 400 ºC			
Ring number	**Ring radius (1/nm)**	**d-spacing (Å)**	**(hkl)**
1	2.410	4.148	100
2	3.455	2.894	110
3	4.2321	2.362	111
4	4.874	2.051	200
5	5.455	1.832	210
6	5.959	1.677	211
7	6.910	1.447	220
8	7.310	1.367	221
9	7.701	1.298	310
10	8.071	1.238	311
11	8.397	1.190	222
12	9.117	1.096	321

Table 9. Electron diffraction data shown in Figure 103 (a) collected from the large CT-BT-400 ºC particle. The d-spacing is referenced against the cubic ICDD file and labelled with the (hkl) indices. Splitting of the (200) ring is no longer visible, as expected for a cubic phase.

Individual CT-BT nanoparticle - RT			
Ring number	**Ring radius (1/nm)**	**d-spacing (Å)**	**(hkl)**
1	2.43	4.12	001
2	3.46	2.89	101
3	4.25	2.35	111
4	**4.92**	**2.03**	**002**
5	**5.01**	**1.99**	**200**
6	5.98	1.67	112
7	6.86	1.46	202
8	7.34	1.36	003
9	8.11	1.23	113
10	8.91	1.12	203
11	9.20	1.09	302
12	**9.86**	**1.01**	**004**
13	**10.31**	**0.97**	**400**

Table 10. Electron diffraction data shown in Figure 101 collected from the isolated CT-BT nanoparticle. The d-spacing is referenced against the tetragonal ICDD file and labelled with the (hkl) indices. The tetragonal splitting of the (002)/(200) and (004)/(400) rings are highlighted in bold.

Individual CT-BT nanoparticle – 400 ^{o}C			
Ring number	**Ring radius (1/nm)**	**d-spacing (Å)**	**(hkl)**
1	2.45	4.09	100
2	3.51	2.85	110
3	4.24	2.36	111
4	4.89	2.05	200
5	5.98	1.67	211
6	7.02	1.42	220
7	8.09	1.24	311
8	8.83	1.13	320
9	9.26	1.08	321

Table 11. Electron diffraction data shown in Figure 103 (b) collected from the isolated CT-BT-400 ^{o}C nanoparticle. The d-spacing is referenced against the cubic ICDD file and labelled with the (hkl) indices. Splitting of the (200) ring is no longer visible here also, as expected for a cubic phase.

The electron diffraction data collected at room temperature (RT) and 400 ^{o}C were referenced against the modelled tetragonal and cubic $BaTiO_3$ ICDD files: 04-015-2711 and 01-078-4475 respectively.

The room temperature CT-BT electron diffraction patterns from the large and isolated nanoparticles were referenced to a tetragonal diffraction pattern; Figure 99 – Table 8 & Figure 101 – Table 10 respectively; tetragonal splitting of the (002/200) diffraction peaks were evident in both these patterns.

In comparison, the electron diffraction data acquired at 400 ^{o}C (above the Curie point) were referenced to a cubic diffraction pattern for both the large and isolated CT-BT particles; Figure 103 –Table 9 & Table 11 respectively; no tetragonal splitting of the (200) peaks was observed in these patterns.

The electron diffraction data confirmed that the expected phase transition from tetragonal to cubic occurred when the CT-BT sample was heated to 400 ^{o}C i.e. well above the Curie point (of 130 ^{o}C). Therefore, the CT-BT sample was suitable for providing reference tetragonal (RT) and cubic (400 ^{o}C) EEL spectra, and only the EELS data collected from the thinner, isolated particle are discussed herein.

5.1.1 EELS analysis of CT-BT nanoparticles.

An experimental Ti-$L_{2,3}$ core loss edge from the CT-BT sample at room temperature (CT-BT-RT) is shown in Figure 104 with Gaussian fittings to the respective t_{2g}, e_g peaks. Diffraction coupled EELS were collected using a monochromated electron source with an energy resolution of 0.43 eV. The Gaussian fitting uses a least-squares model and peaks were fitted using Gatan Digital Micrograph software (version 2.30) with the EELS plugin.

The Gaussian fitting parameters for the CT-BT-RT sample are summarised in Table 12.

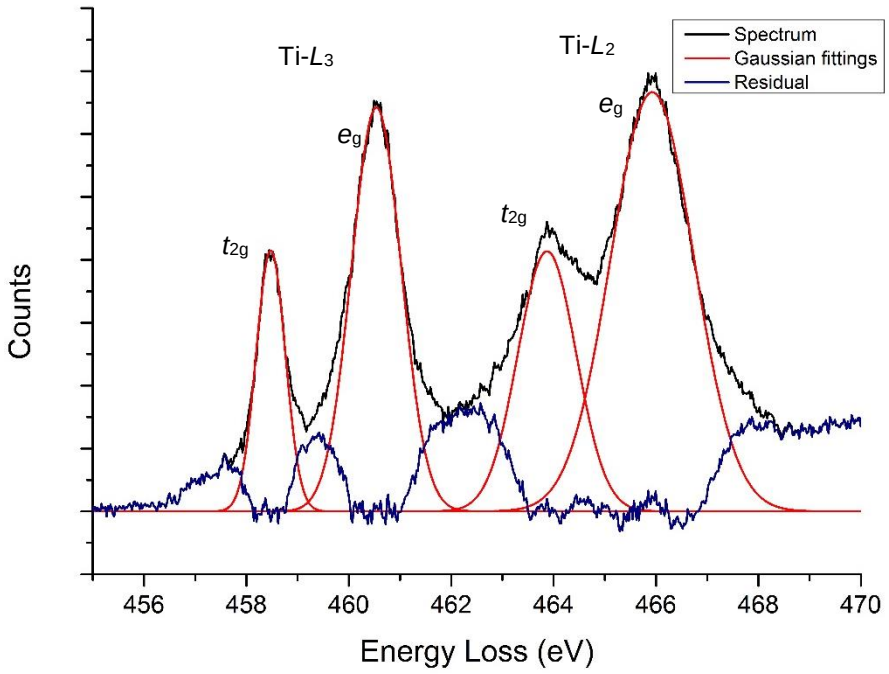

Figure 104. Electron energy loss Ti-$L_{2,3}$ edge acquired at room temperature from an individual CT-BT nanoparticle (Figure 100) that shows the background extracted Ti-$L_{2,3}$ edge (black) with Gaussian fitted peaks underneath the t_{2g} and e_g peaks (red). The residual of the fittings (blue) suggests that at least an additional two peaks could be fitted in between the Ti-L_3 e_g and Ti-L_2 t_{2g} peaks and between the Ti-L_3 t_{2g} and e_g peaks. However, the existing 4 peak fit is sufficient to describe the crystal phase-dependant crystal field splitting of the t_{2g} and e_g peaks.

Gaussian fittings	Ti-L_3 t_{2g}	Ti-L_3 e_g	Ti-L_2 t_{2g}	Ti-L_2 e_g
Gaussian centre (eV)	458.47	460.54	463.87	465.93
e_g-t_{2g} peak separation (eV)	2.07		2.06	
FWHM (eV)	0.67	1.14	1.34	1.91

Table 12. Peak centre and full width half-maximum (FWHM) values of the CT-BT Gaussian peak fit at the Ti-$L_{2,3}$ edge. The peak separation of the t_{2g} and e_g peaks for both edges are shown. The FWHM values of the Gaussian fittings were unconstrained to allow the Gaussian fitting centres to be optimised. These FWHM values were then fixed for subsequent spectral fittings.

The extracted Gaussian fitting data for room temperature CT-BT (Table 12) was used as a reference tetragonal EEL fingerprint. When $BaTiO_3$ is heated above the Curie point of 130 ^oC, (CT-BT-400 ^oC) a phase transition from tetragonal to cubic occurs as evidenced by electron diffraction [22,71]. This phase transition adjusts the Ti-L_3 t_{2g} and e_g peak positions to lower peak separation values [68,93,97].

The Gaussian fitting parameters for CT-BT-RT (Table 12) were then used on the experimental CT-BT-400 ^oC EEL spectrum and the FWHM values fixed and applied to the 400^oC experimental spectrum. The Gaussian centres were unconstrained to adjust to the CT-BT-400^oC experimental data and the Gaussian peak values were extracted to acquire a cubic reference of the Ti-$L_{2,3}$ t_{2g}-e_g peak separation. The Ti-$L_{2,3}$ core loss edge for CT-BT-400 ^oC is shown in Figure 105.

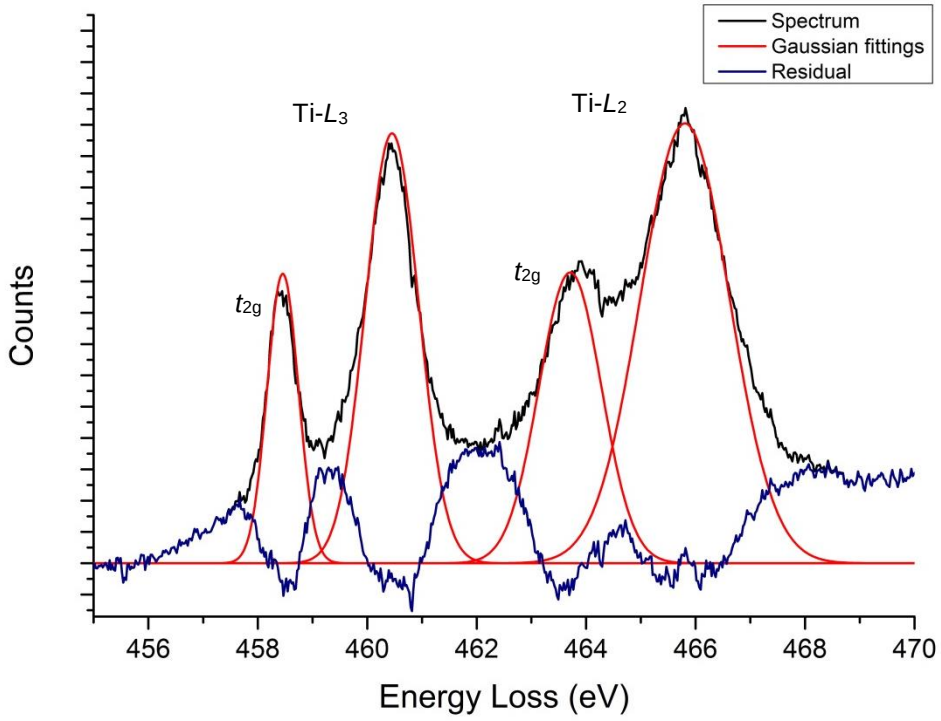

Figure 105. Ti-$L_{2,3}$ edge acquired from the individual CT-BT-400°C nanoparticle. The Gaussian fittings have the FWHM parameters constrained to those of the CT-BT-RT values. The Gaussian peak centres were unconstrained, adjusted to fit the experimental data and are shown in Table 13. The residual fitting is relatively poor on both t_{2g} and e_g peaks.

Gaussian fittings	Ti-L_3 t_{2g}	Ti-L_3 e_g	Ti-L_2 t_{2g}	Ti-L_2 e_g
Gaussian centre (eV)	458.46	460.45	463.71	465.81
e_g-t_{2g} peak separation (eV)	2.00		2.10	
FWHM (eV)	0.67	1.14	1.34	1.91

Table 13. Gaussian peak centres and full width half-maximum (FWHM) values of the fit to the Ti-$L_{2,3}$ edge from the CT-BT-400 °C nanoparticle. The FWHM values were constrained to the model from the room temperature CT-BT fitting parameters (Table 12).

Figure 105 shows a poor residual after Gaussian fitting of the Ti-$L_{2,3}$ t_{2g} and e_g peaks of CT-BT-400ºC using the FWHMs derived from CT-BT-RT peaks (Figure 104). Suggesting that a phase transition from tetragonal to cubic $BaTiO_3$ has occurred [20,73].

The CT-BT-400ºC EEL spectrum is used later as a cubic standard and therefore the Gaussian fitting parameters were re-applied, unconstrained by those of the CT-BT-RT fitting parameters; Figure 106.

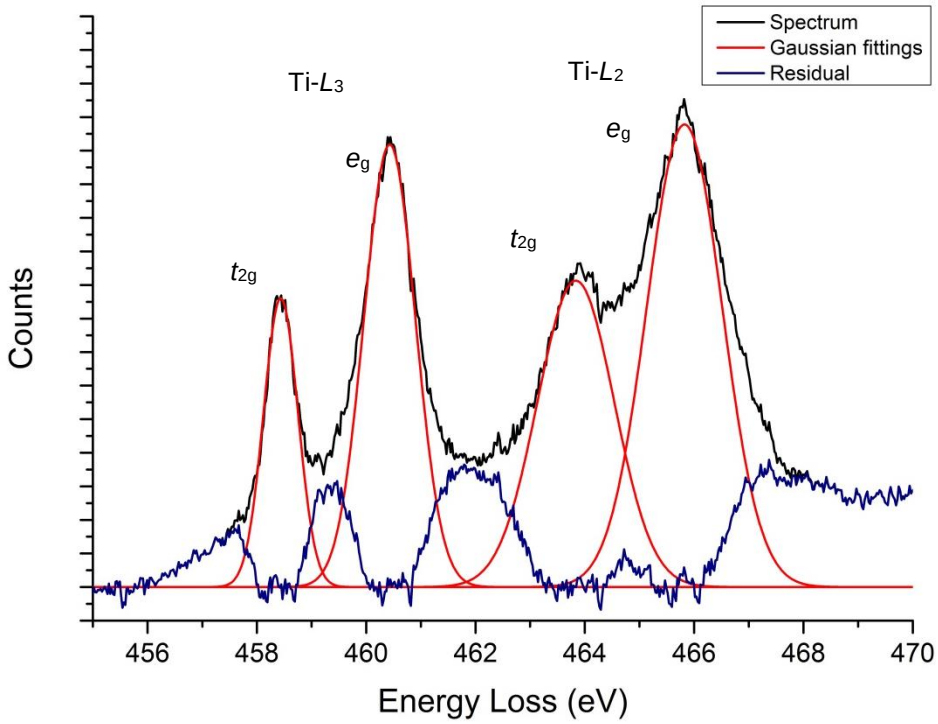

Figure 106. Ti-$L_{2,3}$ EELS edge of the individual CT-BT-400 ºC nanoparticle. The Gaussian fittings were completely unconstrained from those of room temperature CT-BT sample. A residual fit similar to that obtained for the CT-BT-RT Gaussian fitting is now evident.

Gaussian fittings	Ti-L_3 t_{2g}	Ti-L_3 e_g	Ti-L_2 t_{2g}	Ti-L_2 e_g
Gaussian centre (eV)	458.44	460.43	463.84	465.83
e_g-t_{2g} peak separation (eV)	1.99		1.99	
FWHM (eV)	0.74	1.11	1.65	1.62

Table 14. Gaussian fitting parameters of CT-BT-400 ºC that are independent of RT CT-BT, showing the Gaussian centre and FWHM values of the Gaussian fittings for the respective Ti-$L_{2,3}$ edges. The peak separation of t_{2g} and e_g peaks for both Ti-*L* edges are shown.

A comparison of the CT-BT and CT-BT-400 ºC Gaussian fitting parameters are summarised in Table 15.

Gaussian fitting	Ti-L_3 t_{2g} (eV)	Ti-L_3 e_g (eV)	e_g-t_{2g} peak separation (eV)	Ti-L_2 t_{2g} (eV)	Ti-L_2 e_g (eV)	e_g-t_{2g} peak separation (eV)
RT	458.47	460.54	**2.07**	463.87	465.93	**2.06**
400 ºC	458.44	460.43	**1.99**	463.84	465.83	**1.99**

Table 15. Comparison of the CT-BT Ti-$L_{2,3}$ edges at room temperature (RT) and 400 ºC. The t_{2g}-e_g peak separations for the EEL spectra acquired at 400 ºC are reduced for the Ti-$L_{2,3}$ edge when compared to the spectra collected at RT (highlighted columns). This reduction in Ti-$L_{2,3}$ t_{2g}-e_g peak separation has also been shown in other research published by Bugnet *et al.* [68]**.**

A visual comparison of the Ti-$L_{2,3}$ t_{2g} and e_g peaks for the RT and 400 ºC spectra are shown in Figure 107 and for the O-*K* edge in Figure 107.

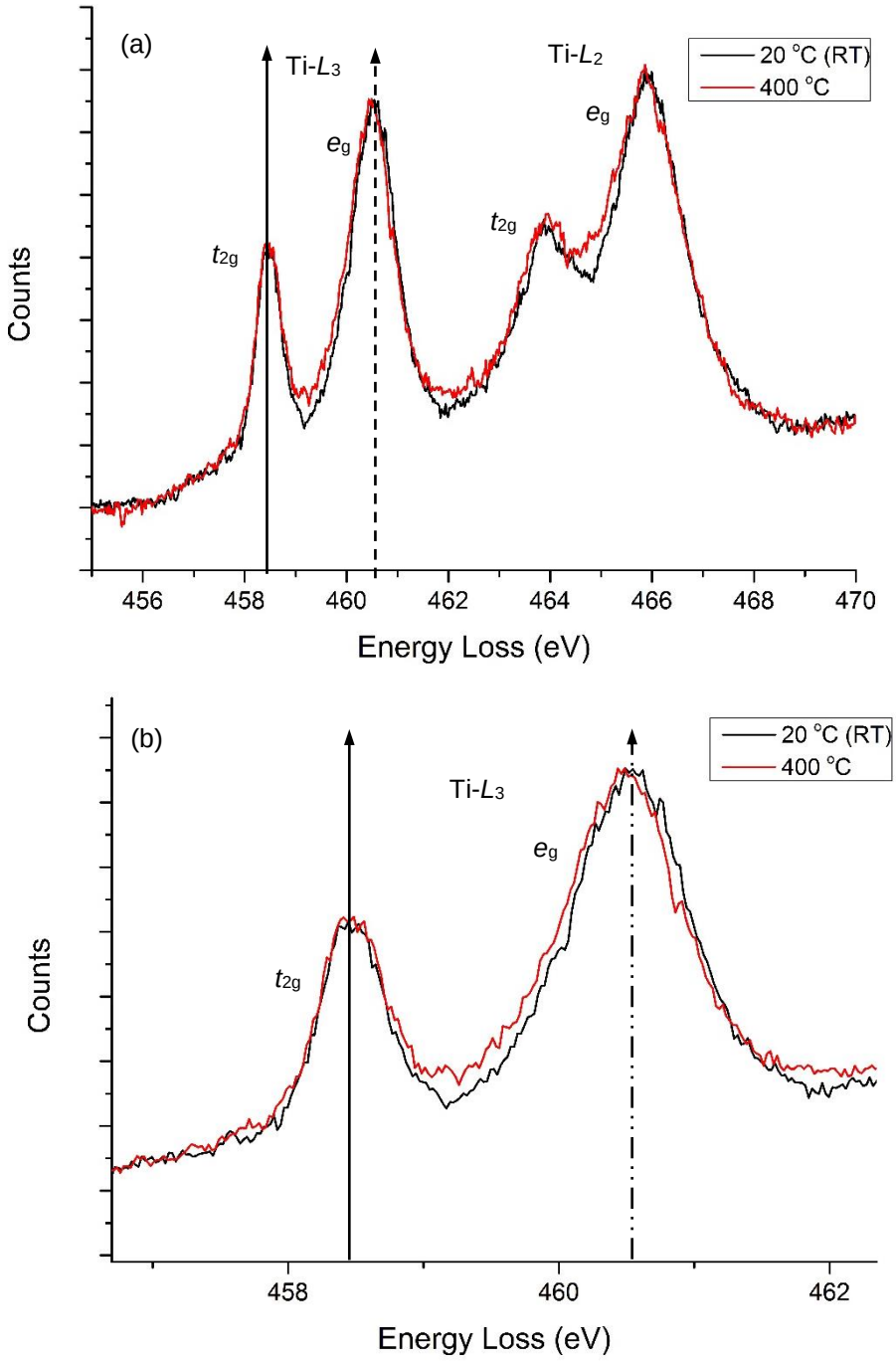

Figure 107. Comparison of Ti-$L_{2,3}$ t_{2g} and e_g peaks for CT-BT at room temperature (black) and 400 °C (red). The spectra are aligned to absolute edge energies from the zero loss peak. (a) Showing both the Ti-L_3 and Ti-L_2 edges and (b) showing just the Ti-L_3 t_{2g} and e_g peaks to highlight the marginal difference in peak splitting. The dashed line is aligned to the RT Ti-L_3 e_g peak maxima highlighting the small shift to lower energy for the e_g peak at 400 °C.

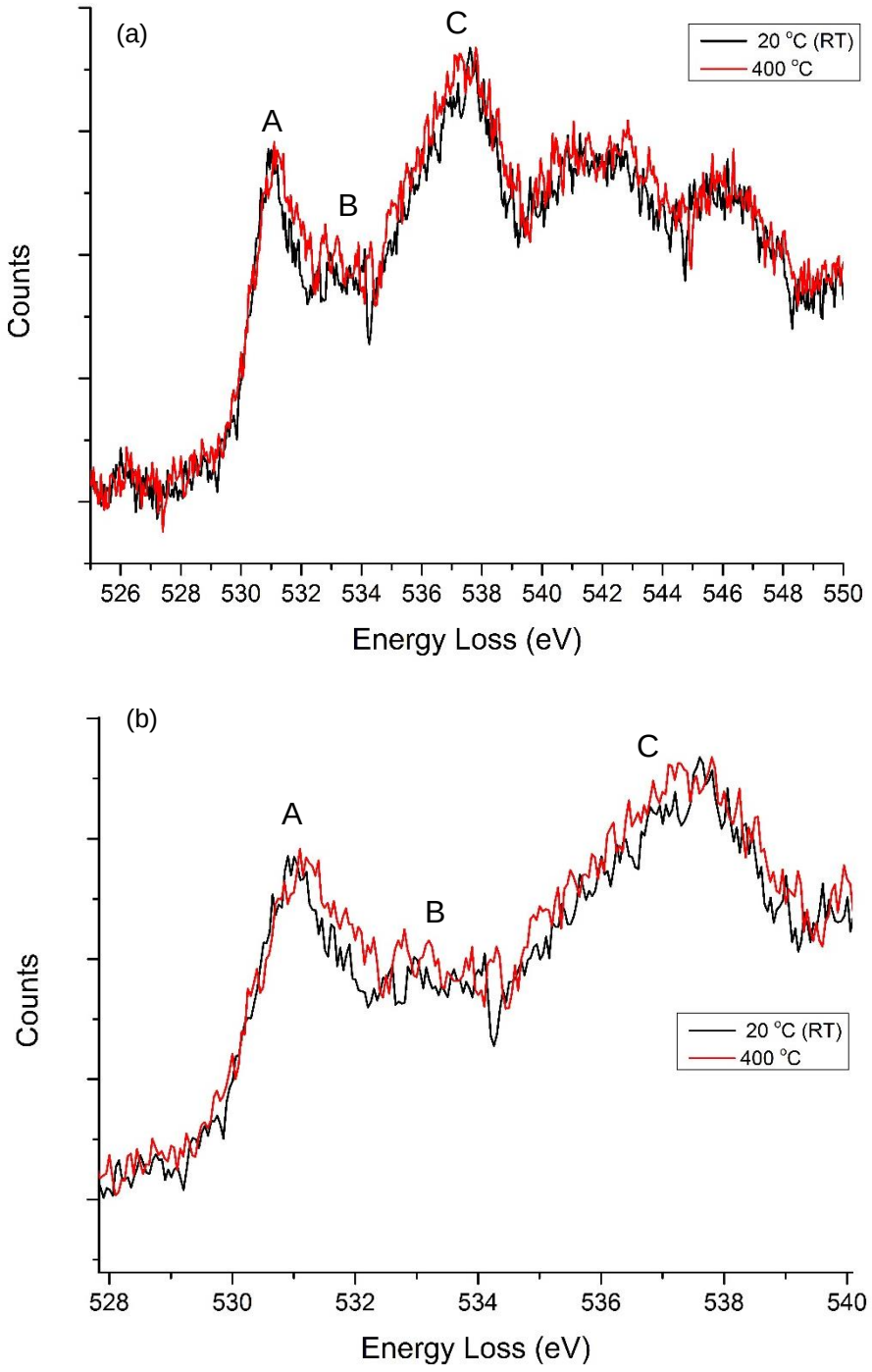

Figure 108. Experimental O-*K* core loss edges at room temperature (black) and 400 ºC (red). The spectra are aligned to absolute edge energies from the zero-loss peak. (a) The letters indicate the key features of the spectra that relate to the hybridised O-2*p* and Ti-3*d* states split into t_{2g} (A) and e_g (B) with feature (C) relating to the O-2*p* and Ba-5*d* states. (b) The magnified O-*K* edge shows a difference in CT-BT-400 ºC A and B peak positions compared to the RT spectrum.

The EEL spectra of the CT-BT nanoparticle collected at RT and 400 ^{o}C showed a repeatable difference in the separation of the Ti-$L_{2,3}$ t_{2g} and e_g peaks (Figure 107 – Table 15). In this experiment, the EELS data were collected 270 ^{o}C above the Curie temperature in order to account for any heat loss or heat dissipation of the support film of the DensSolutions wildfire chip.

The Ti-$L_{2,3}$ core loss edges are associated with the excitation to hybridised Ti-3*d* –O-2*p* antibonding molecular orbitals (Figure 30; Chapter 2). When CT-BT is heated to 400 ^{o}C, there is a reduction in the t_{2g}-e_g peak splitting. This implies there is a change in the unit cell parameters and in particular the change in the Ti-O bond lengths. Shorter bond lengths should increase the t_{2g}-e_g splitting and (the tetragonal titanium offset to an oxygen anion) and transformation to the cubic phase will reduce the t_{2g}-e_g splitting, due to all bond lengths becoming equal (discussed further in Chapter 7). The O-*K* edges of the CT-BT sample collected at RT and 400 ^{o}C (Figure 108) show a shift in the positions of peak maxima and broader peaks for both ‘A’ and ‘B’ features which are attributed to the hybridized O-2*p* and Ti-3*d* t_{2g} and e_g antibonding orbitals respectively.

The t_{2g}-e_g peak splitting at the Ti-$L_{2,3}$ edge was quantified by fitting Gaussians peaks to the experimental data (Table 15). This core loss edge was investigated for the H-BT sample using STEM-EELS linescans at room temperature and 400 ^{o}C. The fitting of Gaussian peaks to the Ti-$L_{2,3}$ edge across the nanoparticle could indicate whether the nanoparticle phases are tetragonal or cubic and whether there is an *inter*- or *intra*-particle phase distribution. The O-*K* edge was qualitatively investigated across a nanoparticle using STEM-EELS by observing the peak shape across the nanoparticle (at RT and 400 ^{o}C).

5.1.2 Hydrothermal Barium Titanate (H-BT)

EELS analysis of H-BT nanoparticles (Figure 109) was conducted using the FEI Titan Themis microscope at RT and 400 ^{o}C. HAADF-STEM EELS linescans had an energy resolution of 0.40 eV using a monochromated electron source. Similar to the CT-BT sample, the crystal structure of the H-BT nanoparticles was first investigated by electron diffraction.

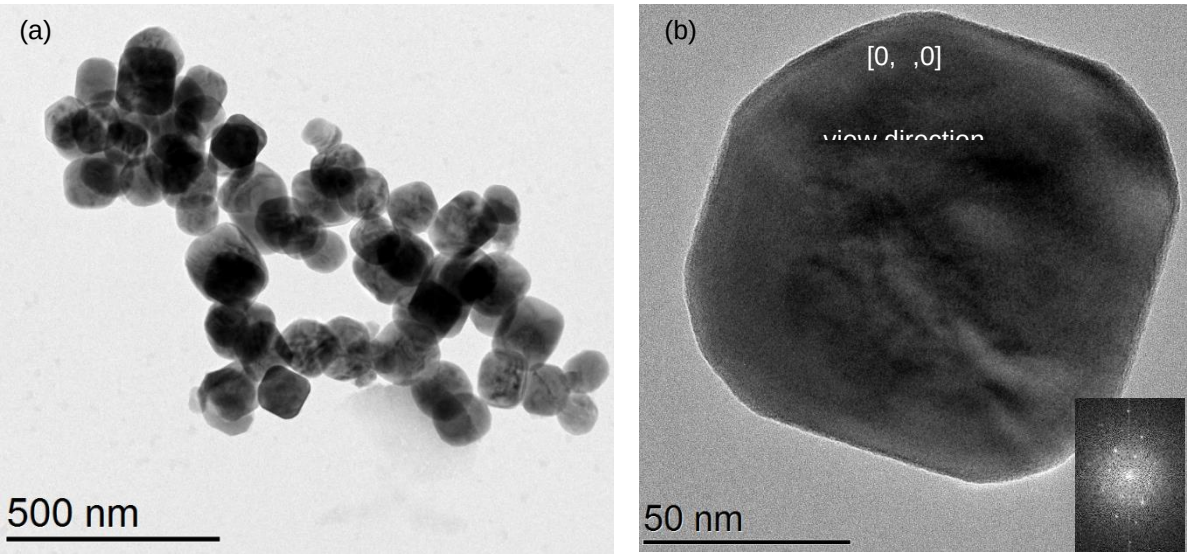

Figure 109. (a) Bright field TEM image of agglomerated H-BT nanoparticles. (b) Bright field TEM image of an isolated H-BT nanoparticle used for STEM-EEL spectroscopy. The single crystal particle is being view down the [0,,0] direction.

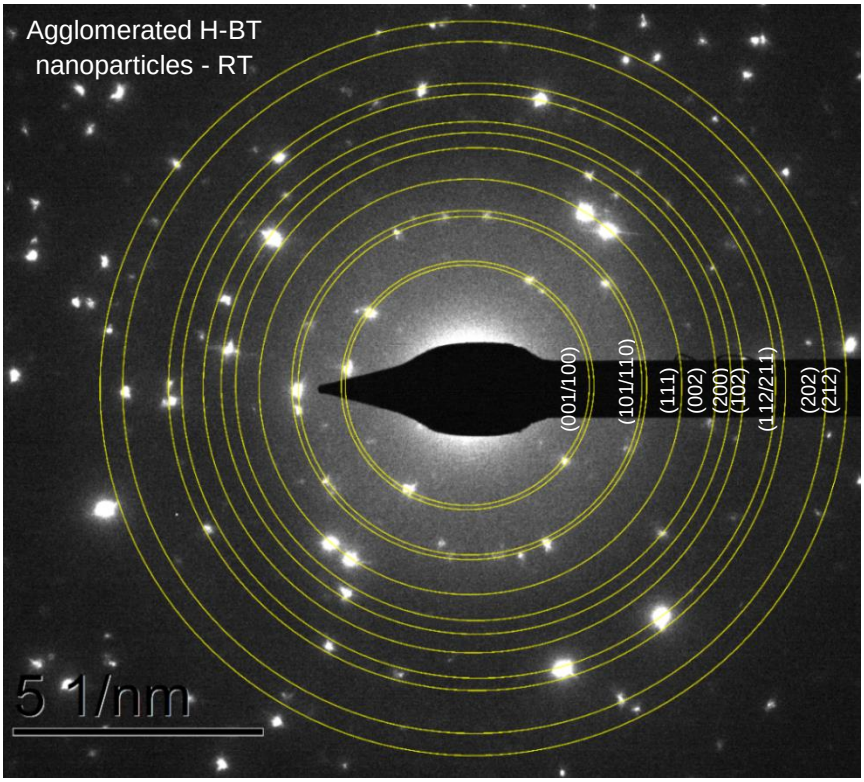

Figure 110. Electron diffraction pattern of agglomerated H-BT nanoparticles at RT shown in Figure 109, highlighting tetragonal reflections labelled with the (hkl) indices; Table 16.

Agglomerated H-BT nanoparticles – RT			
Ring number	**Ring radius (1/nm)**	**d-spacing (Å)**	**(hkl)**
1	2.45	4.08	***001***
2	2.54	3.94	***100***
3	3.45	2.89	***101***
4	3.56	2.81	***110***
5	4.24	2.35	111
6	**4.83**	**2.07**	***002***
7	**5.12**	**1.95**	***200***
8	5.42	1.85	102
9	5.96	1.67	***112***
10	6.20	1.61	***211***
11	7.06	1.42	202
12	7.49	1.34	212

Table 16. Electron diffraction data of agglomerated H-BT nanoparticles collected at RT (Figure 110). The d-spacing is referenced against the tetragonal ICDD file and labelled with the (hkl) indices. A (002/200) peak splitting is clearly evident.

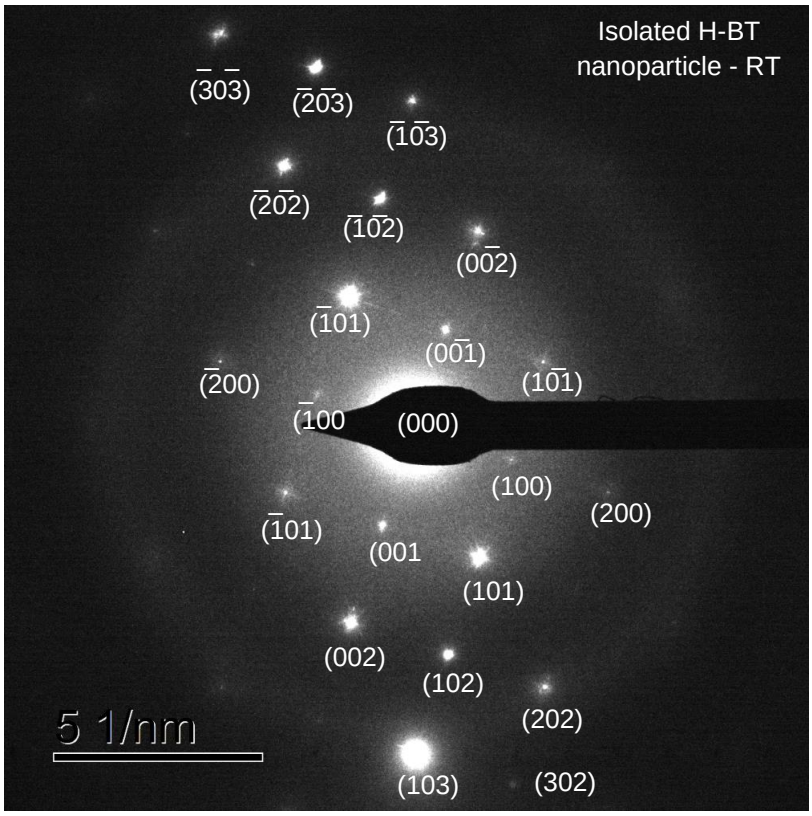

Figure 111. Electron diffraction pattern of the isolated H-BT nanoparticle at RT shown in Figure 109, highlighting reflections labelled with the tetragonal (hkl) indices in Table 17.

Isolated H-BT nanoparticle – RT		
Ring radius (1/nm)	**d-spacing (Å)**	**(hkl)**
2.48	4.03	100
2.50	4.00	001
3.34	2.99	101
4.92	2.03	**002**
4.96	2.01	**200**
5.55	1.80	102
7.04	1.42	202
7.85	1.27	103

Table 17. Electron diffraction data of the isolated H-BT nanoparticle at RT (Figure 111). The d-spacing is referenced against the tetragonal ICDD file and labelled with the (hkl) Miller indices to the tetragonal phase. Specific (002) and (200) spots are visible in this zone, (002/200) tetragonal splitting is identified in this orientation (and the pattern is therefore distinguishable from the cubic phase).

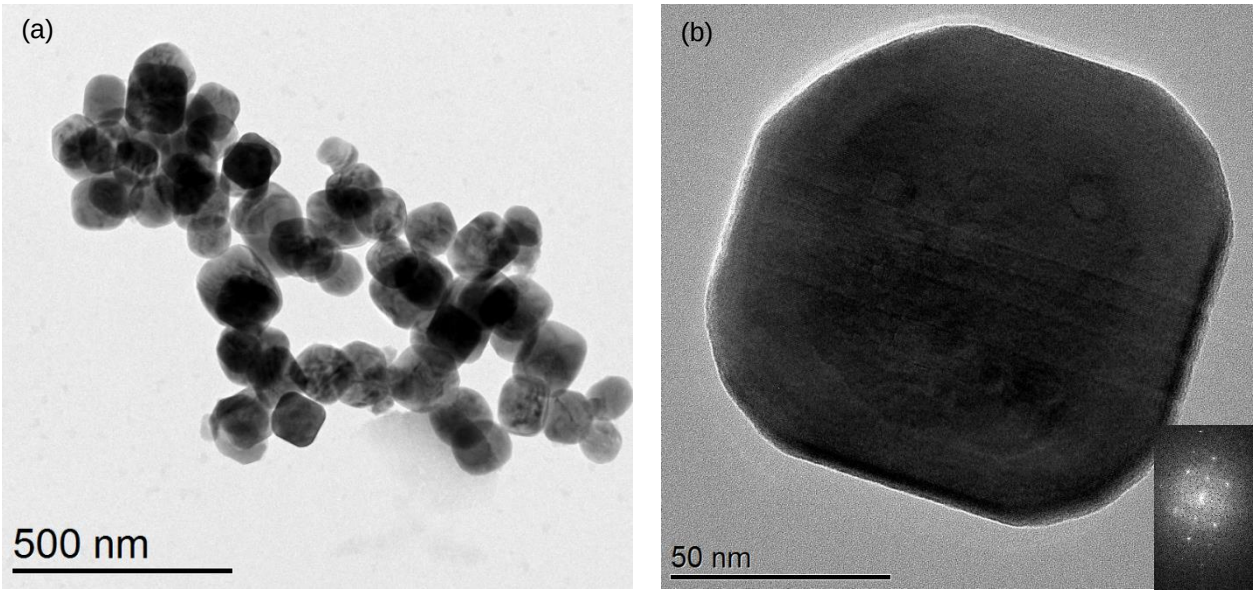

Figure 112. (a) Bright field TEM image of the agglomerated H-BT nanoparticles now imaged at 400 ºC. (b) Bright field TEM image of the individual H-BT nanoparticle collected at 400 ºC after STEM-EELS linescans. The crystal is still being view down the [0,-1,0] direction.

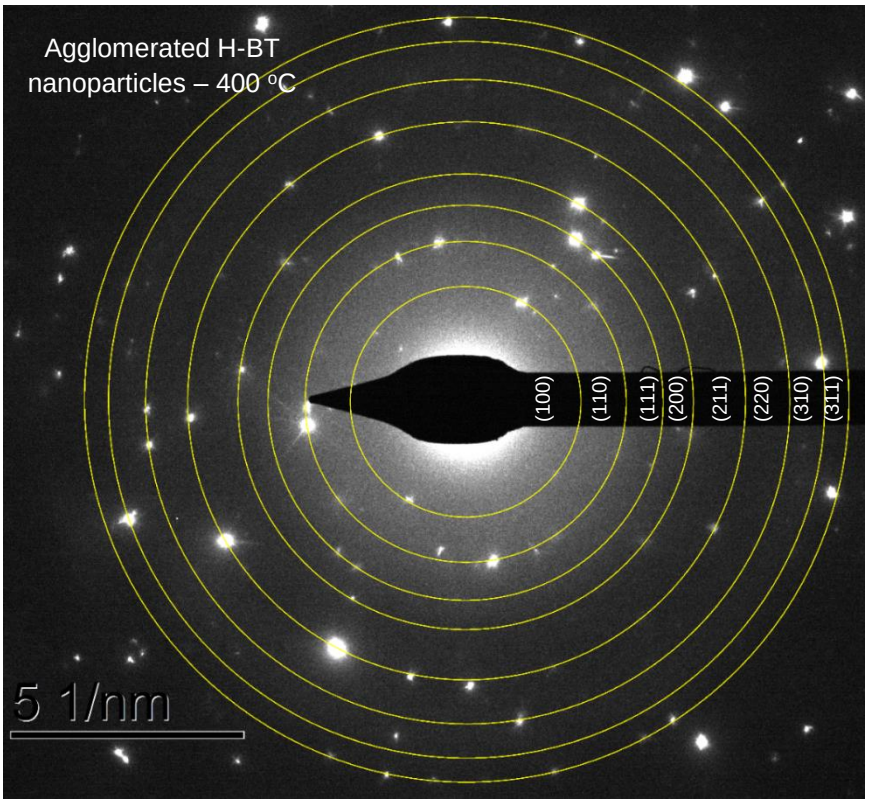

Figure 113. Electron diffraction pattern of H-BT agglomerated nanoparticles at 400 ºC (Figure 112), highlighting cubic reflections labelled with the (hkl) indices in Table. i.e. splitting of (002) reflections are no longer visible.

Agglomerated H-BT nanoparticles – 400 ºC			
Ring number	**Ring radius (1/nm)**	**d-spacing (Å)**	**(hkl)**
1	2.45	4.02	100
2	3.45	2.89	101
3	4.25	2.35	111
4	4.90	2.04	200
5	6.00	1.67	211
6	6.93	1.44	220
7	7.71	1.29	310
8	8.23	1.22	311

Table 18. Electron diffraction data of the agglomerated H-BT nanoparticles at 400 ºC (Figure 113). The d-spacing is referenced against the cubic ICDD file and labelled with the (hkl) indices.

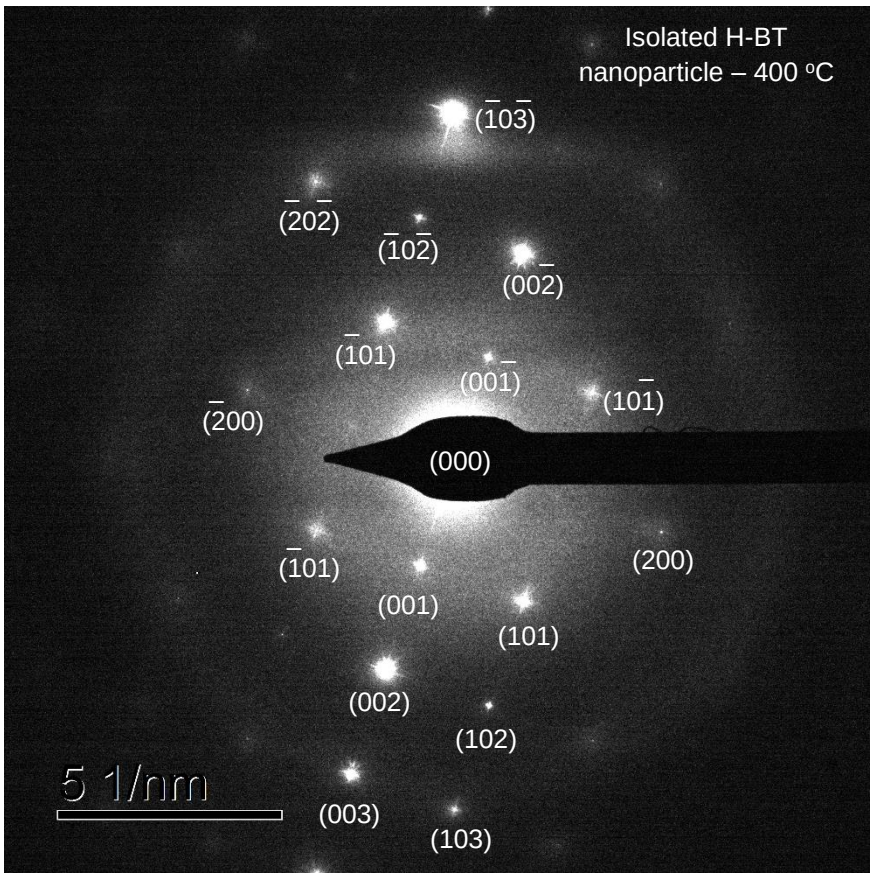

Figure 114. Electron diffraction pattern of the individual H-BT nanoparticle at 400 ºC (Figure 112). The crystal is now presumed to be cubic because the [0,-1,0] orientation does not reveal tetragonal splitting; albeit the (002/200) are shown, they are the same spacing as each other. The labelled (hkl) reflections shown in Table 19.

Isolated H-BT nanoparticle – 400 ºC			
Ring number	**Ring radius (1/nm)**	**d-spacing (Å)**	**(hkl)**
1	2.49	4.01	001
2	3.48	2.87	101
3	4.90	2.04	002
4	4.90	2.04	200
5	5.51	1.81	102
6	7.08	1.41	202
7	7.79	1.28	103

Table 19. Electron diffraction data of the individual H-BT nanoparticle at 400 ºC (Figure 113). The d-spacing is referenced against the cubic ICDD file and labelled with the (hkl) indices. The (200) and (002) reflections are shown to be the same (within error) after heating to 400 ºC.

The electron diffraction of agglomerated nanoparticles (Figure 110) shows tetragonal crystal structure reflections in the random orientation of nanoparticles. The individual H-BT nanoparticle electron diffraction pattern shows the tetragonal (002/200) splitting at room temperature and upon heating to 400 ºC the (200) and (002) reflections assume the same d-spacing; thus suggests the particle is tetragonal as XRD (laboratory and synchrotron) analysis shows a tetragonal phase fraction is present. The H-BT nanoparticles evidently became cubic at 400 ºC as shown by the hot stage XRD (Chapter 4).

STEM-EELS of the H-BT nanoparticle was collected using the Titan Themis microscope. The monochromated electron source has a 0.40 eV energy resolution and the EELS data were initially extracted from a full spectrum image (Figure 62, Chapter 3) and then at each pixel to determine the *intra*-particle phase distribution. The H-BT EELS data were initially fitted with the CT-BT Gaussian peak centres and FWHM peak fitting parameters however this produced a poor fit for the Ti-L_3 t_{2g} and e_g peaks, as shown by the residuals in

Figure 115. The Ti-$L_{2,3}$ edges were then fitted unconstrained Gaussian peak positions and peak widths and compared to the CT-BT reference sample.

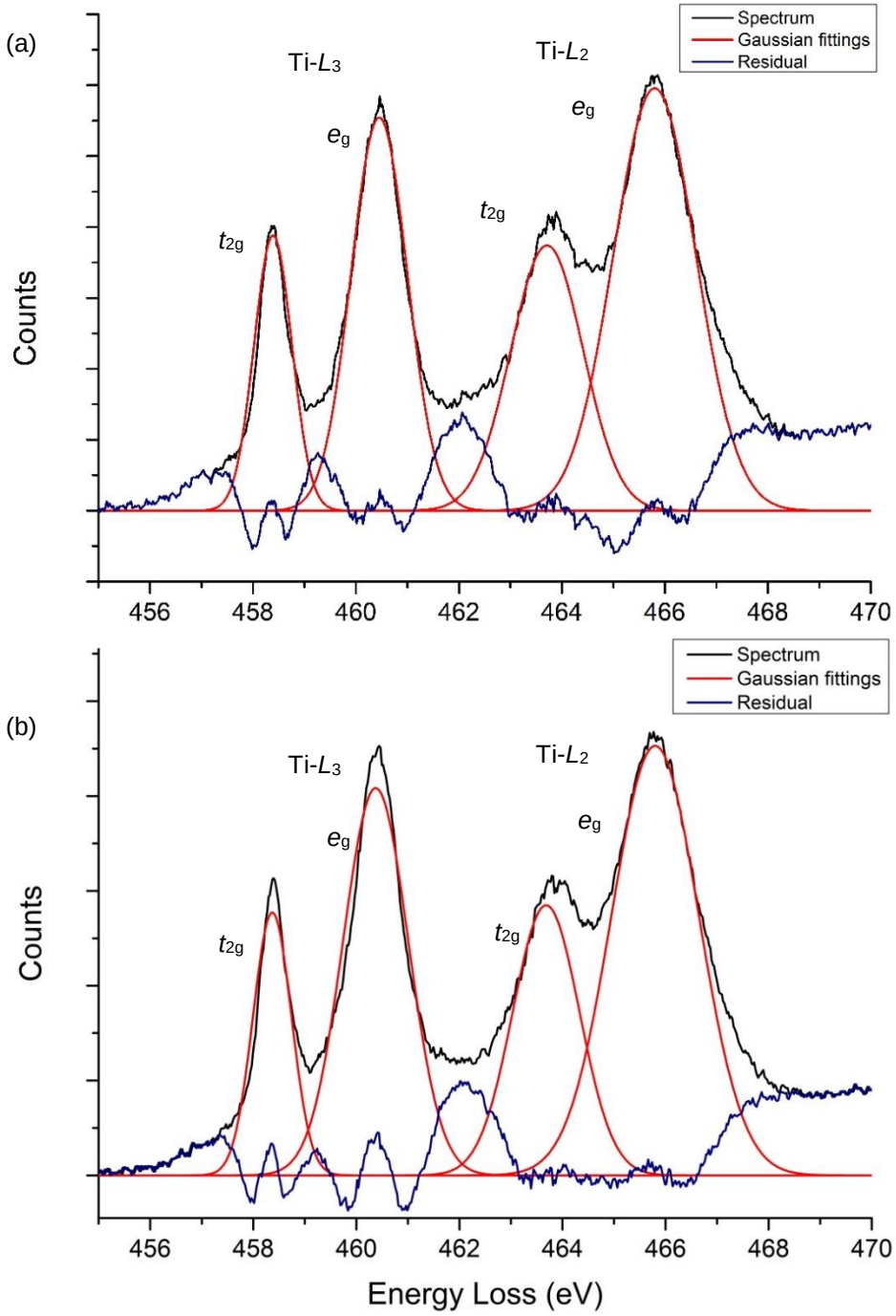

Figure 115. The H-BT Ti-$L_{2,3}$ EEL spectrum acquired at room temperature. The Gaussian fits used (a) the previously determined CT-BT Gaussian fitting parameters and (b), the previously determined CT-BT-400 ºC Gaussian fitting parameters. The residuals to both fits are poor.

Figure 115 shows The H-BT EEL spectrum with the CT-BT and CT-BT-400 ^{o}C Gaussian fitting parameters applied as model tetragonal and cubic EEL spectra respectively. Neither the tetragonal (CT-BT) nor the cubic (CT-BT-400^{o}C) reference Gaussian fitting parameters produced a good residual fit to the H-BT Ti-L_3 edge and t_{2g} and e_g peaks. Thus we can conclude that the existing CT-BT and CT-BT-400 ^{o}C Gaussian fitting parameters are unsuitable for phase determination of the H-BT material. The Gaussian fits were then repeated without prior constraints on fitting parameters (Figure 116); this produced a significantly better fit. The independent Gaussian fitting parameters of H-BT are summarised in Table 20, which lists the Gaussian centre and FWHM values for the respective Ti-$L_{2,3}$ edges. The peak separation of the t_{2g} and e_g peaks for both Ti-*L* edges are shown and are compared to the CT-BT, CT-BT-400 ^{o}C and H-BT-400 ^{o}C Gaussian parameters in Table 22.

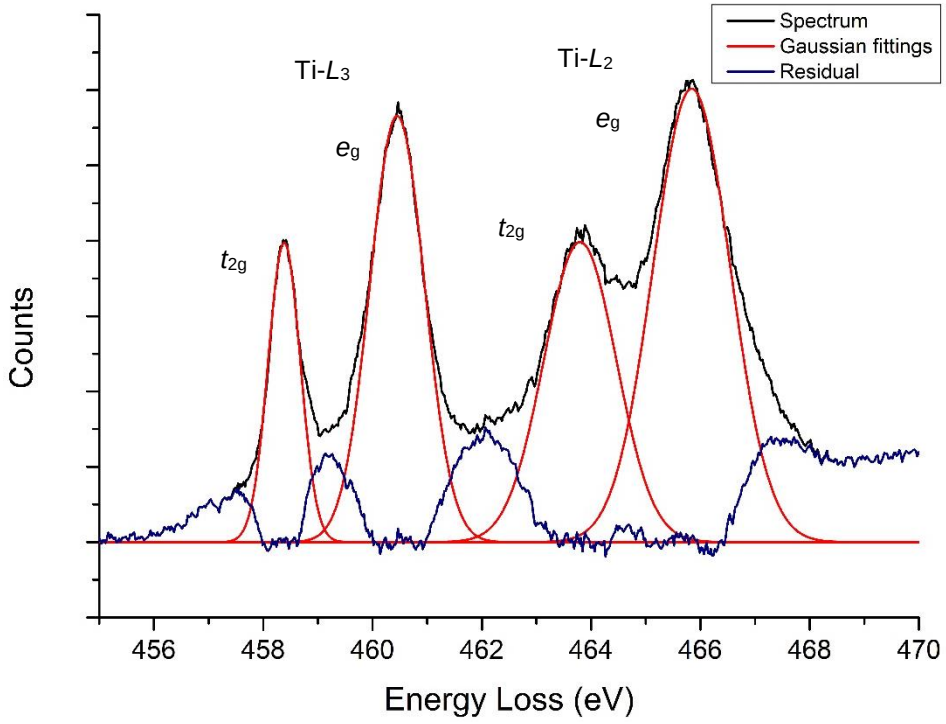

Figure 116. Ti-$L_{2,3}$ EELS edge of the individual HT-BT nanoparticle shown in Figure 109 (b). The Gaussian fit parameters were not constrained to the prior settings of the CT-BT reference sample. The optimum H-BT Gaussian fitting parameters are summarised in Table 20.

Gaussian fittings	Ti-L_3 t_{2g}	Ti-L_3 e_g	Ti-L_2 t_{2g}	Ti-L_2 e_g
Gaussian centre (eV)	458.38	460.45	463.80	465.84
e_g-t_{2g} peak separation (eV)	2.07		2.04	
FWHM (eV)	0.70	1.18	1.57	1.67

Table 20. Gaussian fitting parameters of H-BT, showing the Gaussian centre and FWHM values of the fitted peaks for the respective Ti-$L_{2,3}$ edges. The peak separation of t_{2g} and e_g peaks for both Ti-L edges are shown and suggest a tetragonal phase particle.

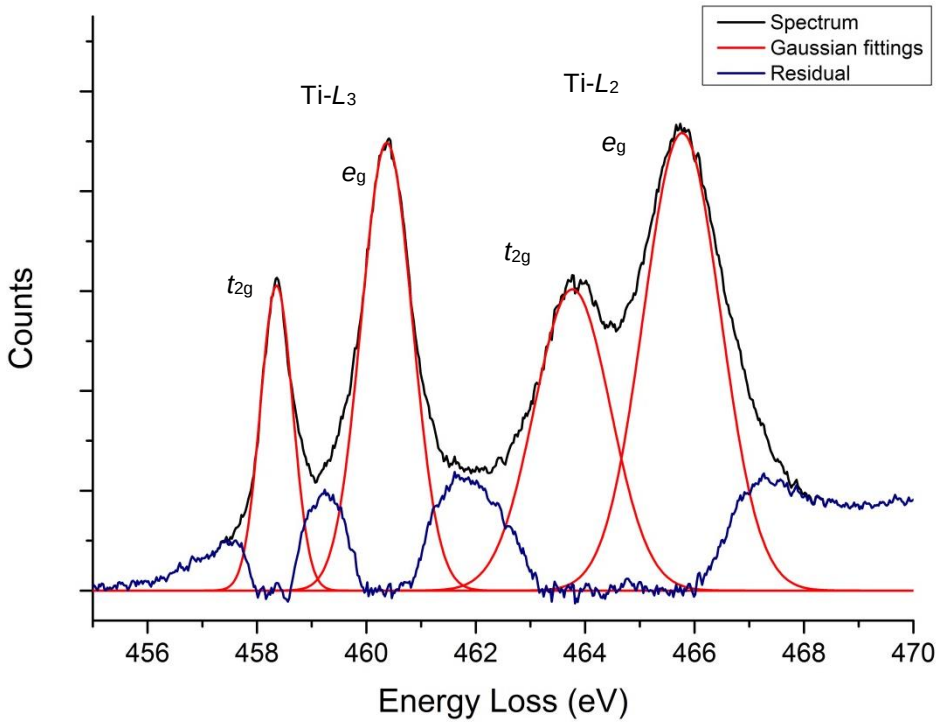

Figure 117. Ti-$L_{2,3}$ EELS edge of the individual HT-BT-400 ºC nanoparticle. The Gaussian fitting parameters were not constrained to the prior settings of the CT-BT sample. The H-BT Gaussian fitting parameters are summarised in Table 21.

Gaussian fittings	Ti-L_3 t_{2g}	Ti-L_3 e_g	Ti-L_2 t_{2g}	Ti-L_2 e_g
Gaussian centre (eV)	458.35	460.37	463.76	465.77
e_g-t_{2g} peak separation (eV)	2.02		2.01	
FWHM (eV)	0.70	1.10	1.64	1.66

Table 21. Gaussian fitting parameters of H-BT-400 ºC, showing the Gaussian centre and FWHM values of the fitted Gaussian peaks for the respective Ti-$L_{2,3}$ edges. The peak separation of t_{2g} and e_g peaks for both Ti-*L* edges are shown and are suggest the presence of a cubic phase.

Figure 118 shows a direct comparison of the Ti-$L_{2,3}$ edge for H-BT and H-BT-400 ^{o}C samples and the Gaussian peak positions are given in Table 22.

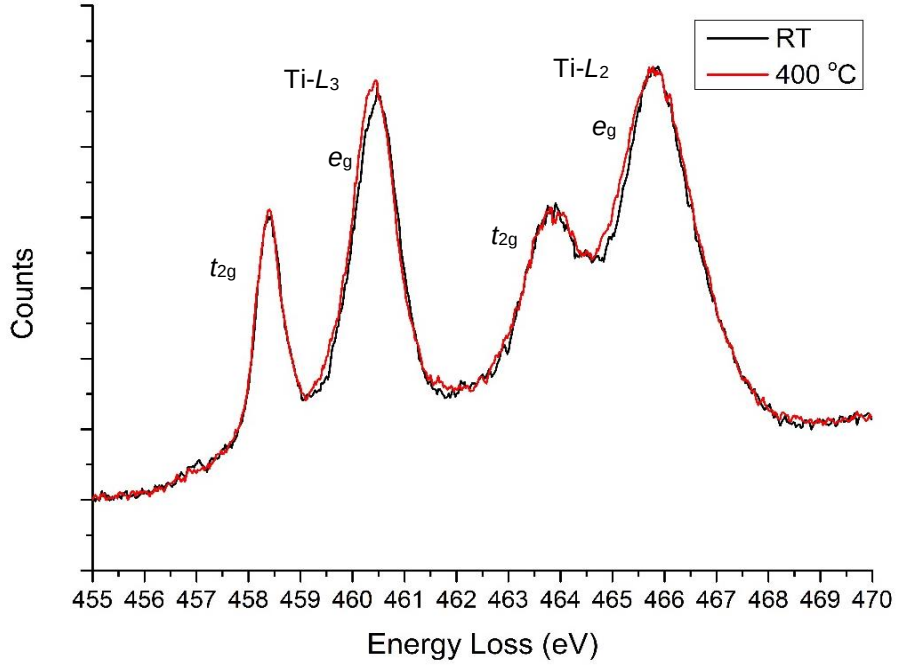

Figure 118. Comparison of the H-BT Ti-$L_{2,3}$ edge at RT and 400 ^{o}C showing a shift in the Ti-$L_{2,3}$ e_g peaks to lower energy loss values. As shown in Table 22 both spectra were energy calibrated to absolute energies from the ZLP (acquired in Dual EELS mode).

Gaussian fitting	Ti-L_3 t_{2g} (eV)	Ti-L_3 e_g (eV)	e_g-t_{2g} peak separation (eV)	Ti-L_2 t_{2g} (eV)	Ti-L_2 e_g (eV)	e_g-t_{2g} peak separation (eV)
CT-BT (RT)	458.47	460.54	**2.07**	463.87	465.93	**2.06**
CT-BT (400 ^{o}C)	458.44	460.43	**1.99**	463.84	465.83	**1.99**
H-BT (RT)	458.38	460.45	**2.07**	463.80	465.84	**2.04**
H-BT (400 ^{o}C)	458.35	460.37	**2.02**	463.76	465.77	**2.01**

Table 22. Comparison of the CT-BT and H-BT Gaussian fitting parameters Ti-$L_{2,3}$ edge t_{2g}, e_g peaks collected at RT and 400 ^{o}C. The dispersion of the EELS data was 0.025 eV/channel, giving the accuracy to the best resolution of 0.01 eV/channel. The data suggests the H-BT starts tetragonal and transforms to the cubic phase.

The Gaussian fits to the CT-BT nanoparticle and H-BT nanoparticle Ti-$L_{2,3}$ edge spectra at room temperature (RT) and above the Curie point (400 ^{o}C) show a consistent difference in the t_{2g}-e_g peak splitting. The Gaussian fits also suggest a small reduction in the Ti-L_2 edge t_{2g}-e_g peak separation for the CT-BT and H-BT sample relative to the Ti-L_3 edge.

When CT-BT and H-BT were heated to 400 ^{o}C; the CT-BT Ti-$L_{2,3}$ edge t_{2g}-e_g peak splitting values were reduced suggesting a phase transition from tetragonal (RT) to cubic (400 ^{o}C) occurs in agreement with the electron diffraction data.

The H-BT EEL spectra presented so far (Figure 115 to Figure 118) are an average of a full spectrum image, i.e. an average over a whole particle. However, the tetragonal/cubic phase fractions determined by XRD and SHG (when correlated to SEM) suggested the phase separation to be *intra*-particle. Thus the H-BT Ti-L_3 edge t_{2g}-e_g peak separation was next measured at each STEM-EELS pixel (2nm) of a linescan across an individual H-BT particles viewed by HAADF imaging on the Titan microscope (1.4 Å probe size) and the data is shown in Figure 119 & Figure 120. The splitting values shown in Figure 119 & Figure 120

do not exactly correspond to the values determined by Gaussian fitting because they were measured direct from the spectra.

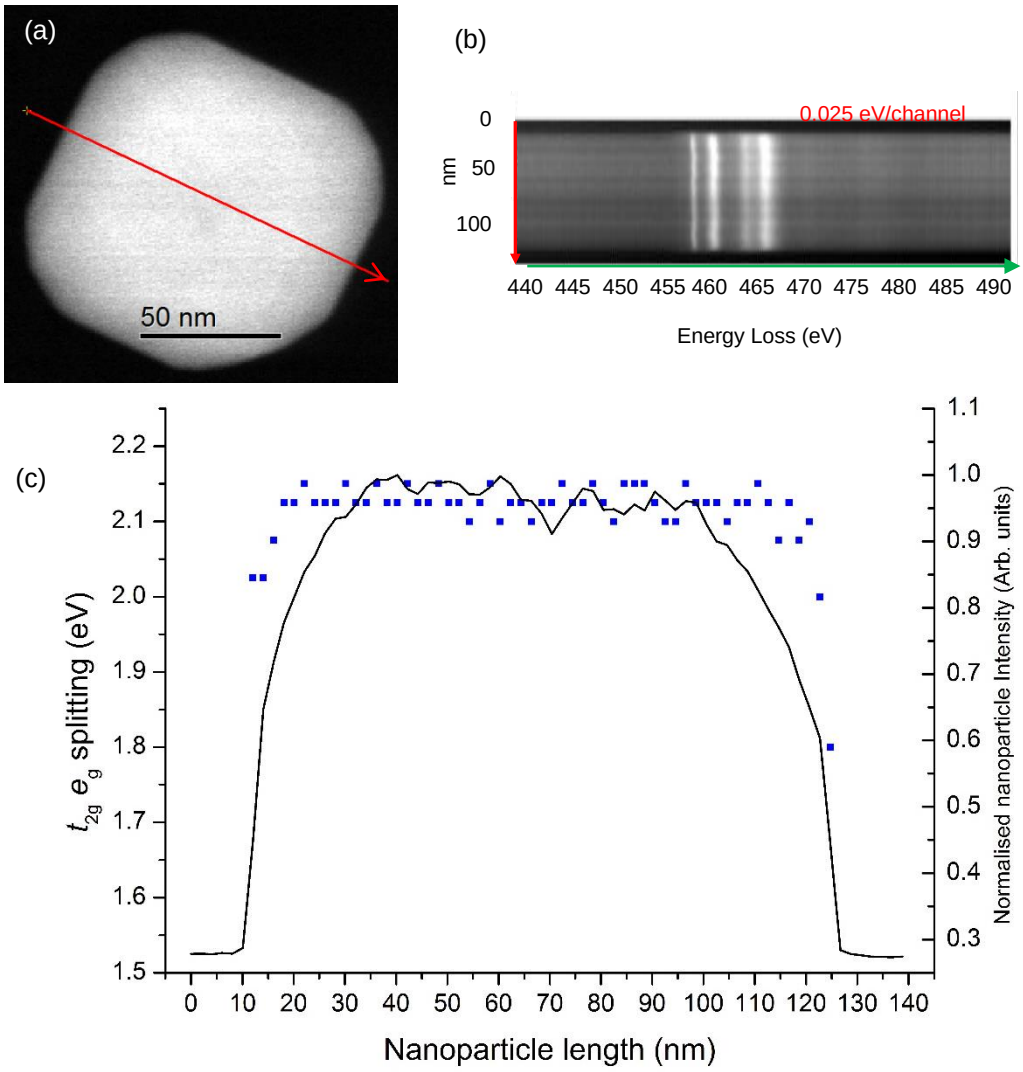

Figure 119. (a) HAADF-STEM image of a H-BT nanoparticle collected at RT showing the EELS linescan of a nanoparticle (red arrow). (b) Spectrum image of the STEM-EELS linescan of the H-BT nanoparticle. The y-axis is the total length of the linescan with each spectrum taken at 2 nm intervals on the linescan across the HAADF image. (c) The H-BT nanoparticle HAADF intensity profile (solid black) highlighting the projected nanoparticle shape. The blue data points are the Ti-L_3 edge t_{2g}-e_g peak splitting values extracted from each spectrum on the spectrum linescan. The separation between the peaks are shown on the left hand side y-axis on the graph. The average separation value is 2.13 eV. However, spectra at the edges of the nanoparticle shows a more cubic like 2.02 eV splitting.

The Ti-L_3 edge t_{2g}-e_g peak splitting for the H-BT nanoparticle at room temperature (Figure 119), showed a reduction in the t_{2g}-e_g peak separation at the surfaces of the nanoparticle as compared to the core. This indicates that the H-BT nanoparticle at room temperature has a cubic surface and a tetragonal core. The change in the Ti-L_3 t_{2g}-e_g peak splitting occurs at around ~ 5 nm from the surface. Thus the cubic/tetragonal phase fraction for this nanoparticle can be estimated; with the assumption that the nanoparticle is a 100 nm perfect cube in shape (Equation 11).

$$100\ x\ \frac{(100\ \times 10^{-9})^3 - (90\ \times 10^{-9})^3}{(100\ \times 10^{-9})^3} = \sim 27\ \%\ cubic\ \therefore \sim 73\ \%\ tetragonal$$

Equation 11. Estimated surface phase fraction by volume (~ 27 %) suggesting a cubic surface layer around a 100 nm cubic-shaped nanoparticle. Implying the remaining tetragonal phase fraction is ~ 73 % by volume. The estimated ~5 nm surface layer (~10 nm overall) is shown in the reduced t_{2g}-e_g peak separation in Figure 119 (c).

Although the estimated phase volume fractions of H-BT determined by STEM-EELS suggest a ~27 % cubic surface phase and a ~73 % tetragonal core phase fraction, the estimated tetragonal phase fraction acquired by Rietveld fitting of synchrotron diffraction data (Figure 83, Chapter 4) suggests that the tetragonal phase fraction is ~59 %, (with a ~41 % cubic phase present). Assuming that STEM-EELS is accurate, then the ~15 % difference between the estimated tetragonal fractions by STEM-EELS and XRD can be explained by the presence of local defects/distortions. These local defects/distortions provide a local 'tetragonal-like' structure that is highlighted by the Ti-L_3 t_{2g}-e_g peak

splitting when scanning the probe across the nanoparticle (Figure 119). Similar Ti-L_3 t_{2g}-e_g peak splitting data were plotted for the H-BT sample heated above the Curie point in Figure 120.

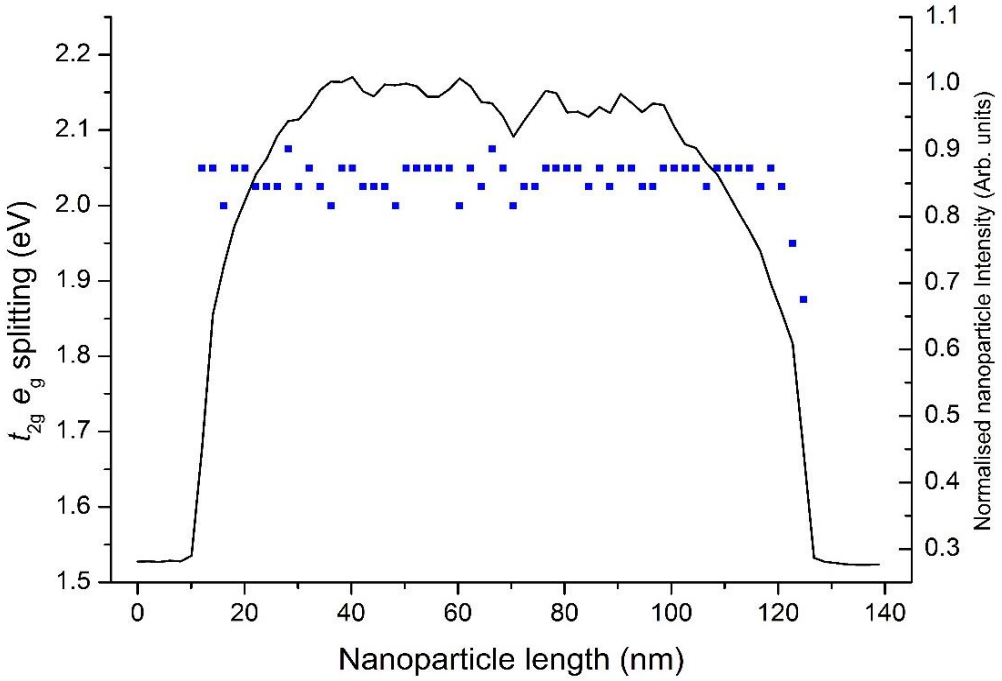

Figure 120. The H-BT nanoparticle HAADF intensity profile (solid black) highlighting the nanoparticle morphology. The blue data points are the Ti-L_3 edge t_{2g}-e_g splitting values extracted from each pixel on the spectrum image (not shown). The separation between the peaks are shown on the LHS y-axis on the graph. The average separation value is 2.05 eV i.e. cubic like. Only 2 spectra show a value less than 2.0 eV at the very right hand particle edge.

Figure 119 and Figure 120 allows comparison of the H-BT Ti-L_3, t_{2g}-e_g peak separation across a nanoparticle at both RT and 400 ^{o}C. When the sample was heated to 400 ^{o}C i.e. above the phase transition temperature, the t_{2g}-e_g peak separation decreased consistent with the formation of a cubic phase and possibly the removal of any tetragonal distortions/defects on heating above the Curie point. The t_{2g}-e_g peak splitting decrease at the surface of the tetragonal

nanoparticles was correlated with high resolution atomic lattice images at SuperSTEM (see later). However, first we compare the O-*K* edges of the H-BT-RT and H-BT-400 ^{o}C samples (full spectrum images) with the CT-BT-RT sample in Figure 121.

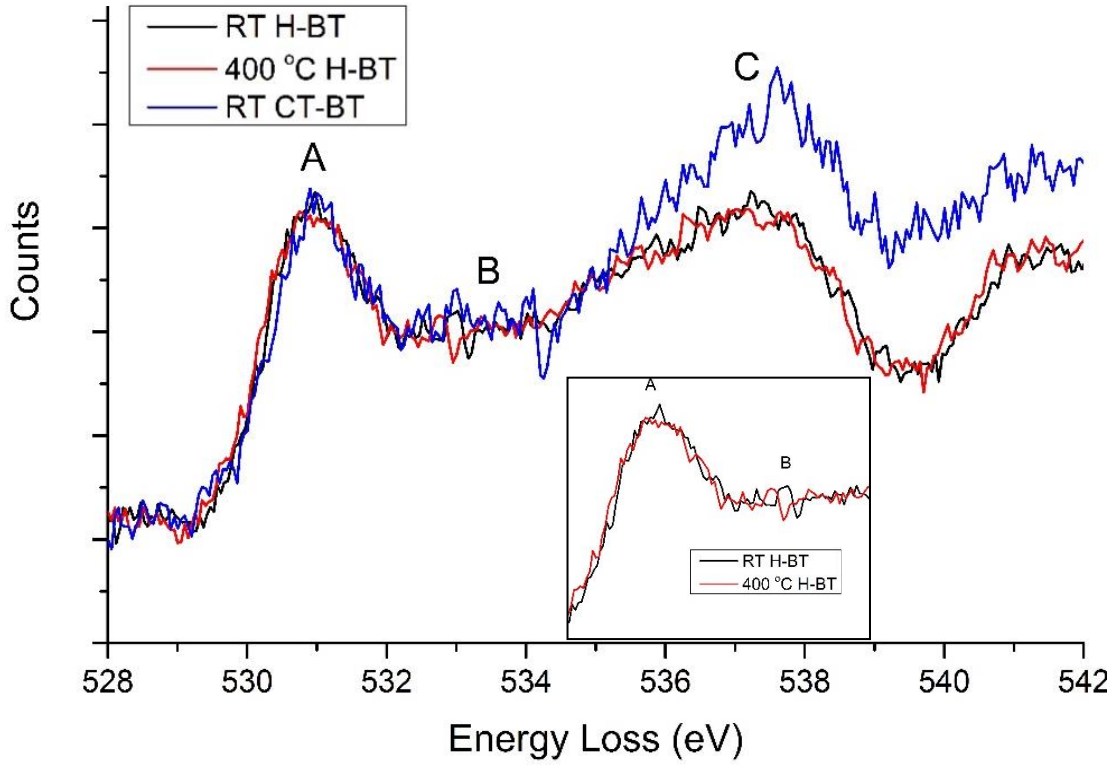

Figure 121. Comparison of the H-BT O-*K* edge averaged across the whole particle at RT (black) and 400 ^{o}C (red) and also compared with CT-BT-RT (blue). The magnified O-*K* edge shows little difference in peaks 'A' and 'B' in comparison to the CT-BT O-*K* edge (blue – Figure 108). The H-BT EEL spectra are aligned to the CT-BT O-*K* edge peak 'A' maxima. Inset – A magnified O-*K* edge of peaks A and B for H-BT-RT and H-BT-400^{o}C aligned by absolute energy).

A comparison of the O-*K* edges of H-BT at RT and 400 ^{o}C averaged across the whole particle is shown in Figure 121. This revealed no significant difference between the collected O-*K* spectra, compared to the same CT-BT-RT and CT-

BT-400^{o}C comparison (Figure 108). So only the Ti-L_3 t_{2g} e_g peak separation will be investigated here after.

EEL spectroscopy allowed *in-situ* data collection of a commercial tetragonal sample (CT-BT), a cubic standard (CT-BT-400 ^{o}C) and the comparison of these standards to a hydrothermally prepared sample (H-BT and H-BT-400 ^{o}C). The hydrothermally prepared H-BT sample showed similar Ti-$L_{2,3}$ t_{2g}-e_g peak splitting to the commercial reference standards (CT-BT and CT-BT-400^{o}C) indicating that a phase transition occurred from tetragonal to cubic phase upon *in-situ* heating.

The H-BT sample was then further analysed at SuperSTEM to collect high resolution lattice images and EEL spectra of H-BT nanoparticles at room temperature. The experiment primarily investigated the Ti-L_3 t_{2g}-e_g peak separation analysed by STEM-EELS linescans and STEM-EELS mapping of nanoparticles.

5.2 SuperSTEM experiments

The SuperSTEM data presented here are a collection of H-BT EELS linescans conducted at room temperature; Figure 122. The EELS data had a dispersion of 0.3 eV/channel with a cold-FEG giving ~0.8 eV energy resolution. The STEM probe size was and 0.8 Å STEM probe size.

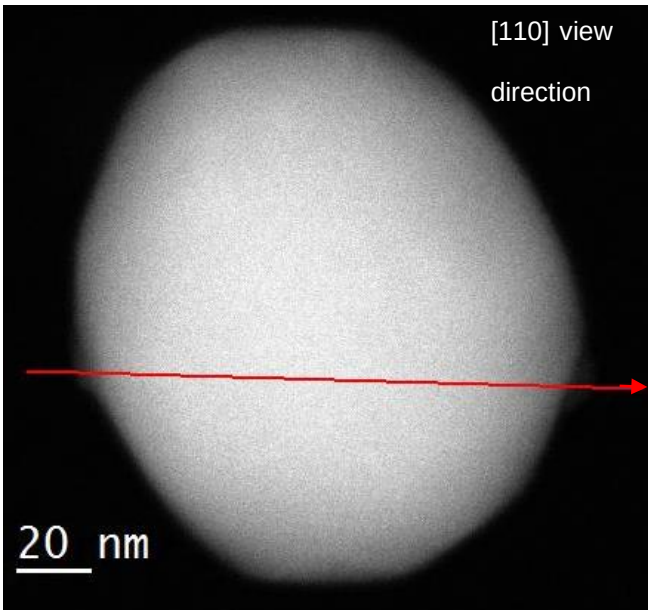

Figure 122. HAADF-STEM image of the H-BT nanoparticle with line spectra collected across the nanoparticle from left to right (red) at 0.4 nm pixel size.

The purpose of the study was to investigate any reduction in Ti-L_3 edge t_{2g}-e_g splitting at the surface of the nanoparticles. A reduced linescan was used to investigate the surface of the nanoparticle shown in Figure 122 and the CCD-projected Ti-$L_{2,3}$ edge EEL spectra, are shown in Figure 123.

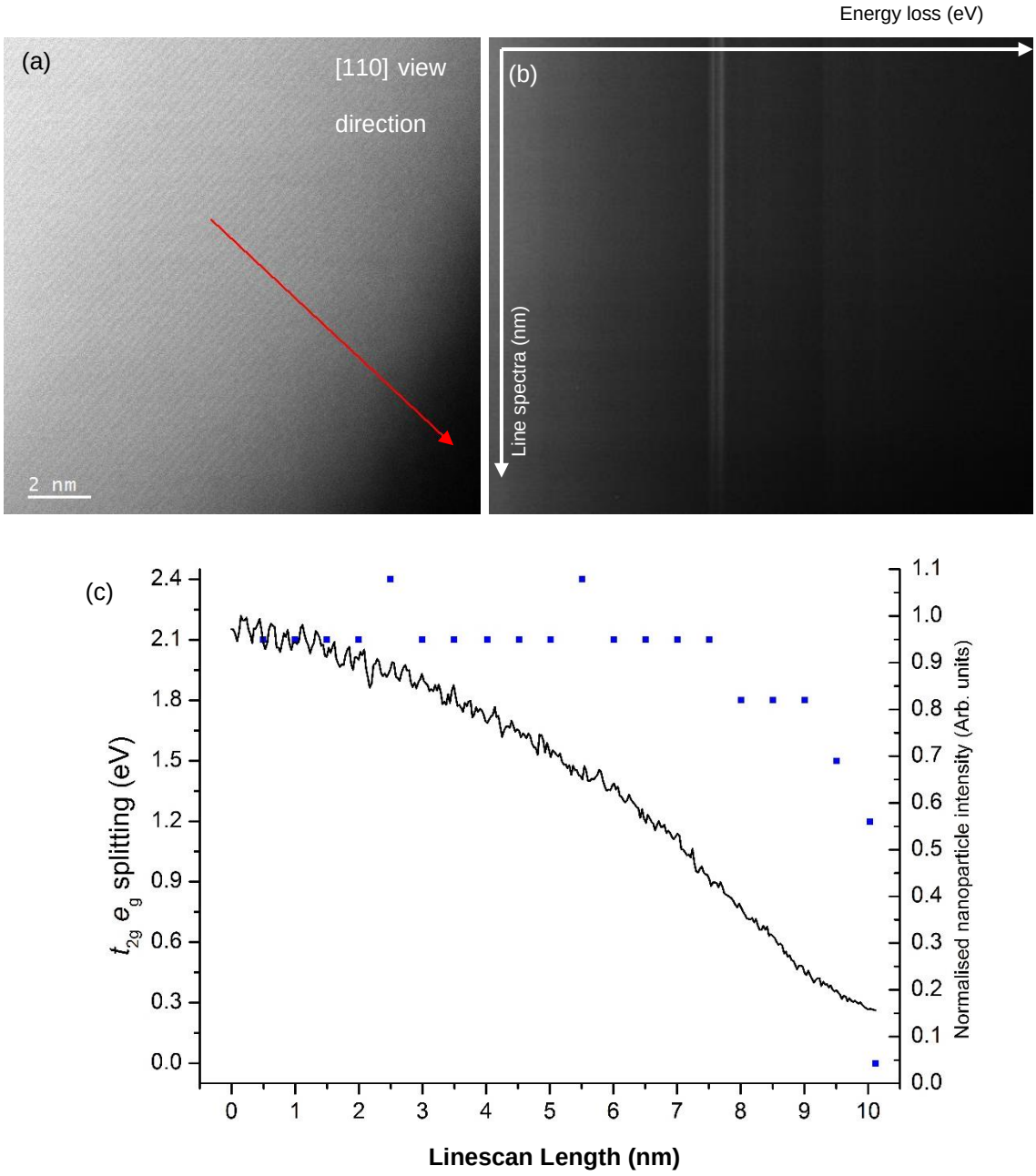

Figure 123. (a) HAADF-STEM lattice image of the H-BT nanoparticle in Figure 122. The linescan is collected from 10 nm inside the nanoparticle out to the surface of the nanoparticle at 0.5 nm intervals (red arrow). (b) The EELS spectrum image generated from (a) shows the energy loss on the x-axis and length of STEM-EELS linescan on the y-axis. (c) Plot showing the measured Ti-L_3 t_{2g} e_g peak separation across the nanoparticle (blue data points) in 0.5 nm intervals. The HAADF line profile of the nanoparticle (black), starts from the centre of the nanoparticle towards the surface of the nanoparticle.

A prominent feature present in the Ti-L_3 edge t_{2g}-e_g peak splitting data extracted from the STEM-EEL spectra (Figure 123) is the decrease in t_{2g}-e_g peak splitting at the surface of the nanoparticle. Figure 124 shows the extracted Ti-$L_{2,3}$ of the SuperSTEM data acquired in (Figure 123) at 0.5 nm spacing across the particle. The Ti-L_3 edge t_{2g}-e_g peak splitting in Figure 124 decreases ~4 nm away from the surface (denoted by the red asterisk at 6.5 nm). The Ti-L_3 peak splitting past the red asterisks were not measured due to the low signal to background shown in Figure 124.

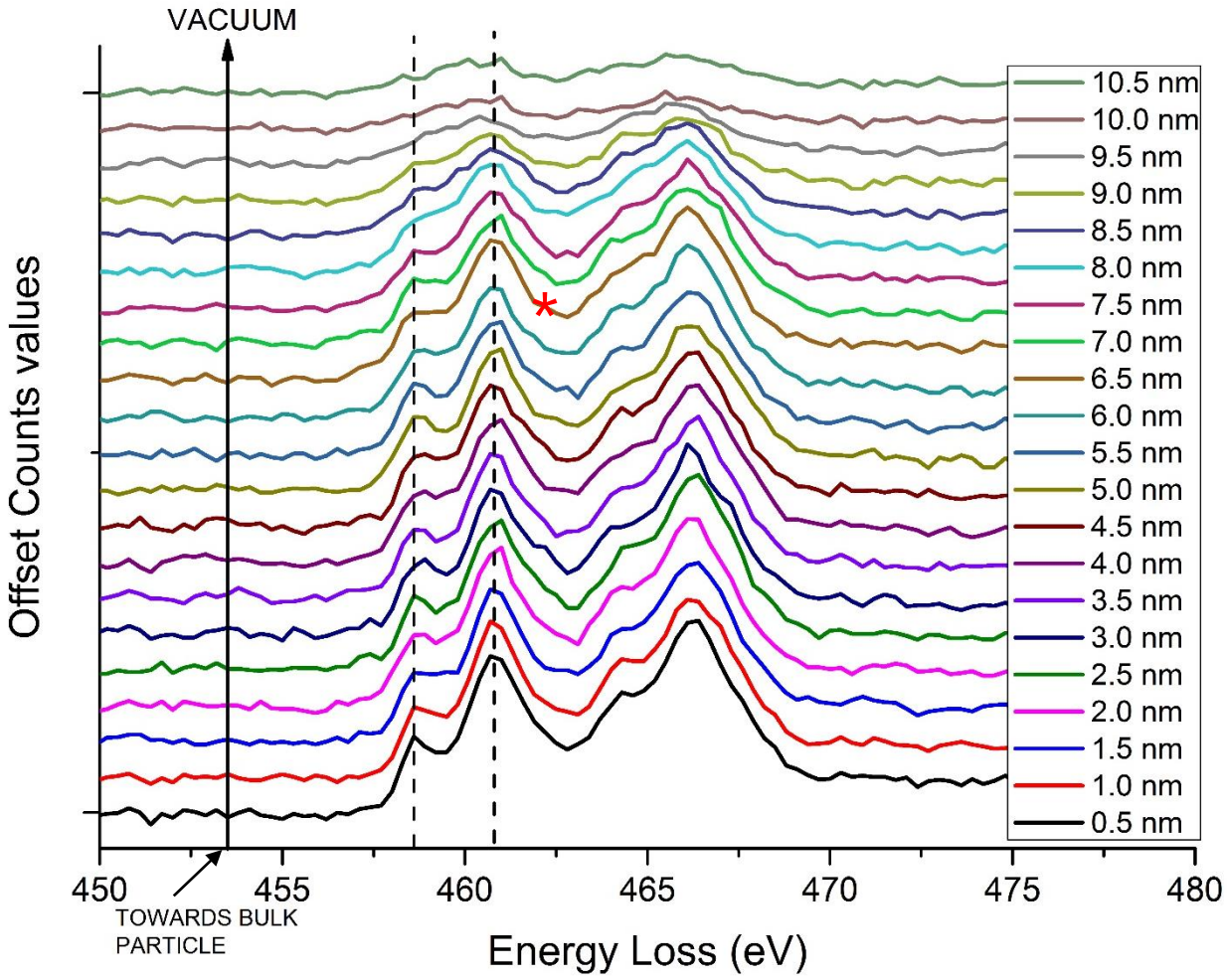

Figure 124. The extracted EEL spectra series of the nanoparticle shown in Figure 122 starting from the centre of the nanoparticle to the surface of the nanoparticle. The black arrow shows the beginning of the collected EEL spectra and each spectrum was extracted at 0.5 nm intervals.

The Ti-L_3 edge t_{2g}-e_g splitting was investigated by STEM-EELS spectrum imaging at a pixel size of ~2 x 2 Å^2 (i.e. half a unit cell parameter) from the edge of a particle which was simultaneously imaged using HAADF-STEM ([100] zone axis) The data is shown in Figure 125.

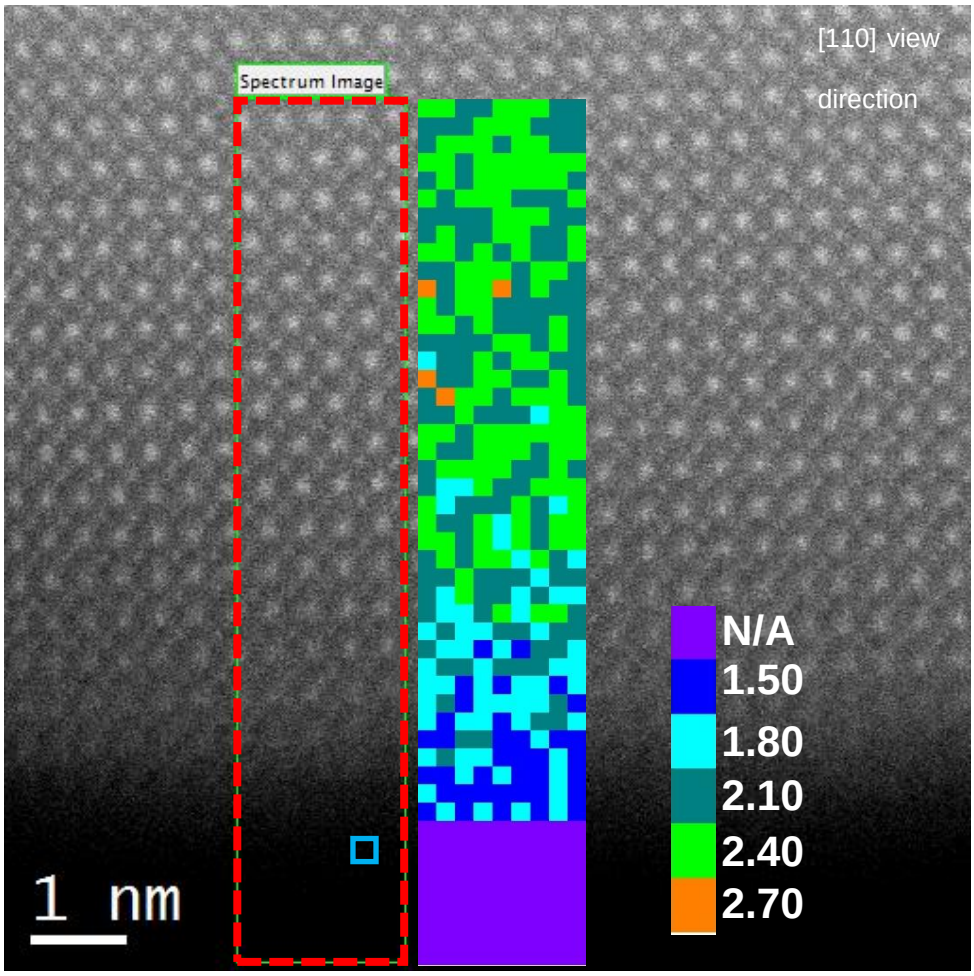

Figure 125. EELS mapping data of the nanoparticle shown in Figure 122. The EEL spectra were acquired from an area 0.195 x 0.195 nm^2 (blue box) and the Ti-L_3 t_{2g}-e_g peak separation distances were measured at each pixel. The colour coded key are the separation values of the Ti-L_3 edge t_{2g}-e_g peak separation in eV. The EELS data suggests a difference in the EEL spectra acquired within the nanoparticle (mainly green) to the surface of the nanoparticle (mainly blue) in terms of the t_{2g}-e_g peak separation.

In total, 10 $BaTiO_3$ and 7 $Ba_{0.8}Sr_{0.2}TiO_3$ nanoparticles were analysed by EELS (not shown), using both SuperSTEM and Titan microscopes. All data revealed a difference between the Ti-L_3 t_{2g}-e_g peak splitting from the bulk of the nanoparticle compared to the surface. Suggesting that there is an *intra*-particle phase distribution in the nanoparticles with the surface showing more of a cubic-like peak splitting and the core showing 'tetragonal' like peak splitting.

The difference in Ti-L_3 edge t_{2g} e_g peak splitting values for Titan and SuperSTEM data (Figure 119 and Figure 123 respectively) are due to the different energy dispersions the data were collected at (0.3 eV/channel for SuperSTEM and 0.025 eV/channel for Titan) i.e. under-sampled at SuperSTEM compared to Titan data. In addition, the working resolution of EELS data acquired at SuperSTEM was poor compared to the Titan microscope (~0.8 and ~0.43 eV respectively Figure 126), shown by the zero loss peaks (ZLP). Theoretically it should have been similar and the reduction could have been due to incorrect spectrometer focusing and under-sampling.

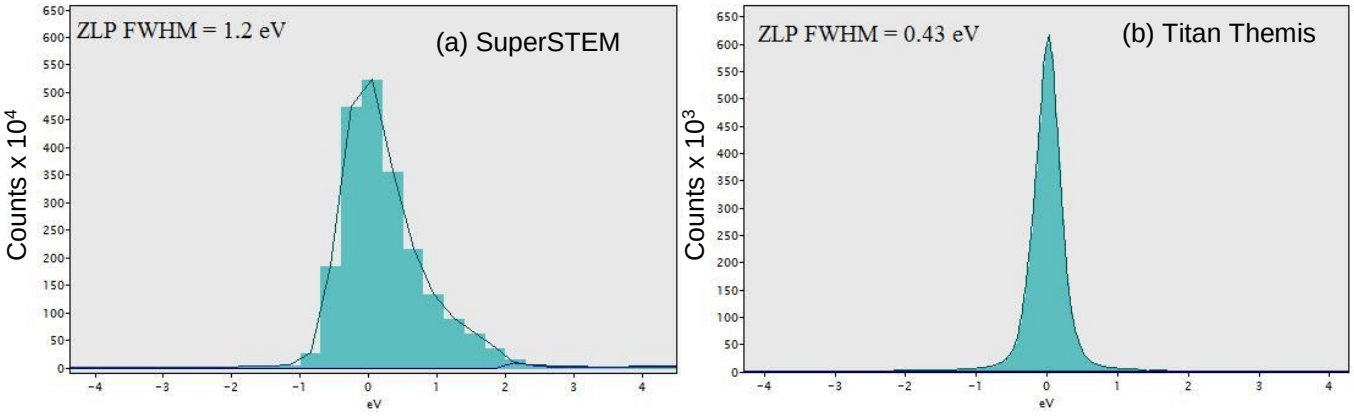

Figure 126. Extracted ZLP of H-BT and CT-BT nanoparticle at SuperSTEM and Titan microscope respectively. STEM-EEL linescan acquired at (a) SuperSTEM showing a 1.2 eV working resolution for a H-BT nanoparticle and (b) a 0.43 eV working resolution from the Titan microscope for the CT-BT nanoparticle.

The correct sampling and the better ZLP resolution resulted in better resolved peaks for data collected on the Titan; Figure 127. Therefore, the Titan data was used for robust EELS analysis and SuperSTEM data for high resolution atomic lattice imaging, due to the SuperSTEM probe size being smaller and thus able to resolve finer detail (~0.8 Å as compared to ~1.4 Å). The HAADF-STEM atomic resolution images provided information about the local crystal structure of H-BT as compared in Figure 128.

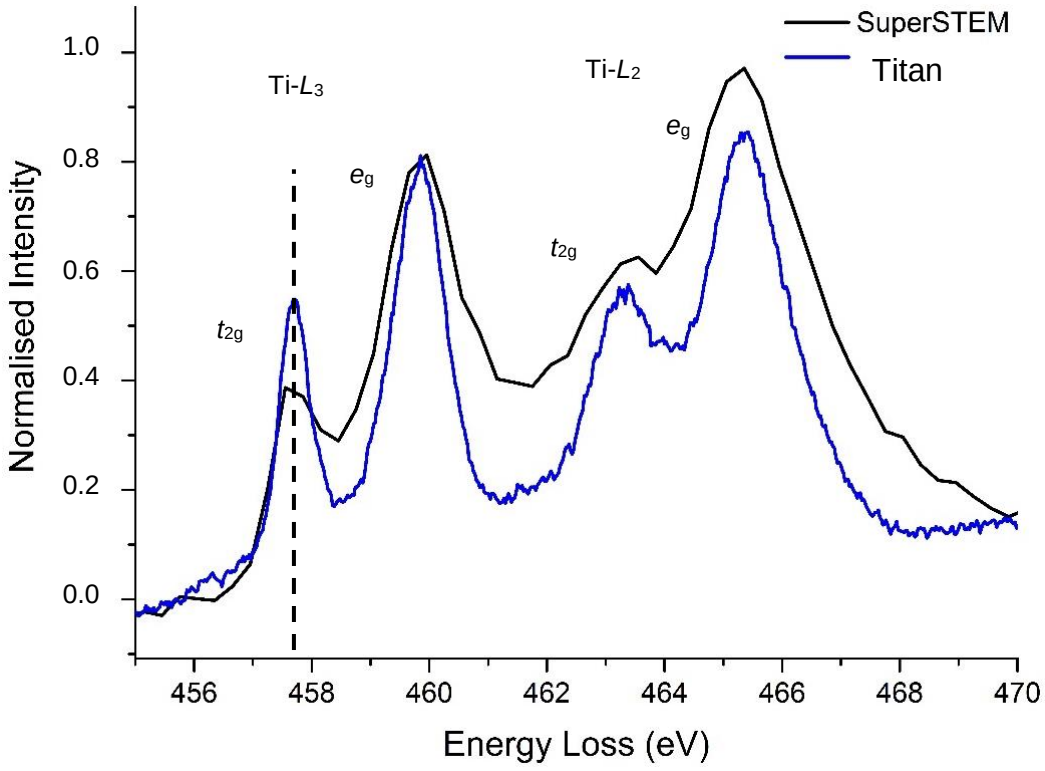

Figure 127. Extracted H-BT EEL spectra for the Ti-$L_{2,3}$ edge at SuperSTEM (black) and Titan microscope (blue) are shown overlaid to compare the EELS data. The energy loss is calibrated to the Titan Ti-L_3 t_{2g} EELS peak. The Titan data is collected at a lower dispersion (0.025 eV/ channel compared to 0.3 eV/channel) resulting in a noisier but better resolved EEL spectrum.

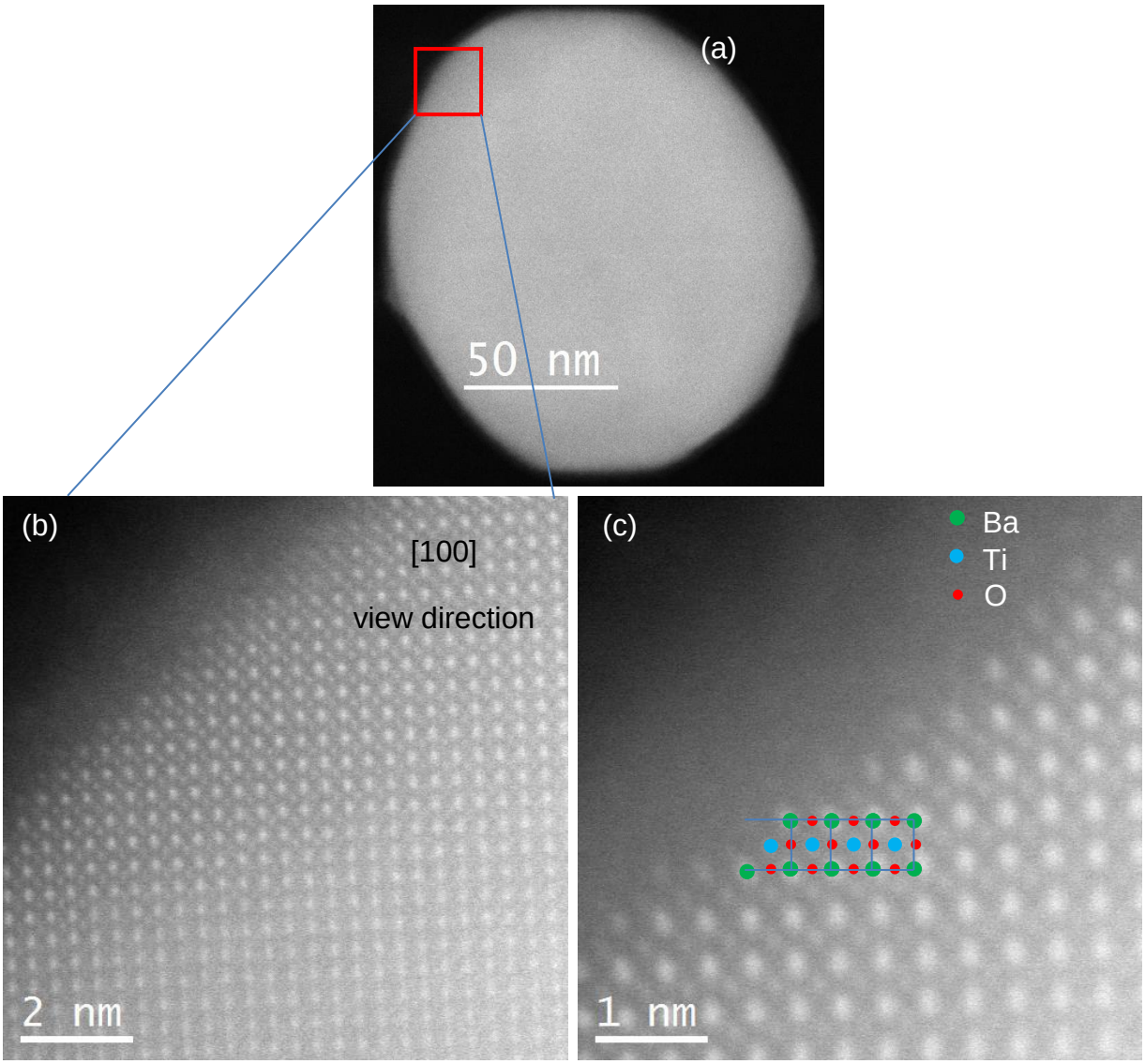

Figure 128. HAADF-STEM images of the [100] oriented H-BT nanoparticle shown in Figure 122 with the area of (b) and (c) shown by the red box. (b) High resolution HAADF-STEM image of the area shown in (a). The right columns are Ba, with lower intensity Ti-O columns in the centre of each square. (c) Higher magnification HAADF-STEM image of the surface shown in (b) showing incomplete unit cells at the surface producing an atomically 'rough' layer. The $BaTiO_3$ unit cell schematic is overlaid and repeated to the surface to highlight the missing atom positions.

The atomic resolution HAADF STEM images in Figure 128 show the H-BT nanoparticle surface is atomically 'rough' and the $BaTiO_3$ unit cells are incomplete around the surface of the nanoparticle. This rough nanoparticle surface will affect the Ti-L_3 edge t_{2g}-e_g peak splitting and any incomplete unit cells are likely to cause a t_{2g}-e_g splitting decrease because the electrostatic crystal field splitting at the Ti site depends on the number of oxygen anions and their Ti-O distances (a shorter distance gives a bigger splitting).

Research conducted by Polking *et al.* suggests that local structural distortions (Figure 125) are likely to be a surface-induced phenomenon [78], where cubic shaped particles exhibit nearly atomically flat surfaces with low internal stresses in comparison to spherically shaped nanoparticles with irregular surfaces that have high internal stresses of the order of GPa for <10 nm nanoparticles; this in turn reduces the coherence of Ti-atom distortions in $BaTiO_3$ nanoparticles [78].

Analysis of Ti-site atomic column positions in the H-BT nanoparticle was performed using Matlab software (conducted by Dr David Hernandez-Maldonado at SuperSTEM) which can map the Titanium atom displacements in the central atomic columns, the results are displayed Figure 129. The image analysis shows the Ti-atoms in the bulk of the H-BT nanoparticle possess a random asymmetric distortion within each unit cell of the nanoparticle.

This asymmetric distortion is assumed to be a contributing source to the second harmonic light production. When characterising these nanoparticles by bulk measurement techniques they appear to have tetragonal and cubic phase fractions (Chapter 4). These terms (tetragonal and cubic) are not entirely accurate, because Ti-atom mapping and HAADF imaging shows there is no *net*

direction for the displacement of the titanium atoms, therefore it is suggested that there may be no ‘tetragonal’ phase but instead a random distribution of asymmetric Ti-atom distortions that give rise to an overall tetragonal-like character to the nanoparticle. This random distribution of asymmetric distortions will likely cause broadening of the (002/200) peak when analysing the bulk of the sample, however it may be unlikely to produce the (002/200) peak splitting that is observed by XRD analysis (Figure 83, Chapter 4) giving a c/a ratio of 1.006. This suggests that there may be a small net direction of these asymmetric distortions that appear random on small areas of individual nanoparticles imaged by STEM (Figure 129).

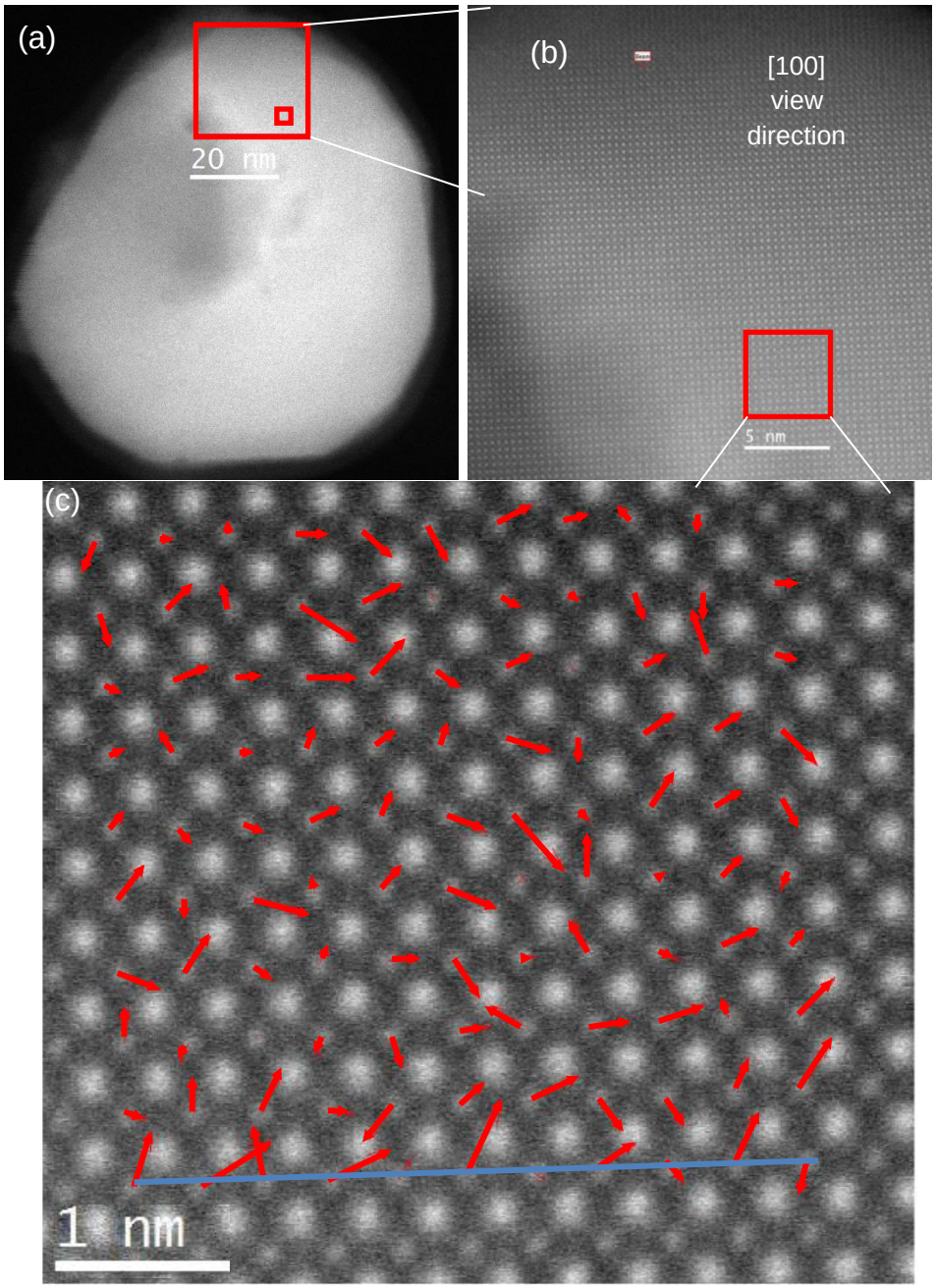

Figure 129. (a) HAADF-STEM image of the H-BT nanoparticle used for Ti-atom displacement analysis. The red box shows the area magnified in (b). A low magnification atomic resolution HAADF-STEM image with the red box highlighting the area magnified in (c). An atomic resolution HAADF-STEM image for Ti-atom displacement analysis acquired towards the bulk of the nanoparticle. The red arrows in (c) shows the magnitude and direction of displacement for the central Ti-atom column. The image highlights no net direction of Ti-atom column displacement in the nanoparticle with a maximum displacement of 0.4 Å. The magnitudes are summarised in Figure 130. The blue line shows where the mapping area stops.

The H-BT Titanium atom column displacements shows random asymmetric distortions with no net displacement. A histogram of the magnitude of the titanium atom column displacement distances is displayed in Figure 130. The displacement values above 0.4 Å (Figure 130) are due to the mapping area being cut off during the analysis seen in Figure 129 (the bottom row of arrows). The average magnitude of the Ti-atom column displacements shown in Figure 130 (~0.2 Å) can be compared to Ti-atom column displacement mapping data acquired by Polking *et al.* for a 15 nm sized $BaTiO_3$ nanoparticle which showed a maximum displacement of ~0.15 Å [78].

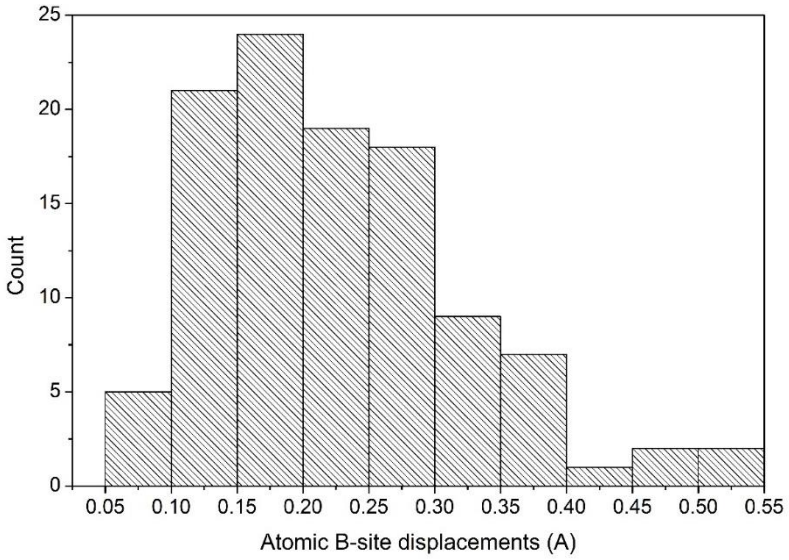

Figure 130. (a) A histogram of the magnitude of the displacement values of the titanium column in STEM-HAADF images of the H-BT nanoparticle, showing the average magnitude of the displacement being around 0.15 – 0.2 Å.

The Rietveld fitting of synchrotron data for H-BT nanoparticles estimated the unit cell parameters to be c = 4.03 Å and a = 4.005 Å (c/a = 1.006). This indicates that estimation of the magnitude of the overall tetragonal distortion is much less when measured by bulk techniques (~0.02 Å by synchrotron XRD

vs. ~0.2 Å by HAADF-STEM). This implies that XRD analysis shows the long range net distortion in a particular direction as compared to the random local distortions measured by HAADF-STEM.

HAADF atomic resolution imaging also highlighted atomically rough surfaces for H-BT that are likely to contribute to the SHG of light in addition to the asymmetric distortions of Ti-atom columns identified by displacement mapping towards the bulk of the nanoparticle. EELS analysis showed a similarity in Ti-$L_{2,3}$ edge t_{2g}-e_g peak separations between the CT-BT and H-BT samples collected at RT. The Ti-L_3 t_{2g}-e_g peak separation reduced for both samples on heating to 400 ^oC, suggesting that both H-BT and CT-BT are tetragonal-like at room temperature and transform to a cubic-like phase when heated above the Curie temperature.

The Ti-L_3 edge t_{2g} e_g peak splitting analysis and the Ti-atom displacement mapping will be conducted for H-BST nanoparticle to see if the origin of SHG in this material could be due to a similar surface and bulk contribution, discussed in Section 5.2.1.

5.2.1 Hydrothermal barium strontium titanate.

The EELS data from H-BST nanoparticles collected at SuperSTEM shows the Ti-L_3 edge t_{2g}-e_g splitting across a nanoparticle in Figure 131 and Figure 132.

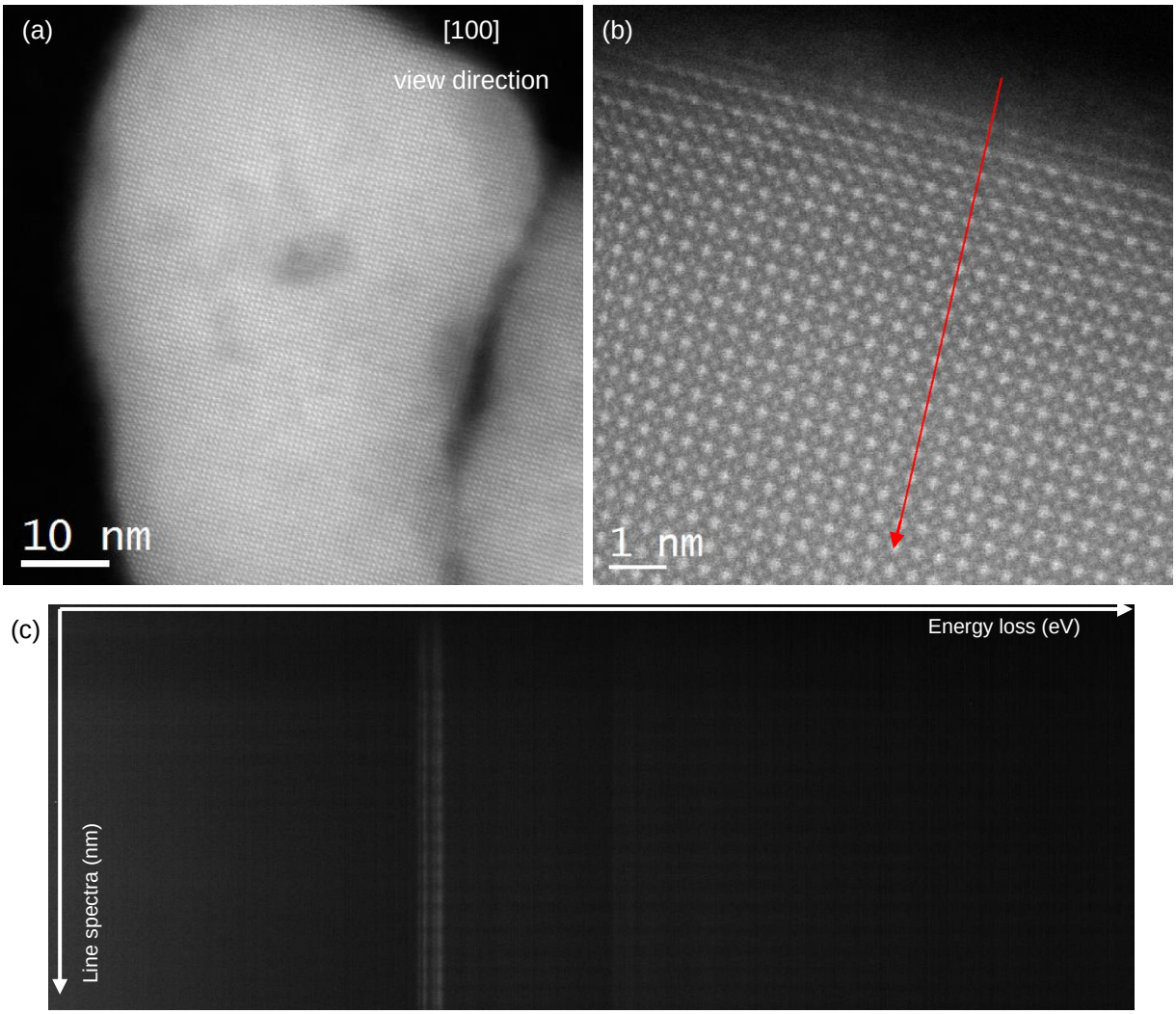

Figure 131. (a) HAADF-STEM image of a H-BST nanoparticle collected at SuperSTEM with the crystal orientation labelled. (b) HAADF-STEM image of the surface of the nanoparticle with a STEM-EELS linescan collected from the region marked in red. (c) The resulting STEM EELS spectrum image shown with spectra extracted every 0.5 nm; the spectra are shown in Figure 132.

The STEM-EELS linescan analysis of H-BST at room temperature shows a mixture of phases from the surface to the core (a cubic surface and tetragonal core) due to the variation in t_{2g}-e_g peak splitting across the nanoparticle.

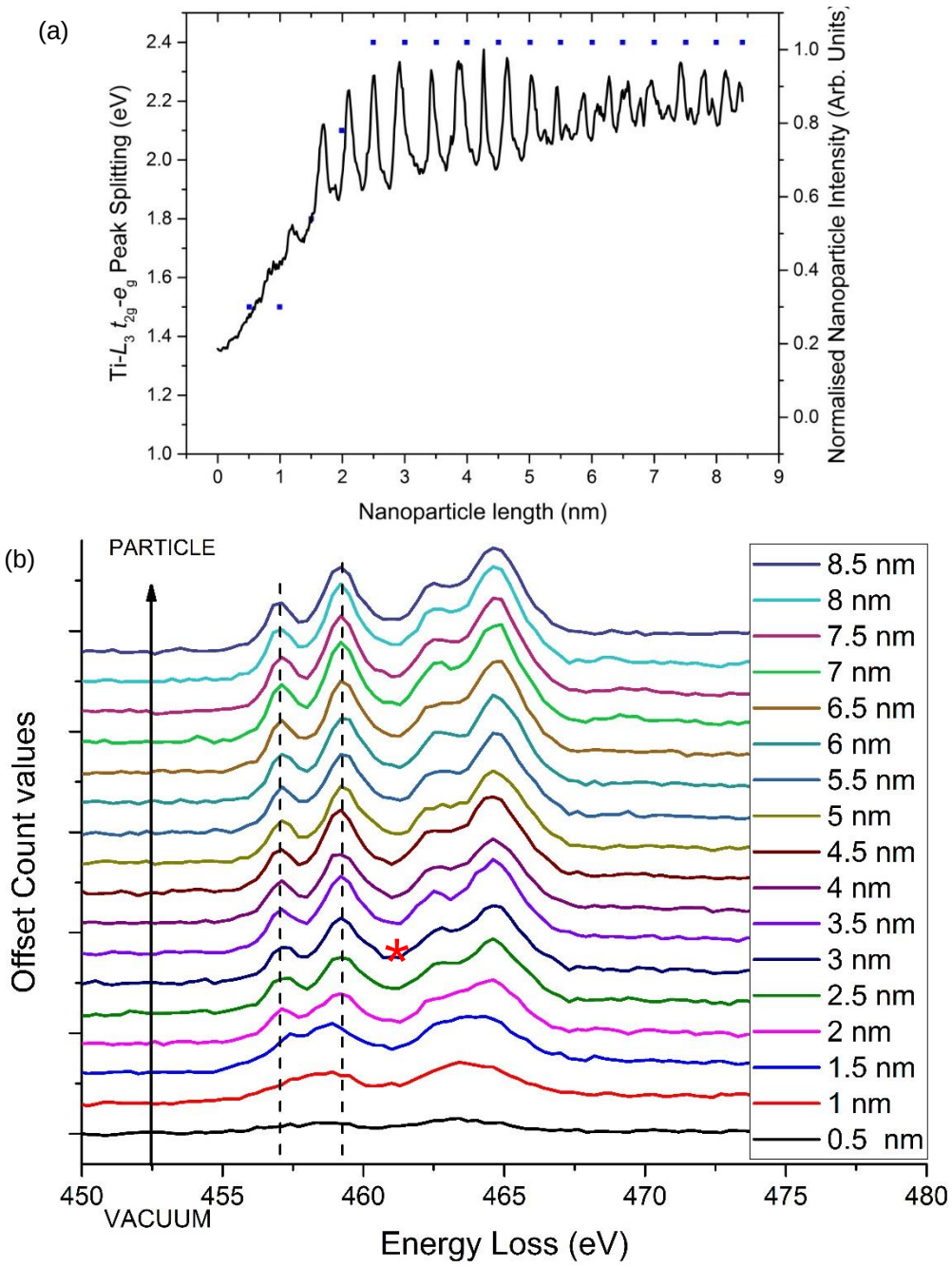

Figure 132. (a) Graph showing the measured Ti-L_3 t_{2g} e_g peak separation (blue data points) across the nanoparticle shown in Figure 131 at 0.5 nm intervals. The HAADF linescan profile of the nanoparticle (black), starts from the surface of the nanoparticle (0 nm) and moves towards the centre (8.5 nm). (b) The extracted EEL spectral series from the linescan shown in Figure 131b, starting from vacuum (bottom) and moving towards the bulk of the nanoparticle (top) at 0.5 nm intervals. The red asterisk highlights the spectrum where the Ti-L_3 t_{2g}-e_g peak splitting increases at around ~ 3 nm into the nanoparticle.

The change in the Ti-L_3 t_{2g}-e_g peak splitting occurs around ~3 nm from the surface of the particle i.e. 6 spectra (Figure 132, red asterisk), presumably due to atomically rough surfaces and incomplete unit cells Figure 131 (b).

The cubic/tetragonal phase fraction for this BST nanoparticle can be estimated; with the assumption that most nanoparticles are cubes of average size ~45 nm (Figure 91, Chapter 4), that have a ~6 nm distorted surface layer (shown in Figure 132) in Equation 12.

$$100x\frac{(45\times10^{-9})^3-(39\times10^{-9})^3}{(45\times10^{-9})^3}=\sim35\ \%\ cubic\ \therefore\ \sim65\ \%\ tetragonal$$

Equation 12. Estimated cubic phase surface fraction (~35 %) implying the remaining tetragonal phase fraction is ~65 %. Thus assumes a ~3 nm surface layer (~6 nm layer in total, shown by the plot in Figure 132) and that the H-BST nanoparticle is cubic.

The estimated volume fractions of the different phases in H-BST by STEM-EELS suggest a ~35 % surface cubic phase and a ~65 % tetragonal bulk phase fraction. The estimated tetragonal phase acquired by Rietveld fitting of synchrotron diffraction data (Figure 91, Chapter 4) suggested a 74 % tetragonal phase fraction present (and a ~26 % cubic phase was present). Thus, there is reasonable agreement between the two techniques.

SuperSTEM Ti-site atomic column centre analysis of H-BST towards the surface of the nanoparticle was performed using Matlab software conducted by Dr David Hernandez-Maldonado at SuperSTEM and is shown in Figure 133. This agreement in tetragonal phase fraction for H-BST could be due to the

smaller distortions observed in H-BST nanoparticles measured by HAADF-STEM as opposed to H-BT (Figure 133 and Figure 130 respectively).

HAADF-STEM Ti-atom column analysis (Figure 133) suggested the Ti-atom columns in the H-BST nanoparticle possessed small regions of net polarisation which implies this is tetragonal. This contradicts the Ti-L_3 EELS data which suggested from the t_{2g}-e_g peak splitting that this region was cubic.

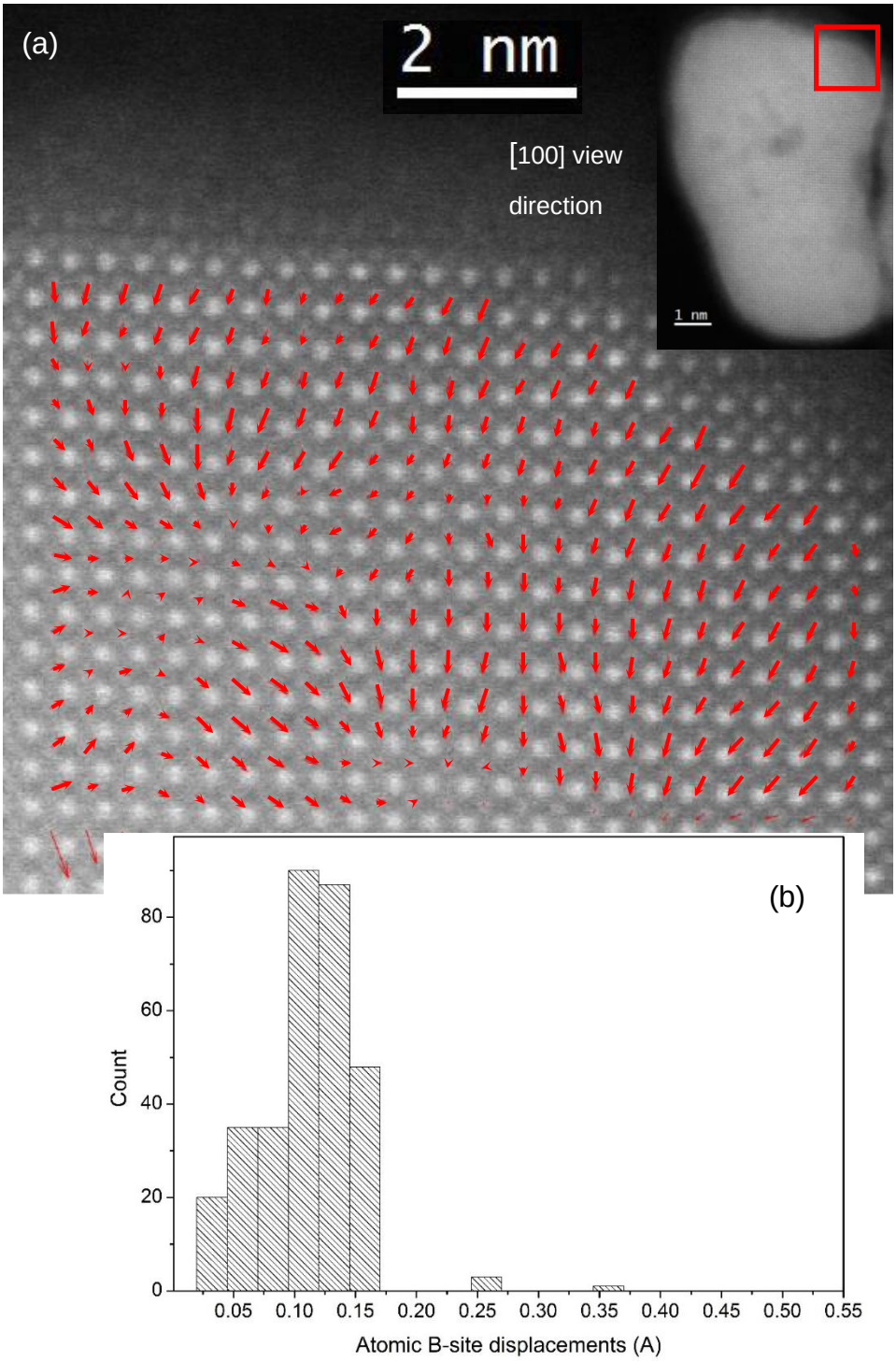

Figure 133. High resolution atomic HAADF STEM image of H-BST nanoparticle surface with the Ti-site atom column displacement analysis shown by the red arrows (full nanoparticle shown inset with the area of analysis highlighted with a red box). The magnitude and direction of the displacements are shown and summarised in (b). The magnitude of the average displacement of the H-BST nanoparticle is 0.10 – 0.15 Å, i.e. less than H-BT displacement (Figure 130).

The average magnitude of the Ti-atom column displacements for H-BST shown in Figure 133 (0.1 – 0.15 Å) were in good agreement with displacement mapping data acquired by Polking *et al.* for a 15 nm $BaTiO_3$ nanoparticles (~0.15 Å) [78].

The Rietveld refinement fitting of synchrotron data for H-BST nanoparticles estimated the unit cell parameters were c = 3.988 Å and a = 3.986 Å (c/a = 1.0004).

This again indicated that the estimation of the overall magnitude of the tetragonal distortion was significantly less (~0.002 Å) when measured by Rietveld analysis of synchrotron-XRD data.

Although H-BST was not extensively analysed by EELS unlike H-BT, the technique was used to apply the phase analysis results of the model systems (like CT-BT and H-BT) to understand the modified $BaTiO_3$ system (H-BST). The results suggested that all barium titanate systems would produce second harmonic light; primarily from the bulk of the nanoparticle due to the random asymmetric nature of the Ti-atom column distortions, in addition to the non-centrosymmetric nature of the atomically rough nanoparticle surfaces (despite STEM-EELS analysis suggesting a cubic surface layer ~4nm for H-BT and ~3 nm for H-BST by Ti-L_3 t_{2g}-e_g peak splitting).

Although the STEM-EELS linescans suggested a cubic surface phase fraction (~14 % for H-BT, ~19 % for H-BST) and a bulk tetragonal phase fraction; second harmonic light is produced primarily from the nanoparticle bulk with an additional contribution from the atomically rough surface. This explains why

SHG is exhibited by all samples (even those that appear 100 % cubic by XRD; Chapter 4).

5.3 Chapter Summary

- CT-BT and CT-BT-400^{o}C EELS spectra were used as calibration spectra for tetragonal and cubic phases respectively.
- Electron diffraction patterns of CT-BT and CT-BT-400^{o}C confirmed the expected tetragonal to cubic phase transition occurred when heated above the Curie point.
- Electron diffraction of H-BT and H-BT-400^{o}C also showed that the tetragonal to cubic phase transition occurs when heating above the Curie point.
- Gaussian fitting of the H-BT and H-BT-400^{o}C EEL spectra showed the same reduction in the Ti-$L_{2,3}$ edge t_{2g}-e_g peak separation as CT-BT and CT-BT-400^{o}C when transformed to a cubic phase following heating above the Curie point.
- The Ti-L_3 edge t_{2g}-e_g peak separation in H-BT is reduced at the surface of the nanoparticles and up to 10 nm into the bulk. This indicates an *intra*-particle phase variation accounting for a core volume fraction of ca. ~73 % (compared to ~ 60 % by XRD – Chapter 4)
- Atomically resolved HAADF-STEM images of H-BT acquired at SuperSTEM showed an atomically ‘rough’ nanoparticle surface that may be cubic (by STEM-EELS) but might still contribute to SHG light production through incomplete unit cells.

- HAADF-STEM Ti-atom column centre analysis (towards the centre of the nanoparticle) conducted at SuperSTEM suggested that the Ti-atom in each H-BT unit cell possessed a ~0.2 Å random asymmetric displacement associated with local defects or strains. However, XRD suggests that there is a net displacement of ~0.02 Å.
- H-BST showed a similar reduction of Ti-L_3 edge t_{2g}-e_g splitting up to ~6 nm in from the surface of the nanoparticle as compared to the bulk. This indicates an *intra*-particle phase variation accounting for a core volume fraction of ca. ~65 % (compared to ~75 % by synchrotron XRD – Chapter 4).
- HAADF-STEM Ti-atom column centre analysis suggested a ~0.1/0.15 Å local displacement while XRD suggests a *net* unit cell distortion of ~0.002 Å i.e. smaller than for H-BT. The local distortions are however shown by HAADF-STEM to continue to the surface of the nanoparticle despite STEM-EELS suggesting this surface layer is cubic.
- SHG of light in all the samples (shown in Chapter 4) would likely be a combination of the non-centrosymmetric nature of the unit cells shown by the local and net asymmetric distortions throughout the nanoparticles as well as the atomically 'rough' nanoparticle surfaces. i.e. they are likely to be both a surface and bulk effect.

Chapter 6 – Exposure of hydrothermally synthesised barium titanate and barium strontium titanate nanoparticles to lung epithelial cells.

The previous results chapters have focused on the crystal phase characterisation of hydrothermally synthesised barium titanate and barium strontium titanate nanoparticles. Chapter 4 discussed the X-Ray analysis (laboratory and synchrotron) and optical second harmonic generation of the nanoparticles, both techniques suggesting that a tetragonal phase fraction is present (up to ~60 % for H-BT and ~75 % for H-BST by the estimates of Rietveld analysis of data). Chapter 5 investigated individual particles by *in-situ* heating STEM-EELS and HAADF-STEM imaging showing that there is a surface layer of cubic-like character present on all nanoparticles in addition to an asymmetric distortion of the central Ti-atom position in the $BaTiO_3$ unit cell throughout particles. Overall, the characterisation from the previous chapters showed an *intra*-particle phase variation of $BaTiO_3$ involving a tetragonal core and a 'cubic-like' surface (~ 5 nm thick).

This chapter investigates the behaviour of the nanoparticles in aqueous suspensions (including cell media) and nanoparticle delivery into lung epithelial (A549) cells. The cytotoxic and genotoxic *in-vitro* assays of uncoated and poly-L-lysine (PLL) coated nanoparticles are presented initially in order to highlight the cell viability/genotoxic differences between the two nanoparticle coatings. The cytotoxic and genotoxic results are then supplemented with characterisation of nanoparticle suspensions in water at certain delivery concentrations by FTIR, dynamic light scattering and zeta potential measurements. Dynamic light scatting of nanoparticles in water, serum-free

media and complete cell culture media provided hydrodynamic size ranges. Zeta potential measurements provided surface charge values of uncoated and PLL coated nanoparticles dispersed in water.

Cellular uptake of nanoparticles was confirmed by low and high kV SEM of critically point dried cells and serial focused ion beam (FIB) sectioning by SEM. Further uptake was evidenced by TEM and HAADF-STEM characterisation of resin embedded cell sections. The HAADF-STEM data showed the nanoparticles were internalised and this was confirmed with elemental analysis by TEM-EDX. Finally, the nanoparticle suspension behaviour was characterised by cryo-TEM to identify changes in nanoparticle dispersion between H-BT and H-BT-PLL at 100 µg/mL in complete cell culture media.

The A549 cell viability (MTT assay) and genotoxicity (Comet assay) of H-BT, H-BT-PLL, H-BST and H-BST-PLL were undertaken and analysed by Dr Olga Posada-Estefan (School of Medicine, University of Leeds, UK). The MTT assay results for the uncoated and PLL coated nanoparticles are shown in Figure 134 & Figure 135 and Comet assay results are shown in Figure 136 & Figure 137 respectively.

6.1 Cell viability MTT assays and genotoxic Comet assays

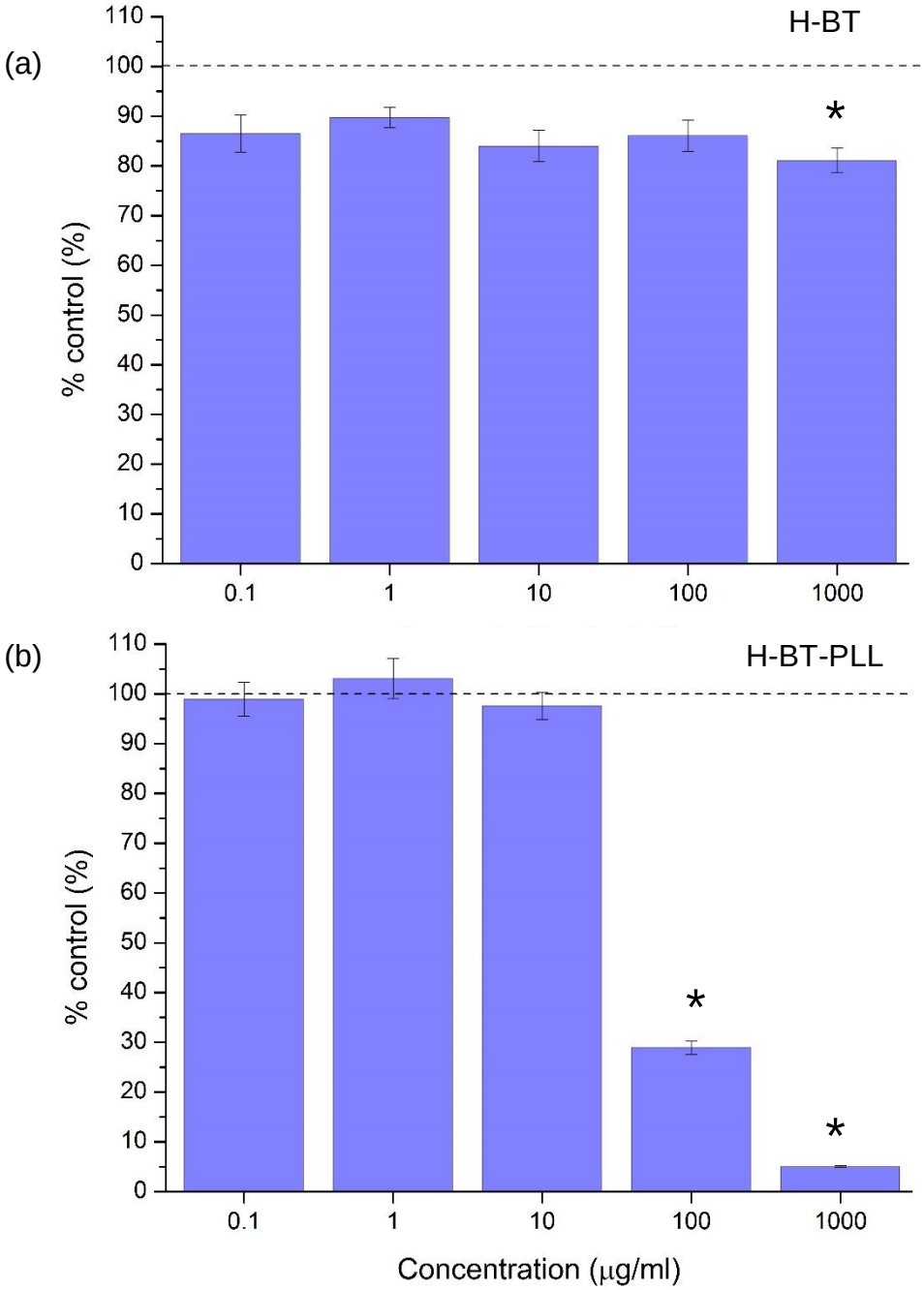

Figure 134. MTT Cell viability assay of H-BT and H-BT-PLL nanoparticles at varying concentrations against the control (horizontal dotted line at 100 %). (a) H-BT shows a significant difference only at exposure of 1000 µg/mL, analysed by ANOVA ($p<0.05$). (b) H-BT-PLL shows a significant difference at exposures of 100 and 1000 µg/mL, analysed by ANOVA ($p<0.05$).

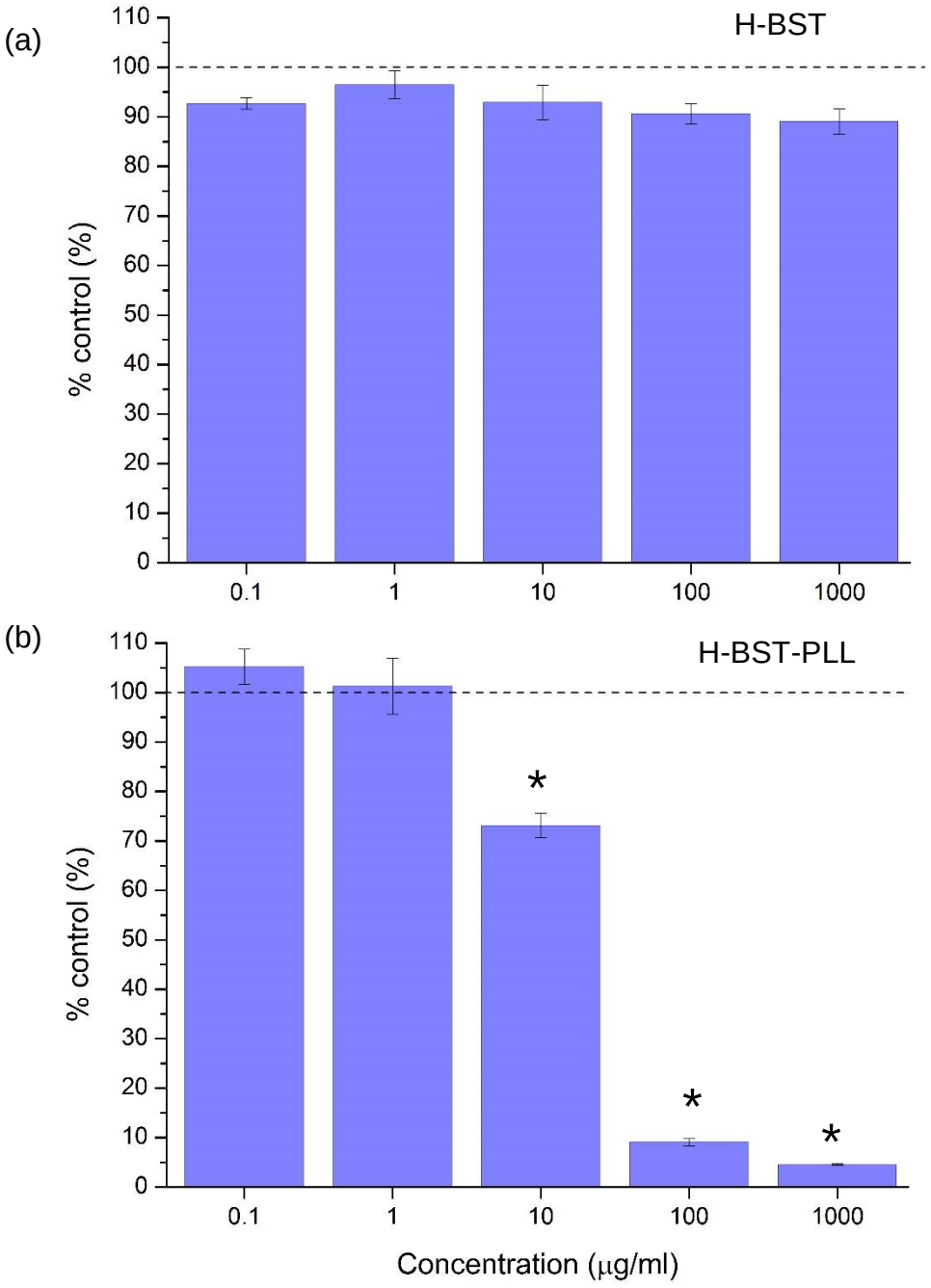

Figure 135. MTT Cell viability assay of H-BST and H-BST-PLL nanoparticles at varying concentrations against the control (horizontal dotted line at 100 %). (a) H-BST shows a significant difference only at exposure of 1000 µg/mL, analysed by ANOVA ($p<0.05$). (b) H-BST-PLL shows a significant difference at exposures of 10, 100 and 1000 µg/mL, analysed by ANOVA ($p<0.05$).

The MTT assays of H-BT, H-BT-PLL (Figure 134) H-BST and H-BST-PLL (Figure 135) that showed exposure concentrations with a significant difference from the control were marked with an asterisk and were mainly present at high doses. The difference in cell viability between the uncoated and PLL-coated nanoparticles showed that coated samples caused significant drops in cell viability at exposures above 100 µg/mL for H-BT-PLL and above 10 µg/mL for H-BST-PLL.

The decrease in cell viability for H-BT and H-BST nanoparticles at 1000 µg/mL is likely to be due to the high concentration of nanoparticles present, which might then overload the cells. For the coated H-BT-PLL and H-BST-PLL coated nanoparticles, the cell viability was significantly reduced for the higher nanoparticle concentrations. This decrease in cell viability may at first glance be due to the positively charged PLL-coating around the nanoparticle. The positive charge possesses a higher affinity than a neutral or negatively charged nanoparticle to the negatively charged A549 cell surface [51] and as a result, more nanoparticles may have undergone endocytic uptake in comparison to H-BT or H-BST nanoparticles (negative surface charge). This will be explored in detail later.

The genotoxic comet assays for the same samples are summarised in the same format in Figure 136 & Figure 137.

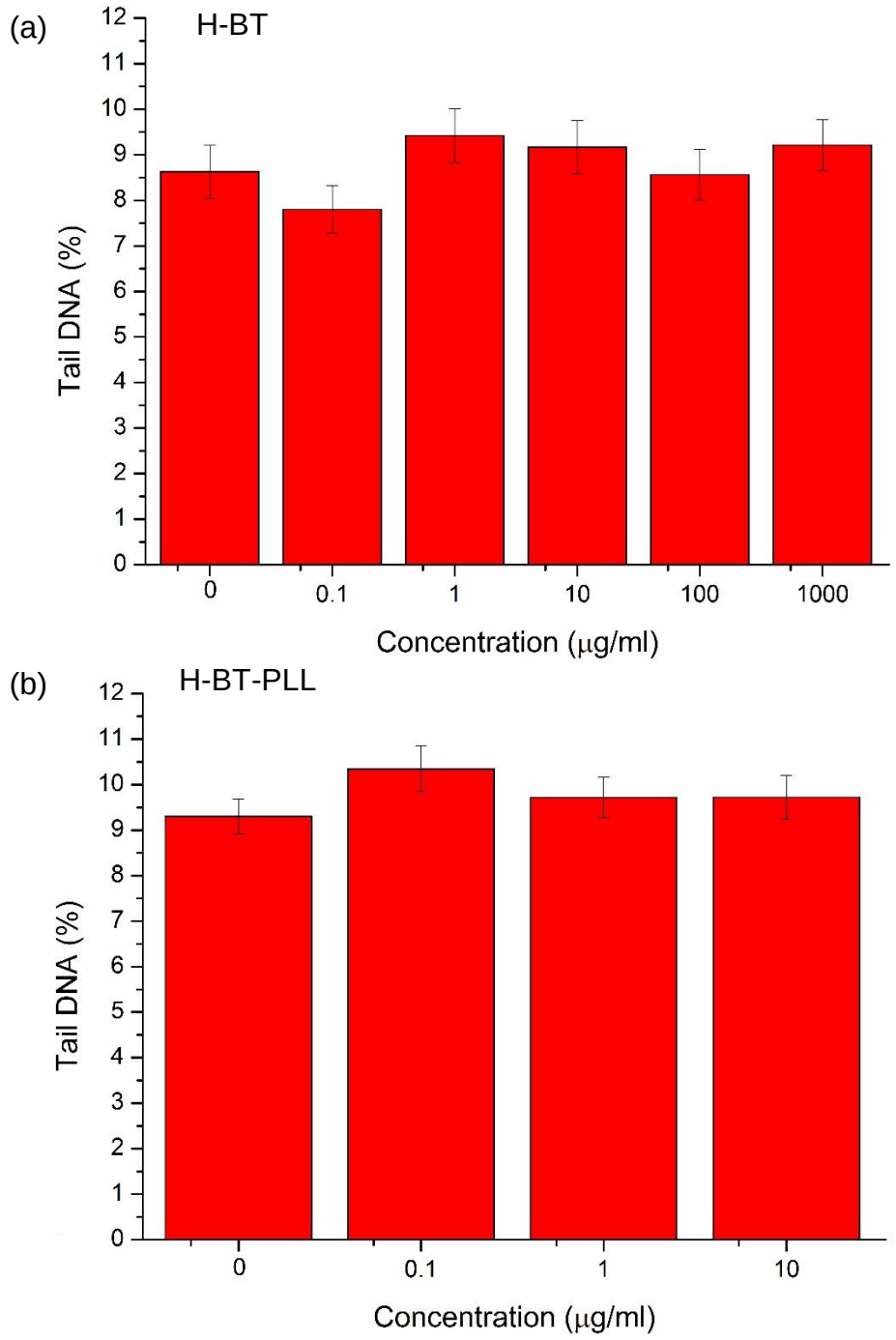

Figure 136. COMET assay of (a) H-BT and (b) H-BT-PLL nanoparticles with the control concentration shown as 0 μg/mL. Error bars show the standard deviation at 4 replicates per exposure. The change in concentration between the H-BT and H-BT-PLL nanoparticles is due to the COMET assay failing (explained in discussion) for nanoparticle concentrations higher than 10 μg/mL for H-BST-PLL. The results shown above however, display no significant difference with the control ($p < 0.05$) at any exposure concentrations.

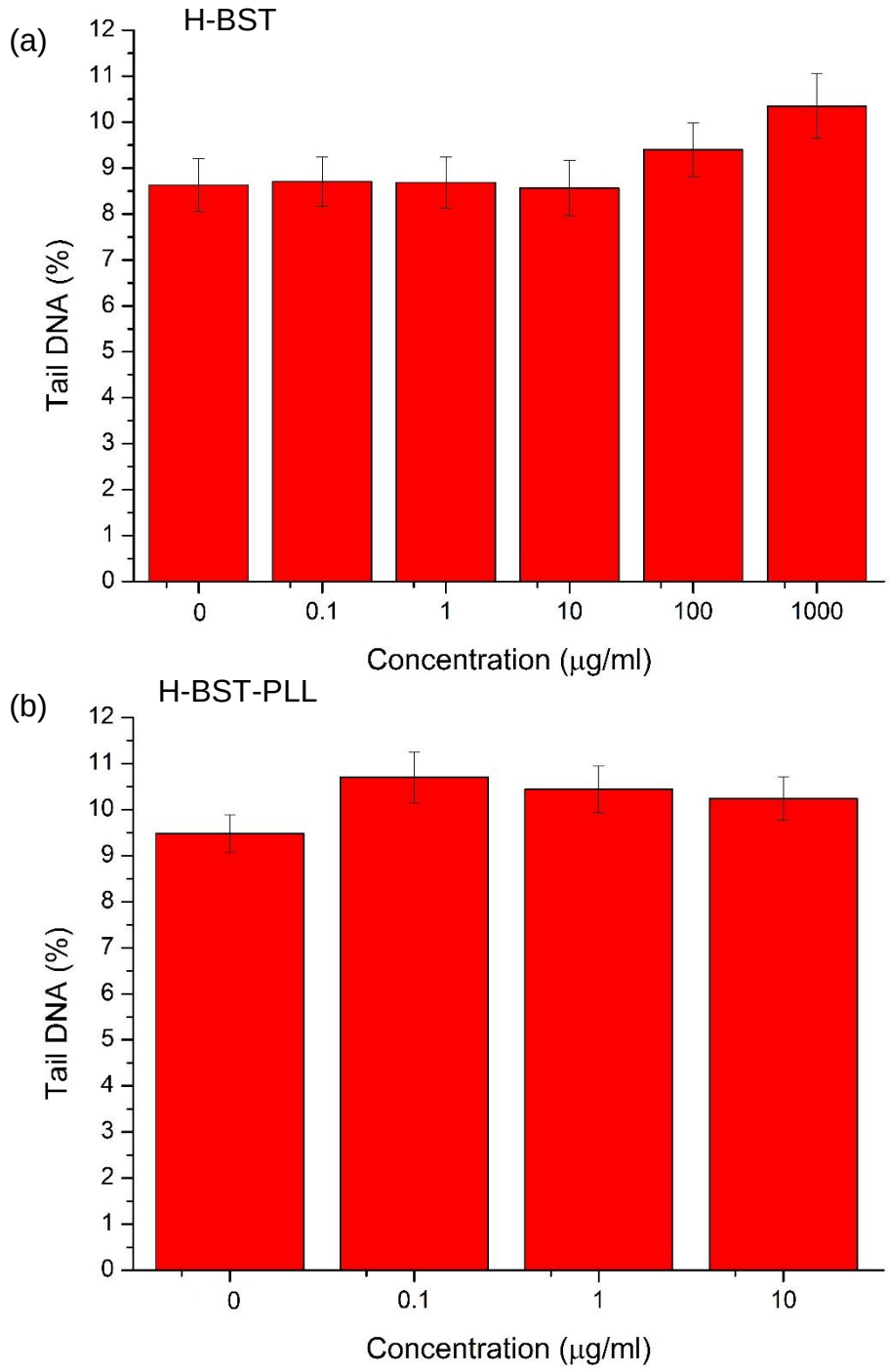

Figure 137. COMET assay of (a) H-BST and (b) H-BST-PLL nanoparticles with the control concentration shown as 0 µg/mL. Error bars show the standard deviation at 4 replicates per exposure. The change in concentration between the H-BST and H-BST-PLL nanoparticles is due to the COMET assay failing (explained in discussion) for nanoparticle concentrations higher than 10 µg/mL for H-BST-PLL. The results shown above however, display no significant difference with the control ($p < 0.05$) at any exposure concentrations.

The Comet assay is a measure of the denatured DNA generated in the A549 cells over a 24-hour period. The repeated failure of the comet assay above 10 µg/mL for the PLL-nanoparticle concentrations may be due to the interaction of the positively charged polymer with the comet assay or the failure of DNA separation during electrophoresis (due to a larger positive charge present because of the higher nanoparticle concentrations). The comet assay shown for H-BT nanoparticles shows no significant difference between the nanoparticle concentrations and suggests they produce no genotoxic effects. There is an increase in DNA damage for H-BST nanoparticle concentrations above 10 µg/mL but it is not a significant difference ($p<0.05$) when compared with the control.

The cell viability and genotoxic assays (Figure 134 & Figure 136) have shown that there is a significant difference between the response of A549 cells to exposure of uncoated H-BT nanoparticles and PLL coated H-BT nanoparticles. These particular assays were considered when the nanoparticles and the nanoparticle dispersions were characterised by further techniques.

To confirm PLL is coating the nanoparticles, FTIR of H-BT, H-BT-PLL, H-BST and H-BST-PLL were analysed qualitatively from the spectra. The PLL-coating was then imaged by conventional bright field TEM supplemented with zeta potential data given in Section 6.2.

6.2 Nanoparticle coating

The ATR-FTIR spectra of poly-L-lysine, H-BT, H-BT-PLL and H-BST, H-BST-PLL respectively are shown in Figure 138. To confirm that the nanoparticles were successfully coated with PLL, FTIR vibrations are compared in Table 23. The coating was then visualised by conventional bright field TEM of H-BT-PLL and H-BST-PLL shown in Figure 139.

Zeta potential measurements of uncoated and PLL coated nanoparticles in water provided data on the electrical surface potential of the nanoparticle-water electrical double layer (discussed in Chapter 2, Figure 34). The data revealed a change in surface potential when the poly-L-lysine coating was successful (Figure 140).

The behaviour of nanoparticles suspended in water, serum free media and complete cell culture media were characterised by dynamic light scattering. This technique estimates the hydrodynamic size of agglomerates and outputs particle size distribution against scattering intensity, volume and number.

SEM imaging of critically-point dried A549 cells, FIB-SEM imaging of resin embedded A549 cell sections and HAADF-STEM of resin embedded cell sections confirmed cellular uptake of nanoparticles. Cryo-TEM of plunge frozen H-BT and H-BT-PLL nanoparticle suspensions were collected in water and complete cell culture media in order to correlate DLS suspension data and quantitative cryo-TEM analysis.

The FTIR data is presented on the following pages.

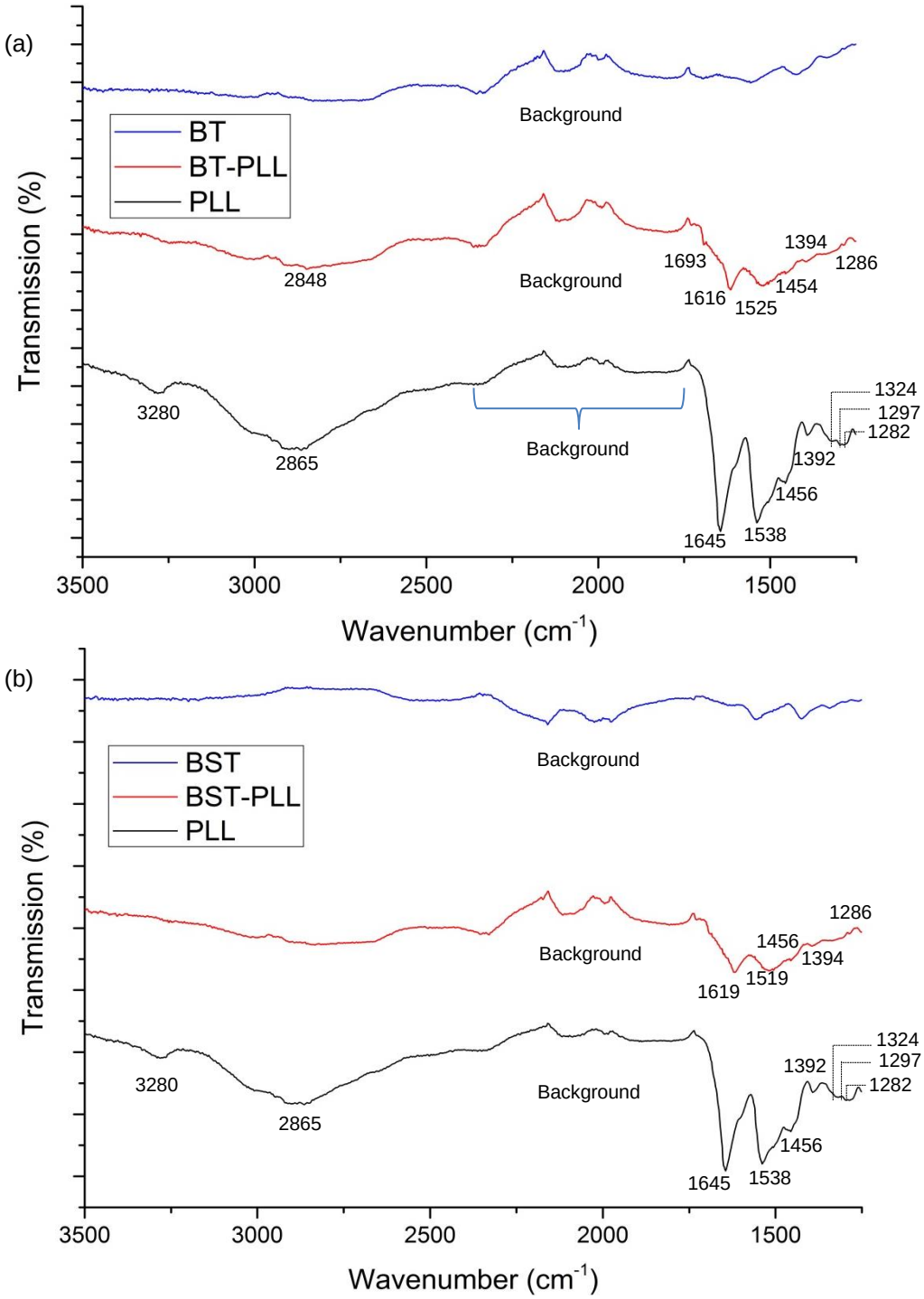

Figure 138. Qualitative FTIR comparison of H-BT-PLL and H-BST-PLL (red) spectra shows key vibrations common with PLL (black). (a) FTIR spectra of uncoated H-BT (blue), H-BT-PLL and poly-L-lysine. (b) FTIR spectra of H-BST, H-BST-PLL and poly-L-lysine. The PLL peaks that are labelled are attributed to the CH_2NH_2 wagging (1456 cm^{-1}), secondary amide OC-NH (1538 cm^{-1}) and primary amine NH_2 (1645 cm^{-1}) vibrations; summarised in Table 23.

Vibration	PLL Wavenumbers (cm^{-1})	Vibration	H-BT-PLL Wavenumbers (cm^{-1})	Vibration	H-BST-PLL Wavenumbers (cm^{-1})
Rocking/ twisting of NH_2	1282	Rocking/ twisting of NH_2	1286	Rocking/ twisting of NH_2	1285
Rocking/ twisting of NH_2	1297				
Amide III peak	1324				
O-H bending for carboxylic acid	1392	O-H bending for carboxylic acid	1394	O-H bending for carboxylic acid	1394
CH_2NH_2 wagging	1456	CH_2NH_2 wagging	1454	CH_2NH_2 wagging	1456
Secondary amide OC-NH	1538	Secondary amide OC-NH	1525	Secondary amide OC-NH	1519
Primary amine NH_2	1645	Primary amine NH_2	1616	Primary amine NH_2	1619
CH_2	2865	PLL–β sheet structure	1693		
OC-NH peptide group	3280	CH_2	2848		

Table 23. Summary of FTIR vibrations for PLL, H-BT-PLL and H-BST-PLL samples. All the PLL vibrations are shown against the relevant H-BT-PLL and H-BST-PLL vibrations. The PLL-β sheet vibration present in H-BT-PLL, was due to the slow drying of the sample as opposed to random coil structures forming when dried quickly; as seen by Rozenberg *et al.* [143].

The FTIR data (Table 23) showed the vibrations of PLL, H-BT-PLL and H-BST-PLL spectra and highlighted the NH_2 rocking/twisting, CH_2NH_2 wagging, secondary amide (OC-NH) and primary amine (NH_2) vibrations. This confirmed the co-localisation of PLL in the nanoparticle samples.

The H-BT-PLL and H-BST-PLL nanoparticles were suspended in water and dropcast onto a holey carbon support film suspended on a copper TEM grid and imaged by bright field TEM as shown in Figure 139.

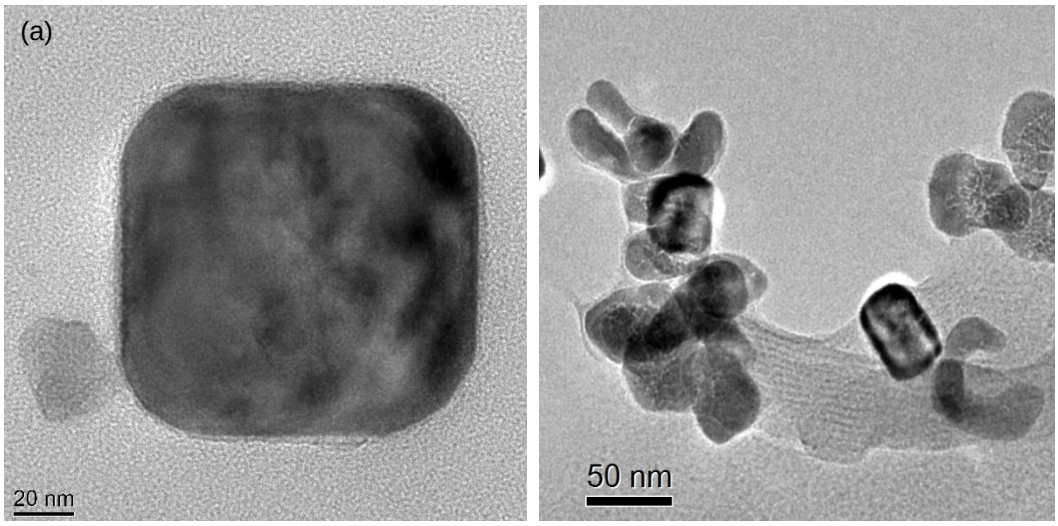

Figure 139. (a) Bright field TEM image of a H-BT-PLL nanoparticle with the PLL layer compressed on to the surface. (b) Bright field TEM image of H-BST-PLL nanoparticles. The microscope was defocused to provide sufficient contrast in the PLL layer. Such amorphous coatings were not visible at any defocus in the uncoated nanoparticles (Figure 87 and Figure 93 in Chapter 4).

The PLL coating on barium titanate and barium strontium titanate nanoparticles (described in Section 3.2) can effect the overall particle size by two main properties of the polymer. The first being the polymer molecular weight. If there is a large range in polymer molecular weight (i.e. 70,000 to 300,000) then some coated nanoparticles will appear smaller in size than others due to some lower

molecular weight polymers coating the nanoparticles, in comparison to the coating with larger molecular weight polymers which will produce a larger nanoparticle size. In addition, the ratio of polymer to particle concentrations will also effect the size of the nanoparticles in two ways. If the polymer to particle ratio is small, the polymer will likely adsorb to the particle surface, relax and form bridges with surrounding nanoparticles due to favouring bond forming enthalpy [106] this will therefore increase the measured nanoparticle size. If the poly-particle ratio is high, then fast adsorption will occur with no relaxation of the adsorbed polymer and will produce a sterically stabilised nanoparticle suspension.

Zeta-potential measurements of uncoated H-BT and H-BST nanoparticles and PLL-coated nanoparticles are shown in Figure 140 and the change in zeta potential from uncoated, negatively charged nanoparticles to positively charged, PLL-coated particles revealed that coating of H-BT and H-BST with PLL was successful.

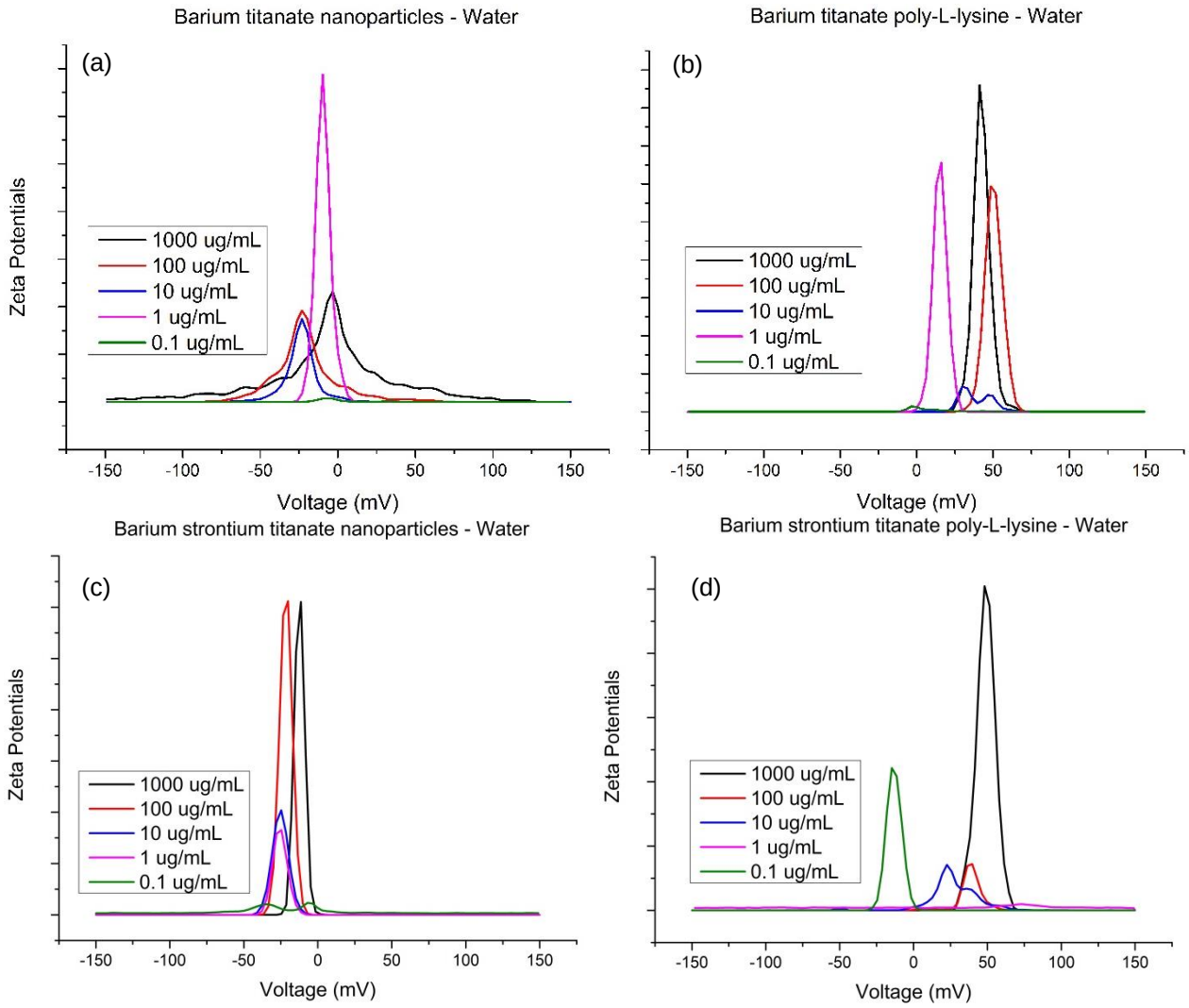

Figure 140. The average zeta potential measurements of nanoparticles suspended in water at each concentration. (a) H-BT average zeta potential value of – 28 mV. (b) The H-BT-PLL average zeta potential value of + 49 mV. (c) H-BST average zeta potential value of – 29 mV. (d) H-BST-PLL average zeta potential value of + 47 mV. The H-BST-PLL 0.1 µg/mL concentration 'failed' (showing a negative zeta potential) as a result of the signal being too weak to measure.

When combined the FTIR data, bright field TEM images and zeta potential measurements showed that PLL coating of the nanoparticles was successful. The uncoated (H-BT, H-BST) and PLL-coated (H-BT-PLL, H-BST-PLL) nanoparticle suspension behaviour was then investigated by DLS suspended in water, serum free media and complete cell culture media in a range of concentrations the results are given in Section 6.3.

6.3 DLS of uncoated and PLL-coated nanoparticle suspensions

The uncoated and PLL-coated nanoparticle suspensions were investigated by dynamic light scattering (DLS) in suspending media; the hydrodynamic sizes were plotted against scattering intensity, particle volume and particle number distributions.

The stability of a nanoparticle suspension is affected by the surface charge of the nanoparticle interacting with the suspending media. Changing either the surface of the nanoparticle or the suspending media, will polarise any media components at the nanoparticle surfaces differently. Work here presents the nanoparticle suspensions in water, serum free cell culture media and complete cell culture media. The dynamic light scattering of H-BT and H-BT-PLL nanoparticles are shown in Figure 141 and Figure 143 respectively for water, serum free media and complete cell culture media. DLS of H-BST and H-BST-PLL nanoparticles suspensions are shown in Figure 144 and Figure 145 respectively for the case of water, serum free media and complete cell culture media. The DLS plots are shown for consistent serial dilution concentrations (1000, 100, 10, 1, 0.1 µg/mL) similar to the cell culture experiments for the MTT assays (Figure 134 & Figure 135) and Comet assays (Figure 136 & Figure 137). The dispersion indices for the H-BT and H-BT-PLL are summarised in Table 24 and Table 25 respectively. The dispersion indices for the H-BST and H-BST-PLL are summarised in Table 26, and a descriptive summary of the dynamic light scattering graphs is shown in Table 27.

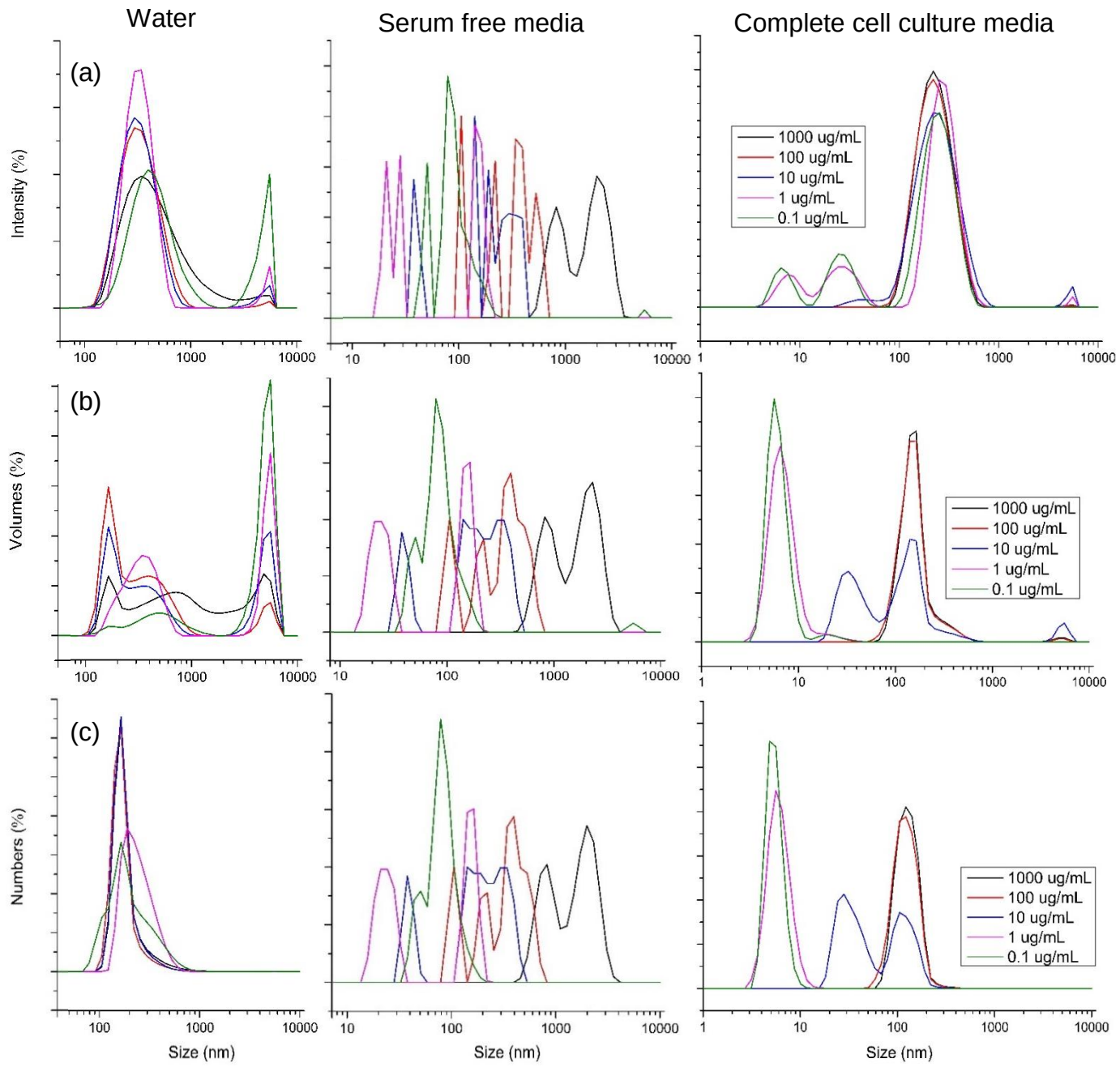

Figure 141. Dynamic light scattering of H-BT nanoparticles displayed in columns of: water, serum free media and complete cell culture media. The particle frequency distributions are plotted against hydrodynamic size at: 1000, 100, 10, 1 and 0.1 µg/mL. (a) The H-BT nanoparticle intensity distribution, (b) H-BT volume distribution and (c) H-BT number distribution in the labelled suspending media (water, serum free and complete media). The DLS graphs will be discussed by intensity, volume and number distribution for each suspending media.

6.3.1 DLS of H-BT nanoparticles suspended in water.

Chapter 4 showed that the average primary particle size of H-BT measured by TEM was ~140 nm. H-BT nanoparticles dispersed in water and measured by DLS intensity showed a reasonably monodisperse system, where small agglomerates of primary particle size dominated (shown at ~300 nm) but large agglomerates (shown at 10,000 nm) were also clearly observed. The same DLS results plotted by volume showed a similar distribution to that by intensity, where there are small nanoparticle clusters similar to the primary particle size (~100–300 nm) in addition to large nanoparticle agglomerates at ~10,000 nm.

In the same data plotted in terms of number, the nanoparticle suspension appeared much more monodisperse and the size roughly corresponded to clusters of relatively few primary H-BT nanoparticles (~100–300 nm). The absence of large agglomerate sizes at 10,000 nm suggested that these are relatively few in frequency/number even if seen/detected by volume. The distributions in Figure 141 revealed the nanoparticle behaviour in water and schematic diagrams of the types of suspended nanoparticle clusters are shown in Figure 142.

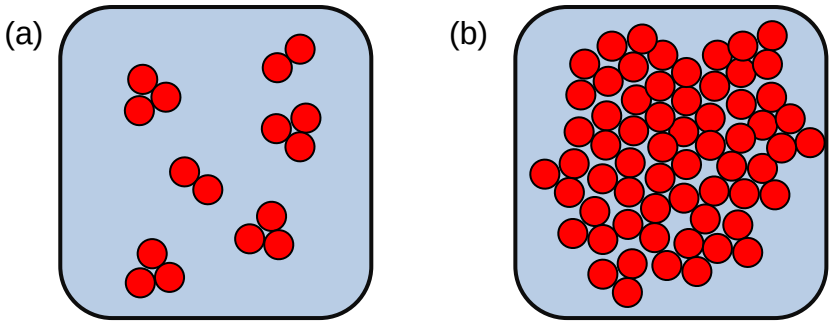

Figure 142. Schematic representations of the H-BT nanoparticles (red) with a primary particle size of ~ 130 nm. (a) The DLS graphs showing the majority of the H-BT hydrodynamic nanoparticles are of the order of the primary particle size (ranging from ~100 – 300 nm). (b) Heavily agglomerated H-BT nanoparticles (at ~10,000 nm) are present in volume and intensity distributions but not present (relatively) by number and are therefore present in low frequency in comparison to the smaller clusters of H-BT nanoparticles.

6.3.2 DLS of H-BT nanoparticles suspended in serum free media.

The DLS results measured for nanoparticle dispersions in serum free media (Figure 141) suggested that these were polydisperse at all nanoparticle concentrations. The distributions by intensity, number or volume all showed a similar behaviour. It was possible that the inorganic salts and electrolytes in the serum free media interfered with the DLS measurements [161,162].

6.3.3 DLS of nanoparticles suspended in complete cell culture media.

Complete cell culture media consisted of: DMEM, 10 % by volume of Foetal calf serum and 1 % by volume of Penicillin-Streptomycin typically between 5-50 nm [161,163] (prepared by Dr Olga Posada-Estefan, School of Medicine, University of Leeds). These additional components present in the suspension were seen in each distribution plot (~1 – 50 nm). Thus, the remaining scatter

was interpreted as the H-BT nanoparticles dispersed in complete media which showed a similar distribution by intensity to H-BT nanoparticles in water, i.e. small clusters of the H-BT primary particle size (~100-300 nm) and some larger clusters. The DLS results from H-BT nanoparticles suspended in complete media size were dominated by the smaller components of the serum proteins and crucially also showed that small clusters of H-BT primary particles were present in suspension; this is explored later by Cryo-TEM analysis (Section 6.6). The DLS data generates a probability (Poisson) distribution that is normalised and interpreted by a dispersion index. If the DLS peak width is as big as the height (i.e. height/width = 1) then the suspensions are polydisperse and the dispersion index will be 1. Dispersion index values <0.25 – 0.3 means that the suspensions are near monodisperse [146]. The distributions summarised in Table 24 showed that H-BT nanoparticles (in general) were reasonably monodisperse in both water and complete cell culture media (DI <0.2), whereas the nanoparticles suspended in serum-free media were polydisperse or the media interfered with the light scattering (most dispersion indices were equal to 1).

Concentration (µg/mL)	**H-BT**		
	Water	**Serum free media**	**Complete media**
1000	0.28	0.52	0.16
100	0.19	1.0	0.20
10	0.21	1.0	0.42
1	0.44	1.0	0.35
0.1	0.48	1.0	0.48

Table 24. The intensity distribution dispersion indices of the H-BT nanoparticles suspended in water, serum free media and complete cell culture media.

The dispersion indices showed a concentration dependence, where low nanoparticle concentrations were apparently more polydisperse, presumably this was because there are relatively few clusters to dominate the intensity scatter at these concentrations.

The H-BT-PLL nanoparticle suspensions in water, serum free media and complete cell culture media are shown in Figure 143. The H-BT-PLL nanoparticle dispersion are discussed and dispersion indices given in Table 25.

6.3.4 DLS of H-BT-PLL nanoparticles suspended in water.

The H-BT-PLL nanoparticles dispersed in water were similar in size distribution to the H-BT nanoparticles; there were small clusters of primary particle size (at ~100–600 nm) by intensity and there were also large agglomerates (~10,000 nm) present in the intensity size distribution.

By volume, the H-BT-PLL nanoparticles showed a multimodal size distribution where there were nanoparticles of primary particle size (~100–200 nm), small clusters of primary particles (~500–1000 nm) and large agglomerates also present (~10,000 nm).

By number, the H-BT-PLL nanoparticle suspension showed a broader dispersion than the primary particle size (~100–1000 nm) with only some secondary clusters of a few primary H-BT-PLL nanoparticles at the lower concentrations. Once again the large agglomerates (>1000 nm) were absent by suggesting they are low in frequency (similar to the nanoparticle size distribution seen for H-BT in water – Figure 141 and Figure 142).

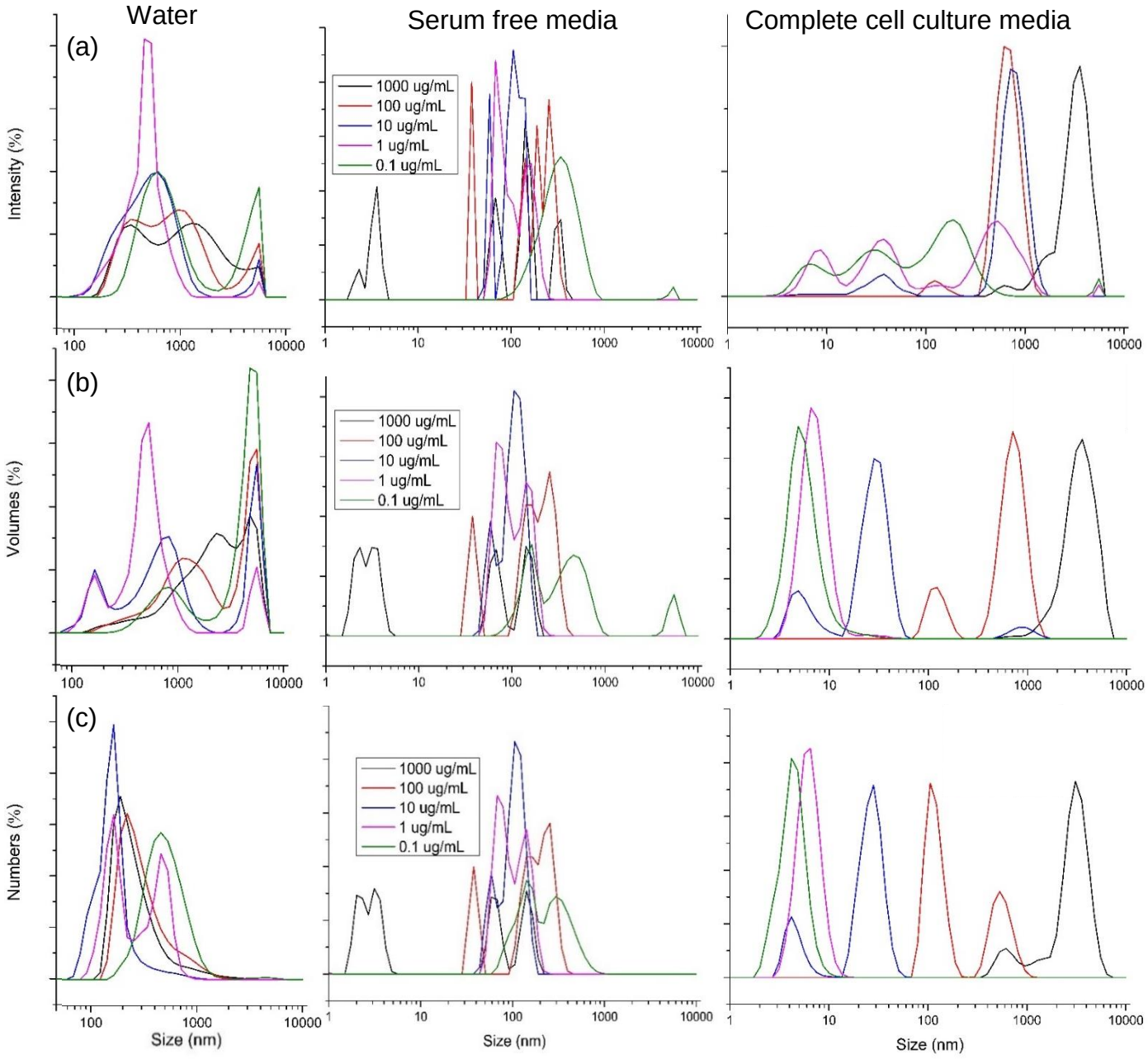

Figure 143. Dynamic light scattering of H-BT-PLL nanoparticles displayed in columns of: water, serum free media and complete cell culture media. The particle distributions are plotted against hydrodynamic size at: 1000, 100, 10, 1 and 0.1 µg/mL. (a) The H-BT-PLL nanoparticle intensity distribution, (b) H-BT-PLL volume distribution and (c) H-BT-PLL number distribution in the labelled suspending media. The DLS graphs will be discussed by intensity, volume and number distribution for each suspending media.

6.3.5 DLS of H-BT-PLL nanoparticles suspended in serum free media.

The nanoparticle dispersion shown in Figure 143 showed that the nanoparticles were polydisperse at all concentrations. The size distribution of H-BT-PLL nanoparticles would suggest that different electrolytes present in the cell culture media interacts with the polymer causing an unstable suspension. Electrolytes present in serum free media (such as: Ca^{2+} and Mg^{2+}) will cause coagulation by reducing the double layer which will produce a polydisperse nanoparticle suspension. The nanoparticle size distributions by intensity, number or volume all showed similar behaviour. The dispersion indices are summarised in Table 25. It is possible that the serum free media interfered with the DLS measurements.

6.3.6 DLS of H-BT-PLL nanoparticles suspended in complete cell culture media.

The DLS intensity distribution of H-BT-PLL nanoparticles dispersed in complete cell culture media (Figure 143) showed a similar behaviour to H-BT nanoparticles dispersed in complete media (Figure 141). Serum components were present around ~10–50 nm in addition to small clusters of the H-BT-PLL primary particle size (~100–500 nm) with large agglomerates present at ~10,000 nm by intensity, volume and number. Electrolytes present in complete cell culture media (such as: Ca^{2+}, Mg^{2+}, foetal bovine serum and antibiotics) will effect the double layer of PLL coating on $BaTiO_3$ nanoparticles. Bridging flocculation may occur as a result of a low polymer to particle ratio with increasing nanoparticle concentrations (100 µg/mL and higher) which may

produce larger hydrodynamic sizes that were measured in the H-BT-PLL distributions (Figure 143). However this will be a result of the synthesis parameters described in Chapter 3 and will not be investigated in this work.

The volume distribution showed that the suspension is dominated mainly by the smaller serum components of complete cell culture media (~1–50 nm). The concentration at 100 µg/mL showed a bimodal distribution of H-BT-PLL primary particle size (~100 nm) and small clusters of primary particles (~500–1000 nm). The number distribution of H-BT-PLL nanoparticles suspended in complete media (Figure 143) showed that the serum proteins were dominant (~1–50 nm). The concentration at 100 µg/mL showed the H-BT-PLL primary particle size at (~100 nm) in addition to an intermediate particle size at (~500 nm). The number distribution also showed that an intermediate particle size (~500 nm) was present at 1000 µg/mL but reduced in number as the dispersion mainly consisted of large agglomerates (~10,000 nm).

The dispersion indices for H-BT-PLL nanoparticles suspended in water, serum free media and complete cell culture media are summarised in Table 25.

Concentration (µg/mL)	**H-BT-PLL**		
	Water	**Serum free media**	**Complete media**
1000	0.44	0.69	0.09
100	0.56	1.0	0.56
10	0.46	1.0	0.54
1	0.53	1.0	0.43
0.1	0.52	0.11	0.24

Table 25. The intensity distribution dispersion indices of the H-BT-PLL nanoparticles suspended in water, serum free media and complete cell culture media.

The dispersion indices shown in Table 25 highlighted that the H-BT-PLL nanoparticles followed a similar trend to that of H-BT nanoparticles. The dispersion in water showed that the H-BT-PLL nanoparticles are reasonably stable. The dispersion in serum free media gave problems during measurement (similar dispersion indices to those of H-BT; Table 24) whilst the H-BT-PLL nanoparticles in complete cell culture media were reasonably stable (although as already discussed the distributions were dominated by the components in the media).

Summaries of the H-BT and H-BT-PLL DLS results are shown in Table 27 where the dispersion is discussed for each concentration and dispersion type. However, the following section will discuss the dynamic light scattering results from H-BST and H-BST-PLL nanoparticles suspended in water, serum free media and complete cell culture media.

6.3.7 DLS of H-BST nanoparticles suspended in water, serum free media and complete cell culture media.

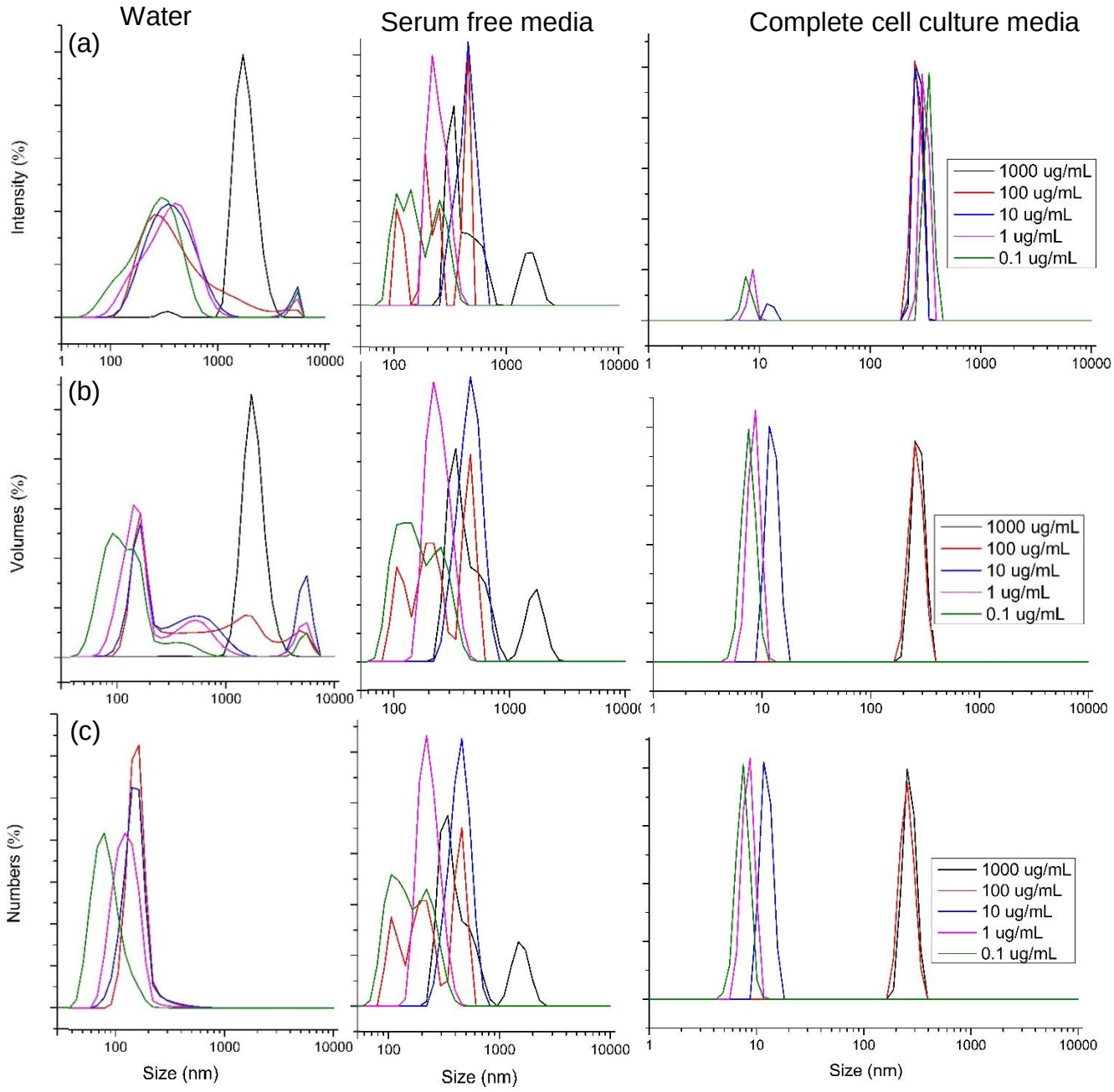

Figure 144. Dynamic light scattering of H-BST nanoparticles displayed in columns of: water, serum free media and complete cell culture media. The particle distributions are plotted against hydrodynamic size at: 1000, 100, 10, 1 and 0.1 µg/mL. (a) The H-BST nanoparticle intensity distribution, (b) H-BST volume distribution and (c) H-BST number distribution in the labelled suspending media. The dispersion indices are summarised in Table 26.

The average primary particle size of H-BST nanoparticles measured by TEM analysis was shown to be ~45 nm (Figure 93, Chapter 4). The DLS data however, showed a similar dispersion to H-BT nanoparticles in water in that small clusters of primary particle size were dominant (by intensity) at ~100–200 nm and there were also large agglomerates present at lower intensity. The dispersion indices for H-BST nanoparticles in water, serum free media and complete cell culture media are given in Table 26, these suggested a broad dispersion that was not polydisperse.

H-BST nanoparticles suspended in water showed intensity and volume distributions that were bimodal; exhibiting dominant clusters of H-BST nanoparticles (~100–500 nm) and some large agglomerates (~1000–10,000 nm). DLS results by number suggested that H-BST nanoparticles suspended in water were monodisperse (~100–200nm) and no large agglomerates were detected suggesting they were large in size but small in number. The dispersion indices implied that the H-BT nanoparticles were reasonably stable in water (Table 26). The H-BST nanoparticles suspended in serum free media showed polydisperse suspensions across the concentration range (similar dispersion to H-BT nanoparticles in Figure 141). The dispersion indices showed similar values to the H-BT nanoparticles in serum free media and it is possible the inorganic salts and electrolytes in serum free media interfered with the DLS measurements [161,162].

The H-BST nanoparticles in complete cell culture media were reasonably monodisperse, with small clusters of nanoparticles (~200–400 nm) present in the intensity, volume and number distributions plots. There were some smaller components of the cell culture media present in each of the size distribution

plots which became more dominant by number (~10–50 nm), again these were attributed to the serum proteins in the media. The dispersion indices confirmed that H-BST nanoparticles were monodisperse (DI = <0.3) in complete cell culture media (Table 26). The H-BST-PLL nanoparticles are discussed in Section 6.3.8.

6.3.8 DLS of H-BST-PLL nanoparticles suspended in water, serum free media and complete cell culture media.

The H-BST-PLL nanoparticles suspended in water showed intensity and volume distributions which were bimodal: small clusters of primary particle size H-BST-PLL nanoparticles were dominant at ~100–500 nm and there were relatively few large agglomerates at ~1000–10,000 nm. By number, the H-BST nanoparticles suspended in water appeared reasonably monodisperse (~100–200nm) and no large agglomerates were detected suggesting they were again relatively few in number (excluding the lower nanoparticle concentration bimodal distributions).

The H-BST-PLL nanoparticles suspended in serum free media showed the nanoparticles to be relatively monodisperse (similar to water) where there were clusters of H-BST-PLL nanoparticles (~100–500 nm). The hydrodynamic size of H-BST-PLL nanoparticles changed across the nanoparticle concentration range (i.e. at 100 µg/mL ~300 nm compared to ~600 nm at 10 µg/mL). The size distribution of H-BST-PLL nanoparticles in serum free media would suggest that the polymer to nanoparticle ratio is high enough due to the reduced H-BST nanoparticle size (~45 nm) to produce a good coverage of the particle surface for a relatively monodisperse nanoparticle suspension, however the measured

sizes by DLS of (100 – 300 nm) suggests that there may be ~2-5 nanoparticles bridged together by the PLL polymer (Figure 145).

DLS results suggested that the H-BST-PLL nanoparticles in complete cell culture media were monodisperse by intensity, volume and number; with clusters of nanoparticles appearing at ~400 nm. The smaller components of the cell culture media were only identified at 0.1 µg/mL (~10 nm). The dispersion indices of the H-BST-PLL nanoparticle in complete media suggested that the dispersion was monodisperse (Table 26). In complete cell culture media, the H-BST-PLL polymer to particle ratio is sufficiently high at all applied nanoparticle dose concentrations where coated suspensions are stable at ~400 nm (Figure 145).

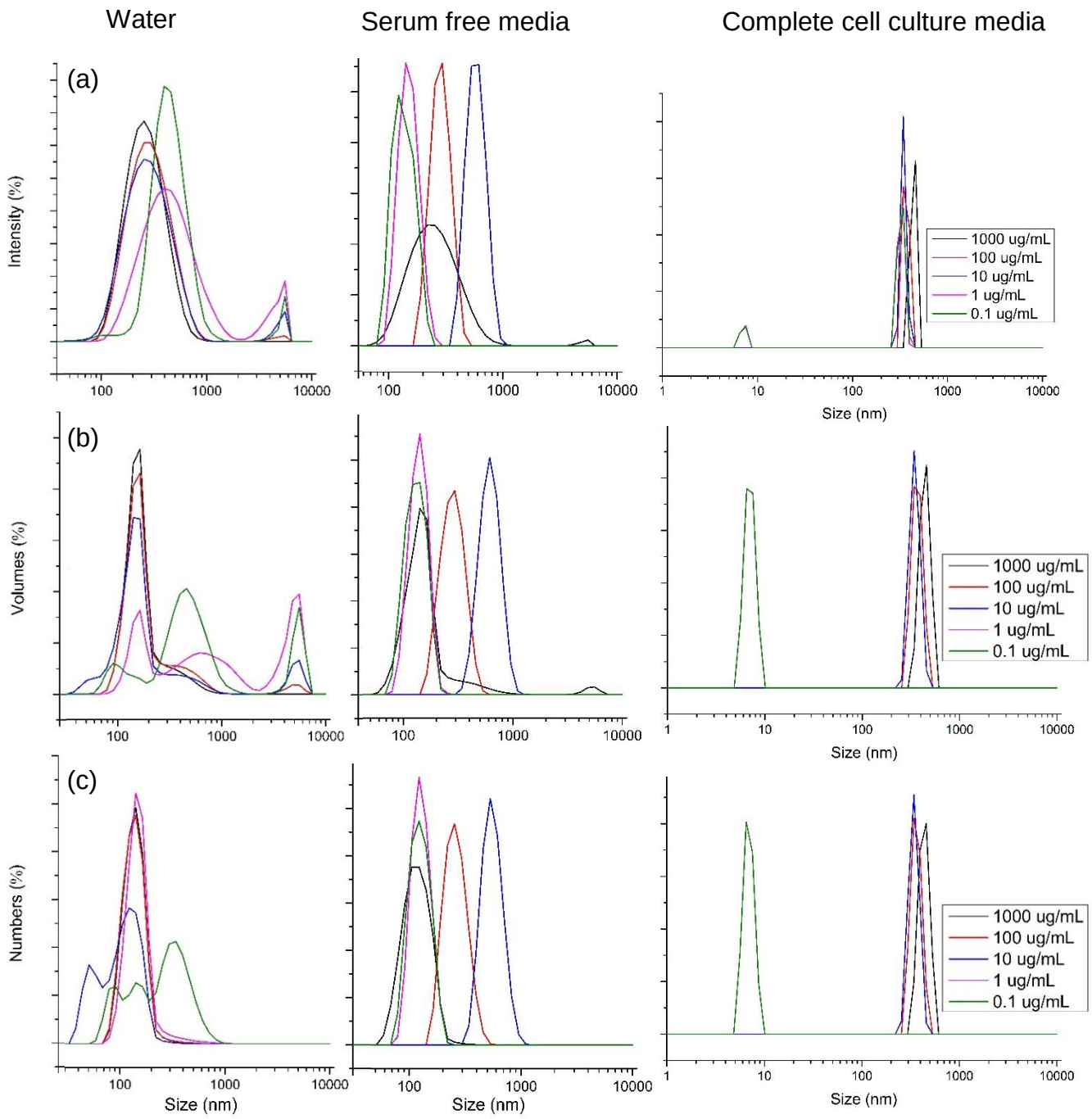

Figure 145. Dynamic light scattering of H-BST-PLL nanoparticles displayed in columns of: water, serum free media and complete cell culture media. The particle distributions are plotted against hydrodynamic size at: 1000, 100, 10, 1 and 0.1 µg/mL. (a) The H-BST-PLL nanoparticle intensity distribution, (b) H-BST-PLL volume distribution and (c) H-BST-PLL number distribution in the labelled suspending media. The dispersion indices are summarised in Table 26.

Concentration (µg/mL)	H-BST	H-BST-PLL	H-BST	H-BST-PLL	H-BST	H-BST-PLL
	Water		Serum free media		Complete media	
1000	0.64	0.20	0.47	0.20	0.64	0.20
100	0.25	0.20	1.0	0.38	0.25	0.20
10	0.38	0.25	0.82	0.05	0.38	0.25
1	0.48	0.57	0.61	0.24	0.48	0.57
0.1	0.45	0.59	0.50	0.36	0.45	0.59

Table 26. The dispersion indices of the H-BST and H-BST-PLL nanoparticles suspended in water, serum free media and complete media. Dispersion indices closer to 0.25–0.3 are considered monodisperse and 1 is polydisperse.

The dispersion indices shown in Table 26 highlighted that the H-BST-PLL nanoparticles followed a similar trend to that of H-BST nanoparticles, where the dispersions were reasonably monodisperse at particle concentrations of 100 and 10 µg/mL and more polydisperse at lower nanoparticle concentrations (1 and 0.1 µg/mL).

In general, the dispersion indices indicated that H-BST-PLL nanoparticles were more stable than H-BST nanoparticles in water, serum free media and also complete cell culture media.

The DLS data are summarised and discussed in Table 27 to provide an overview of the behaviour of nanoparticle suspensions.

Concentration (µg/mL)	Water	Serum free media	Complete media
H-BT	Bimodal distribution by intensity and volume. Lots of small primary particle clusters (100–500 nm) and some large agglomerates of many primary particles (>1,000 nm). By number it appears reasonably monodisperse (only ~100 – 300 nm clusters detected).	Fully polydisperse – The distributions by intensity, number or volume all show similar behaviour. It is possible the inorganic salts and electrolytes in serum free media are interfering with the DLS measurements [161,162].	The intensity, volume and number distribution show the serum components present at ~10–50 nm. The plots by intensity and volume show a bimodal particle distribution with large agglomerates present at ~10,000 nm. Small clusters of the primary particle size are present at ~ 100 nm and are dominant by number.
H-BT-PLL	Bimodal distribution by intensity and volume. Lots of small primary particle clusters (300–1000 nm) and some large agglomerates of many primary particles (~10,000 nm). By number it appears reasonably monodisperse (~100–300 nm clusters) with only the lower concentrations showing a bimodal distribution (100 & 500 nm clusters).	Similar to H-BT, the H-BT-PLL nanoparticles are fully polydisperse but marginally less so by comparison. The intensity, volume and number distribution show that either the serum free media is causing a change in agglomeration, or the components of serum free media are confusing the measurement. Electrolytes present in serum free media (such as: Ca^{2+} and Mg^{2+}) will cause coagulation by reducing the double layer which will produce a polydisperse nanoparticle suspension.	The plots by intensity, volume and number show the serum components present at ~10–50 nm. At 100 µg/mL the distribution plots show the primary particle size (~100 nm) and an intermediate size (~500 nm). At lower concentrations i.e. <100 µg/mL the suspensions are polydisperse. The intermediate size is also present in the higher particle concentration of 1000 µg/mL and will be investigated further in the plunge frozen cryo-TEM section. Higher nanoparticle doses may produce bridging flocculation measured in the H-BT-PLL distributions.

H-BST	Bimodal distribution by intensity and volume. Lots of small clusters of primary particle size (~100–500 nm) and some large agglomerates of many primary particles (>1,000 nm). By number it appears reasonably monodisperse (~100 – 200 nm clusters).	Fully polydisperse – The distributions by intensity, number or volume all show similar behaviour. It is possible the inorganic salts and electrolytes in serum free media are interfering with the DLS measurements [161,162].	The intensity, volume and number distribution show the serum components present at ~10–50 nm. The small clusters of the primary particle size are dominant at ~200–400 nm at the nanoparticle concentrations of 1000 and 100 µg/mL. At lower nanoparticle concentrations (<100 µg/mL) the suspensions are more polydisperse.
H-BST-PLL	Bimodal distribution by intensity and volume. Lots of small clusters of primary particle size (~100–700 nm) and some large agglomerates of many primary particles (~10,000 nm). By number it appears reasonably monodisperse (only ~100–200 nm clusters are detected) with the lower concentrations showing a multimodal distribution (~50, ~100 & 500 nm).	H-BST-PLL nanoparticles appear to be monodisperse where there are clusters of H-BST-PLL nanoparticles (~100–500 nm). The hydrodynamic size of H-BST-PLL nanoparticles changes across the nanoparticle concentration range (i.e. at 100 µg/mL ~300 nm compared to 10 µg/mL ~ 600 nm). It is a possibility that the polymer to nanoparticle ratio is adequate to produce a relatively monodisperse nanoparticle suspension.	The intensity, volume and number distribution show the nanoparticle suspensions to be monodisperse. The serum components are detected at ~10–50 nm only at 0.1 µg/mL. Small clusters of the primary particle size are dominant at ~200–400 nm for the remaining nanoparticle concentrations. It is a possibility that the polymer to nanoparticle ratio is adequate to produce a relatively monodisperse nanoparticle suspension.

Table 27. Summary of the DLS measurements acquired for H-BT, H-BT-PLL (Figure 141 and Figure 143 respectively), H-BST and H-BST-PLL (Figure 144 and Figure 145 respectively). The table summarises the interpretation of the overall dispersions measured over the range of nanoparticle concentrations.

The DLS data for H-BT, H-BT-PLL, H-BST and H-BST-PLL nanoparticles in water, serum free media and complete cell culture media, provided insight into the nanoparticle behaviour in suspensions. However, the data showed no indication as to how the nanoparticle suspensions interacted with the A549 cells. Nor did the data indicate whether the nanoparticles were internalised by the cells.

Sections 6.4 & 6.5 discuss the nanoparticle uptake in using critically point dried cell SEM images as well as FIB-SEM and HAADF-STEM imaging of resin embedded thin cell sections.

6.4 HAADF-STEM imaging of resin embedded A549 cell sections.

To show that the nanoparticles were actually being internalised by the cells at a 1 µg/mL nanoparticle dose after a 24-hour exposure (Figure 134 – Figure 137), secondary electron (SE) and backscattered (BSE) images of exposed, fixed cells were acquired at different SEM accelerating voltages. So changing the penetration depth of the electron beam which revealed nanoparticles present at 15 kV but not at 2 kV. This highlighted that the nanoparticles were not on the surface of the cell but internalised because of the increased penetration depth of the 15 kV beam (Figure 147).

Qualitative analysis of nanoparticle uptake into A549 cells was also shown by FIB-SEM serial sectioning of resin-embedded cells. This technique images the block face of the resin-embedded cells, the same area is then ion beam milled to a depth of 10 to 20 nm and then imaged again. This demonstration data was acquired by three microscope companies FEI (H-BT), Zeiss (H-BST) and

Tescan (H-BT-PLL) and are shown in Figure 148 – Figure 150 at random sectioning (nm) distances to highlight internalised nanoparticles Further confirmation of cellular uptake was shown by HAADF-STEM images given in Figure 151 of resin embedded thin cell sections for H-BT, H-BT-PLL, H-BST and H-BST-PLL with the corresponding bright field TEM image and EDX spectra presented so as to confirm the chemistry of the imaged nanoparticles is that of $BaTiO_3$ or $Ba_{1-x}Sr_xTiO_3$.

The low magnification SEM image of A549 cells critically point dried on a glass substrate highlighted the presence of nanoparticle agglomerates (blue box). Due to the topographical appearance of SE(L) SEM images at 15 kV, the nanoparticles appeared as if they were on the cell surface; Figure 146.

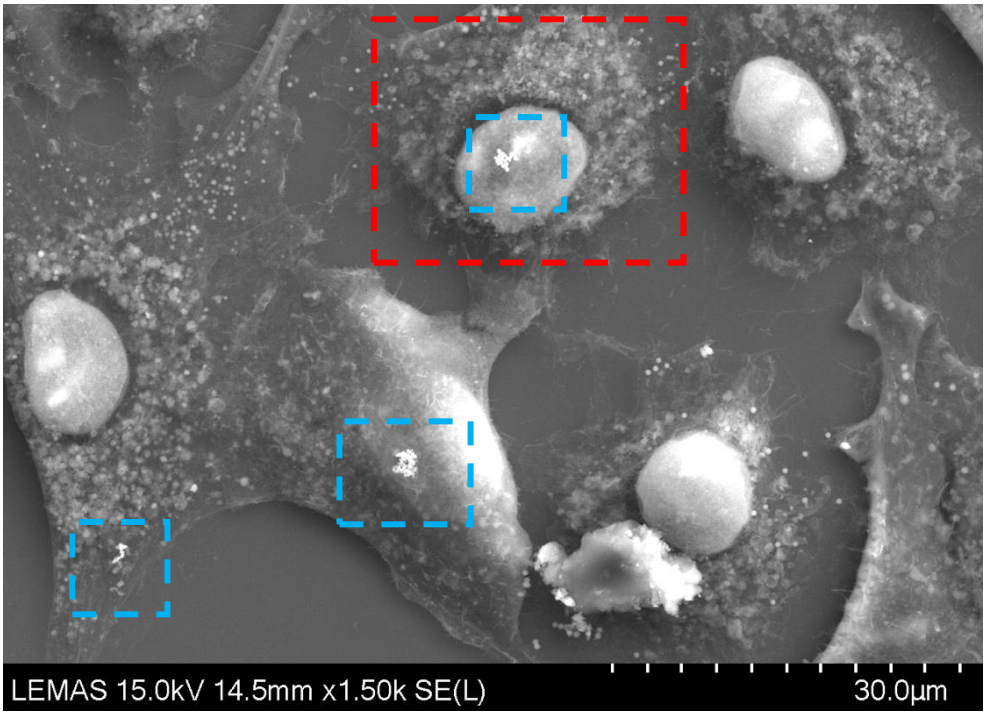

Figure 146. Overview of A549 critically point dried cells originally grown on a glass substrate. The red box indicates the area which is shown in Figure 147 at 15 kV and 2 kV accelerating voltages to show that the nanoparticle agglomerates (bright contrast) are indeed internalised. The blue boxes indicate the areas in which H-BT nanoparticle agglomerates are present.

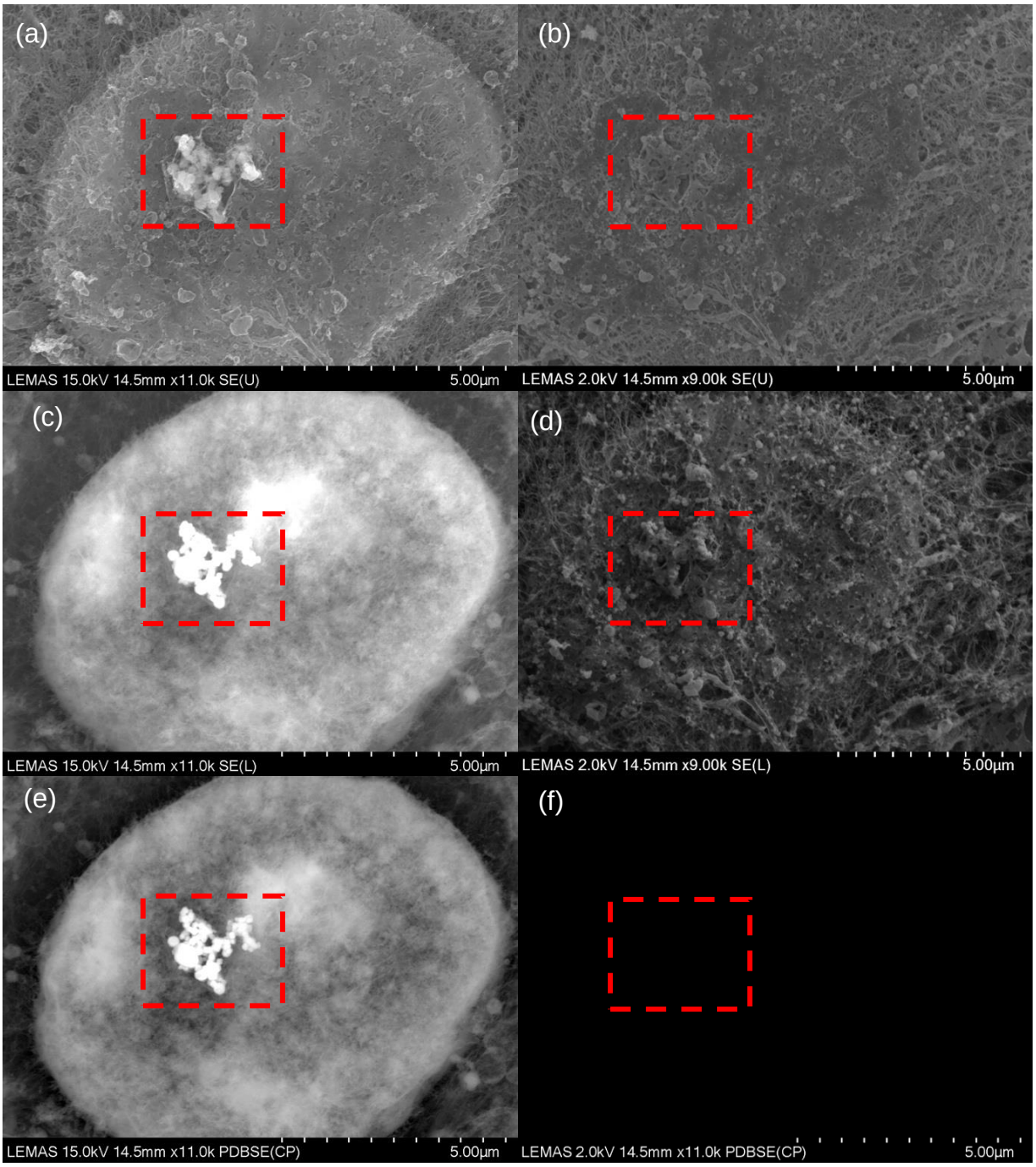

Figure 147. SE upper, SE lower and BSE electron images (labelled at the bottom of each image) were collected from the A549 cell highlighted in Figure 146 with H-BT nanoparticles internalised. (a), (c) and (e) were collected at 15 kV with the nanoparticles highlighted by the red box. The 15 kV images show surface and internal detail. The images collected at 2 kV (b), (d) and (f) were at a lower magnification to show cellular structure, showing no visible nanoparticles with only details of the sample surface. (f) Intentionally left blank as the working distance (14.5mm) is too long to collect the backscattered signal.

Figure 147 shows the secondary electron upper (SE-U, in-lens detector) image and the secondary electron lower (SE-L, Everhart-Thorley detector) image and backscattered electron (BSE) image at both 15 kV and 2 kV and showed that the nanoparticles were internalised in the A549 cells (because 2 kV is only sensitive to the surface and no particles were visible in the images).

6.5 FIB-SEM and serial thin-sectioning of A549 cells.

The resin embedded A549 cells were imaged on the resin block face and FIB-milled in serial sections at 10–20 nm intervals through the block face to show internalised nanoparticles. This technique can be used for 3D reconstructions of the cell and to provide qualitative information regarding internalisation of the nanoparticles by cells. As these were microscope demonstration data acquired at different microscope companies, the cell sections for H-BT (Figure 148), H-BST (Figure 149) and H-BT-PLL (Figure 150) nanoparticles showed all particle types are internalised to some extent.

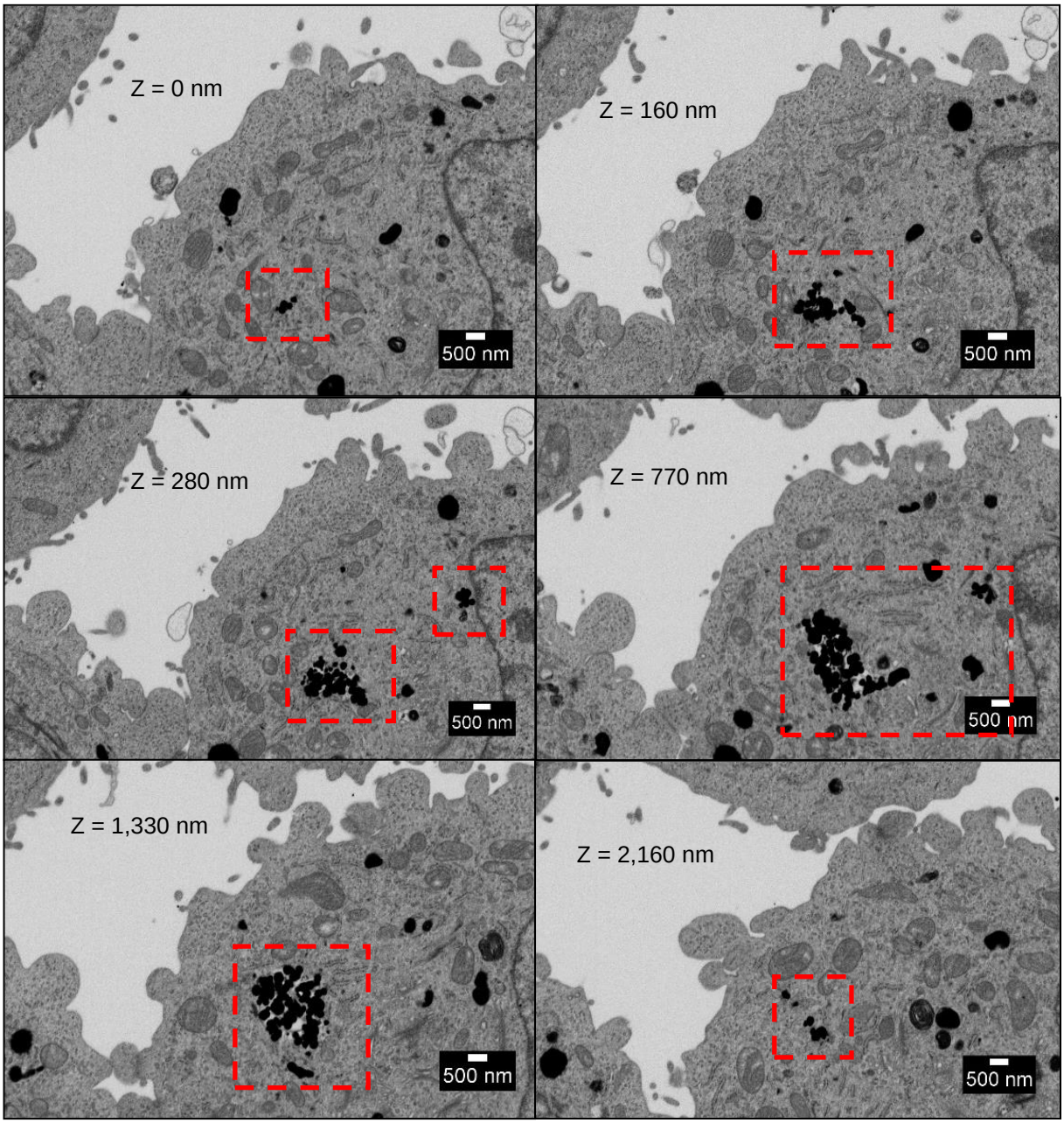

Figure 148. FIB-SEM inverted contrast BSE image of irregular shaped clusters of H-BT nanoparticles in A549 cells (red boxes). These images were collected using a monochromated FEI Helios G4 at 2 kV, with a slicing thickness of 10 nm. The slicing depth (Z) is selected to show the best frames and Z is labelled on each image. The larger, more round black blobs within the cells are osmium decorated lipid filled vesicles.

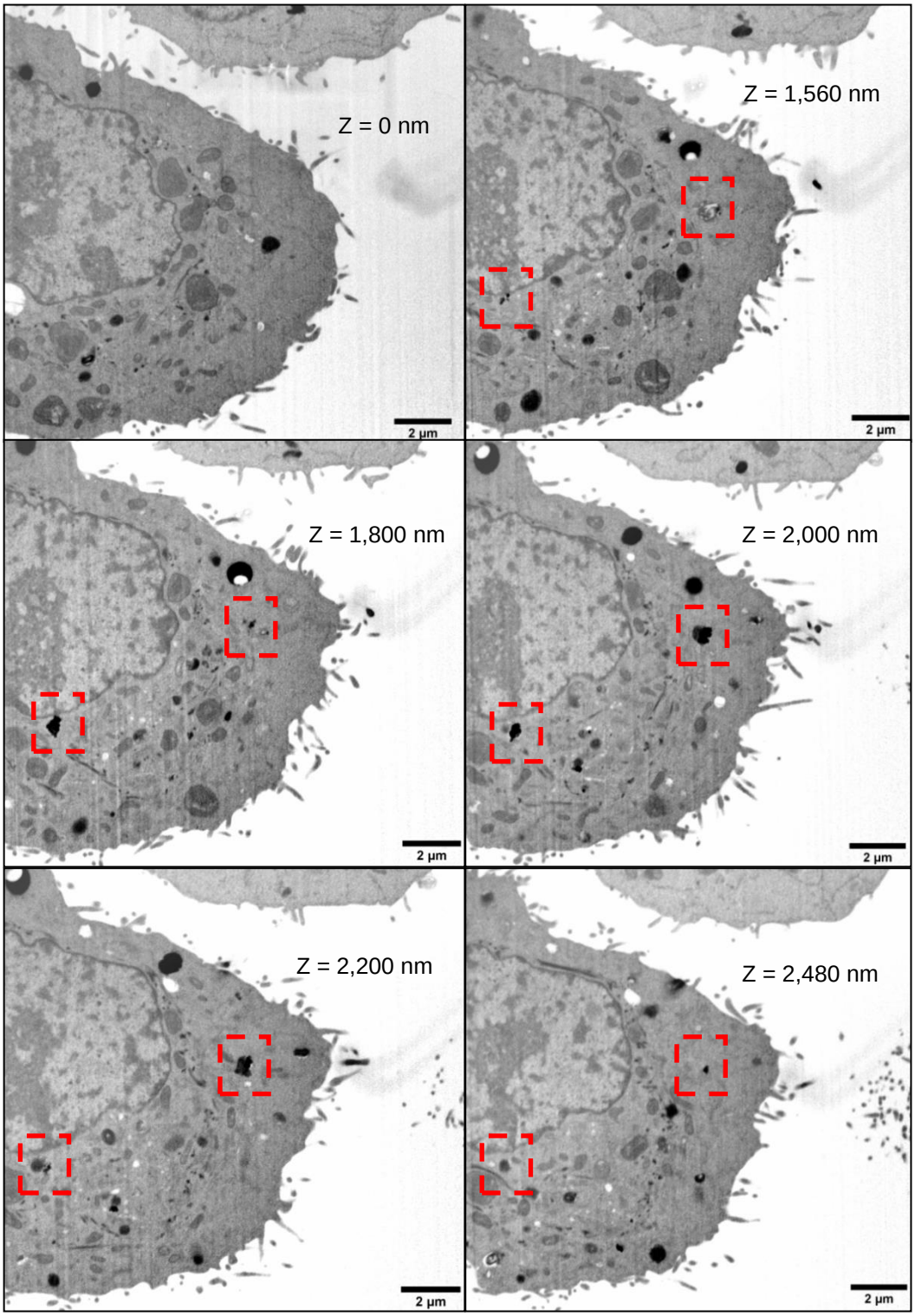

Figure 149. FIB-SEM inverted contrast BSE image series of H-BST nanoparticles in A549 cell (red boxes). These images were collected using Tescan GAIA3-2016 microscope at 3 kV, with a slicing thickness of 20 nm. The slicing depth (Z) is selected to show the best frames and are labelled on each image.

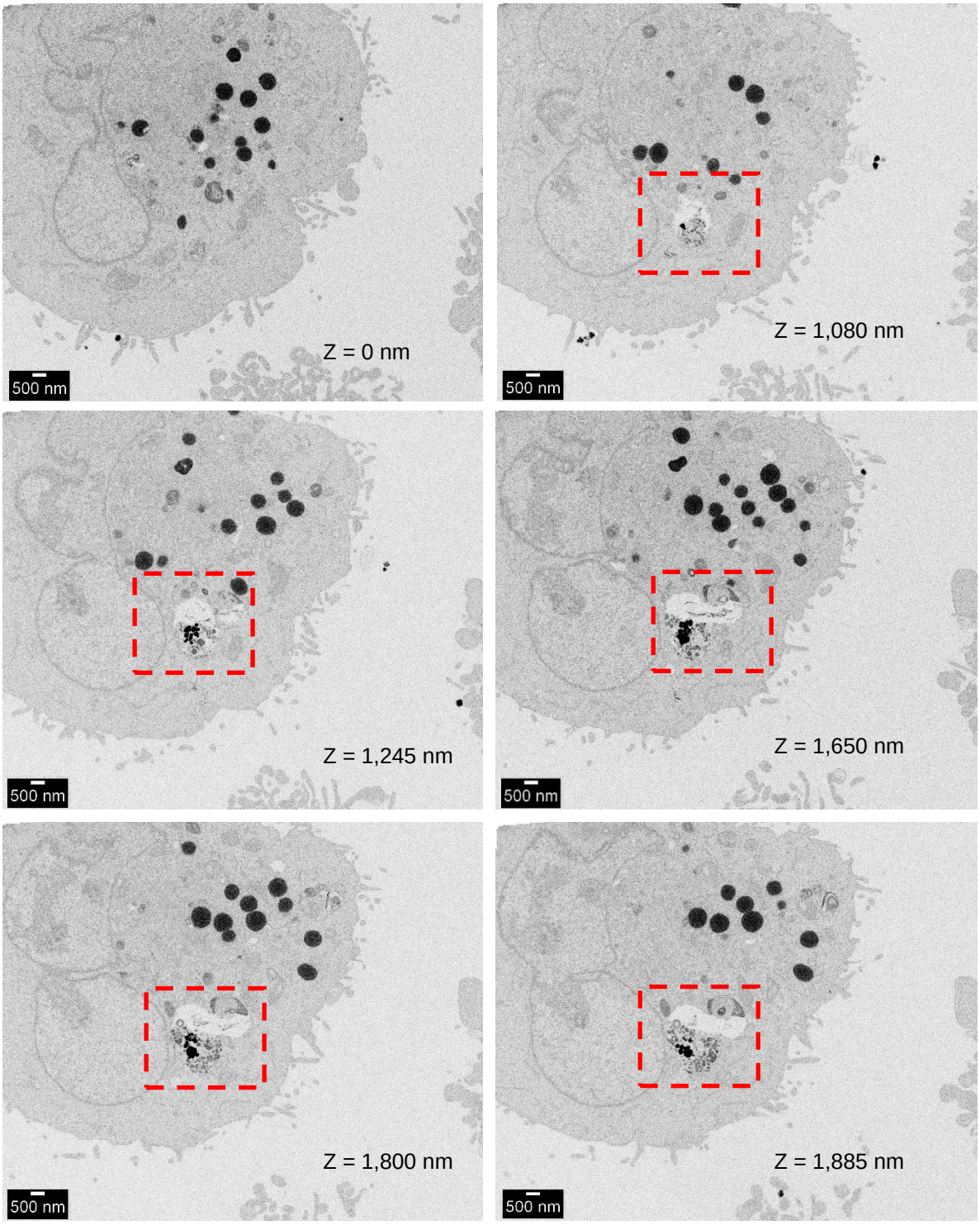

Figure 150. FIB-SEM inverted contrast BSE image series of resin embedded A549 cell section with internalised H-BT-PLL nanoparticles (red boxes). These images were collected using Zeiss crossbeam 540 EsB detector at 1.7 kV, with a slicing thickness of 10 nm. The slicing depth (Z) is selected to show the best frames and are labelled on each image.

Further evidence of nanoparticle cell uptake was shown by HAADF-STEM, TEM images and TEM-EDX of H-BT, H-BT-PLL, H-BST and H-BST-PLL nanoparticles internal to A549 thin cell sections.

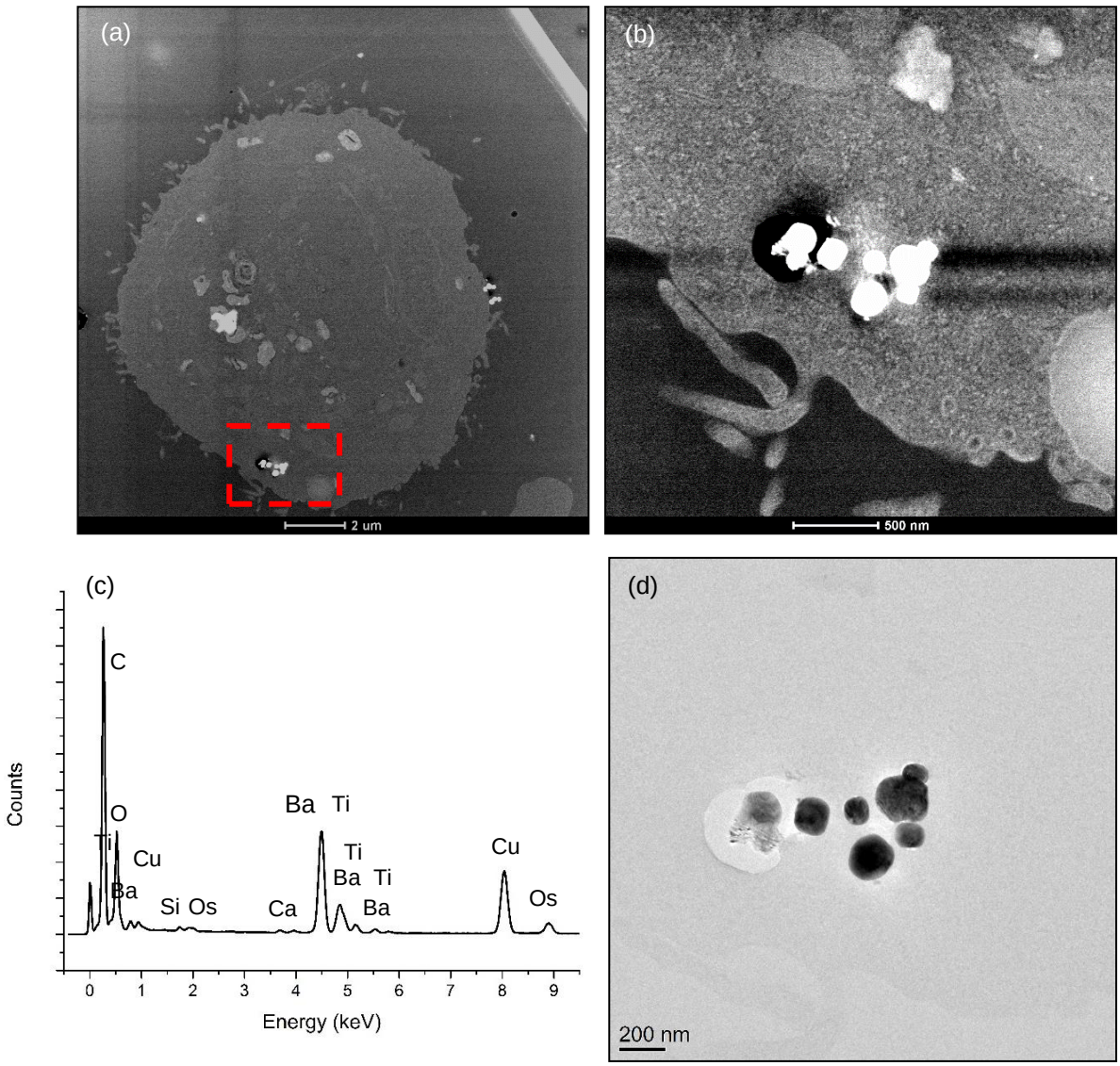

Figure 151. (a) HAADF-STEM image of a resin embedded thin section of A549 cell with H-BT nanoparticles internalised (red dashed box) following exposure in complete cell culture media. (b) Higher magnification HAADF-STEM image of the internalised nanoparticles. (c) EDX spectrum of the internalised H-BT nanoparticles in complete media. (d) Bright field TEM image of the internalised H-BT nanoparticles.

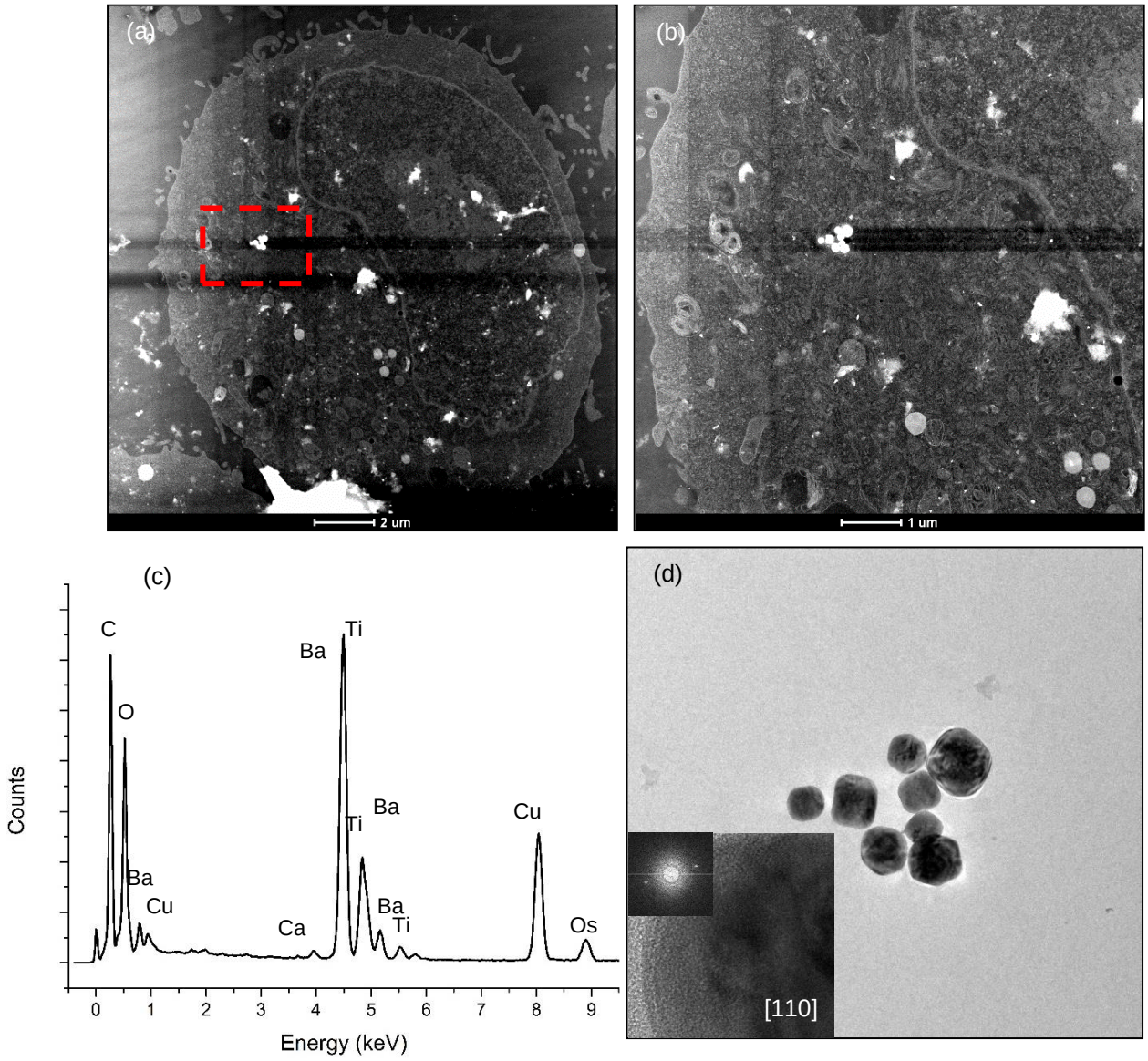

Figure 152. (a) HAADF-STEM image of a resin embedded thin section of A549 cells with H-BT-PLL nanoparticles internalised (red dashed box) following exposure in complete cell culture media. (b) Higher magnification HAADF-STEM image of the internalised nanoparticles. (c) EDX spectrum of the internalised nanoparticles. (d) Bright field TEM image of the internalised nanoparticles with a high resolution image and FTT (inset) confirming it is barium titanate imaged down the [110] view direction with no visible PLL coating.

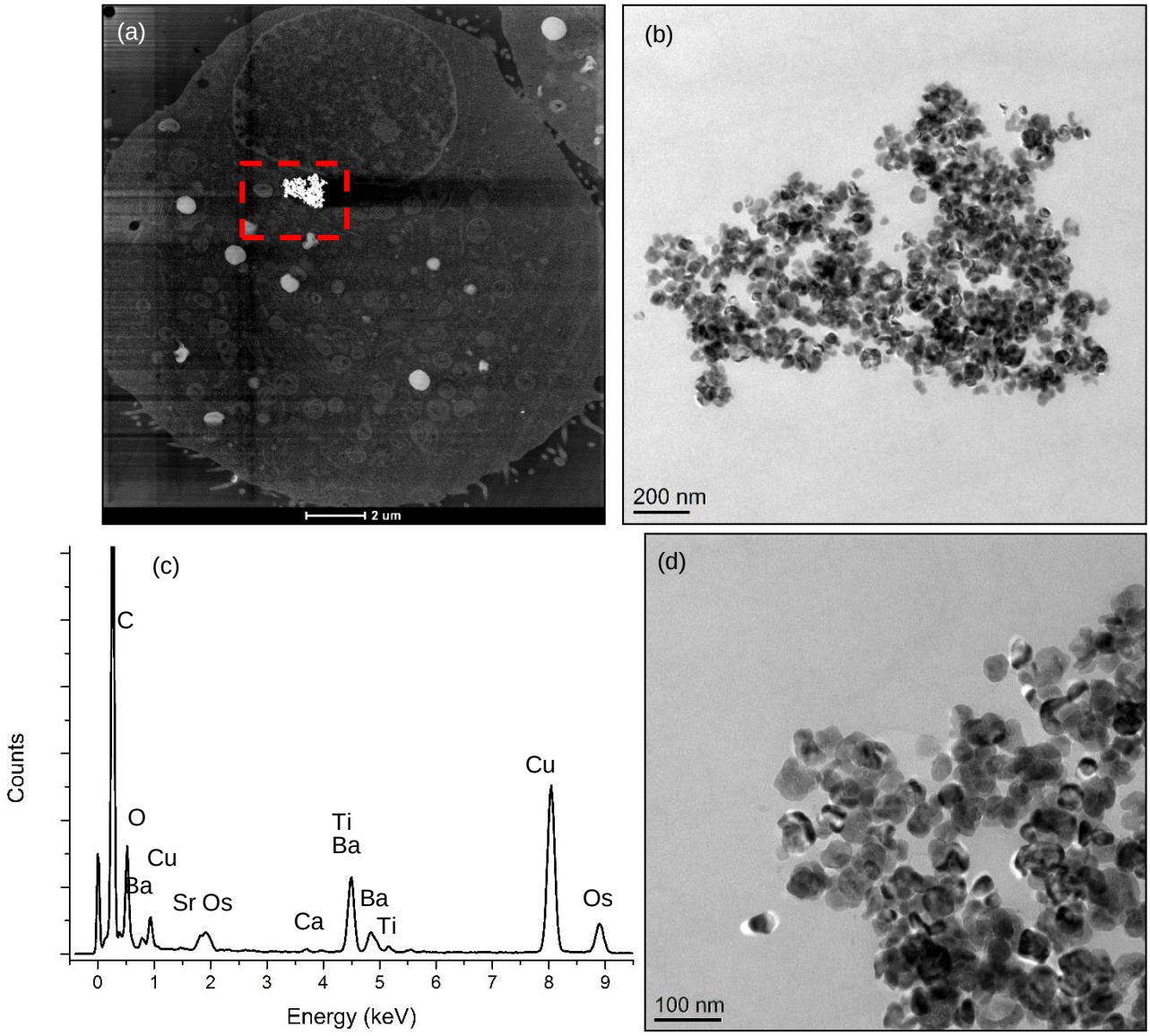

Figure 153. (a) HAADF-STEM image of resin embedded thin section of an A549 cell with H-BST nanoparticles internalised (red dashed box) following exposure in complete cell culture media. (b) Bright field TEM image of the internalised H-BST nanoparticles. (c) EDX spectrum of the nanoparticles showing strontium is present. (d) Higher magnification bright field TEM image of H-BST nanoparticles where the EDX spectrum was acquired.

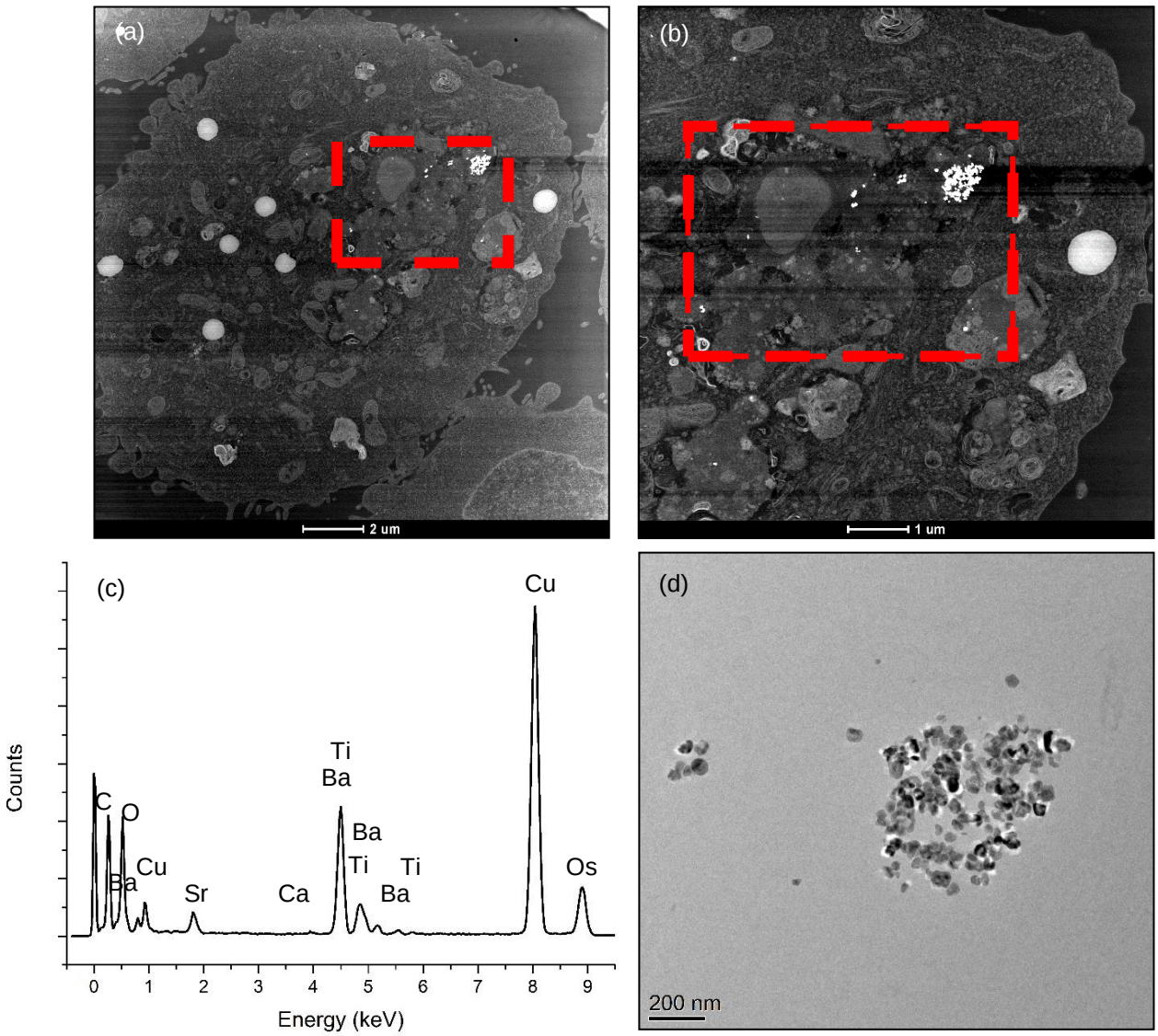

Figure 154. (a) HAADF-STEM image of resin embedded thin section of an A549 cell with H-BST-PLL nanoparticles internalised (red dashed box) following exposure in complete cell culture media. (b) Higher magnification HAADF-STEM image of the internalised nanoparticles. (c) EDX spectrum of the internalised nanoparticles. (d) Bright field TEM image of the internalised nanoparticles with no visible PLL coating.

The SEM, FIB-SEM and HAADF-STEM images of the nanoparticles internalised in the critically point dried and resin embedded A549 cells and resin embedded cell sections provided a snapshot of the cells after 24 hours' exposure. Qualitatively, there was no difference between H-BT and H-BT-PLL nanoparticle uptake (Figure 151 and Figure 152), however there was a clear decrease in cell viability at concentrations > 100 µg/mL by the MTT assay (Figure 134). Moreover, H-BT-PLL nanoparticles showed no clear coating around the nanoparticle surface when internalised in the A549 cells. This means that either the cells were processing the PLL coating or the PLL coating was not around all the nanoparticles present in the suspensions (which was not in agreement with by DLS).

The DLS data from H-BT-PLL nanoparticles (Figure 143 – Table 27) broadly suggested a multimodal distribution. The smallest size fraction was consistent with the components of the complete cell culture media (10–50 nm) [163]. The dominant H-BT-PLL particle size fraction in suspension appeared to be small clusters of primary particle sizes (~100 nm) and there were a small number of large agglomerates (>1,000 nm). There was also an intermediate particle size fraction (~500 nm) that appeared for 100 µg/mL (and a small number at 1000 µg/mL) that suggested the H-BT-PLL nanoparticles in complete cell culture media (Figure 143) clustered differently to their H-BT equivalents (Figure 141) as summarised in Table 27.

To characterise the nanoparticle suspensions by imaging, cryo-TEM was used to vitrify the samples onto a carbon-coated copper grid by plunge freezing the samples into liquid ethane.

6.6 Cryo-TEM of H-BT and H-BT-PLL nanoparticles.

Cryo-TEM was used to quantify H-BT and H-BT-PLL nanoparticle agglomerate sizes in water and complete cell culture media suspensions. This was not possible by simple TEM sample preparation by dropcasting and drying due to movement of particles caused by evaporation of the liquid and movement of the liquid meniscus.

Cryo-TEM freezes the nanoparticle suspensions in their native state in order to give true nanoparticle/agglomerate sizes in the suspension. The H-BT and H-BT-PLL nanoparticles are shown suspended in vitreous ice (i.e. suspended in water, then plunge frozen) with a clear coating around the H-BT-PLL sample, as seen in Figure 155.

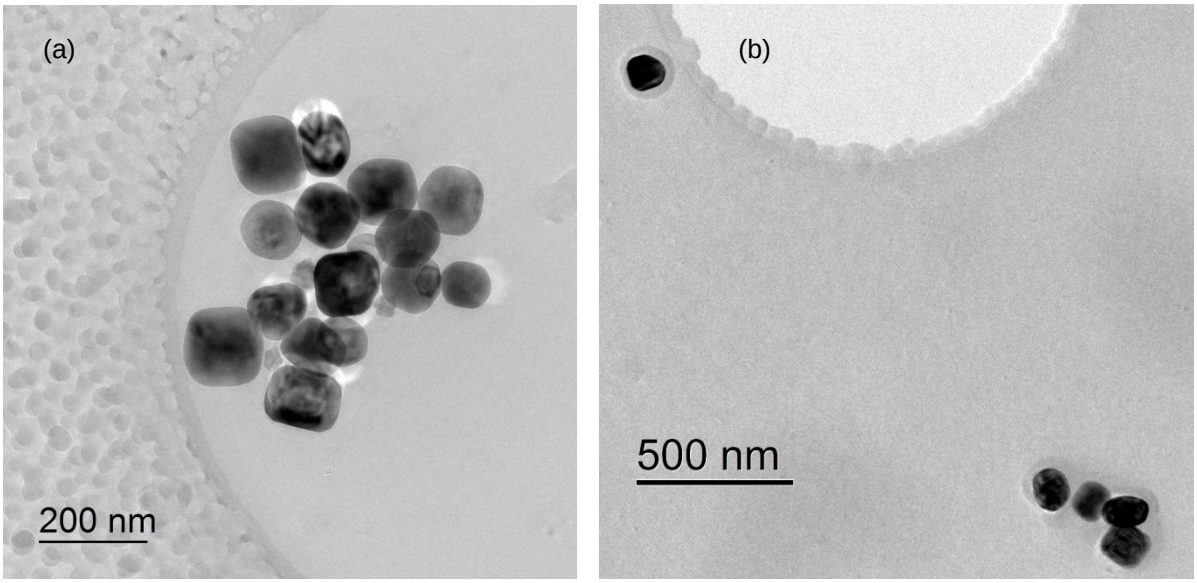

Figure 155. Cryo-TEM of (a) H-BT nanoparticles and (b) H-BT-PLL nanoparticles suspended in vitreous ice at a concentration of 100 µg/mL. A clear coating is visible around the H-BT-PLL particles.

As the cell viability assay showed a decrease in cell viability at a concentration of H-BT-PLL of ≥ 100 µg/mL, cryo-TEM of the nanoparticle suspensions were imaged at 100 µg/mL. The cryo-TEM images of H-BT and H-BT-PLL nanoparticle suspensions in complete cell culture media are shown in Figure 156 and Figure 157 respectively.

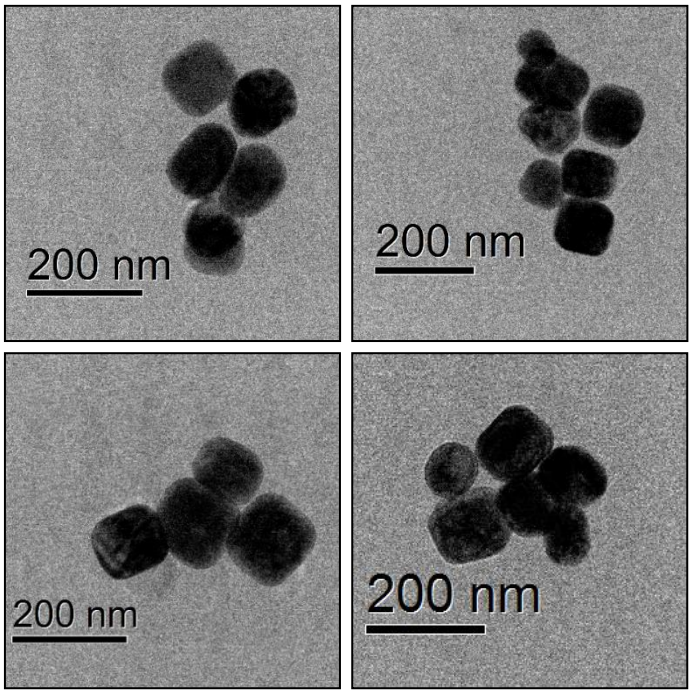

Figure 156. Bright field cryo-TEM of H-BT nanoparticles suspended in complete cell culture media at a concentration of 100 µg/mL. No coatings are visible around the nanoparticles.

The cryo-TEM images of H-BT-PLL at 100 µg/mL (Figure 157) showed (some) nanoparticles with an obvious coating in the frozen nanoparticle suspension compared to no visible coating in the resin embedded cell section (Figure 152). However, not all H-BT-PLL nanoparticles were fully coated, some appeared uncoated i.e. some apparently uncoated H-BT in a H-BT-PLL sample.

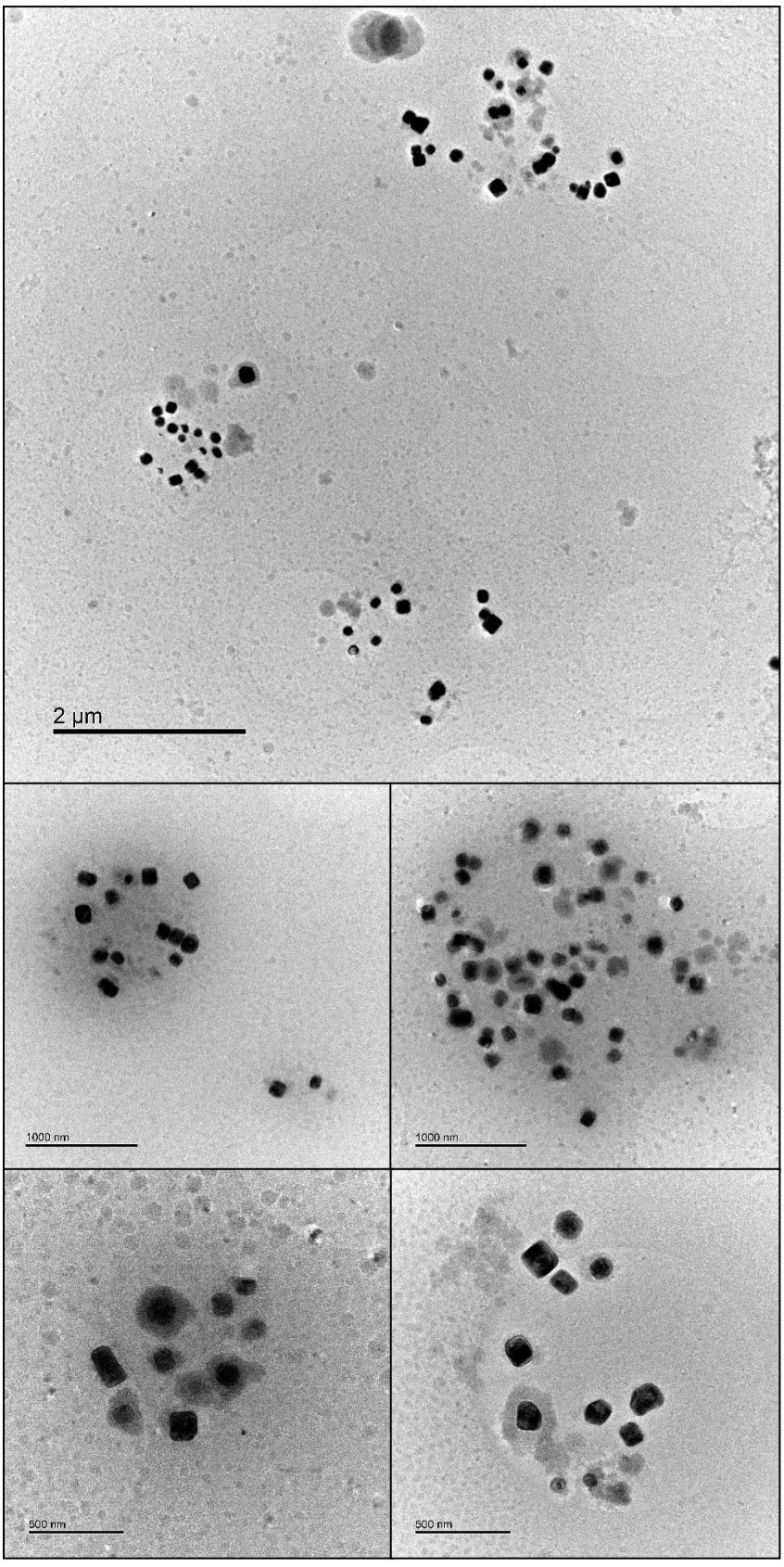

Figure 157. Bright field cryo-TEM of H-BT-PLL nanoparticles suspended in complete cell culture media at a concentration of 100 µg/mL. Showing some nanoparticles with a clear coating and others with none.

Cryo-TEM of the H-BT-PLL nanoparticles at 100 µg/mL (Figure 158, Figure 159 and Figure 160) were analysed by bright field-TEM and STEM EDX-mapping of the obviously coated and uncoated H-BT-PLL nanoparticles respectively.

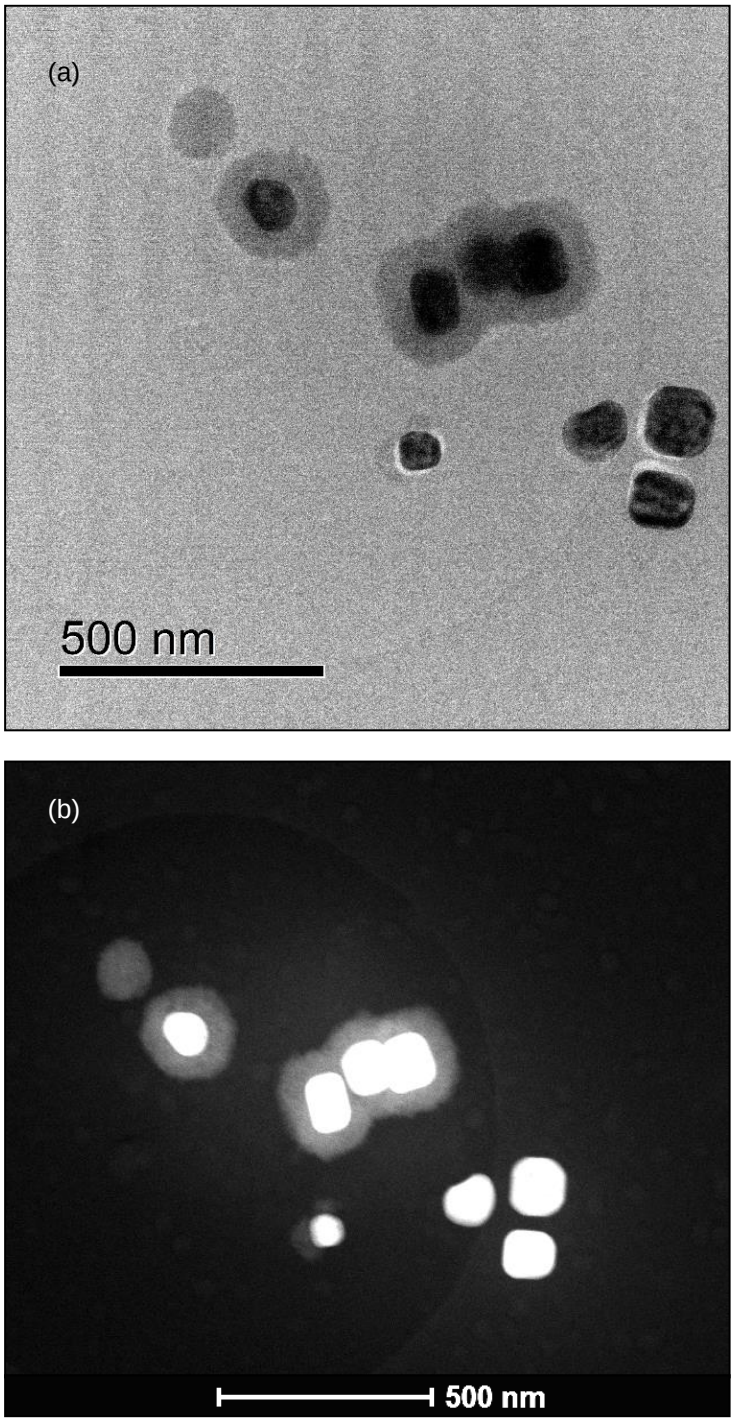

Figure 158. (a) Bright field cryo-TEM image of H-BT-PLL nanoparticles at 100 µg/mL in complete cell culture media. The bright field TEM image shows 50% of the nanoparticles coated. (b) HAADF-STEM image of the same area, the EDX-mapping of the particles is shown in Figure 159.

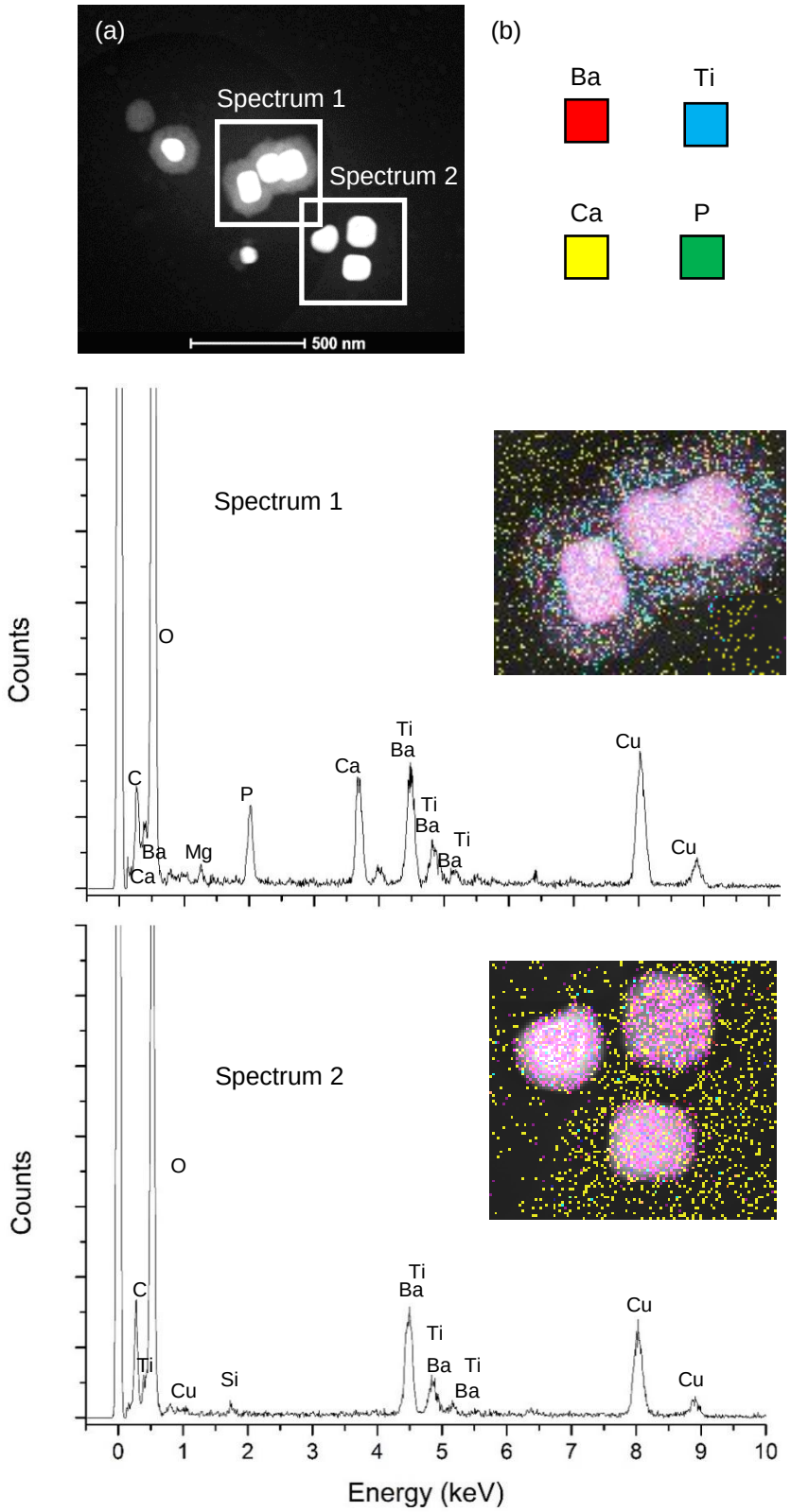

Figure 159. (a) The cryo-HAADF-STEM image with EDX mapping areas from Figure 158. (b) Colour code of EDX mapping elements. The corresponding HAADF-STEM EDX map area (inset) shows the corresponding EDX spectrum labelled with the elements. Oxygen was mapped but is not shown due to oxygen being present throughout the whole sample. The coated particles clearly had a calcium phosphorous rich shell.

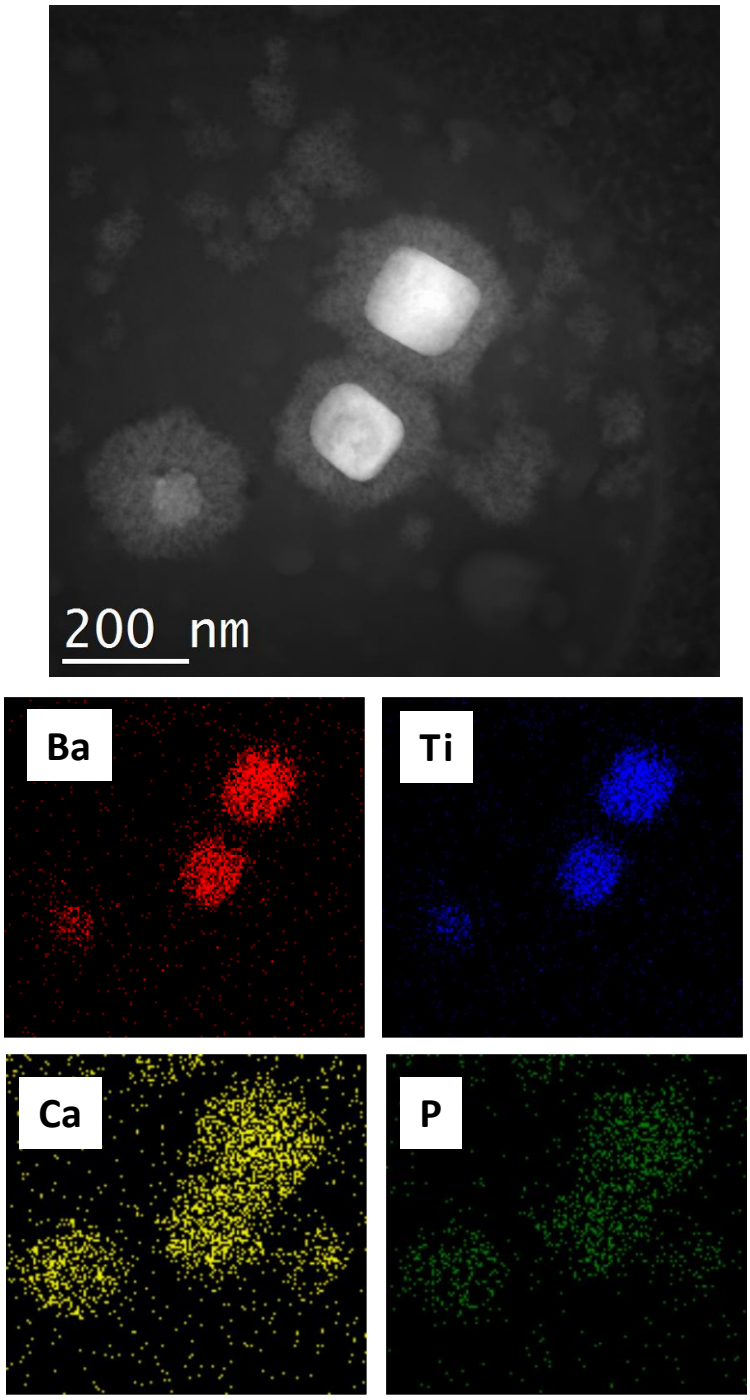

Figure 160. Cryo-HAADF-STEM image of a different area of H-BT-PLL nanoparticles at 100 µg/mL. The EDX mapping data suggests a shell that is rich in calcium and phosphorus.

EDX-mapping data of the H-BT-PLL nanoparticles showed that there was a calcium and phosphorous-rich area around the coated H-BT-PLL nanoparticles

when the nanoparticles were suspended in complete cell culture media (Figure 159 & Figure 160). The calcium & phosphorous-rich coating will be referred to as calcium phosphate herein (but could be a mono, di or tri-calcium phosphate). STEM-EDX showed that calcium phosphate was most probably adsorbed to the surface of H-BT-PLL nanoparticles from the complete cell culture media (which contains 200 µg/mL of calcium chloride and 400 µg/mL of sodium phosphate i.e. in excess compared to the nanoparticles) [164].

It is likely that the H-BT-PLL nanoparticles still had the PLL coverage, as shown by the FTIR data and zeta potential measurements (Figure 138 & Figure 140 respectively) highlighting that the coating was successful and the zeta potential increased from negative (when uncoated) to positive when coated. The formation of a calcium & phosphorous-rich coating around the nanoparticle may be due to the positively charged H-BT-PLL nanoparticles adsorbing a calcium phosphate complex or attracting phosphate ions that in turn attracts Ca ions.

EDX mapping of the H-BT-PLL nanoparticles also highlighted the presence of nitrogen on both coated & oppositely coated nanoparticles (Figure 161). This implies that H-BT-PLL nanoparticles that appear uncoated, do in fact still have a PLL coating.

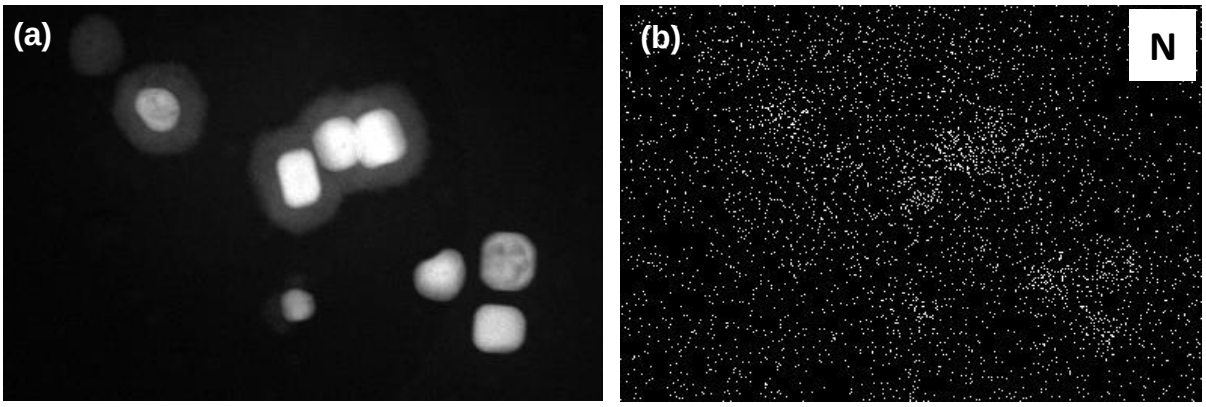

Figure 161. (a) HAADF-STEM image of the nanoparticles in Figure 25. (b) EDX mapping of the nitrogen signal from the nanoparticles showing that all nanoparticles contain some Nitrogen suggesting that all have the PLL coating.

The H-BT-PLL nanoparticles show a fraction of nanoparticles with a calcium phosphate rich coating at 100 µg/mL, leaving a remaining fraction of calcium phosphate *uncoated* H-BT-PLL nanoparticles.

This apparent uncoated/coated particle fraction shown in Figure 158 provides an explanation for the primary and intermediate particle size seen in the DLS number distribution at 100 µg/mL (Figure 143). Where small clusters of the H-BT-PLL primary particle size fraction (~100–200 nm) were present these were calcium phosphate *uncoated*-particles. In addition, the intermediate particle size fraction (~500 nm) were the calcium phosphate-coated H-BT-PLL nanoparticles.

The calcium phosphate coated and the uncoated particle fraction will have affected the interaction of H-BT-PLL nanoparticles with A549 cells due to the different charges remaining at the surface of the nanoparticles. The H-BT-PLL nanoparticles had a positive surface charge (shown by the zeta potential

measurements – Figure 140) in comparison to the calcium phosphate screened–PLL surface charge (which one might presume was overall more neutral) remaining on the coated H-BT-PLL nanoparticles. The calcium phosphate/PLL coated nanoparticles might be expected to be relatively inert compared to the uncoated H-BT-PLL nanoparticles.

The difference in coatings and consequent surface charge could be the likely cause of reduced cell viability when the nanoparticle concentration increased (above 10/100 µg/mL); shown in the MTT cell viability assay (Figure 134). The calcium phosphate components in the cell culture media were being used up at a certain concentration between 10 and 100 µg/mL, this would have led to the presence of an uncoated particle fraction, which may have been more toxic.

It can be shown with simple calculations and a few assumptions (detailed below) that the stock Ca ions in the media (200 µg/mL of calcium chloride) were used up at a nanoparticle concentration of ~ 100 µg/mL (shown in Section 6.6.1).

6.6.1 Estimation of the Ca ion concentration in complete cell culture media.

Assumptions

- The $BaTiO_3$ nanoparticles (density = 6.02 g cm^{-3}) are perfectly cubic in morphology and near monodisperse– justified by DLS number plots (Figure 143).
- The calcium phosphate in the coating has the same packing density as hydroxyapatite ($Ca_5(PO_4)_3(OH)$) with a Ca: P ratio of 1.6:1. The Ca: P ratio is measured to be ~1.3:1 by EDX. Hydroxyapatite is used here

because the density/volume is well known [165], however it may also be amorphous calcium phosphate but the density of this is not well established.

- the visibly apparent coating is a 50 % PLL and 50 % $CaPO_4$ uniform coating around the nanoparticle.

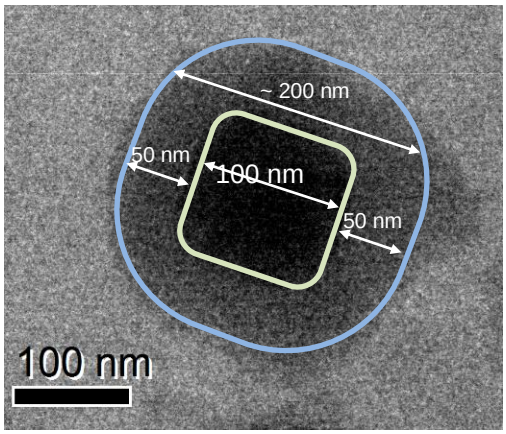

Figure 162. Annotated cryo-TEM of a $CaPO_4$ coated H-BT-PLL nanoparticle in complete cell culture media dispersed at a concentration of at 100 µg/mL; to highlight the assumptions in particle and shell size used for the following calculations.

Total volume of BT particles in suspension (Mass = Volume x Density):

100×10^{-6} g/mL, density of $BaTiO_3$ = 6.02 g cm^{-3}

Therefore, the total volume of BT in 1 mL = 16.6×10^{-6} cm^3.

Volume of one BT nanoparticle (100 nm cube)

$$(100 \times 10^{-9})^3 = 1 \times 10^{-21}\ m^3$$

Volume of Coating around one BT particle

$$= (200 \times 10^{-9})^3 - (100 \times 10^{-9})^3 = (8 \times 10^{-21} - 1 \times 10^{-21})$$

$= 7 \times 10^{-21}$ m^3 (i.e. 7 times volume of $BaTiO_3$) So:

Coating volume in 1 mL of solution = $7 \times 16.6 \times 10^{-6}$ cm^{-3} = 1.162×10^{-4} cm^3

Assuming $Ca_5(PO_4)_3(OH)$ is 50 % of coating then volume of $Ca_5(PO_4)_3OH$ in 1 mL of solution is:

$$1.162 \times 10^{-4}\ cm^3 \times 0.5 = 0.58 \times 10^{-4}\ cm^3$$

Calcium ions in Hydroxyapatite 1 mL of solution (density = 3.16 g/cm^3, molar mass 502.3 g/mol)

Mass of Hydroxyapatite in 1 mL = $0.58 \times 10^{-4}\ cm^3 \times 3.16\ g/cm^3 = 1.83 \times 10^{-4}$ g

Ca Molar mass = (= 40.01 g/mol x 5) = 200.4 g/mol

Ca Molar mass to Hydroxyapatite ratio = 200.4 g/mol/502.3 g/mol ≈ 0.4

Concentration of Ca ions used in 1 mL of suspension.

(mass of Ca ions x Ca Molar mass ratio) = $0.4 \times 1.83 \times 10^{-4}$ g

= 0.73×10^{-4} g ≈ 70 µg/mL of Ca

Concentration of Ca ions used from $CaCl_2$ in complete cell culture media ($CaCl_2$ concentration of 200 µg/mL [164])

Molar mass of Ca = 40.01 g/mol, Molar mass of Cl = 35.45 g/mol

so Ca Molar mass ratio to $CaCl_2$ = 0.36

0.36 x 200 µg/mL = 72 µg/mL ≈ 70 µg/mL of Ca

Therefore ≈70 µg/mL of Ca ions used to coat 100 µg/mL of BT

Equation 13. Simple calculation to show that Calcium ions are used up coating 100 µg/mL of $BaTiO_3$. Stock of Ca ions in 200 µg/mL of $CaCl_2$ is 72 µg/mL of Ca ions, so all available Ca ions would be used up by coating 100 µg/mL of BT.

Cryo-TEM imaging of H-BT-PLL nanoparticles at 100 µg/mL (Figure 157) showed coated H-BT-PLL nanoparticles with a Ca: P rich-coating and H-BT-PLL nanoparticles without a Ca: P coating. The estimation given in Equation 13 suggested ~70 µg/mL of Ca ions were needed to coat 100 µg/mL of H-BT. This implies all the calcium ions were used up at nanoparticle concentrations of ≥ 100 µg/mL, which could account for the reason why some nanoparticles were not calcium phosphate coated by cryo-TEM at 100 µg/mL H-BT-PLL.

Assuming the calcium phosphate layer forms because of ionic interactions that screen the positive surface charge of H-BT-PLL then this would have left the remaining H-BT-PLL with a positive surface charge (Figure 140). This remaining fraction of positively charged H-BT-PLL nanoparticles are likely to have had an effect on cytotoxicity. It has been reported that positively charged nanoparticles were more cytotoxic than negative nanoparticles of similar size in non-phagocytic (A549) cells [51]. In addition, Research has shown that positively charged particles are more readily taken up by cells than the respective anionic nanoparticle [51,166] and further research has shown PLL to be toxic [167,168].

Thus the reduction in the MTT cell viability for H-BT-PLL nanoparticles (Figure 134) between 10–100 µg/mL could be due to the calcium phosphate *uncoated* H-BT-PLL nanoparticle fraction with a greater positive surface charge than that of calcium phosphate coated H-BT-PLL nanoparticle fraction; due to either the positive surface charge or direct exposure to PLL.

Calcium ions take part in many cellular functions such as movement, metabolism and proliferation of cellular life cycles [169], and if *all* the calcium ions are being used to coat the barium titanate nanoparticles (at concentrations

of ≥ 100 µg/mL) this may reduce the cell viability. Loss of calcium is known to alter the different cellular pathways that require Ca ions [170].

This intermediate particle size fraction which we attributed to calcium phosphate coated H-BT-PLL nanoparticle clusters (~500 nm) was seen in the number plot of the H-BT-PLL DLS measurement in complete cell culture media at 100 µg/mL (Figure 143). H-BT-PLL nanoparticles at the same concentration (100 µg/mL) were quantitatively analysed by Cryo-TEM, showing that this intermediate particle size was indeed the calcium phosphate coated H-BT-PLL nanoparticles.

The comparison of the DLS and cryo-TEM number distributions are compared in Figure 163 for H-BT and H-BT-PLL in complete cell culture media.

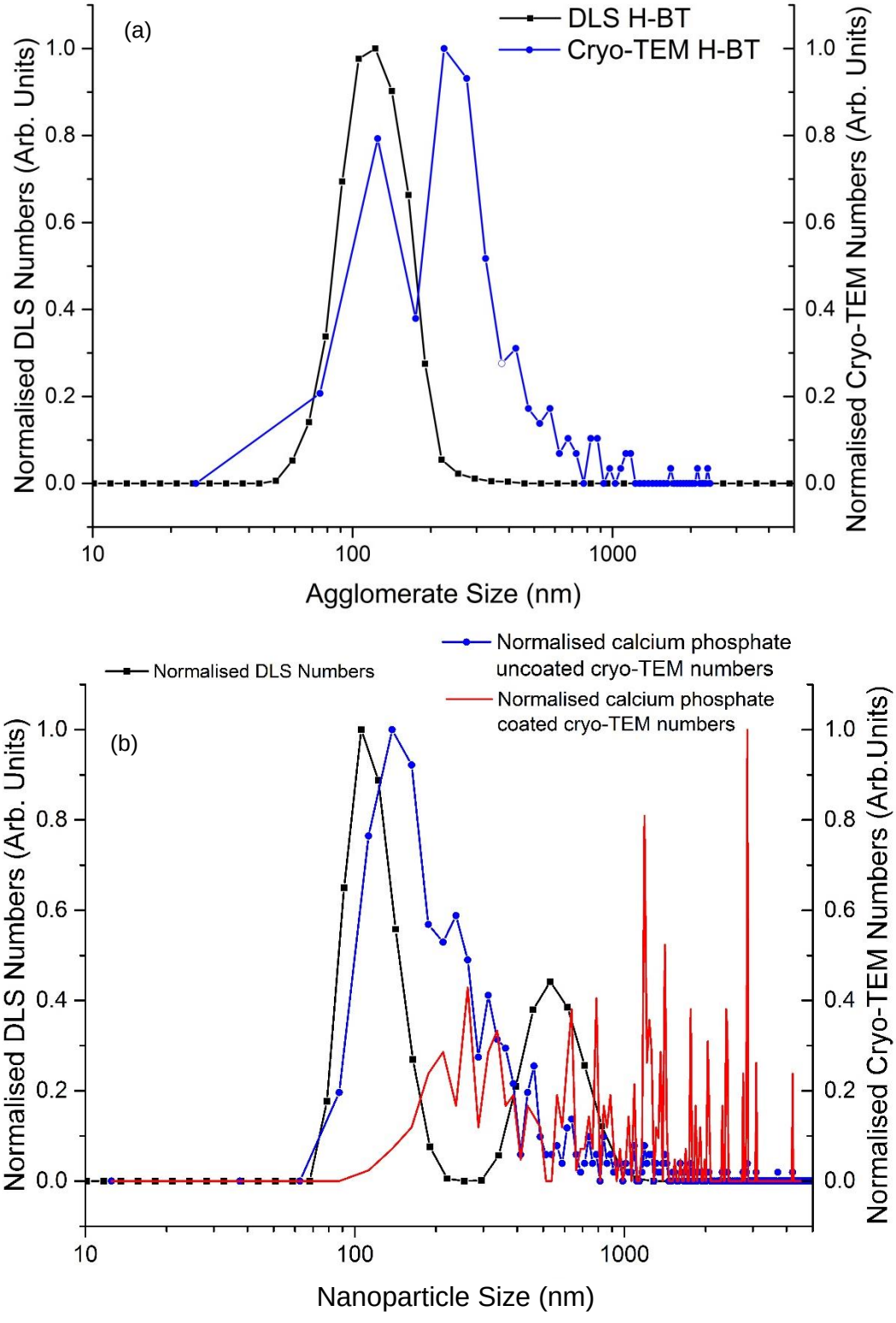

Figure 163. Comparison of the dynamic light scattering and Cryo-TEM data of (a) H-BT in complete cell culture media and (b) H-BST-PLL nanoparticles in complete cell culture media.

Figure 163 shows the number distributions of H-BT and H-BT-PLL nanoparticles in complete cell culture media collected by DLS and cryo-TEM. The cryo-TEM analysis shows that the calcium phosphate uncoated H-BT-PLL nanoparticles matched the DLS data of small agglomerates of primary particle size (~100–200 nm) whereas the calcium phosphate coated H-BT-PLL cluster sizes broadly matched the intermediate particle size identified by DLS (~500 nm). Cryo-TEM also showed that large agglomerates are present for calcium phosphate coated and uncoated H-BT-PLL nanoparticles (>1,000 nm), as predicted by DLS.

6.7 Chapter Summary

- MTT cell viability assays showed a decrease in viability for nanoparticle concentrations of 1000 µg/mL for H-BT and above 100 µg/mL for H-BT-PLL and above 10 µg/mL for H-BST-PLL (Figure 134)
- The genotoxic (Comet) assay showed that nanoparticles caused no DNA damage (aside from the failed assays for PLL coated nanoparticles above 10 µg/mL) – Figure 136.
- FTIR spectra of coated nanoparticles showed vibrations associated with PLL and the presence of this coating was confirmed by dropcast bright field TEM (Figure 138).
- The zeta potential measurements of H-BT and H-BT-PLL nanoparticle surface charge in water increased from negative to positive mV when PLL was coated on the nanoparticles (Figure 140)

- Dynamic light scattering showed large numbers of small agglomerates of primary particle size and relatively few large agglomerates for most nanoparticle suspensions (Figure 142).
- For H-BT-PLL nanoparticles in complete cell culture media there was the presence of an additional, intermediate agglomerate size fraction (~ 500 nm) Figure 143.
- Overall, DLS data showed the nanoparticle suspensions in different media were broadly similar at a range of concentrations (Table 27).
- The SEM and FIB milling showed that the nanoparticles were internalised by A549 cells (Figure 147 – Figure 150).
- HAADF-STEM and TEM-EDX confirmed that the nanoparticles were internalised by A549 cells. However, the PLL coated nanoparticle samples showed no significant coating when inside the cell (Figure 152).
- Cryo-TEM of 100 µg/mL was conducted to confirm changes seen by DLS in the dispersion between H-BT and H-BT-PLL and to provide mechanistic causes of the reduced cell viability (Figure 157).
- A calcium phosphate-rich coating of some of the H-BT-PLL nanoparticles was identified by cryo-TEM (Figure 161). However, some fraction of the H-BT-PLL particles remained uncoated at 100 µg/mL (Figure 163). It has been shown that a 50 nm thick calcium phosphate rich shell around each H-BT-PLL nanoparticle would have used up all the Ca ions available in the complete cell culture media at a concentration of 100 µg/mL maximum (Section 6.6.1) and this may explain why a fraction remained uncoated.

- This calcium phosphate uncoated H-BT-PLL fraction may have been the cause of the reduction in cell viability above 10 µg/mL in H-BT-PLL (discussion – Section 6.6.1).
- Another possibility of reduced cell viability is the lack of calcium ions in the media for cell signalling pathways which ultimately leads to cell death.

Chapter 7 – Results and Discussion

Hydrothermal barium titanate (H-BT) and barium strontium titanate (H-BST) nanoparticles of ~140 nm and ~45 nm have been successfully synthesised for their second harmonic imaging applications using a multiphoton laser source.

7.1.1 Synthesis and characterisation of tetragonal barium titanate and barium strontium titanate.

Chapter 4 presented the Rietveld peak fitting of X-Ray powder diffraction data (laboratory and synchrotron) for commercial and synthesised hydrothermal, $BaTiO_3$ and $Ba_{1-x}Sr_xTiO_3$ samples. Rietveld analysis showed all samples, except the as-bought CT-BT exhibited a mixture of tetragonal and cubic crystal phases. The CT-BT sample had evidence for a clear (002/200) peak splitting (and c/a of 1.01) and was presumed to be 100 % tetragonal due to no cubic phase being required for the fit (Figure 77, Chapter 4). When the CT-BT sample was heated through the Curie point (at 130 ^oC) to 170 ^oC, laboratory-XRD observed the tetragonal (002/200) split peak change to a single cubic (200) peak, indicating a phase transition from tetragonal to cubic occurred; Figure 79, Chapter 4 [22,62]. Because the CT-BT sample showed a 100 % tetragonal phase by synchrotron radiation and a tetragonal to cubic transition upon heating, this sample was used as a tetragonal calibration standard for EELS analysis in Chapter 5.

Rietveld peak fitting of the synthesised H-BT estimated that ~60 % of a tetragonal phase was present (and c/a of 1.006). This sample showed a tetragonal (002/200) peak splitting but the sample also had showed the

presence of a ~40 % cubic phase. When the sample was heated through the Curie point to 170 ^{o}C the tetragonally split (002/200) peak transformed to a single (200) cubic peak (Figure 84, Chapter 4). However, Rietveld analysis showed a tetragonal phase could still be fitted to the data (54 % phase fraction), suggesting a tetragonal phase remained above the Curie temperature. *In-situ* TEM analysis by Li *et al.* implies that strain relaxation at the surface of barium titanate allows all phases (cubic, tetragonal, orthorhombic and rhombohedral) to co-exist in $BaTiO_3$ nanoparticles (of 2–10 nm sizes) up to a temperature of 600 ^{o}C [171]. However, it is likely the tetragonal phase Rietveld fitting could be a result of a broad (200) diffraction peak base caused by internal defects (such as hydroxyl defects) and strain in the nanoparticles [81,172].

To further confirm barium titanate nanoparticles were successfully synthesised; SEM with EDX and TEM with electron diffraction was employed (Chapter 4, Figure 86 and Figure 87). SEM with EDX showed the morphology and expected elemental composition of the nanoparticles, whereas TEM with electron diffraction highlighted the particle size distribution and confirmed a barium titanate crystal structure.

The first batch of hydrothermally synthesised barium strontium titanate (HBST-01) nanoparticles showed a bi-modal incorporation of strontium ions in the barium titanate lattice, with a barium-rich BST producing a (002/200) diffraction peak splitting and strontium-rich BST producing a separate (200) diffraction peak (Figure 88). This was undesirable because not all particles would emit SHG at the same intensity and so a batch was re-synthesised following Roeder *et al*. [92]. The newly synthesised H-BST showed a more consistent strontium

incorporation by TEM-EDX (Figure 92) and Rietveld analysis showed a ~75 % tetragonal phase fraction present (and c/a ratio of 1.0002; Figure 91).

Experimentally determining the phase of $BaTiO_3$ nanoparticles has been extensively discussed in literature. Characterising the phase of $BaTiO_3$ nanoparticles using 'bulk' techniques (like laboratory-XRD and X-Ray synchrotron diffraction) are difficult and are used to try and determine the phase of individual nanoparticles. This leads to characterising the global/net phase of the nanoparticles as opposed to individual nanoparticles and the post-data analysis (like Rietveld and PDF) can be dependent on resolution of data and user experience [74,173].

Regardless of the precise mixture of tetragonal and cubic crystal phases, all samples produced SHG of light (Figure 95, Chapter 4) with CC-BT and H-BST requiring an increase in laser power – likely due to the smaller particle size of the nanoparticles, as demonstrated by Kim *et al.* [39]. This was the first instance where barium strontium titanate nanoparticles have been used to produce second harmonic light and supports the reason for Sr ion addition (to enhance SHG output due to the increased dielectric constant). It can be argued that second harmonic emission from ~45 nm H-BST nanoparticles was enhanced because emission was detected from particles smaller than H-BT (~140 nm) but no direct comparison can be made due to the difference in size [22,28,40]. Correlative SHG and SEM qualitatively showed all nanoparticles to emit second harmonic light (Figure 97, Chapter 4). Moreover, samples that show no tetragonal (002/200) peak splitting in the XRD pattern (such as CC-BT and H-BST) also produced second harmonic light and this is also seen in particle sizes down to 22 nm; Kim *et al*. [39]. Although the generally accepted

size-dependent phase transition mechanism suggests a tetragonal-core and cubic-shell structure (Figure 4, Chapter 1), it is generally accepted that the surface layer is atomically-rough/disordered and can be an origin of SHG in these cases [39].

7.1.2 Origin of second harmonic generation

To address the origin of SHG in these nanoparticles, Chapter 5 presented the results of *in-situ* heating in the TEM of CT-BT and H-BT nanoparticles to 400 ^{o}C and electron energy loss spectra were collected from a whole CT-BT nanoparticle (diffraction coupled) and scanned across a H-BT nanoparticle (STEM-EELS). Furthermore, high resolution HAADF-STEM Ti-atom position analysis and STEM-EELS analysis of H-BT was collected by aberration corrected STEM (at room temperature) shown in Section 5.2 in Chapter 5.

Electron diffraction data of CT-BT and H-BT samples showed the (002/200) tetragonal reflections disappearing when heated through the Curie point (Figure 103 and Figure 114 in Chapter 5), providing evidence of a tetragonal to cubic phase transition of individual and many nanoparticles. This suggested that a phase transition does occur in XRD above the Curie point (Figure 79 and Figure 84, Chapter 4). *In-situ*, diffraction coupled EELS of CT-BT and STEM-EELS of H-BT showed a reduction in the Ti-L_3 edge t_{2g}-e_g peak separation when heated through the Curie point, in agreement with Bugnet *et al*. and Moon *et al.* [68,93].

The strength of the crystal field splitting at the Ti-L_3 edge (i.e. the t_{2g}-e_g splitting) is inversely proportional to the Ti-O distance [68,134,174]. In the tetragonal unit cell (Figure 20, Chapter 2) there is an offset Ti-atom in the c-direction, meaning

that there is one oxygen anion closer to the Ti-atom (~1.8 Å) and another further away (~2.1 Å) however, the increased electrostatic interaction between the closer ions will increase the crystal field splitting. This was observed for the CT-BT Ti-$L_{2,3}$ edge t_{2g}-e_g splitting where the peak separation at room temperature was ~2.05 eV (having shown that it is was 100 % tetragonal by XRD; Figure 79, Chapter 4 and, Table 22 Chapter 5). When the sample was heated above the Curie point, the Ti-O distances become equal (~1.95 Å), which would imply in first approximation that, the crystal field splitting should decrease and it was observed that when the CT-BT and H-BT samples were heated above the Curie point, there was a decrease in Ti-L_3 t_{2g}-e_g peak separation to ~2.0 eV (Table 15, Chapter 5). This is consistent with the tetragonal to cubic phase change already observed by electron diffraction occurring because cubic phases have an increase in unit cell volume. The cubic ICDD reference pattern quotes a larger unit cell volume (ICDD: 01-078-4475), and this was also confirmed experimentally by Rietveld and PDF analysis of synchrotron diffraction data (Smith *et al*. [74]). This suggests that the decrease in the Ti-$L_{2,3}$ edge t_{2g}-e_g peak separation is because of the increased unit cell volume produced by the tetragonal to cubic phase transition (and therefore ultimately a decrease in electrostatic interaction). Ultimately, this enables us to state that any t_{2g}-e_g splitting above 2.05 eV is tetragonal-like and below 2.0 eV is cubic-like.

This EELS phase fingerprint was used to probe individual H-BT nanoparticles by STEM-EELS linescans. This highlighted tetragonal-like t_{2g}-e_g peak splitting in the bulk of a nanoparticle and a cubic-like t_{2g}-e_g splitting at the surface (Figure 119, Chapter 5). The opposite peak splitting was observed by Moon *et*

al. where the Ti-L_3 t_{2g}-e_g peak splitting of their barium titanate sample showed a tetragonal-like surface and cubic-like core [93]. Moon *et al*. hydrothermally synthesised 50 nm $BaTiO_3$ nanoparticles using only hydroxide precursors carried out at 180 ^oC for 6 hours. Their Ti-L_3 edge t_{2g}-e_g splitting results are not consistent with the conventional phase gradient core-shell model presented in the literature review [20,77,93]. However, their research did confirm that the Ti-L_3 edge t_{2g}-e_g peak separation was reduced for cubic phase samples [68,93].

The presence of a tetragonal-core and cubic-surface phase fraction identified by STEM-EELS was compared to the estimated phase fractions estimated by XRD (Chapter 4). This suggested an *intra*-particle phase variation in agreement with the conventional size-dependent phase mechanism i.e. a tetragonal-core and a cubic-shell [20,100]. The estimated tetragonal fraction of ~60 % for H-BT by Rietveld analysis was compared to a calculated ~73 % by STEM-EELS analysis (Table 6), Chapter 4 and Equation 11, Chapter 5) which assumed a cubic surface layer of ~10 nm in an average-sized particle.

The STEM-EEL spectra acquired at SuperSTEM showed poor resolution and under-sampled spectra (Figure 127, Chapter 5). However, high resolution atomic lattice images of H-BT provided information on the surface and core of the nanoparticle (Figure 129, Chapter 5). The qualitative image analysis of the H-BT surface showed an atomically rough layer with incomplete unit cells (Figure 128) and an apparent cubic-like ‘strain relaxed’ surface (based on the previous STEM-EELS data). Li *et al*. claim a ‘strain relaxed’ surface in barium titanate nanoparticles can account for ferroelectricity above the Curie point due to the coexistence of all phases [171]. However, it is likely that complete ‘relaxation’ of defects or strains only occurs when the sample is heated through

the Curie temperature to a 100 % cubic phase; i.e. when the H-BT sample is heated to 170 ^{o}C and 400 ^{o}C analysed by XRD and STEM-EELS respectively (in Figure 84 in Chapter 4 and Figure 120 in Chapter 5).

Ti-atom displacement mapping at the core of H-BT (Figure 129) showed, random distortions in the lattice. The magnitude of the Ti-atom displacements measured by HAADF-STEM imaging were ~0.2 Å and this is larger than the maximum displacement (~0.15 Å) analysed by Polking *et al*. in 15 nm sized barium titanate [78]. Rietveld peak fitting of XRD data suggests a *net* distortion of central Ti-atom columns of ~0.02 Å (Table 6, Chapter 4) compared to ~0.2 Å characterised locally by HAADF-STEM (Figure 129). The larger but randomly oriented distortions are *assumed* to be associated with internal defects/strains [175]. The bulk measurement and lower 'net' distortion in XRD, is likely due to the global measurement of the random distortions observed locally by HAADF-STEM.

Thus, we arrive at a model of the H-BT nanoparticles with internal defects and strains (induced by the hydrothermal growth process) and a phase gradient from shell to core that is consistent with the strain relaxation and the core-shell model present in the literature [20,77]. Wada *et al.* proposed the source of the defects in hydrothermal barium titanate were internalised hydroxyl ions and barium vacancies that arise during the hydrothermal synthesis [81,172].

A similar *intra*-particle phase variation can be seen for H-BST with a Rietveld refinement-estimated tetragonal core-volume fraction of ~74 % (Figure 91, Chapter 4) compared to ~65 % by STEM-EELS analysis (Equation 12, Chapter 5). Rietveld analysis suggests the *net* tetragonal distortion is 0.002 Å (Table 7, Chapter 4) compared to the local strain induced distortion of ~0.15 Å by

HAADF-STEM analysis (Figure 130, Chapter 5; similar to that found by Polking *et al*. [78]). The Ti-atom position distortion also continues to the surface of the nanoparticles (albeit smaller in magnitude compared to nanoparticle bulk as per the H-BT sample) even though this sample only had a ~6 nm cubic layer by STEM-EELS t_{2g}-e_g peak splitting analysis (Figure 132, Chapter 5) (compared to 10 nm in H-BT).

Overall, the characterisation of H-BT and H-BST nanoparticles suggests that surface roughness and internal defects/strains of the nanoparticles (Figure 129, Chapter 5) could give rise to a two-phase character to the particles (a tetragonal-like core and a cubic-like shell). This *intra*-particle variation in structure will certainly give rise to SHG because of the non-centrosymmetric *local* distortions identified by STEM-EELS and HAADF-STEM imaging and the global *net* distortions identified by XRD; i.e. second harmonic light is produced by all samples because it is likely to be both a surface and bulk effect [36,39]. Thus it is suggested that strain and internal defects may be critical parameters for all $BaTiO_3$ nanoparticles if they are to produce SHG – Kim *et al.* [39,172].

7.1.3 Nanoparticle suspension behaviour

Having established the potential origin of SHG, Chapter 6 investigated lung epithelial (A549) cell viability and genotoxicity after a 24-hour exposure to uncoated and poly-L-lysine (PLL) coated barium titanate nanoparticles. The cell viability (MTT) assay of H-BT and H-BST nanoparticles showed no significant reduction in cell viability at any nanoparticle concentration (up to 1000 µg/mL), whereas the H-BT-PLL and H-BST-PLL nanoparticles show a significant

decrease in cell viability at nanoparticle concentrations at ≥100 µg/mL and ≥10 µg/mL, respectively (Figure 134 and Figure 135).

The genotoxic (comet) assay for H-BT and H-BST nanoparticles samples showed no significant DNA damage to A549 cells across the nanoparticle concentrations (up to 1000 µg/mL). However, the H-BT-PLL and H-BST-PLL comet assays failed at nanoparticle concentrations higher than 10 µg/mL (Figure 136 and Figure 137) due to difficulties in electrophoretic separation at high nanoparticle concentrations, presumably due to a large positive charge being present (arising from the PLL).

The PLL coating protocol was first shown by Ciofani *et al*. and used to improve nanoparticle colloid stabilisation for SHG purposes [116]. Successful PLL coating was shown here by: qualitative FTIR spectroscopy (Table 23), bright-field TEM imaging (Figure 138) and a change in zeta potential (from -29 mV when uncoated to +49 mV when PLL coated) when the nanoparticles were suspended in water (Figure 140) in Section 6.2. The zeta potential measurement of the uncoated and PLL coated nanoparticles was attempted in cell culture media, but it produced varying and unreliable results; likely due to the interaction of the nanoparticles with the media.

The stability of uncoated and PLL-coated nanoparticles was characterised by dynamic light scattering of particle suspensions in water, serum free media and complete cell culture media at a range of nanoparticle concentrations (0.1 to 1000 µg/mL). This provided insight into the nanoparticle behaviour in suspension before they were introduced to cells (summarised in Table 27). Nanoparticles suspended in water showed a reasonably monodisperse suspension with small nanoparticle agglomerates close to the primary particle

size (~140 nm) being dominant by number and agglomerates of 1000's of particles (~10,000 nm) being dominant by volume. The serum-free media suspensions however, were polydisperse by their intensity, volume and number distribution and the inorganic salts and electrolytes in serum free media were presumed to interfere with the DLS measurements [161,162].

The intensity, volume and number distributions of nanoparticles suspended in complete cell culture media shows the presence of serum at ~10–50 nm, dominating the scattering measurement (also shown by Hondow *et al*. [163]). The H-BT nanoparticle suspension in complete cell culture media however showed the same particle distribution that was seen in the water suspension with large numbers of nanoparticles near to the primary particle size (~140 nm) and relatively few large agglomerates of nanoparticles (~10,000 nm). H-BT-PLL nanoparticles suspended in complete cell culture media showed a similar monodisperse system up to 100 µg/mL and above this concentration where the size distribution was then bimodal. At 100 µg/mL the number plot highlighted scattering at a primary particle size (~140 nm) and an intermediate particle size (~500 nm). The reported cluster size measured by Ciofani *et al*. was ~300 nm at their maximum nanoparticle concentration of 20 µg/mL [116]. Measuring higher concentrations than Ciofani *et al.* allowed for a different interpretation of the nanoparticle dispersion behaviour.

The H-BST nanoparticle suspensions in complete cell culture media also showed the presence of serum at ~10–50 nm and a number-dominant agglomerate size (~200-400 nm) compared to the ~45 nm measured particle size by TEM (Figure 93, Chapter 4). The H-BST-PLL nanoparticles only showed the presence of serum at 0.1 µg/mL, with the other concentrations

showing the nanoparticle cluster size (~200-400 nm) to be dominant by number and volume.

Overall, the DLS data gives an understanding of the nanoparticle suspensions before cell exposure. There are two main particle sizes that are exposed to cells: (a) agglomerates of near primary particle size (~140 nm) and (b) few relatively large agglomerates that might dominate the dose but would only kill a few cells. Because the MTT and Comet assays showed little change in cell viability and impact on the genotoxicity, the cells are able to cope with exposure to lots of small agglomerates (assuming the nanoparticles are taken up into the cell).

The cell uptake of nanoparticles was confirmed by electron microscopy of critically point dried and resin embedded cells (SEM, FIB-SEM and HAADF-STEM). Electron microscopy showed that varying amounts of nanoparticles were taken up into the cells after a 24-hour exposure (Figure 147). The cells appeared viable and had exhibited small nanoparticle agglomerates that has been internalised (Figure 151, Chapter 6); consistent with the DLS summary. However, for the PLL-coated nanoparticles, no clear coating was visible after they were internalised by the cells (Figure 150). This was also present in the work by Ciofani *et al*. and they suggested that poly-L-lysine undergoes dissolution upon cell internalisation [116]. Cryo-TEM of H-BT and H-BT-PLL nanoparticles suspended in water (vitreous ice) showed an obvious coating for H-BT-PLL nanoparticles (Figure 155, Chapter 6). Cryo-TEM of H-BT and H-BT-PLL nanoparticles suspended in complete cell culture media were acquired in order to understand their dispersion behaviour when being introduced to cells.

When H-BT nanoparticles were suspended in complete cell culture media at 100 µg/mL, plunge frozen and imaged by TEM (Figure 156) they showed cluster sizes of ~200 nm which were similar to the size measured by DLS (Figure 143). H-BT-PLL nanoparticles in complete cell culture media on the other hand showed a number of particles that were obviously coated and another fraction which were not (Figure 157). This accounted for the bimodal number plot distribution seen by DLS measurements (Figure 143), where the coated H-BT-PLL nanoparticles seen in TEM are the intermediate particle size (~500 nm) identified by DLS and the uncoated nanoparticles seen in TEM are the primary particle size agglomerates (~140 nm) identified by DLS. Cryo-TEM with HAADF-STEM EDX mapping was used to determine the composition of the coating around the H-BT nanoparticle which was revealed to be calcium-phosphate (Figure 159). The complete cell culture medium contained 200 µg/mL of calcium chloride and 400 µg/mL of sodium phosphate [164].

If it is still assumed that the H-BT-PLL nanoparticles had a poly-L-lysine coating, as identified by the positive zeta potential measurements and other TEM images (in Section 6.2), it could be that a calcium phosphate layer forms from the media to screen the net positive charge of the PLL coating (initially by phosphate group migration and then by calcium migration). At a sufficient nanoparticle concentration all the Ca ions in the media could be used up. This leaves a fraction of H-BT-PLL nanoparticles not coated in calcium phosphate. This fraction with only PLL at the surface, could on exposure to cells reduce cell viability as observed here (Figure 134) and presented by Ciofani *et al*. [116]. Moreover, increased uptake could occur due to the positive surface charge of the nanoparticle and increased cytotoxicity may follow (Fröhlich [51]).

The impact of direct cellular contact with poly-L-lysine is described by other research [51,167,168]. It is also possible that the resulting lack of calcium ions in the media (which are typically used for cell signalling) may also lead to cell death [170].

It is possible to show that all the calcium ions in the complete cell culture media would be used to coat the 100 nm H-BT nanoparticles at a concentration of ~70 µg/mL or higher (Section 6.6.1 in Chapter 6). This is consistent with the observed onset of a bimodal distribution at 100 µg/mL of primary particle size agglomerates (~140 nm) and intermediate size agglomerates (~500 nm) by DLS (Figure 143) and by cryo-TEM size measurements (Figure 163).

In summary, hydrothermal synthesis of $BaTiO_3$ nanoparticles has been shown to be an appropriate route to produce SHG biomarkers because of potential internal defects and strains that produce a core-shell phase structure ideal for SHG production. Sr additions are shown to potentially enhance SHG, although this cannot be confirmed because the resulting particle sizes are smaller than the equivalent H-BT particles. Uncoated hydrothermal H-BT nanoparticles are shown to be biocompatible and induce very little cytotoxicity, despite being taken up by lung epithelial cells. This is because: (a) $BaTiO_3$ is not especially toxic [40] and (b) the nanoparticles disperse reasonably well in cell culture media, producing small clusters of few primary particles (number dominant) with only some large clusters of nanoparticles (volume dominant). Therefore, most cells will only be exposed to small clusters of nanoparticles and hardly any exposed to large nanoparticle agglomerates (seen in the cell uptake by electron microscopy; Figure 152). If the cells can tolerate nanoparticle

internalisation (of small agglomerates) as evidenced by TEM data; then most cells will be unaffected by exposure to the barium titanate nanoparticles.

Functionalising the nanoparticles with PLL aimed to enhance cellular uptake by using a positively charged coating, however it had a very different impact and the coating ‘interacted’ with the delivery media in an unexpected way. Here, we show a positively charged coating potentially takes all of the vital calcium ions out the media (by causing them to precipitate electrostatically into an additional coating on the positively charged polymer coated-nanoparticle). This has significant impact on the exposed cells (either through direct exposure to PLL or calcium ion deficiency) and makes such a coating unsuitable for long-term biomarker applications.

7.1.4 Summary

Thus, this work adds to the body of knowledge on H-BT nanoparticles for biomarkers by showing the potential source of SHG in hydrothermally prepared H-BT nanoparticles (if not all barium titanate nanoparticles shown in this work). In addition, I have shown that understanding the dispersion behaviour of such nanoparticles in delivery media is essential prior to cellular or tissue exposure for biomarker applications.

Chapter 8 – Conclusions and future work.

The aim of this project was to explore barium titanate nanoparticle systems for biomarker applications. Using a hydrothermal synthesis method, barium titanate (H-BT) and barium strontium titanate (H-BST) nanoparticles were successfully synthesised and were characterised for their multiphoton second harmonic generation of light and their associated biomarker applications.

8.1 Outcomes:

8.1.1 Structural characterisation and underpinning Science

Successful hydrothermal syntheses of $BaTiO_3$ and $Ba_{0.8}Sr_{0.2}TiO_3$ nanoparticles were characterised by X-Ray diffraction (XRD), electron microscopy (TEM and SEM), electron energy loss spectroscopy (EELS) and multiphoton second harmonic generation (SHG). The homogenous incorporation of strontium ions into the barium titanate lattice was proposed in order to increase the dielectric constant (and therefore increase the net polarisation) at a lower Curie temperature, and therefore enhance the SHG output overall. However, smaller H-BST nanoparticles (~45 nm) in comparison to H-BT (~140 nm) required more laser power which increases the risk of damage to cellular and tissue structures. i.e. the need for a higher flux of near-infrared incident radiation would increase the damage risk to exposed biological material. Although, successful SHG was possible from H-BST, a direct size comparison would be required to determine whether strontium incorporation truly enhances SHG. The crystal phase of the nanoparticles was characterised by Rietveld refinement of synchrotron XRD data, which estimated

that most nanoparticles were a combination of tetragonal and cubic crystal phases (except for a commercial tetragonal barium titanate sample, CT-BT). The H-BT and H-BST samples were estimated to have a tetragonal phase fraction of ~60 % and ~75 % respectively. High resolution electron microscopy and electron energy loss spectroscopy determined the source of SHG to be both a surface and bulk effect; due to the random Ti-atom displacement present in the bulk of the nanoparticle (meaning it is non-centrosymmetric) and an atomically rough surface layer of the nanoparticles (with a corresponding lack of inversion symmetry i.e. non-centrosymmetric). XRD showed the presence of two phases (cubic and tetragonal), whereas SHG showed that all particles emit and STEM-EELS suggested a tetragonal core and a cubic surface. Therefore, we suggest agreement with recent research indicating a core-shell structure for these nanoparticles. This was consistent with high-resolution STEM imaging data which although showed Ti-atom distortion towards the surface of the nanoparticle, the displacement was found to be smaller at the surface as compared to the bulk of the nanoparticle, suggesting a gradient-lattice strain layer; [77]. *In-situ* STEM-EELS showed a mixed phase tetragonal-like core and cubic-like shell when the Ti-L_3 edge t_{2g}-e_g peak splitting was measured across the nanoparticle when heated. When the H-BT sample was heated *in-situ* above the Curie point, STEM-EELS showed a cubic-like Ti-L_3 edge t_{2g}-e_g peak splitting across the whole nanoparticle, suggesting a tetragonal to cubic phase transformation occurred. This was also confirmed by electron diffraction of CT-BT and H-BT particles, showing a tetragonal to cubic phase change when heated above the Curie point. This work

presents the underpinning science that shows hydrothermal synthesis induces growth defects and strain gradients that produce core-shell nanoparticles suitable for SHG.

8.1.2 Application and underpinning coating mechanisms

Nanoparticles were successfully coated with a positively charged poly-L-lysine (PLL) polymer shown by FTIR, electron microscopy and zeta potential measurements. The PLL coating was used to try to enhance or to promote cellular uptake, (due to the net negative charge of the A549 lung epithelial cell) however, no quantitative study was performed to compare the uptake of uncoated and PLL-coated nanoparticles. MTT and Comet assays were used to measure the cell viability and genotoxicity of uncoated and PLL coated nanoparticles after 24-hour exposure to the A549 lung epithelial cells, showing a decrease in cell viability for PLL coated nanoparticles at high exposure concentrations (≥100 μg/mL).

The nanoparticle suspensions in water, serum free media and complete cell culture media were measured by dynamic light scattering (DLS) and most of the suspensions appeared reasonably monodisperse with dominant numbers of agglomerates close to the primary particle size (~200 nm) and a few large nanoparticle agglomerates that were significant by volume (~10,000 nm in size) being present. DLS data suggested that nanoparticle clusters (near primary particle size) would dominate uptake by cells as they were number dominant. H-BT-PLL nanoparticles suspended in complete cell culture media at above critical concentrations ≥100 μg/mL, showed a bimodal number distribution of near primary

particle size agglomerates (~150 nm) and intermediate size agglomerates (~500 nm), as well as the expected low fraction of large volume agglomerates.

Cell uptake was identified by electron microscopy of critically point dried and resin embedded cells, showing primarily that small agglomerates were taken up by cells, and confirming that $BaTiO_3$ and $Ba_{1-x}Sr_xTiO_3$ nanoparticles can be used for biomarker work. However, the cell viability drops at high dosing concentrations and is significantly lower for positively charged nanoparticles, which is likely due to the interaction with complete cell culture media identified by Cryo-TEM (see below). Electron microscopy of H-BT-PLL nanoparticles showed cell uptake with no visible PLL coating present.

H-BT-PLL was analysed by cryo-TEM to understand the nanoparticle suspension behaviour in cell culture media before being introduced to the cells. It was observed that H-BT-PLL nanoparticles interacted with constituent ions from the complete cell culture media to give nanoparticles coated in a ~ 100 nm thick calcium phosphate layer. Potentially this removed all the calcium ions from the stock complete cell culture media at nanoparticle concentrations of ~70 µg/mL and above, resulting in either a portion of H-BT-PLL nanoparticles without a calcium phosphate coating being in direct contact with the cell, or the removal of calcium ions in the media that are used for cell signalling. Either possibility could have led to cell death. This nanoparticle interaction has not been identified before and is not currently well understood.

8.2 Recommendations for Future work

An overall recommendation from this work is to use $BaTiO_3$ and $Ba_{1-x}Sr_xTiO_3$ nanoparticles for future SHG work. The source of SHG in hydrothermally synthesised nanoparticles has been identified by EELS and high resolution electron microscopy arising from a core-shell nanoparticle structure. This plus other research has shown SHG to occur for particle sizes down to 22 nm (~45 nm in this research), even though the particles are expected to be cubic in phase at this size [39]. Future work could explore:

- Using similar $BaTiO_3$ and $BaSrTiO_3$ nanoparticle sizes to quantify the SHG output and determine quantitatively whether strontium addition improves SHG output.
- Quantify the uptake of uncoated and coated $BaTiO_3$ and $BaSrTiO_3$ nanoparticles by high-throughput screening of SHG using flow cytometry as well as low throughput electron microscopy (similar to work published by Summers *et al.* on quantum dots [176]).
- To measure the SHG output of $BaTiO_3$ and $BaSrTiO_3$ nanoparticles in cells to quantify the output signal generated from the nanoparticles *in vitro* similar to the survey of nanoparticles by Staedler *et al*. [40].
- Investigating polymer coatings on barium titanate nanoparticles such as the interaction of polymer in different electrolytes and also the effect of changing the nanoparticle:polymer ratios.

- Undertake a survey of polymers for functionalisation of the $BaTiO_3$ nanoparticle system, using different polymer systems (adjusting the surface charge or attachment to the particle) and assessing which nanoparticle system is best for dispersion and SHG imaging for intravital microscopy (i.e. least cyto- or genotoxic).
- From the results of these studies, the nanoparticle system could then be used to look at specific targeting. Due to the size of the nanoparticles it would be best to target tumours as opposed to cells) and apply these techniques to intravital microscopy. A clear exploratory route forwards would be to use the H-B(S)T system with specific surface targeting for tumours and apply this to surgical resection by intravital microscopy.

Chapter 9 – Bibliography.

[1] O. Matar, O.M. Posada, N.S. Hondow, C. Wälti, M. Saunders, C.A. Murray, R.M.D. Brydson, S.J. Milne, A.P. Brown, Barium Titanate Nanoparticles for Biomarker Applications, J. Phys. Conf. Ser. 644 (2015) 12037.

[2] O. Matar, N. Hondow, O. Posada, M. Routledge, D. Hernandez-Maldonado, C. Wälti, C. Murray, R. Brydson, S. Milne, A. Brown, Analytical electron microscopy of barium titanate and barium-strontium titanate nanoparticles for second-harmonic biomarkers, in: Eur. Microsc. Congr. 2016 Proc., Wiley-VCH Verlag GmbH & Co. KGaA, 2016.

[3] M. Chalfie, Y. Tu, G. Euskirchen, W. W. Ward, D.C. Prasher, Green

fluorescent protein as a marker for gene expression, Science (80-.). 263 (1994) 802–805.

[4] O. Shimomura, F. H. Johnson, Y. Saiga, Extraction, Purification and Properties of Aequorin, a Bioluminescent Protein from the Luminous Hydromedusan, Aequorea, J. Cell. Comp. Physiol. 59 (1962) 223–239.

[5] R.Y. Tsien, The Green Fluorescent Protein, Annu. Rev. 67 (1998) 509–544.

[6] L. Song, E. J. Hennink, I. T. Young, H.J. Tanke, Photobleaching kinetics of fluorescein in quantitative fluorescence microscopy, Biophys. J. 68 (1995) 2588–2600.

[7] M.W. Davidson, http://micro.magnet.fsu.edu/primer/java/fluorescence/photobleaching/index.html, (2015).

[8] L. Oldach, J. Zhang, Genetically Encoded Fluorescent Biosensors for Live-Cell Visualization of Protein Phosphorylation, Chem. Biol. 21 (2014) 186–197.

[9] I.L. Medintz, H.T. Uyeda, E.R. Goldman, H. Mattoussi, Quantum dot bioconjugates for imaging, labelling and sensing., Nat. Mater. 4 (2005) 435–446.

[10] J. Tang, R.A. Marcus, Mechanisms of fluorescence blinking in semiconductor nanocrystal quantum dots, J. Chem. Phys. 123 (2005).

[11] A. M. Derfus, W. C. W. Chan, S.N. Bhatia, Probing the Cytotoxicity of Semiconductor Quantum Dots, Nano Lett. 4 (2003) 11–18.

[12] V. M. Fthenakis, S. C. Morris, P. D. Moskowitz, D.L. Morgan, Toxicity of cadmium telluride, copper indium diselenide, and copper gallium diselenide, Prog. Photovoltaics Res. Appl. 7 (1999) 489–497.

[13] A. a Cordones, S.R. Leone, Mechanisms for charge trapping in single semiconductor nanocrystals probed by fluorescence blinking., Chem. Soc. Rev. 42 (2013) 3209–21.

[14] J.P. Heath, Super-Resolution Microscopy, (2014). http://www.leica-microsystems.com/science-lab/super-resolution-microscopy-get-your-free-e-book-for-download/ (accessed November 16, 2015).

[15] N.M. AB, The Nobel Prize in Chemistry 2014, Nobelprize.org. (2014) http://www.nobelprize.org/nobel_prizes/chemistry/l. http://www.nobelprize.org/nobel_prizes/chemistry/laureates/2014/%3E.

[16] A. Yariv, Optical Electronics - Fourth Edition, Oxford University Press, ISBN: 0-03-053239-6, 1991.

[17] W. P. Dempsey, S. E. Fraser, P. Pantazis, W.P. Dempsey, S.E. Fraser, P. Pantazis, SHG nanoprobes: Advancing harmonic imaging in biology, BioEssays. 34 (2012) 351–360.

[18] D.H. Yoon, Tetragonality of barium titanate powder for a ceramic capacitor application, J. Ceram. Process. Res. 7 (2006) 343–354.

[19] J.F. Scott, Applications of Modern Ferroelectrics, Science (80-.). 315 (2007) 954–959. http://www.sciencemag.org/content/315/5814/954.abstract.

[20] R Asiaie, W D Zhu, S Akbar, P.K. Dutta, Characterization of Submicron

Particles of Tetragonal BaTiO3, Chem. Mater. 8 (1996) 226.

[21] K.A. Razak, A. Asadov, J. Yoo, E. Haemmerle, W. Gao, Structural and dielectric properties of barium strontium titanate produced by high temperature hydrothermal method, J. Alloys Compd. 449 (2008) 19–23.

[22] B. Jaffe, W. R. Cook, H. Jaffe, Piezoelectric Ceramics, ACADEMIC PRESS INC., ISBN: 0-12-379550-8, 1971.

[23] R.D. Shannon, C.T. Prewitt, Effective Ionic Radii in Oxides and Fluorides, Acta Cryst. B25. 925 (1969) 925–946.

[24] P. Atkins, J. de Paula, R. Friedman, Quanta, Matter and Change: A molecular approach to physical chemistry, Oxford University Press, 2009.

[25] S.R. Marder, J.E. Sohn, G.D. Stucky, Materials for Nonlinear Optics Chemical Perspectives, (n.d.).

[26] D.J. Williams, Second-Order Nonlinear Optical Processes in Molecules and Solids, in: Mater. Nonlinear Opt., American Chemical Society, 1991: pp. 31–49.

[27] F. Helmchen, W. Denk, A. Bolshakova, O. Vlasova, I. Bezprozvanny, F. Helmchen, W. Denk, M. Ke, S. Fujimoto, T. Imai, H. Dodt, U. Leischner, A. Schierloh, N. Jährling, C. Mauch, K. Deininger, J. Deussing, M. Eder, W. Zieglgänsberger, K. Becker, T. Staudt, M. Lang, R. Medda, J. Engelhardt, S. Hell, P. Gonzalez-Bellido, T. Wardill, K. Chung, J. Wallace, S. Kim, S. Kalyanasundaram, A. Andalman, T. Davidson, J. Mirzabekov, K. Zalocusky, J. Mattis, A. Denisin, S. Pak, H. Bernstein, C. Ramakrishnan, L. Grosenick,

V. Gradinaru, K. Deisseroth, G. Feng, R. Mellor, M. Bernstein, C. Keller-Peck, Q. Nguyen, M. Wallace, J. Nerbonne, J. Lichtman, J. Sanes, Deep tissue two-photon microscopy, Nat. Methods. 2 (2005) 932–940.

[28] L. Bonacina, Nonlinear Nanomedecine: Harmonic Nanoparticles toward Targeted Diagnosis and Therapy, Mol. Pharm. 10 (2012) 783–792.

[29] P. A. Franken, A. E. Hill, C. W. Peters, G. Weinreich, Generation of Optical Harmonics, Phys. Rev. Lett. 7 (1961) 118–119.

[30] X. Zhang, S. Bloch, W. Akers, S. Achilefu, Near-infrared molecular probes for in vivo imaging, Curr. Protoc. Cytom. (2012) 1–28.

[31] A.M. Smith, M.C. Mancini, S. Nie, Bioimaging: Second window for in vivo imaging, Nat Nano. 4 (2009) 710–711.

[32] P. J. Campagnola, L.M. Loew, P.J. Campagnola, L.M. Loew, Second-harmonic imaging microscopy for visualizing biomolecular arrays in cells, tissues and organisms, Nat Biotech. 21 (2003) 1356–1360.

[33] P. BIANCHINI, A. Diaspro, Second Harmonic Generation Imaging Microscopy: Theory and Applications, in: Nanoscopy Multidimens. Opt. Fluoresc. Microsc., Chapman and Hall/CRC, 2010: p. pp.9-1-9-14.

[34] K. König, P. T. C. So, W. W. Mantulin, E. Gratton, K. König, P.T. So, W.W. Mantulin, E. Gratton, Cellular response to near-infrared femtosecond laser pulses in two-photon microscopes, Opt. Lett. 22 (1997) 135–136.

[35] D.J. Taatjes, B.T. Mossman, Cell Imaging Techniques Methods and Protocols, Humana Press, 2006.

[36] C. L. Hsieh, Y. Pu, R. Grange, D. Psaltis, Second harmonic generation from nanocrystals under linearly and circularly polarized excitations, Opt. Express. 18 (2010) 11917–11932.

[37] P.J. Campagnola, Second Harmonic Generation Imaging Microscopy: Applications to Diseases Diagnostics, Anal. Chem. 83 (2011) 3224–3231.

[38] T. T. Le, I. M. Langohr, M. J. Locker, M. Sturek, J.X. Cheng, Label-free molecular imaging of atherosclerotic lesions using multimodal nonlinear optical microscopy, J. Biomed. Opt. 12 (2007) 54007–54010.

[39] E. Kim, A. Steinbrück, M. T. Buscaglia, V. Buscaglia, T. Pertsch, R. Grange, E. Kim, A. Steinbrück, M.T. Buscaglia, V. Buscaglia, T. Pertsch, R. Grange, Second-Harmonic Generation of Single BaTiO3 Nanoparticles down to 22 nm Diameter, ACS Nano. 7 (2013) 5343–5349.

[40] D. Staedler, T. Magouroux, R. Hadji, C. Joulaud, J. Extermann, S. Schwung, S. Passemard, C. Kasparian, G. Clarke, M. Gerrmann, R. Le Dantec, Y. Mugnier, D. Rytz, D. Ciepielewski, C. Galez, S. Gerber-Lemaire, L. Juillerat-Jeanneret, L. Bonacina, J.P. Wolf, D. Staedler, T. Magouroux, R. Hadji, C. Joulaud, J. Extermann, S. Schwung, S. Passemard, C. Kasparian, G. Clarke, M. Gerrmann, R. Dantec, Y. Mugnier, D. Rytz, D. Ciepielewski, C. Galez, S. Gerber-Lemaire, L. Juillerat-Jeanneret, L. Bonacina, J.P. Wolf, Harmonic Nanocrystals for Biolabeling: A Survey of Optical Properties and Biocompatibility, ACS Nano. 6 (2012) 2542–2549.

[41] D. Staedler, S. Passemard, T. Magouroux, A. Rogov, C.M. Maguire, B.M.

Mohamed, S. Schwung, D. Rytz, T. Jüstel, S. Hwu, Y. Mugnier, R. Le Dantec, Y. Volkov, S. Gerber-Lemaire, A. Prina-Mello, L. Bonacina, J.-P. Wolf, Cellular uptake and biocompatibility of bismuth ferrite harmonic advanced nanoparticles, Nanomedicine Nanotechnology, Biol. Med. (2015).

[42] R. Grange, T. Lanvin, C.-L. Hsieh, Y. Pu, D. Psaltis, R. Grange, T. Lanvin, C. L. Hsieh, Y. Pu, D. Psaltis, Imaging with second-harmonic radiation probes in living tissue, Biomed. Opt. Express. 2 (2011) 2532–2539.

[43] A. Masedunskas, O. Milberg, N. Porat-Shliom, M. Sramkova, T. Wigand, P. Amornphimoltham, R. Weigert, Intravital microscopy: A practical guide on imaging intracellular structures in live animals, Bioarchitecture. 2 (2012) 143–157. doi:10.4161/bioa.21758.

[44] J. Condeelis, J.E. Segall, Intravital imaging of cell movement in tumours., Nat. Rev. Cancer. 3 (2003) 921–930. doi:10.1038/nrc1231.

[45] W. Wang, J.B. Wyckoff, V.C. Frohlich, Y. Oleynikov, S. Hüttelmaier, J. Zavadil, L. Cermak, E.P. Bottinger, R.H. Singer, J.G. White, J.E. Segall, J.S. Condeelis, Single cell behavior in metastatic primary mammary tumors correlated with gene expression patterns revealed by molecular profiling, Cancer Res. 62 (2002) 6278–6288.

[46] P. Pantazis, J. Maloney, D. Wu, S.E. Fraser, P. Pantazis, J. Maloney, D. Wu, S.E. Fraser, Second harmonic generating (SHG) nanoprobes for in vivo imaging, Proc. Natl. Acad. Sci. 107 (2010) 14535–14540.

[47] J. Ĉulić-Viskota, W.P. Dempsey, S.E. Fraser, P. Pantazis, Surface

Functionalization of Barium Titanate SHG Nanoprobes for in vivo Imaging in Zebrafish, Nat. Protoc. (2012).

[48] H.C. Fischer, W.C. Chan, Nanotoxicity: the growing need for in vivo study, Curr. Opin. Biotechnol. 18 (2007) 565–571.

[49] A. E. Nel, L. Madler, D. Velegol, T. Xia, E. M. V. Hoek, P. Somasundaran, F. Klaessig, V. Castranova, M. Thompson, A.E. Nel, L. Mädler, D. Velegol, T. Xia, E.M. V Hoek, P. Somasundaran, F. Klaessig, V. Castranova, M. Thompson, Understanding biophysicochemical interactions at the nano-bio interface, Nat. Mater. 8 (2009) 543–557.

[50] D. Hames, N. Hooper, BIOS Instant Notes: Biochemistry, Taylor and Francis, ISBN: 0-4153-6778-6, 2005.

[51] E. Fröhlich, The role of surface charge in cellular uptake and cytotoxicity of medical nanoparticles, Int. J. Nanomedicine. 7 (2012) 5577.

[52] A. Lesniak, F. Fenaroli, M.P. Monopoli, C. Åberg, K.A. Dawson, A. Salvati, Effects of the presence or absence of a protein corona on silica nanoparticle uptake and impact on cells, ACS Nano. 6 (2012) 5845–5857.

[53] A. Salvati, C. Åberg, K.A. Dawson, M.P. Monopoli, C. Åberg, A. Salvati, K.A. Dawson, C. Aberg, A. Salvati, K.A. Dawson, Biomolecular coronas provide the biological identity of nanosized materials, Nat. Nanotechnol. 7 (2012) 779–786.

[54] F. Wang, L. Yu, M.P. Monopoli, P. Sandin, E. Mahon, A. Salvati, K.A. Dawson, The biomolecular corona is retained during nanoparticle uptake

and protects the cells from the damage induced by cationic nanoparticles until degraded in the lysosomes, Nanomedicine Nanotechnology, Biol. Med. 9 (2013) 1159–1168.

[55] A. Nel, Toxic Potential of Materials, Science (80-.). 311 (2007) 622–627.

[56] A.A. Vertegel, R.W. Siegel, J.S. Dordick, Silica nanoparticle size influences the structure and enzymatic activity of adsorbed lysozyme, Langmuir. 20 (2004) 6800–6807.

[57] G. Oberdörster, A. Maynard, K. Donaldson, V. Castranova, J. Fitzpatrick, K. Ausman, J. Carter, B. Karn, W. Kreyling, D. Lai, S. Olin, N. Monteiro-Riviere, D. Warheit, H. Yang, Principles for characterizing the potential human health effects from exposure to nanomaterials: elements of a screening strategy, Part. Fibre Toxicol. 2 (2005) 8.

[58] E.M. V Hoek, G.K. Agarwal, Extended DLVO interactions between spherical particles and rough surfaces, J. Colloid Interface Sci. 298 (2006) 50–58.

[59] Y. Xiao, M.R. Wiesner, Characterization of surface hydrophobicity of engineered nanoparticles, J. Hazard. Mater. 215–216 (2012) 146–151.

[60] A. Verma, O. Uzun, Y. Hu, H.-S. Han, N. Watson, S. Chen, D.J. Irvine, F. Stellacci, Surface-structure-regulated cell-membrane penetration by monolayer-protected nanoparticles, Nat. Mater. 7 (2008) 588–595.

[61] S.E. McNeil, Nanoparticle therapeutics: a personal perspective., Wiley Interdiscip. Rev. Nanomed. Nanobiotechnol. 1 264–71.

[62] A. J. Moulson, J.M. Herbert, Electroceramics, WILEY, ISBN: 0471-49748-9,

2003.

[63] H.F. Kay, P. Vousden, XCV . Symmetry changes in barium titanate at low temperatures and their relation to its ferroelectric properties, London, Edinburgh, Dublin Philos. Mag. J. Sci. 40 (1949) 1019–1040.

[64] K.C. Kao, Dielectric Phenomena in Solids, Academic Press, ISBN: 978-0123965-615, 2004.

[65] C. Hammond, The basics of crystallography and diffraction, Oxford University Press, Oxford; New York, 2009.

[66] W. Jackson, W. Reddish, High permittivity crystalline aggregates, Nature. 156 (1945).

[67] L. Zhou, P. M. Vilarinho, J.L.L. Baptista, L. Zhou, P.M. Vilarinho, J.L.L. Baptista, Dependence of the Structural and Dielectric Properties of Ba1-xSrxTiO3 Ceramic Solid Solutions on Raw Material Processing, J. Eur. Ceram. Soc. 19 (1999) 2015–2020.

[68] M. Bugnet, G. Radtke, S.Y. Woo, G.-Z. Zhu, G.A. Botton, Temperature-dependent high energy-resolution EELS of ferroelectric and paraelectric BaTiO 3 phases, Phys. Rev. B. 93 (2016).

[69] A. von Hippel, Ferroelectricity, Domain Structure, and Phase Transitions of Barium Titanate, Rev. Mod. Phys. 22 (1950) 221–237.

[70] D. R. Spearing, J. F. Stebbins, Oxygen Displacement through the Ferroelectric Phase Transition of Barium Titanate—High-Temperature 17O NMR, J. Am. Ceram. Soc. 77 (1994) 3263–3266.

[71] D. Hennings, Barium titanate based ceramic materials for dielectric use, Int. J. High Technol. Ceram. 3 (1987) 91–111.

[72] K. Uchino, E. Sadanaga, T. Hirose, Dependence of the Crystal Structure on Particle Size in Barium Titanate, J. Am. Ceram. Soc. 72 (1989) 1555–1558.

[73] M.H. Frey, D.A. Payne, Grain-size effect on structure and phase transformations for barium titanate, Phys. Rev. B. 54 (1996) 3158–3168.

[74] M B Smith, K Page, T Seigrist, P L Redmond, E C Walter, R Seshadri, L E Brus, M.L. Steigerwald, Crystal Structure and the Paraelectric-to-Ferroelectric Phase Transistion of Nanoscale BaTiO3, J. Am. Chem. Soc. 130 (2008) 6955.

[75] S. Wada, H. Yasuno, T. Hoshina, S. Nam, H. Kakemoto, T. Tsurumi, Preparation of nm-Sized Barium Titanate Fine Particles and Their Powder Dielectric Properties, Jpn. J. Appl. Phys. 42 (2003) 6188.

[76] H.-W. Lee, S. Moon, C.-H. Choi, D.K. Kim, Synthesis and Size Control of Tetragonal Barium Titanate Nanopowders by Facile Solvothermal Method, J. Am. Ceram. Soc. 95 (2012) 2429–2434.

[77] T. HOSHINA, Size effect of barium titanate: fine particles and ceramics, J. Ceram. Soc. Japan. 121 (2013) 156–161.

[78] M J Polking, M G Han, A Yourdkhani, V Petkov, C F Kisielowski, V V Volkov, Y Zhu, G Caruntu, P Alivisatos, R. Ramesh, Ferroelectric order in individual nanometre-scale crystals, Nat. Mater. 11 (2012) 700.

[79] C. Pithan, D. Hennings, R. Waser, Progress in the Synthesis of

Nanocrystalline BaTiO3 Powders for MLCC, Int. J. Appl. Ceram. Technol. 2 (2005) 1–14.

[80] N.J. Welham, Mechanically induced reaction between alkaline earth metal oxides and TiO2, J. Mater. Res. 13 (1998) 1607–1613.

[81] S. Wada, T. Suzuki, T. Noma, Preparation of barium titanate fine particles by hydrothermal method and their characterization, J. Ceram. Soc. Japan. 103 (1995) 1220–1227.

[82] D. Hennings, G. Rosenstein, H. Schreinemacher, Hydrothermal preparation of barium titanate from barium-titanium acetate gel precursors, J. Eur. Ceram. Soc. 8 (1991) 107–115.

[83] M. Wu, J. Long, G. Wang, A. Huang, Y. Luo, S. Feng, R. Xu, Hydrothermal Synthesis of Tetragonal Barium Titanate from Barium Hydroxide and Titanium Dioxide under Moderate Conditions, J. Am. Ceram. Soc. 82 (1999) 3254–3256.

[84] J O Eckert, C C Hung-Houston, B L Gersten, M M Lencka, R.E. Riman, Kinetics and Mechanisms of Hydrothermal Synthesis of Barium Tianate, J. Am. Ceram. Soc. 79 (1996) 2929.

[85] J. H. Adair, J. Crampo, M. M. Mandanas, E. Suvaci, The Role of Material Chemistry in Processing BaTiO3 in Aqueous Suspensions, J. Am. Ceram. Soc. 89 (2006) 1853–1860.

[86] X. Wang, J. Zhuang, Q. Peng, Y. Li, A general strategy for nanocrystal synthesis, Nature. 437 (2005) 121–124.

doi:http://www.nature.com/nature/journal/v437/n7055/suppinfo/nature03968_S1.html.

[87] S. Adireddy, C. Lin, B. Cao, W. Zhou, G. Caruntu, Solution-Based Growth of Monodisperse Cube-Like BaTiO3 Colloidal Nanocrystals, Chem. Mater. 22 (2010) 1946–1948.

[88] S.-G. Kwon, B.-H. Park, K. Choi, E.-S. Choi, S. Nam, J.-W. Kim, J.-H. Kim, Solvothermally synthesized tetragonal barium titanate powders using H2O/EtOH solvent, J. Eur. Ceram. Soc. 26 (2006) 1401–1404.

[89] Y.-M. Chiang, D.P. Birnie, W.D. Kingery, Physical ceramics : principles for ceramic science and engineering, Wiley, New York, 1997.

[90] V. Petkov, M. Gateshki, M. Niederberger, Y. Ren, Atomic-Scale Structure of Nanocrystalline BaxSr1-xTiO3 (x = 1, 0.5, 0) by X-ray Diffraction and the Atomic Pair Distribution Function Technique, Chem. Mater. 18 (2006) 814–821.

[91] K.A. Razak, A. Asadov, W. Gao, Properties of BST ceramics prepared by high temperature hydrothermal process, Ceram. Int. 33 (2007) 1495–1502.

[92] R.K. Roeder, E.B. Slamovich, Stoichiometry Control and Phase Selection in Hydrothermally Derived Ba x Sr 1-x TiO 3 Powders, J. Am. Ceram. Soc. 82 (1999) 1665–1675.

[93] S M Moon, X Wang, N.H. Cho, Identification of Local Phase of Nanoscale BaTiO3 Powders by High-Resolution Electron Energy Loss Spectroscopy, Microsc. Microanal. 19 (2013) 123.

[94] M.D. Rossell, Q.M. Ramasse, S.D. Findlay, F. Rechberger, R. Erni, M. Niederberger, Direct Imaging of Dopant Clustering in Metal-Oxide Nanoparticles, ACS Nano. 6 (2012) 7077–7083.

[95] R.F. Egerton, Electron energy-loss spectroscopy in the TEM, Reports Prog. Phys. 72 (2009) 16502.

[96] D.B. Williams, C.B. Carter, Transmission Electron Microscopy: A Textbook for Materials Science, 2009.

[97] M. Bugnet, G. Radtke, G.A. Botton, Oxygen 1s excitation and tetragonal distortion from core-hole effect in BaTiO3, Phys. Rev. B - Condens. Matter Mater. Phys. (2013).

[98] L.A. Grunes, R.D. Leapman, C.N. Wilker, R. Hoffmann, A.B. Kunz, Oxygen E near-edge fine structure: An electron-energy-loss investigation with comparisons to new theory for selected 3d transition-metal oxides, Phys. Rev. B. 25 (1982).

[99] D. F. K. Hennings, S. Schreinemacher, Characterization of hydrothermal barium titanate, J. Eur. Ceram. Soc. 9 (1992) 41–46.

[100] M. Yashima, T. Hoshina, D. Ishimura, S. Kobayashi, W. Nakamura, T. Tsurumi, S. Wada, Size effect on the crystal structure of barium titanate nanoparticles, J. Appl. Phys. 98 (2005) 14313–14318.

[101] D.H. Yoon, B.I. Lee, BaTiO(3) properties and powder characteristics for ceramic capacitors, J. Ceram. Process. Res. 3 (2002) 41–47.

[102] S.-M. Moon, N.-H.H. Cho, S. M. Moon, N.-H.H. Cho, Investigation of phase

distribution in nanoscale BaTiO3 powders prepared by hydro-thermal synthesis, J. Electroceramics. 23 (2009) 121–126.

[103] S.-M. Moon, N.-H. Cho, Size effects on the crystal structure of nanoscale BaTiO3 powders prepared by hydro-thermal synthesis, Met. Mater. Int. (2007).

[104] P. Kim, S.C. Jones, P.J. Hotchkiss, J.N. Haddock, B. Kippelen, S.R. Marder, J.W. Perry, Phosphonic acid-modified barium titanate polymer nanocomposites with high permittivity and dielectric strength, Adv. Mater. 19 (2007) 1001–1005.

[105] D.H. Everett, Basic Principles of Colloid Science, Royal Society of Chemistry, 1988. https://app.knovel.com/web/toc.v/cid:kpBPCS0001/viewerType:toc/root_slug:basic-principles-colloid/url_slug:basic-principles-colloid?kpromoter=federation (accessed April 7, 2016).

[106] D.J. Shaw, Introduction to Colloid and Surface Chemistry, Elsevier, 1992.

[107] B. Rand, F.L. Riley, M.C. Blanco López, The isoelectric point of BaTiO 3, J. Eur. Ceram. Soc. 20 (2000) 107–118.

[108] M.C. Blanco López, G. Fourlaris, F.L. Riley, Interaction of barium titanate powders with an aqueous suspending medium, J. Eur. Ceram. Soc. 18 (1998) 2183–2192.

[109] M.C. Blanco López, B. Rand, F.L. Riley, The Properties of Aqueous Phase Suspensions of Barium Titanate, J. Eur. Ceram. Soc. 17 (1997) 281–287.

[110] A. Sorkin, M. von Zastrow, Signal transduction and endocytosis: close encounters of many kinds, Nat Rev Mol Cell Biol. 3 (2002) 600–614.

[111] F. Brodard-Severac, G. Guerrero, J. Maquet, P. Florian, C. Gervais, P.H. Mutin, High-Field 17 O MAS NMR Investigation of Phosphonic Acid Monolayers on Titania, Chem. Mater. 20 (2008) 5191–5196.

[112] C. Dempsey, I. Lee, K. R. Cowan, J. Suh, Coating barium titanate nanoparticles with polyethylenimine improves cellular uptake and allows for coupled imaging and gene delivery, Colloids Surfaces B Biointerfaces. 112 (2013) 108–112.

[113] C. L. Hsieh, R. Grange, Y. Pu, D. Psaltis, Three-dimensional harmonic holographic microcopy using nanoparticles as probes for cell imaging, Opt. Express. 17 (2009) 2880–2891.

[114] C. L. Hsieh, R. Grange, Y. Pu, D. Psaltis, C.L. Hsieh, R. Grange, Y. Pu, D. Psaltis, Bioconjugation of barium titanate nanocrystals with immunoglobulin G antibody for second harmonic radiation imaging probes, Biomaterials. 31 (2010) 2272–2277.

[115] T.T. Le, I.M. Langohr, M.J. Locker, M. Sturek, J.-X. Cheng, Label-free molecular imaging of atherosclerotic lesions using multimodal nonlinear optical microscopy, J. Biomed. Opt. 12 (2007) 54007.

[116] G. Ciofani, S. Danti, S. Moscato, L. Albertazzi, D. D'Alessandro, D. Dinucci, F. Chiellini, M. Petrini, A. Menciassi, Preparation of stable dispersion of barium titanate nanoparticles: Potential applications in biomedicine, Colloids

Surfaces B Biointerfaces. 76 (2010) 535–543.

[117] C. L. Hsieh, R. Grange, Y. Pu, D. Psaltis, Characterization of the cytotoxicity and imaging properties of second-harmonic nanoparticles, Proc. SPIE. (2010) 77590T–77590T.

[118] D. Mazia, G. Schatten, W. Sale, Adhesion of cells to surfaces coated with polylysine. Applications to electron microscopy., J. Cell Biol. 66 (1975) 198–200.

[119] S P Thompson, J E Parker, J Potter, T P Hill, A Birt, T M Cobb, F Yuan, C.C. Tang, Beamline I11 at Diamond: A new instrument for high resolution powder diffraction, Rev. Sci. Instrum. 80 (2009) 75107.

[120] A. Lennie, J. Parker, C. Tang, S. Thompson, Science Division Beamline I11 User Manual Science Division, Data Process. (2011).

[121] W.E. Moerner, R.M. Dickson, A.B. Cubitt, R.Y. Tsien, On/off blinking and switching behaviour of single molecules of green fluorescent protein, Nature. 388 (1997) 355–358.

[122] E. Betzig, J.K. Trautman, Near-field optics: microscopy, spectroscopy, and surface modification beyond the diffraction limit., Science. 257 (1992) 189–95.

[123] T.A. Klar, S. Jakobs, M. Dyba, A. Egner, S.W. Hell, Fluorescence microscopy with diffraction resolution barrier broken by stimulated emission Physical Principles and Setup, Proc. Natl. Acad. Sci. 97 (2000) 8206–8210.

[124] B. Huang, M. Bates, X. Zhuang, Super-Resolution Fluorescence

Microscopy, Annu. Rev. Biochem. 78 (2009) 993–1016.

[125] G. Edmund, H.J. Spanner, Cold cathode discharge tube, 1935. https://www.google.com/patents/US1993187.

[126] R. M. Brydson, C. Hammond, Generic Methodologies for Nanotechnology: Electron Microscopy, in: R. W. Kelsall, I. W. Hamley, M. Geoghegan (Eds.), Nanoscale Sci. Technol., John Wiley & Sons, Ltd, 2005: pp. 1–55.

[127] I.M. Watt, The principles and practice of electron microscopy, Cambridge University Press, ISBN: 0-251-25557-0, 1985.

[128] C. Hetherington, Aberration correction for TEM, Mater. Today. 7 (2004) 50–55.

[129] W.C.H. Kuo, M. Briceno, D. Ozkaya, Final Analysis: Characterisation of Catalysts Using Secondary and Backscattered Electron In-lens Detectors, Platin. Met. Rev. 58 (n.d.) 106–110.

[130] K. Kumagai, T. Sekiguchi, Sharing of secondary electrons by in-lens and out-lens detector in low-voltage scanning electron microscope equipped with immersion lens, Ultramicroscopy. 109 (2009) 368–372.

[131] P.J. Goodhew, J. Humphreys, R. Beanland, Electron Microscopy and Analysis, 3rd ed., 2001.

[132] P. Lechner, C. Fiorini, R. Hartmann, J. Kemmer, N. Krause, P. Leutenegger, A. Longoni, H. Soltau, D. Stötter, R. Stötter, L. Strüder, U. Weber, Silicon drift detectors for high count rate X-ray spectroscopy at room temperature, Nucl. Instruments Methods Phys. Res. Sect. A Accel. Spectrometers,

Detect. Assoc. Equip. 458 (2001) 281–287.

[133] R. Brydson, A. Brown, L.G. Benning, K. Livi, Analytical Transmission Electron Microscopy, Rev. Mineral. Geochemistry. 78 (2014) 219–269.

[134] R. Brydson, Electron Energy Loss Spectroscopy, BIOS Scientific Publishers Limited, 2001.

[135] Q.M. Ramasse, SuperSTEM Instrumentation, (2017). www.superstem.org.

[136] Gatan, http://www.eels.info, (2016). http://www.eels.info/about/techniques/spectrum-imaging (accessed December 1, 2016).

[137] K. Jarausch, P. Thomas, D.N. Leonard, R. Twesten, C.R. Booth, Four-dimensional STEM-EELS: Enabling nano-scale chemical tomography, Ultramicroscopy. 109 (2009) 326–337.

[138] P. Atkins, J. de Paula, Physical Chemistry, 7th ed., 2002.

[139] Introduction to Fourier Transform Infrared Spectroscopy - Thermo Nicolet Corporation, Tech. Note. (2016). http://mmrc.caltech.edu/FTIR/FTIRintro.pdf (accessed July 19, 2016).

[140] M.S. Bradley, FT-IR sample analysis (online webinar), (2016). https://thermoscientificwebevent.adobeconnect.com/_a995535185/ftirsampling/ (accessed July 19, 2016).

[141] J.M. Chalmers, G. Dent, Sampling techniques and accessories, in: J.M. Chalmers, G. Dent (Eds.), Ind. Anal. with Vib. Spectrosc., The Royal Society of Chemistry, 1997: pp. 120–175.

[142] J.M. Chalmers, G. Dent, Introduction, basic theory, and principles, in: J.M. Chalmers, G. Dent (Eds.), Ind. Anal. with Vib. Spectrosc., The Royal Society of Chemistry, 1997: pp. 1–36.

[143] M. Rozenberg, G. Shoham, FTIR spectra of solid poly-l-lysine in the stretching NH mode range., Biophys. Chem. 125 (2007) 166–71.

[144] G. Socrates, Infrered and Raman Characteristic Group Frequencies: Tables and Charts, WILEY, ISBN:978-0-470-09307-8, 2001.

[145] R. Wallace, Physicochemical Characterization of Zinc Oxide Nanoparticles for Use in Toxicity Studies, The University of Leeds, 2013.

[146] M. Intstruments, A basic guide to particle characterization, Whitepaper. (n.d.). http://www.malvern.com/en/support/resource-center/Whitepapers/WP120620BasicGuidePartChar.aspx.

[147] S.H. Wemple, M. Didomenico, I. Camlibel, Dielectric and optical properties of melt-grown BaTiO3, J. Phys. Chem. Solids. 29 (1968) 1797–1803.

[148] A.K. BAIN, T.J. JACKSON, Y. KOUTSONAS, M. CRYAN, S. YU, M. HILL, R. VARRAZZA, J. RORISON, M.J. LANCASTER, Optical Properties of Barium Strontium Titanate (BST) Ferroelectric Thin Films, Ferroelectr. Lett. Sect. 34 (2007) 149–154.

[149] K. Asano, C.B. Chee, B. Gaston, C.M. Lilly, C. Gerard, J.M. Drazen, J.S. Stamler, Constitutive and inducible nitric oxide synthase gene expression, regulation, and activity in human lung epithelial cells., Proc. Natl. Acad. Sci. 91 (1994) 10089–10093.

[150] A. van Tonder, A.M. Joubert, A.D. Cromarty, Limitations of the 3-(4,5-dimethylthiazol-2-yl)-2,5-diphenyl-2H-tetrazolium bromide (MTT) assay when compared to three commonly used cell enumeration assays., BMC Res. Notes. 8 (2015) 47.

[151] P.L. Olive, J.P. Banáth, The comet assay: a method to measure DNA damage in individual cells., Nat. Protoc. 1 (2006) 23–9.

[152] V.G. Dmiitriev, G.G. Gurzadyan, D.N. Nikogosyan, Handbook of Nonlinear Optical Crystals, Springer-Verlag, 1991.

[153] M.A. Lerma, Trigonometric Integrals and Trigonometric Substitutions, http://www.math.northwestern.edu/~mlerma/courses/math214-2-03f/notes/c2-trigint.pdf, (2003).

[154] S.D. Evans, Lecture Material published for University of Leeds, Photonics - PHYS 3115, 2013.

[155] N. Bloembergen, Nonlinear Optics, ISBN: 981-02-2598-9, 1965.

[156] R.A. Young, D.B. Wiles, Profile shape functions in Rietveld refinements, J. Appl. Crystallogr. 15 (1982) 430–438.

[157] L.B. Mccusker, R.B. Von Dreele, D.E. Cox, D. Loue È R D, P. Scardi, Rietveld refinement guidelines, Int. Union Crystallogr. J. Appl. Crystallogr. J. Appl. Cryst. 32 (1999) 36–50.

[158] C. Weidenthaler, Pitfalls in the characterization of nanoporous and nanosized materials., Nanoscale. 3 (2011) 792–810.

[159] Gatan, DigitalMicrograph EELS Analysis User's Guide, 1.2.1, 2003.

[160] E. Stoyanov, F. Langenhorst, G. Steinle-Neumann, The effect of valence state and site geometry on Ti-L3,2 and O-K electron energy-loss spectra of TixOy phases, Am. Mineral. 92 (2007) 577 LP-586.

[161] J.P. Wise, B.C. Goodale, S.S. Wise, G.A. Craig, A.F. Pongan, R.B. Walter, W.D. Thompson, A.K. Ng, A.E.M. Aboueissa, H. Mitani, M.J. Spalding, M.D. Mason, Silver nanospheres are cytotoxic and genotoxic to fish cells, Aquat. Toxicol. 97 (2010) 34–41.

[162] G. Madras, B.J. McCoy, Distribution kinetics of Ostwald ripening at large volume fraction and with coalescence, J. Colloid Interface Sci. 261 (2003) 423–433.

[163] N. Hondow, R. Brydson, P. Wang, M.D. Holton, M.R. Brown, P. Rees, H.D. Summers, A. Brown, Quantitative characterization of nanoparticle agglomeration within biological media, J. Nanoparticle Res. 14 (2012) 977.

[164] S. Aldrich, Sigma Aldrich Life Science: Cell Culture Media Formulations, Dulbecco's Modif. Eagles Mediu. Formul. (2016) http://www.sigmaaldrich.com/life-science/cell-cult. http://www.sigmaaldrich.com/life-science/cell-culture/learning-center/media-formulations/dme.html (accessed December 19, 2016).

[165] M. Bilton, S.J. Milne, A.P. Brown, Comparison of Hydrothermal and Sol-Gel Synthesis of Nano-Particulate Hydroxyapatite by Characterisation at the Bulk and Particle Level, Open J. Inorg. Non-Metallic Mater. 2 (2012) 1–10.

[166] L. Chen, J.M. Mccrate, J.C.-M. Lee, H. Li, The role of surface charge on the

uptake and biocompatibility of hydroxyapatite nanoparticles with osteoblast cells., Nanotechnology. 22 (2011) 105708.

[167] K. Isaksson, D. Åkerberg, M. Posaric-Bauden, R. Andersson, B. Tingstedt, In vivo toxicity and biodistribution of intraperitoneal and intravenous poly-l-lysine and poly-l-lysine/poly-l-glutamate in rats, J. Mater. Sci. Mater. Med. 25 (2014) 1293–1299.

[168] D. Fischer, Y. Li, B. Ahlemeyer, J. Krieglstein, T. Kissel, In vitro cytotoxicity testing of polycations: influence of polymer structure on cell viability and hemolysis, Biomaterials. 24 (2003) 1121–1131.

[169] X. Liang, Y. Huang, Intracellular free calcium concentration and cisplatin resistance in human lung adenocarcinoma A549 cells, Biosci. Rep. 20 (2000) 129–138.

[170] G. Ermak, K.J. Davies, Calcium and oxidative stress: from cell signaling to cell death, Mol Immunol. 38 (2002) 713–721.

[171] Y. Li, Z. Liao, F. Fang, X. Wang, L. Li, J. Zhu, Significant increase of Curie temperature in nano-scale BaTiO3, Appl. Phys. Lett. 105 (2014) 1–5.

[172] S. Wada, T. Suzuki, T. Noma, Role of lattice defects in the size effect of barium titanate fine particles - A new model, J. Ceram. Soc. Japan. 104 (1996) 383–392.

[173] L.B. McCusker, R.B. Von Dreele, D.E. Cox, D. Louër, P. Scardi, Rietveld refinement guidelines, J. Appl. Crystallogr. 32 (1999) 36–50.

[174] H. Kurata, E. Lefèvre, C. Colliex, R. Brydson, Electron-energy-loss near-

edge structures in the oxygen K-edge spectra of transition-metal oxides, Phys. Rev. B. 47 (1993) 13763–13768.

[175] W. Callister, D. Rethwisch, Materials science and engineering: An introduction, 2007.

[176] H.D. Summers, M.R. Brown, M.D. Holton, J.A. Tonkin, N. Hondow, A.P. Brown, R. Brydson, P. Rees, Quantification of nanoparticle dose and vesicular inheritance in proliferating cells, ACS Nano. 7 (2013) 6129–6137.